The
University
Of
Sheffield.

The Influence of Blade Chord on the Aerodynamics and Performance of Vertical Axis Wind Turbines

A Thesis Submitted for the Degree of Doctor of Philosophy

by

Okeoghene Eboibi

The University of Sheffield

Mechanical Engineering Department

October 2013

Abstract

The climate change due to emissions from the combustion of fossil fuel to meet the ever increasing energy demands of the growing world population has roused the attention of governments and individuals to protect the environment. The formulated policies to protect the environment have aroused interest in wind turbines as an alternative source of energy. The suitability of the vertical axis wind turbines (VAWTs) in harnessing energy from the wind in the built areas have been shown, but there still exists a large knowledge gaps in the aerodynamics and performance of the VAWT especially in the design and selection of an appropriate blade chord. This thesis studied the influence of the blade chord on the aerodynamics and performance of vertical axis wind turbines through experimental and computational fluid dynamics methods. Two VAWT configurations of blade chords 0.04m (AR = 15) and 0.03m (AR = 20) with corresponding solidities of 0.34 and 0.26 were used for the investigations. The performance and the flow fields of the two configurations were measured experimentally through the use of performance measurement method and Particle Image Velocimentry (PIV) measurement techniques. All the experimental tests were conducted in a low-speed open suction wind tunnel and the results are presented. Computational fluid dynamics modelling based on the Unsteady Reynolds Average Navier-stokes (URANS) was employed to simulate the two configurations at the same wind tunnel test conditions to complement the revelations from the experimental tests. The developed CFD models after a parametric study that enabled the selection of the model's features were validated against experimental data by comparing both forces and the flow physics. Vorticity of the CFD flow visualisation and blade forces provided an additional and penetrating insight into the aerodynamics and performance of the VAWTs by linking flow physics, and performance to the aerodynamics. The VAWT flow physics, aerodynamics and performances have been shown to depend on the Reynolds numbers that ranges from $1.27\text{x}10^3$ to $1.1\text{x}10^5$, the blade chord (solidity), the azimuth angle blade stall is initiated and the dynamic stall associated with the flow fields around the blade. At 6m/s test condition, the C = 0.04m VAWT attained peak CP = 0.165 at $\lambda = 4$, while the C = 0.03m VAWT performed in the negative region at all the λ. The better performance attained by the C = 0.04m VAWT over the C = 0.03m VAWT was repeated at all other wind speeds tested in the experiments and also in the computational fluid dynamics investigations. The C = 0.04m VAWT attained a higher peak CP = 0.326 at 8m/s at $\lambda = 3.75$ indicating increased performance with increases in Reynolds numbers. This trend was equally seen with the C = 0.03m VAWT in the experiments and also the computational fluid dynamics results. The VAWT with $\sigma = 0.34$ performed better than $\sigma = 0.26$ VAWT in all the conditions tested due to its higher Reynolds numbers and solidity differences that influence the nature of the dynamic stall phenomenon associated with the flow fields around the blades.

Declaration

The work presented in this thesis is carried out in the Mechanical Engineering Department at the University of Sheffield between November 2010 and September 2013. I declare that no part of the work has been submitted before to the University of Sheffield or at any other University for the award of a degree. The work presented in this thesis is entirely the results of my own efforts and does not include collaborative work except stated otherwise. The thesis contains about 120 figures and approximately 64,000 words.

Signed:

Okeoghene Eboibi

Date: 14/11/2013

This thesis is dedicated to my wife, Carol.

Acknowledgements

First, my acknowledgements go to my supervisor, Dr. Robert Howell, for his helpful expertise, encouragements, and advice during the research period. His amiable disposition, penetrating critiques and consistent mentoring have made my study and stay in Sheffield memorable, indeed I am very grateful.

My acknowledgements go to the research group members including those who have successfully concluded their studies; Jonny, Louis, Dorit, Jon, Kanok, Ethan, Cora, Stu and Danial. Thank you all for your good company. To Jonny and Louis, I am grateful for all the assistance provided to me, in the understanding of the basics of experimentation in VAWTs and also CFD modelling. My gratitude also goes to the technicians in the workshop for the assistance provided for the fabrication works of the experimental equipment. Also, I thank my friends and the Nigerian community in Sheffield.

The Tertiary Education Trust Fund and the Management of the Delta State Polytechnics, Ozoro, Nigeria are appreciatively acknowledged for the financial assistance that enabled me to pursue and accomplish this endeavour. Also, I thank the Ozoro Polytechnic community, especially the School of Engineering for filling in the gaps created by my absence.

To my parents, brothers and sisters, I say thank you for all your supports through prayers and advice of encouragements to hold on, especially when my morale was low. I appreciate you all for your genuine concerns. I am gratefully indebted to my wife, Carol, and our children, Ewomazino D., Elozino F., and Orozino N for all your courage and strength to carry on while I was away from the family for these years. May the good Lord grant our wishes so we can be happier ever when the family reunites. Finally, I thank the almighty God for the strength, guidance, provisions, and also for his grace and the gift of perseverance all through the period of this journey. He has been and remained God forever.

Nomenclature

Symbol

A	hot wire anemometry, constant 1
AR	aspect ratio
B	hot wire anemometry, constant 2
C	blade chord
C_D	drag coefficient
C_L	lift coefficient
C_M	moment coefficient
CP	power coefficient in experiment
CP_{cfd}	power coefficient in experiment
D	wind turbine diameter
d_o	pressure outlet boundary distance from VAWT axis
d_p	particle displacement
E	hotwire voltage
F	capacity factor
F_D	drag force
F_L	lift force
g	acceleration due to gravity
I_{rig}	rotor rotational mass moment of inertia
k–ε	the turbulence model based on turbulent kinetic energy and turbulent dissipation
k-ε RNG	the variant of *k*-ε using Re-Normalisation Group methods
k–ω	turbulence model based on turbulent kinetic energy and specific dissipation
k–ω SST	the variant of k–ω by Menter (1993)
L	aerodynamic loss factor
M_p	particle magnification
N	the number of blades
n	hot wire anemometry, constant 3
P	pressure, rated power
PB	the blade power (three blades)
Pw	the wind power
q	dynamic pressure
R	rotor radius,
R_g	gas constant
Re	blade Reynolds number
R_p	radius of particle
S	wind turbine spacing
S-A	Spallart Allmaras turbulence model
T	temperature
t	time
Δt	inter image time, change in time step
T_B	blade torque
T_{res}	the resistive torque

Symbol continued...

T_u	turbulence intensity
u'	standard deviation of velocity fluctuations
U_{mean}	mean velocity
U_p	particle velocity
V	wind velocity
V_b	the blade velocity
V_R	relative velocity
V_w	free stream wind speed
V_S	settling velocity of particle
y^+	dimensionless wall distance

Greek symbol

α	angle of attack
ΔCP	change in CP
θ	azimuth position
λ	tip speed ratio
μ_f	dynamic viscosity of fluid
ξ	rotor angular acceleration
ζ	vorticity
Γ	circulation
ρ	air density
ρ_f	density of fluid
ρ_p	density of tracer particle
σ	rotor solidity
ω	rotor angular speed

Abbreviations

CFD	Computational Fluid Dynamics
DES	detached eddy simulation
FOV	field of view
HAWT	horizontal axis wind turbine
LES	large eddy simulation
LEV	leading edge vortex
NACA	National Advisory Committee for Aeronautics
PIV	Particle Image Velocimetry
RANS	Reynolds Averaged Navier–Stokes
TEV	trailing edge vortex
URANS	Unsteady RANS
VAWT	vertical axis wind turbine
VTM	vorticity transport model
WPD	wind farm power density

Table of Contents

List of Figures

Chapter 1

Introduction

1.1 The Environment and Wind Energy

The concerns over global warming and greenhouse effects that are caused by human activities have continued to grow in recent years. These concerns have increased the awareness of alternative sources of energies that are friendlier to the environment and these concerns have led to the formulation of policies by the stakeholders in the wind industry. One of such policies was that of the UK government, under the Kyoto Protocol, in which a target was set for the renewable energy generation of 10% of UK energy consumption by 2010. This policy contributed to the achievement of 40% of the UK's renewable energy generated from wind energy in 2010 [1]

Harnessing energy from the wind will not only reduce environmental pollution through minimising carbon emission into the atmosphere but can also provide adequate and affordable energy which can aid in the eradication of poverty thereby raising the living standards. This also encourages the creation of jobs through researches into the improvement, developments, operations and maintenance of wind machines. Wind machines are wind energy converters which harness the kinetic energy in the moving wind through the rotor blade(s), the rotor shaft and the generator that converts the harvested mechanical power to electrical power.

1.2 The Wind Machine

Wind machines are broadly classified into drag-type and lift-type machines. The drag machines attain maximum performance at lower tip speed ratios and also the blades move slower than the wind velocity while the lift machines attained their optimum performance at higher tip speed ratios and the blade speed is always greater than the wind velocity hence move faster. The blades of the lift machines are usually of aerofoil profiles whereas those of the drag machines are not. The drag machines are mostly used in performing tasks in which low power is required, for example, pumping of water for irrigation and other uses while the lift machines are adapted for the generation of electricity.

Electricity can be harnessed from the wind by lift-based wind machines, which are again, broadly classified as horizontal axis wind turbines (HAWT) and vertical axis wind turbines VAWT [2]. HAWT are dominant for large scale energy generation because of many years of research attention they have attracted. The VAWT received little or no attention until 1970 during the oil crisis. This led to the re-invigoration of research interest in many renewable energy conversion systems.

The Sandia National Laboratories of the Department of Energy, USA, the National Research Council of Canada, Reading University in the UK, and Sir

Robert McAlpine and Sons Ltd were the earliest that carried out research on VAWT around Late 1970s and 1980s [3-6]. HAWT are believed to be more efficient for electricity generation in wind farms, and this drastically reduced interest in research of VAWT.

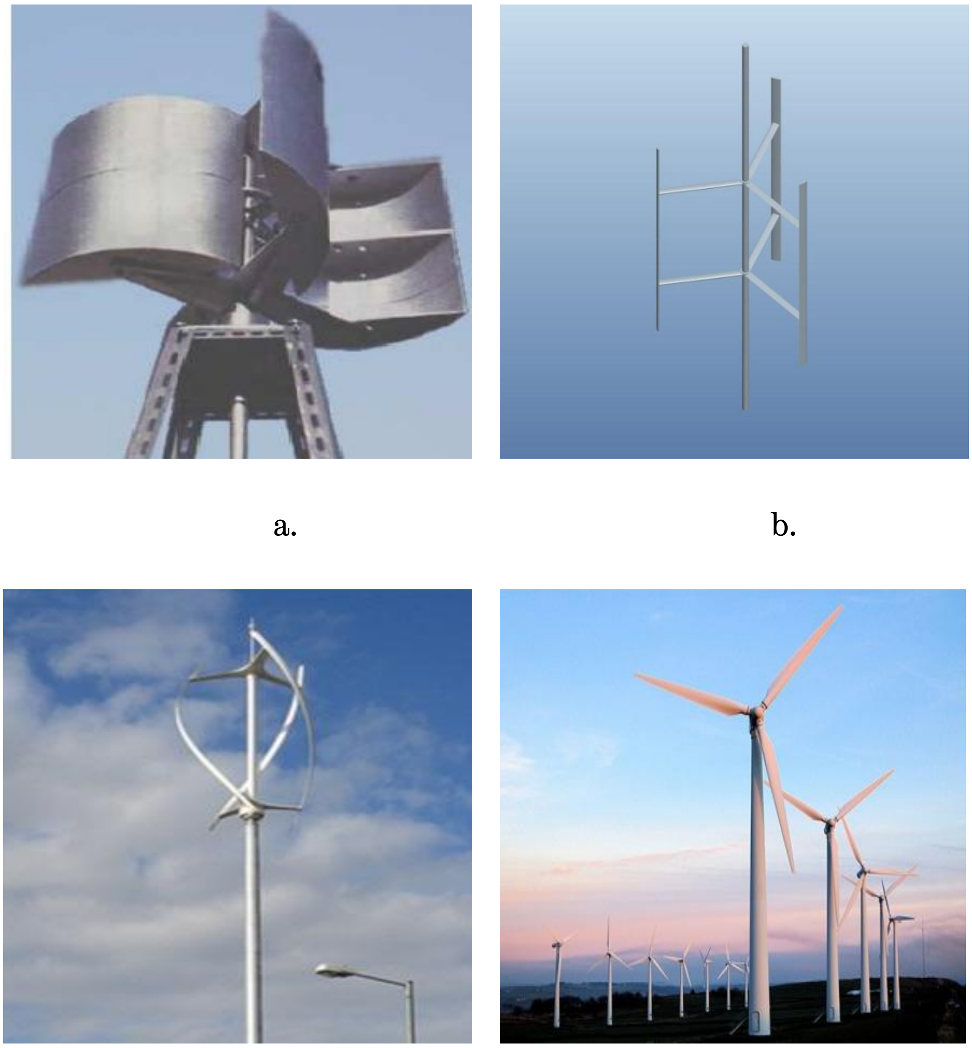

a. b.

c. d.

Figure 1.1. Selected types of wind machines: a) drag VAWT, b) H-type lift VAWT, c) helical twist-type lift VAWT, d) upwind-type lift HAWT.

Evidently, it has not been proven beyond doubt that HAWT are better than VAWT in terms of performance when compared on an equal scale. With the inherent advantages the VAWT has over the HAWT, the VAWT has attracted increasing research interests in recent time. The advantages of VAWT over the more established HAWT, especially when the VAWT is used in the built environments are as follows:

- The blades are made of symmetrical aerofoils without twist and taper which make them easier and cheaper to manufacture whereas the blades of the HAWT are twisted and tapered from the root to the blade tips and usually of several metres in length which make the manufacturing and transportation of the HAWT blade complex and expensive.
- Lower sound emission because of lower blade speeds since, optimum performance is attained at lower tip speed ratios when compared to the higher tip speed ratios at which the HAWT attained its maximum power which generates loud noise.
- The rotor shaft is vertical and placed near the ground therefore, does not need a tall tower like the several metres of tower height required for the HAWT for effective performance.
- The generator and the gearbox can be placed near the ground which makes maintenance easier when compared to the HAWT that has the gear box several metres away from the ground.
- It does not need yawing mechanism since the blades are attached to the rotor at equally spaced angles, for example, $\theta = 120^{\circ}$ for the three bladed VAWT, so the VAWT see wind stream in all directions whereas the vertical plane of the HAWT blades must be perpendicular and opposite in the wind stream direction hence, a yaw mechanism is needed to always keep the blades in the direction of the wind stream.
- Better performance in turbulent air flow [7] when compared to HAWT. This makes the VAWT usable in areas where tall devices are

prohibited by planning permission concerns that are relating to radar [8].

The VAWT also present some disadvantages when compared to the HAWT:

- The short tower makes the VAWT less accessible to higher wind speeds in the higher attitude whereas the HAWT can access higher wind speeds due to the tall tower.
- The HAWT are better optimised due to many years of research it has enjoyed so better overall performance may be achieved over that of the VAWT, and also the HAWT blade pitch can be easily controlled for maximum energy extraction over that of the VAWT.
- The flow around the VAWT is highly unsteady due to the changes in the blades forces with variations in azimuth angles and angle of attack. So the VAWT present complex aerodynamics that can limit the life span, whereas the aerodynamics associated with the HAWT is less complex.

1.3 Kinematics of VAWT

Aerodynamics is fundamental to the understanding of how the VAWT operates; hence it is major contributing aspects considered when improving the VAWT design. The aerodynamics is dependent on the kinematics of the VAWT. So, the kinematics (the geometry of motion) of the VAWT also influence the flow physics as well as determining the performance efficiency. Therefore, the theory that defines the parameters involved in the geometry of motion and their interrelationship with respect to the blade forces must be understood so that the VAWT can be discussed correctly. One of such parameters that influence the performance of the VAWT is the Reynolds number. The Reynolds number is defined in Equation 1.1.

$$\mathrm{Re} = \frac{\rho \mathrm{vC}}{\mu} \tag{1.1}$$

The Reynolds number can be dependent, on the blade speed (V_b) and since a comparison of two VAWT configurations is being made in this study, and with Equation 1.2 defining λ, the Equation 1.1 is modified to Equation 1.3.

$$\lambda = \frac{V_b}{V_w} = \frac{\omega R}{V_w} \qquad 1.2$$

$$Re = \frac{\rho \lambda V_w C}{\mu} \qquad 1.3$$

Figure 1.2 defines the velocity vectors of the VAWT blade as it rotates through one cycle. The angle of attack, α, changes with the blade azimuth position and also with the λ, as the blade travels around a cycle. These variations in the angle of attack which can be deduced From Figure 1.2, and defined in Equation 1.4, can influence the blade stall phenomenon in a cycle.

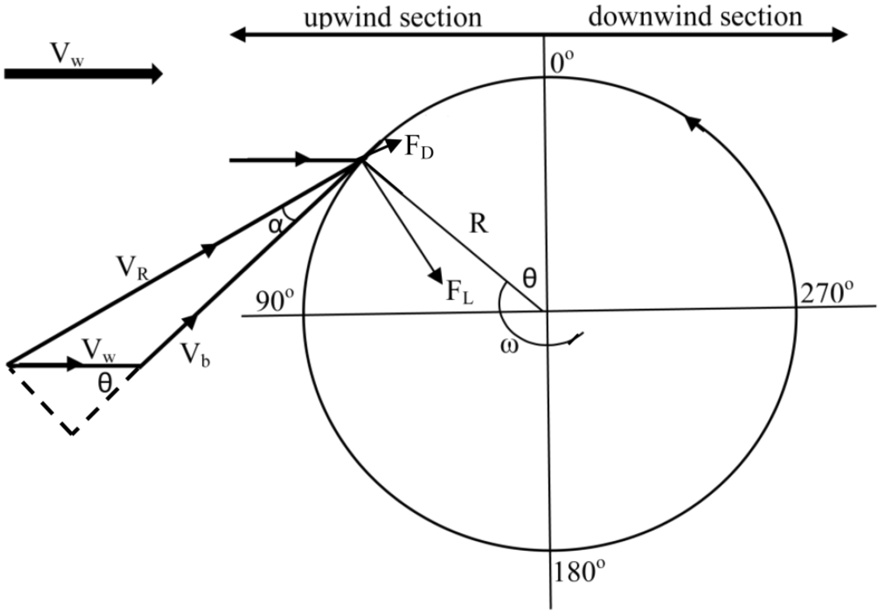

Figure 1.2. Definition of VAWT velocity vectors.

$$\alpha = \tan^{-1}\left(\frac{\sin\theta}{\lambda + \cos\theta}\right) \qquad 1.4$$

The changes in angle of attack also influence the relative velocity which the blade sees and from the Figure 1.2 the relative velocity can be defined as:

$$V_R = V_w \sqrt{\lambda^2 + 2\lambda\cos\theta + 1} \qquad 1.5$$

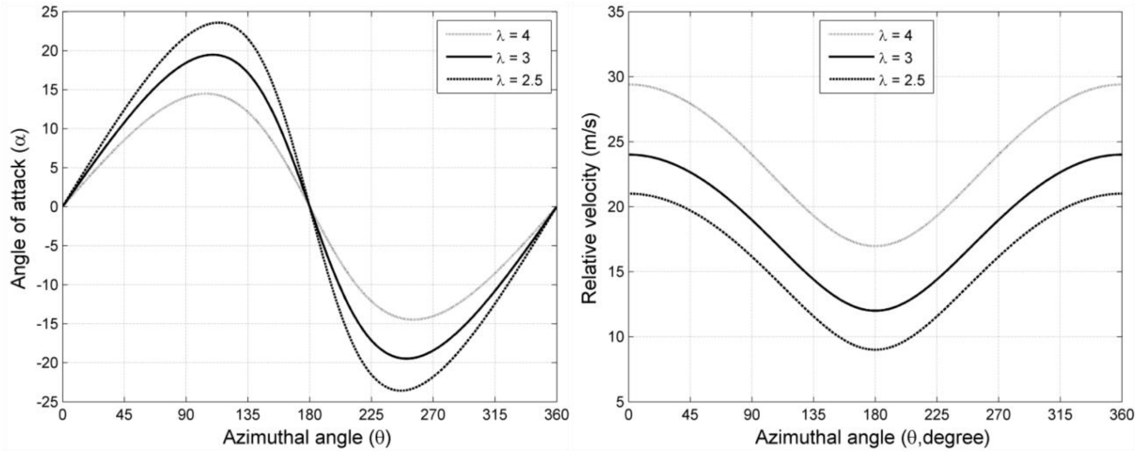

Figure 1.3. Variation of α and V_R with θ and λ.

The variation of the angle of attack and the relative velocity versus azimuth angle with changes in λ (Figure 1.3) are discussed in chapter six, which form the basis for the analysis and description of the computational fluid dynamics results. As the blade rotates the flow incidence on the blade causes the generation of aerodynamic forces. The lift force and the drag force also vary with changes in the blade's azimuth position and the λ. The aerodynamic forces generated can be resolved into the normal force component which is important in structural considerations and the tangential force component which determines the performance attained by a VAWT. For this study the tangential force was considered, since detailed structural analysis of the VAWT is not within the scope of the investigation presented in this thesis. From Figure 1.2 the blade torque can be inferred and defined in Equation 1.6. The drag component of the blade torque always acts in the negative direction.

$$T_B = F_L R\sin\alpha + F_D R\cos\alpha \qquad 1.6$$

Finally, the VAWT coefficient of performance is defined in Equation 1.7. The CP determines how much power the VAWT can extract from the available power in the wind by the ratio of the blade power to the wind power.

$$CP = \frac{P_B}{P_w} \tag{1.7}$$

Where:

$$P_B = T_B \omega N \tag{1.8}$$

$$P_w = 0.5 \rho A V_w^3 \tag{1.9}$$

1.4 Aim of the Study

The literature review presented in chapter two has revealed that much research have been conducted on the understanding of the VAWT, especially the scales that are applicable in the urban environment. These researchers focused on tests of performance parameters in steady wind conditions using various types of VAWTs and recently, investigations have been extended to the unsteady wind conditions. In all these studies in the literature, there has not been any detailed investigation into the effects of changing blade chord on the performance and aerodynamics of VAWT. This gap in VAWT knowledge, the study presented in this thesis is aimed at fulfilling.

The aim will be achieved through the following specific objectives:

- Creation of an additional three bladed VAWT configuration of smaller blade chord (σ = 0.26) to the existing configuration with a bigger blade chord (σ = 0.34), $\sigma = NC/R$.
- Experimental measurements and determination of the power coefficients of the two VAWT configurations at different wind speeds and λ using the “spin down” method in a wind tunnel test cell.

- Application of particle image velocimentery in the visualisation and measurements of the flow fields around the blades of the two VAWT configurations at different wind speeds and λ.
- Analysis and discussion of the experimentally measured performance and flow physics of each VAWT configuration at different wind speeds and tip speed ratios.
- Comparative analysis and descriptions of the performance and flow physics of the two VAWT configurations at different and at the same Reynolds numbers at various tip speed ratios.
- Development of 2D CFD models of similar size to the two VAWT configurations used in the experimental measurements through detailed verification of settings that enhanced the choice of appropriate features of the models and also, through a thorough validation campaign that established the validity of the CFD models and the chosen turbulence model.
- Simulation of the 2D CFD models using Fluent 12.1 while monitoring the forces, which could not be measured experimentally, to complement in the explanation of the aerodynamics and performance of the VAWT.
- Analysis and discussion of the angle of attack, relative velocity of the VAWT. Also the analysis of the monitored forces, of the two configurations including the CFD flow physics and discussion of the influence of tip speed ratios on the forces and flow physics at various wind speeds.
- Comparative analysis and description of the power coefficients, aerodynamics and flow physics of the two configurations, at the different and the same Reynolds numbers and at various tip speed ratios.

These specific objectives formed the core of the body of work presented in this thesis and provided a detailed link amongst power coefficients, forces, angle of attack, relative velocity and dynamic stall phenomenon. Although the VAWT configurations used in this study operate at relatively low

Reynolds numbers due to their small sizes and the performances attained may not be attained by the commercial VAWT due to the differences in the scale, the revelations from this study are adaptable to the commercial wind machines.

1.5 The Thesis Outline

The thesis is divided into three main parts; the introductory part, the main (body) part and the concluding part. The links between all the chapters that form all the parts of the thesis is presented in Figure 1.3. The introductory part, contained in chapter one, introduces the thesis detailing the need for renewable (wind) energy, various types of wind machines, comparison between the VAWT and the HAWT. Also, the geometry of the motion of the VAWT around a complete cycle and the aims and objectives of the study is equally contained in chapter one.

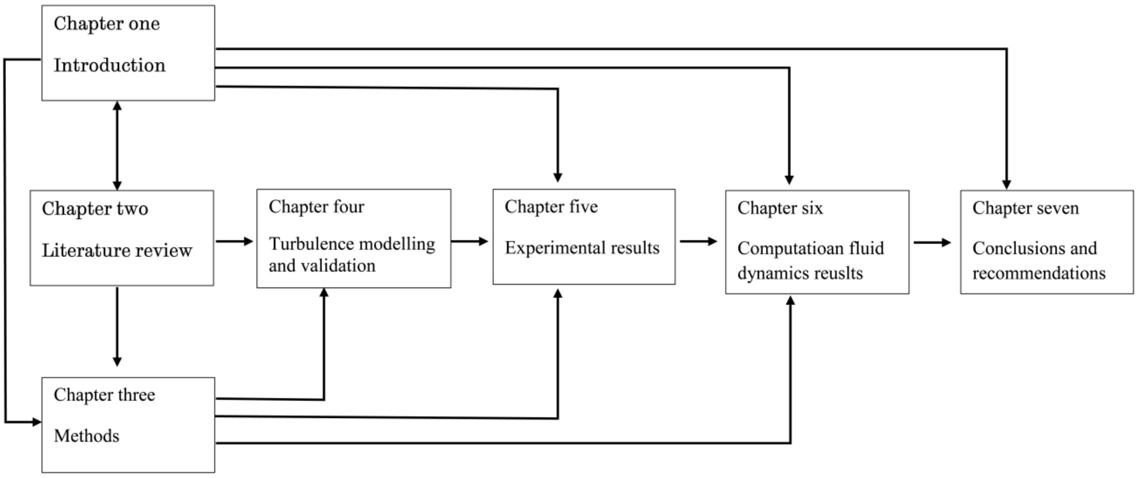

Figure 1.4. The thesis structure.

The main part of the thesis is contained in chapters 2 to 6 inclusive. The chapter two is the literature review. It contains a review of related studies including the evolution of researches in VAWT through the use of momentum models and performance related parameters. The literature review also contained various methods applied in the research into VAWT and the knowledge gaps that justify the need for this study.

The methods adopted for this investigation are presented in chapter three. The methods include the experimental performance measurement techniques, the particle image velocimentry techniques and the development of the computational fluid dynamics models.

The turbulence modelling and CFD validation campaign is presented in chapter four. It contained a static aerofoil study in which a list of turbulence models was tested and reduced to one. Also, the chapter four contains the validation of the developed CFD models using forces and flow physics obtained from the experiments and simulations.

The experimental results are presented in chapter five. The experimental results include the analysis and discussion of the determined power coefficients of the two VAWT configurations, visualised and measured flow fields of the two configurations at various wind speeds and Reynolds numbers. The chapter five also includes the influence of the blade chords on the performance of VAWTs, by a comparative description of the two VAWTs performances using the measured power coefficients and the visualised flow fields at various Reynolds numbers and tip speed ratios.

The chapter six contains the computational fluid dynamics results detailing the power coefficients versus tip speed ratios at various wind speeds for the two configurations, the angle of attack, and the relative velocity versus the azimuth angle. The chapter six also contained the influence of tip speed ratios on the forces and flow physics of the VAWTs, and a comparative description of their performance, aerodynamics and flow physics at various Reynolds numbers and tip speed ratios.

The concluding part is contained in chapter seven. All the major revelations from the investigations (both from the experimental and from the CFD investigations) are summarised in chapter seven which confirm the actualization of the objectives of, and the contributions the study has made to existing knowledge. The chapter seven also contains recommendations for future research.

Chapter 2

Literature Review

2.1 Introduction

This chapter presents a review of publications in the literature that were considered in the course of making some important decisions, and those that are relevant to this investigation with the aim of placing the research conducted in this thesis into perspective and proper context. The review also contains an evaluation of the contributions and shortfalls of the available relevant published materials, so areas that need further research into the understanding and development of VAWT technology is exposed. Some of these gaps this investigation aimed to fulfil.

The chapter is divided into two main sections, namely:

- VAWT performance assessment parameters and,
- VAWT investigative methods and application.

The observations and gains from each of these sections are discussed to show the numerous factors that can affect VAWT performance and aerodynamics, and also the accuracy of results from various available methods of investigations.

2.2 VAWT Performance Assessment Parameters

The design of VAWT is a very sensitive and complex task as it involves a thorough understanding of the different parameters that can affect the longevity and performance of VAWTs. So it is necessary that correct decisions are made in the initial design stages to achieve the desired goals. To make these decisions, the single and collective effects of the different parameters on VAWTs design must be understood, since a single parameter cannot conclusively determine how the VAWT performance and lifespan can be improved.

Following design and scientific research tradition, investigations are divided into units, parameters in the case of VAWT, for tests by varying different parameters for proper understanding of the effects of such parameters varied. Thereafter, the revelations from these separate parameters tested are married for an overall decision regarding solution or improvements. Reviews of literature of some of the important parameters that can affect VAWT performance are therefore presented in the following subsections in relation to this thesis.

2.2.1 Aerofoil Thickness and Camber

The investigation of the performance of the NACA aerofoil profiles by Jacobs and Sherman [9] around 1937 provided performance data sets of symmetrical aerofoil sections on a wide range of Reynolds number which many results from research into VAWT on similar aerofoil are compared. Due to the availability of these performance data sets the symmetrical aerofoil has been a preferred choice for most investigations. Recently, Danao et al [10] examined the effects of aerofoil thickness and camber on the performance of a 5Kw scale VAWT with CFD methods. It is shown that thinner aerofoils performed better than the thicker aerofoils due to the higher pressure coefficient experienced by the thinner aerofoils so more energy is extracted by the thinner aerofoils than the thicker blades. It was also revealed that slightly cambered aerofoils such as LS0421 can improve overall performance of the VAWT better than a highly cambered one. Also, in a similar investigation in which the self-starting capability of the VAWT was studied with emphasis on cambered blades, Beri et al [2] asserted that cambered blades can provide the potentials for the self-starting of the VAWT with the attendant effect of attaining peak performance at optimum wind speeds.

Healy [11] had earlier, in 1978, used the data in NACA TR 568 to compute power coefficients for NACA profiles 0009, 0012, 0015 and 0018 through a computer program based on a multiple-stream tube model. The investigation was conducted at a Reynolds number range of 2×10^5 to 2×10^6 and concluded that thicker blades performed better than thinner aerofoils at low turbine Reynolds numbers due to the thicker aerofoils resistance to stall. Using the same model Healy [12] also investigated the influence of aerofoil camber on VAWT performance and concluded that the closer the cambered aerofoil is to symmetry the better its power output with the added advantage of avoiding excessive turbine speed, which, to some degree, is in agreement with the recent Danao et al [10] and Beri et al [2] investigations but, the authors disagreed on the aerofoil thickness influence on VAWT performance, likely, due to the differences in the numerical methods used in the studies.

Baker [13] in 1983 and Kirk [14] in 1998 conducted similar investigations with the aim of enhancing the starting capabilities of VAWT by analysing the performance of VAWT with cambered aerofoils also. The revelations from the two studies are in agreement concluding that cambered aerofoils can benefit in the maximum extraction of power from the wind at the upwind section of the rotation, hence increasing overall performance of the VAWT, while also aiding in the self-starting ability of the VAWT. Islam et al [15-17] also concluded that cambered aerofoils can improve performance of VAWT.

The parametric studies of McIntosh [18] revealed that thinner aerofoils can attain higher maximum power coefficients than those of thicker sections. Also, that the thicker aerofoil power curves are greatly slopped with a flatter top while the power curves of the thin aerofoils are sharply slopped with higher gradients. The maximum power coefficient is attained at a higher tip speed ratio by the thinner aerofoils than the thicker aerofoils that attained maximum power coefficient at a lower tip speed ratio, so, asserted that thicker aerofoils performed better in gusty (where rapid changes in TSR) air conditions over the thinner aerofoils.

The investigations presented in this thesis are neither focused on the self-starting ability of the VAWT nor the performance of the VAWT in gusty wind conditions. Consideration was limited to the choice of an aerofoil profile based on structural calculations by the author that shows the NACA0012 profile tip deflected by more than twice that of NACA0022 profile when under aerodynamic loading. At 7m/s the deflection of the NACA0022 was $1.3\mathrm{x}10^{-3}$m, while that of the NACA0012 was approximately $3.2\mathrm{x}10^{-3}$m. This was later confirmed during experimental tests where the NACA0012 blades were seen to have deflected and permanently twisted outward (deformed). Therefore, based on structural considerations, the NACA0022 was a better choice for the investigations presented in this thesis.

2.2.2 Solidity

Solidity is an important parameter that can influence the performance of a VAWT even after an appropriate choice of aerofoil thickness and camber is made. For the VAWT, the general definition of solidity by Shedahl et al [19] is expressed in Equation 2. 1.

$$\sigma = \frac{Nc}{R} \tag{2.1}$$

This expression is being adopted in this investigation. So solidity can be altered either by changing the number of blades or the blade chord or rotor radius. In recognition of the effects of solidity on performance of wind machines, a number of authors have conducted research to understand its influence on the aerodynamics and performance of VAWT.

Templin [20] appears in literature as the first author that investigated VAWT solidity. He developed computation programme (single stream tube theory/model), based on Glauert's [21] actuator disc theory that assumed constant velocity induction through the upstream and downstream faces of the swept volume, to test the theoretical effects of blade solidity as a geometric variable within a range of σ = 0.05 to 0.5 inclusive. The single stream tube model (Figure 2.16(a)) assumed a constant velocity induction factor, a, as the free stream velocity flow through the actuator disc, defined in Equation 2.2.

$$a = \frac{V_1 - V_2}{V_1} \tag{2.2}$$

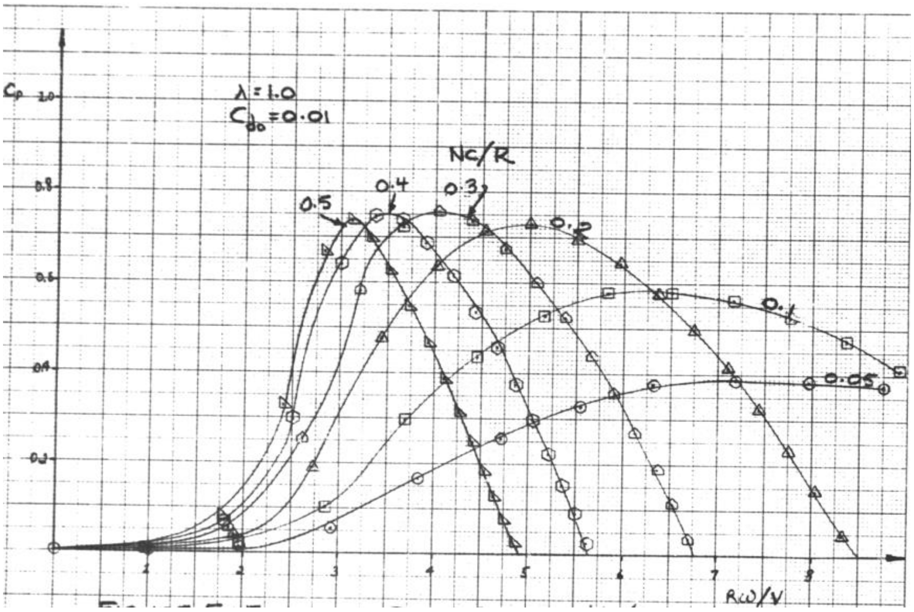

Figure 2.1. Plots of CP versus λ showing the effects of solidity [11].

From the results of the study presented in Figure 2.1, the following conclusions were drawn:

- The maximum power output is not justifiably increased when solidity is increased beyond the value of about 0.2.
- Lower value of solidity can widen the CP – λ optimum operating range of the VAWT but lower maximum power is attained.
- Due to the high rotational speeds that are common with low solidity VAWT, blade centrifugal stresses may increase at low solidity.

Templine acknowledged the limitations of the single stream tube model in over prediction of power output in the lower λ region due to stalling of the blades, and also the overestimation of rotor drag at the higher solidity due to the operational value limit allowed by the assumptions made in the model.

In what is seen as an improvement on the limitations of the single stream tube model is the multiple stream tube models, which is also based on the same principle of the single stream tube model, the difference being the control volume that is divided into multiple strips and each strip having its own actuator disc.

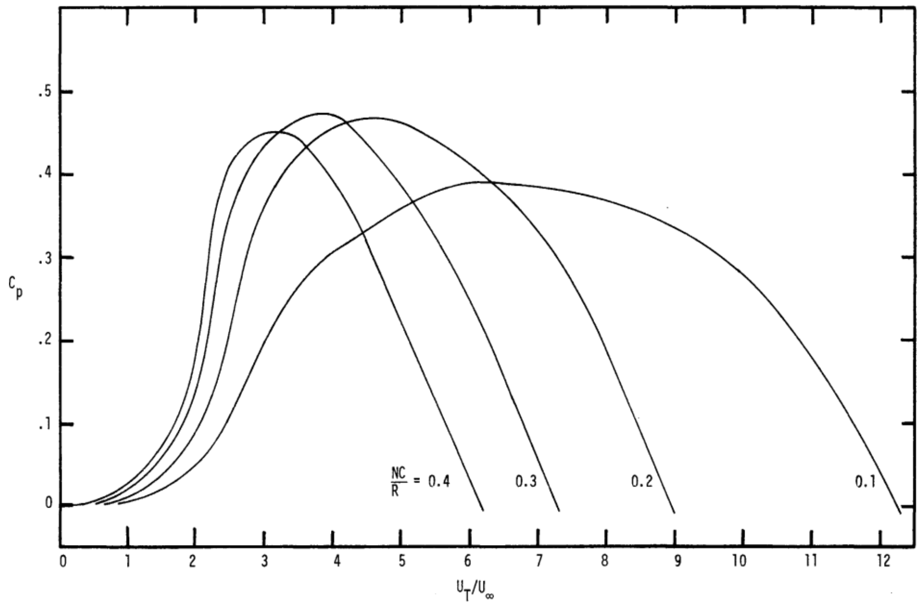

Figure 2.2. Plots of CP versus h showing the effects of solidity [13].

The multiple stream tube model was implemented by Strickland [22], after Wilson and Lissaman [23] had introduced it earlier, to correct the shortfalls of the single stream tube model by taking into account the variation of the induction factor with respect to the orbital blade position for better prediction of the blade loading. This model is also dependent on the lift and drag forces of external sources usually static aerofoil data derived experimentally. The results from this model showed improvement over the single stream tube model results (Figure 2.2) with less overestimation at the higher solidity and also at the lower λ where the blade loading is usually very high.

Mays and Holmes [24] in 1979 used a momentum model also, to study the effects of a high solidity on the performance of vertical axis windmill. Their results complement the works of Templin and Strickland. Despite the tested $\sigma = 0.75$, being higher than the upper limits of the ranges of solidity tested by the previous two authors, the trends of the performance curves of the three studies are similar. Kirke [14] compiled and compared the results from Templin, and Mays and Holmes solidity investigations which is presented in Figure 2.3.

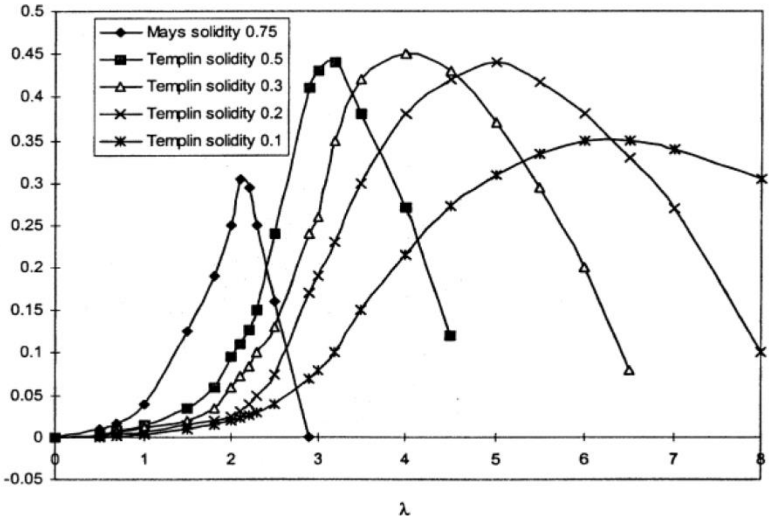

Figure 2.3. The effects of solidity on the performance of VAWTs (data from Templin, and Mays and Holmes) [6].

It is shown that the highest solidity attained the lowest maximum power coefficient in the low λ region. The curve of the highest solidity is most sharply slopped with a pointed triangular top which is completely in line with the revelations from Templin's and Strickland's studies.

Following the limitations of the models adopted for these studies, especially their dependence on external sourced aerofoil data, sufficient information is not available from the studies to properly analyse and explain the changes in VAWT performance at the various λ with the variations in solidity.

Consul et al [25] improved on the solidity investigation from the previous studies by the use of a 2D CFD model to numerically simulate two-bladed and four-bladed VAWTs of NACA0015 profile with corresponding $\sigma = 0.019$ and $\sigma = 0.038$. Although Consul et al [25] VAWT's scale was smaller and the fluid medium is water, a better attempt was made to explain some of the effects of varying solidity on VAWT performance at the various tip speed ratios of $\lambda = 3$, 4 and 8 that were analysed than had been achieved previously.

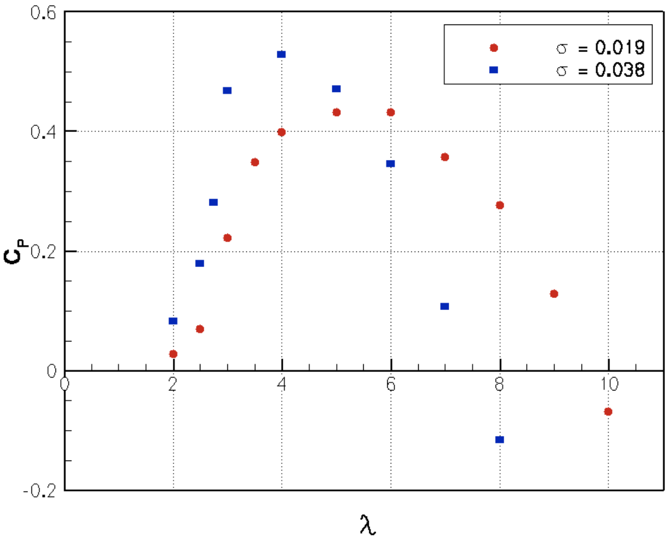

Figure 2.4. The influence of solidity on the performance of VAWTs [25]

From their results and analysis shown in Figures 2.4 and 2.5, the following conclusions can be drawn:

- VAWT maximum power coefficient increased from 0.43 to 0.53 as a result of increase in the number of VAWT's blades from two to four due to decreases in stream wise velocity so the blade of the higher solidity VAWT are presented with a lower angle of attack.

- The entire performance curve of the higher solidity VAWT is shifted to the left hence attaining the maximum power coefficient at a λ =4 while the smaller solidity VAWT attained maximum power coefficient at λ = 6.

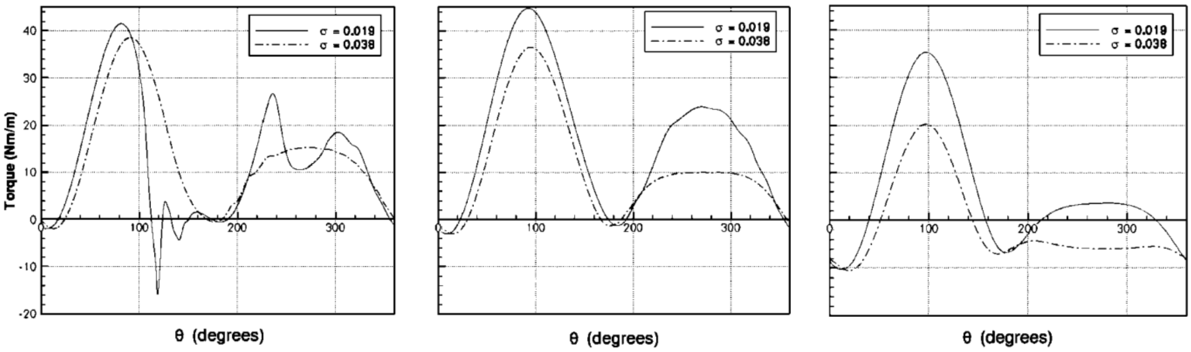

Figure 2.5. Comparison of the torque history of a blade for the two VAWTs at λ = 3, 4 and 8, [25].

The assertions made by Consul et al [25] corroborated the results of the earlier studies and those of [26], [27] and [28], and it can be seen as a good attempt at explaining the underlying aerodynamics that results from changes in VAWT solidity which is lacking in the other studies. This may be due to the superior method of investigation used by Consul et al [25]. However, the evaluations and subsequent conclusions from all these studies are based on VAWT performance on single point power coefficient or the nature and gradient of the CP - λ curves which are seen as limited comparison yardsticks in the author's opinion. Since VAWT performance is strongly influenced by the changes in wind speed and λ, the reasons adduced by Consul et al for the performance of one VAWT's solidity over the other, although arguably correct in the context, is subjective. So further investigation is needed to explain and improve on the understanding of the solidity phenomenon of VAWT.

Howell et al [29] having pointed out the importance of solidity in determining the tip speed ratio at which a VAWT can attain its maximum CP, compared the performance of a small wind tunnel scaled two- and three-bladed VAWTs. They demonstrated experimentally that the two-bladed VAWT attained a higher CP at a higher tip speed ratio, while the three-bladed VAWT attained lower CP at lower tip speed ratio.

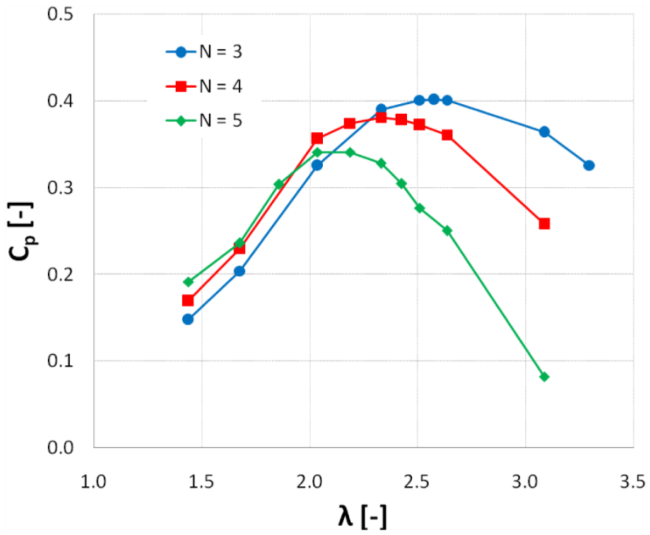

Figure 2.6. The effects of solidity on the performance of VAWTs [30]

Howell et al [29] results seem to contradict the earlier results of Templin [20] and Strickland [22] and even that of Consul et al [25] in which the number of VAWT blades was equally varied. Although, a two bladed VAWT was not tested, Raciti Castelli et al [30] in their studies, in which three-, four- and five-bladed VAWT of NACA0015 profile were compared using CFD, similarly, it was shown that the three-bladed VAWT performed better than the other configurations tested (Figure 2.6). Considering the investigations of Howell et al [29] and Raciti Castelli et al [30], although conflicting with previous studies, there is no economic justification in increasing the number of VAWT blades beyond three. Therefore, the investigation presented in this thesis is solely based on a three bladed vertical axis wind turbine.

McIntosh [18] having recognised the justification for a three bladed VAWT which he adopted in his study, conducted a parametric study using a free vortex model to study the effects of solidity on VAWT by varying the blade chord of a three bladed VAWT. Again, based on the highest power coefficient attained and the nature of the power coefficient curve, the study revealed that maximum CP is attained at a solidity range of σ = 0.2 and 0.25 (Figure 2.7). The curves of the lower solidities sloped gently so have smaller gradients, while those of higher solidities sloped sharply so had higher gradients. No detailed explanation of his results was presented since it was a mere parametric study.

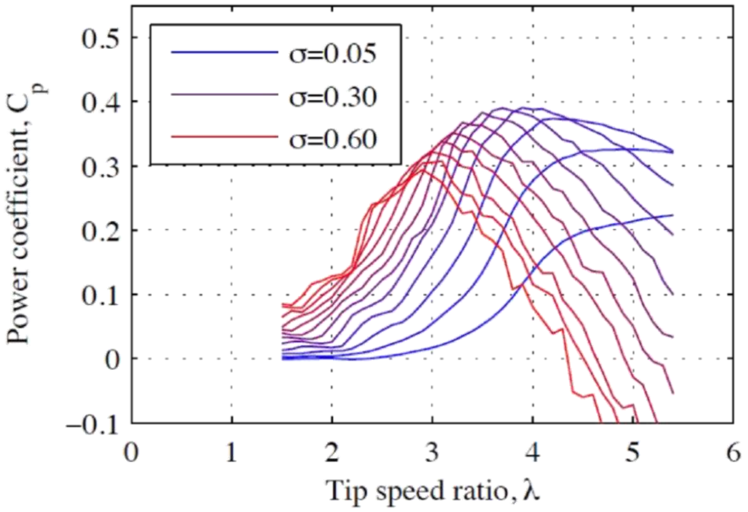

Figure 2.7. The effects of solidity by varying the blade chord [18].

In furtherance of the understanding of solidity, Eboibi et al [31] recently tested and compared the influence of solidity, on the performance of three-bladed VAWT of two NACA profiles at σ = 0.2, σ = 0.6 and σ = 0.98 with the CFD by altering the blade's chords. The power coefficients of the NACA0012 and NACA0022 were compared as well as the CFD flow visualisations. They observed that the VAWT with NACA0012 blade profile attained higher peaks at all the corresponding λ where the maximum power coefficient is reached. Also both VAWTs attained their peak power coefficients at λ = 4.5, λ = 2.5 and λ = 2 at the respective solidity of σ = 0.2, σ = 0.6, and σ = 0.98 (Figure 2.8 (a and b)). For the same solidity and turbine scale, the maximum power coefficient is attained at a similar tip speed ratio irrespective of the blade profile or thickness.

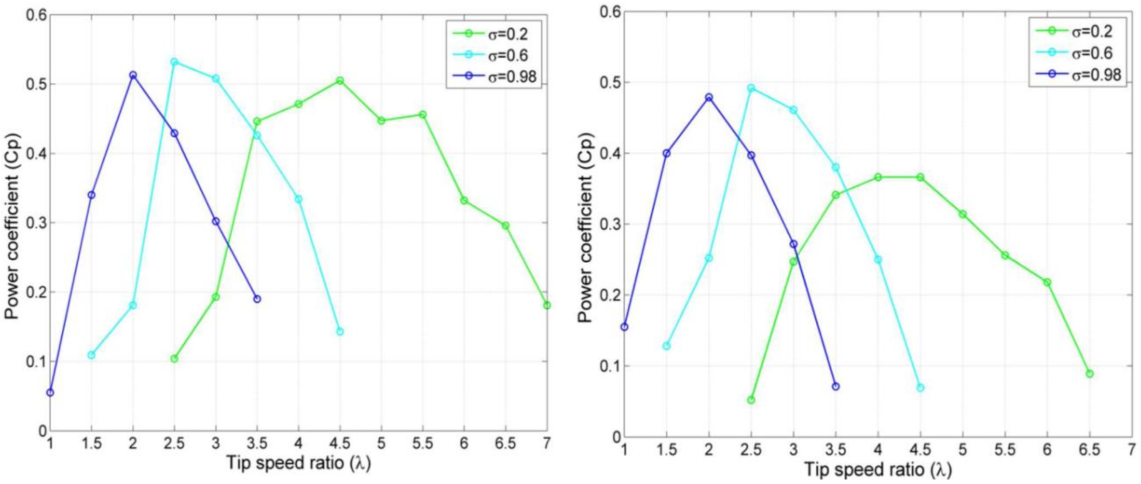

a. NACA0012

b. NACA0022

Figure 2.8. The effects of solidity by varying the blade chord [31]

At the lower tip speed ratios which ranged from λ = 1.5 to λ = 3, the VAWT with NACA0022 profile showed better performance at all the tested solidities. This further confirmed the observations of Templin [20] that thicker blades performed better at lower Reynolds numbers which corresponded to the lower tip speed ratios in this study. With flow visualisation which was related to the torque plot of a single blade for the two VAWTs at all the solidities (Figure 2.9 (a and b)) they evidently explained and attributed the performance differences observed between the solidities tested to the dynamic stall pattern that is associated with the changes of the blade chord.

Moreover, the two VAWT configurations being investigated in this thesis will be compared based on their flow fields surrounding the blades, blade loading and power coefficient. The data obtained from experimental tests including Particle Image Velocimentry (PIV) and the developed CFD investigative methods will be used, so a detailed understanding of solidity will be provided later on in this thesis since, with varying the blade chord, solidity is also varied.

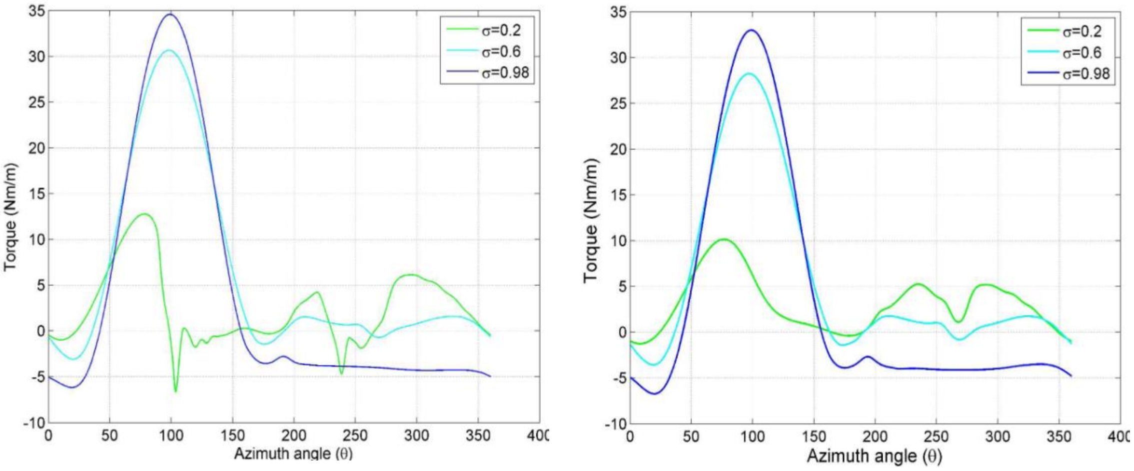

a. NACA0012 b. NACA0022

Figure 2.9. The variation of torque with changes in solidity for two VAWTs with different blade profiles [31].

2.2.3 Flow Curvature and Blade Sweep

Migliore et al [32] further show the influence of the flow around a blade in relation to VAWT performance by comparing the power coefficient of two VAWTs of different blade chords. They based their comparison on blade chord to rotor radius ratio (C/R) instead of solidity. Migliore et al assert that the inflow velocity and the α are different in every section of the chord so the blades are immersed in curvilinear flow instead of the rectilinear flow which most acquired aerofoil data are based. And the flow curvature is more noticeable as the C/R ratio is increased with the resultant effects of decreasing the power coefficient of the VAWT.

They experimentally tested two sets of blades of NACA0015 profile with C/R = 0.11 and 0.26, and also used conformal mapping techniques to transform aerofoils in curvilinear flow fields to their virtual equivalent rectilinear flow. A maximum CP, about three times higher than that of C/R = 0.26 is attained by the C/R = 0.11 despite the C/R = 0.26 seeing higher blade

Reynolds numbers (Figure 2.10). This is due to the large difference in solidity which affirmed the conclusions of the authors whose works on solidity has been reviewed in the preceding section.

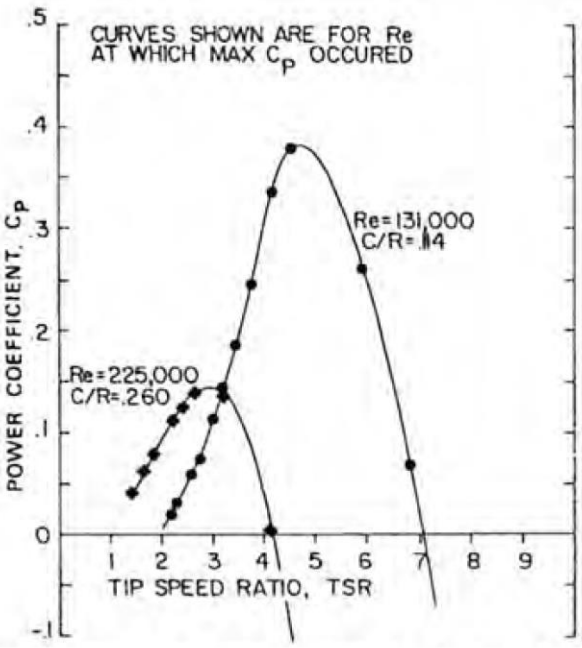

Figure 2.10. The effects of C/R on the performance of VAWT [23].

McIntosh and Babinsky [33] further the understanding in the assembly and attachment of blades to the rotor, by modelling swept and unswept bladed VAWT through the use of a Lagrangian based 2D free vortex model. The helical twisted (swept) VAWT [34] is shown to lower the power coefficient and also push the peak operating λ higher at all sweep angles tested. In consideration of the reduction in cyclic loads that is seen to reduce with increases in sweep angle with corresponding reduction in rotor vibration, which is beneficial, a moderate sweep angle (>30) is recommended. They argued that the gains from the reductions in rotor vibration at these sweep angles can offset the tolerable impact of the reductions in VAWT performance.

In a complementary investigation, three VAWTs: straight blades, curved blades and helical twisted blade configurations, were tested by Scheurich et al [35] and [36] through a vorticity transport model (VTM). Large variations in blade loading that vary with the azimuth which is transmitted as oscillatory power output (Figure 2.11) for the straight- and curved- bladed VAWTs was observed. Also, the curved blade is more disadvantaged due to the smaller radius at the blade tips so experienced oscillations in higher angle of attack with larger amplitudes but, the oscillations associated with the helical twisted blade is less. Less oscillations imply a reduction in associated vibrations of the rotor which can be of benefit in prolonging the lifespan of the VAWT.

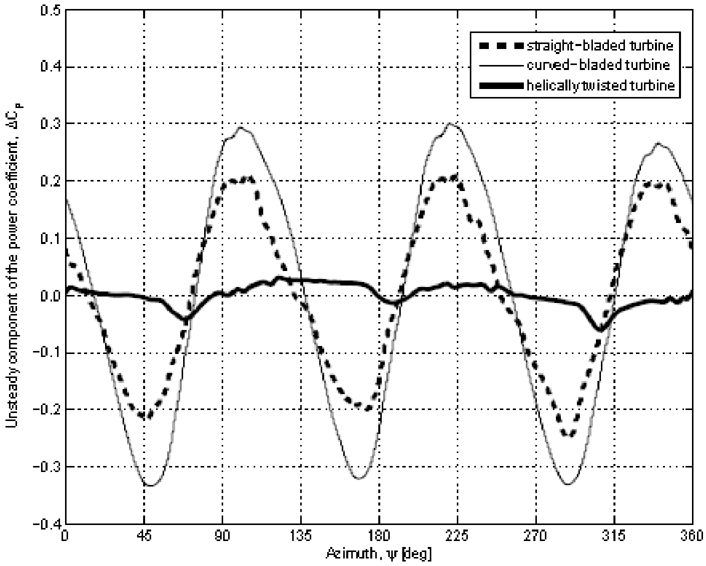

Figure 2.11. Variation of power coefficient with azimuth angle for three turbine configurations [26].

In this thesis, the straight bladed VAWT was adopted for the investigation despite the advantages that the helical twisted blade can offer. This is due to other complementary tests conducted in the wind tunnel which, the straight bladed VAWT is seen as less prone to error especially with the settings of the PIV measurement equipment.

2.2.4 Reynolds Number Effects

The Reynolds number is another very important parameter that must be considered when designing wind machines especially small to medium scaled VAWTs. Although for the purpose of wind tunnel measurements in this study, the Reynolds number is based on blade chord, the relative velocity and the effective Reynolds number the blades see are not constantly in the cyclic motion at each tip speed ratio. Its effects are not only on the extraction efficiency with which energy in the wind is converted to power but also on the lifespan of the machine. In recognition of these effects, numerous studies have been conducted to understand the influence of Reynolds number variations. Jacobs and Sherman [9] tested NACA aerofoil profile at various Reynolds numbers with the aviation industry in mind. So, despite the wide range of changes of aerodynamic lift and drag versus angle of attack shown, their results seem to have little significance in the study of wind turbines.

At the Sandia laboratory, Reynolds number has also been investigated theoretically and experimentally either by varying the free stream velocity while the blade rotation speed is kept constant or by varying the blade rotation speeds while the free stream velocity is constant. In both ways the effects of Reynolds number have been shown consistent on the performance of the VAWT. Templin [20], Blackwell et al [26], Ashwill [37] and Shedahl et al [38] showed increases in power coefficient with increases in Reynolds numbers and also decrease in power coefficient with decrease in Re.

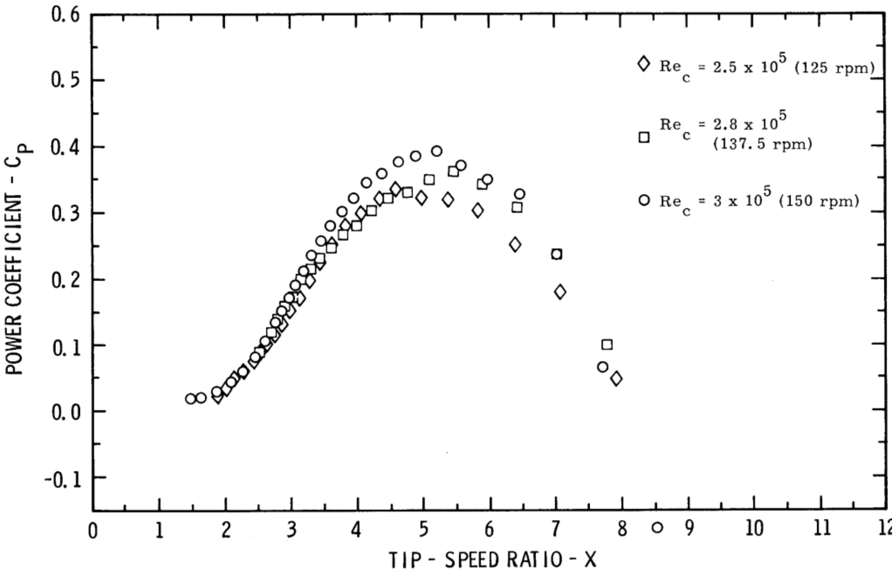

Figure 2.12. The influence of varying Reynolds number on VAWT performance [38]

They tested different scales with different NACA profiles, an example of the result from one of the test is shown in Figure 2. 12. The test of [39] showed a similar trend but with convergence and a shift of the power curves at the peak λ to the left (lower λ region) as the wind speed is increased signifying the VAWT performance approaching Reynolds number independence.

The effects of low Reynolds numbers, below 70,000, on NACA0012 aerofoil have been investigated by Laitone [40] and Kim et al [41]. Laitone [40] experimentally measured the lift force on a NACA0012 in a low turbulence wind tunnel and showed that the NACA0012 is unsuitable for all Reynolds numbers below 50,000 due to its sensitivity to variations in Reynolds numbers or turbulence intensity level. Kim el al also experimentally investigated the aerodynamic characteristics and boundary layer properties of NACA0012 aerofoil at chord Reynolds numbers of 23,000, 33,000 and 48,000 at low angle of attack between 0 and 6^o. The abrupt increased in lift coefficient between $\alpha = 2^o$ and 3^o were adduced to the abrupt formation of the attached boundary layer over the aerofoil surface. The aerodynamic characteristics observed are significantly influenced by the variation in Reynolds numbers in the low Reynolds numbers.

Again, through the testing of the two VAWT configurations at various wind speeds for their performance and flow physics, detailed analysis will be carried out to examine the influence of Reynolds number on the performance and aerodynamics of VAWT. This will be presented later on in this thesis in the experimental and computational fluid dynamics results.

2.2.5 Dynamic Stall

The dynamic stall is an important flow phenomenon that affects the performance of VAWT. It comprises of the initiation of flow separation from the blade's surface, full separation of the boundary layer, detachment, shedding of vortices and reattachment of the flow to the aerofoil surface, hence it influences the power output of VAWT. In the past decades there have been numerous studies to understand the dynamic stall phenomenon associated with the helicopter aerodynamics due to the associated effects of limiting helicopter flights and the focus of aerodynamic research were mainly on the aviation industry so studies were conducted at the corresponding Reynolds and Mach numbers at which these helicopters operates.

McCroskey et al [42] and Car et al [43] were among the first that studied the dynamic stall of aerofoils. While McCroskey et al [42] experimentally studied the flow around the aerofoil through the use of the hot film and hot wire to investigate the influence of dynamic stall on pitching moments, flow fields separation and reattachment and also, the lift and drag forces, Car et al [43] employed a smoke visualisation method to study the influence of Reynolds numbers, reduced frequency and the amplitude of oscillation on the dynamic stall phenomenon of a pitching aerofoil.

In recent times, Fujisawa and Shibuya [44], using a dye injection technique, the phase average velocity around a single bladed Darrieus rotor was visualised and measured by a combination of particle image velocimentry (PIV) and imaging techniques. They observed the generation of two pairs of vortices in one blade rotation cycle. Simao-Ferreira et al [45] also used a single bladed rotor to investigate the influence of dynamic stall on VAWTs. They compared CFD direct eddy simulation (DES) and large eddy simulation (LES) results with the results of their wind tunnel PIV measurements of a straight-bladed VAWT operating under the dynamic stall

All these studies have contributed to the understanding of the dynamic stall phenomenon and notably were that of Lishman [46] that identified the stages of the dynamic stall events from the studies of McCrosky et al and Car et al (Figure 2.12) as follows:

STAGE 1: flow reversal is seen at the trailing edge since the static stall angle is exceeded, thus, initiating the onset of the leading edge vortex formation which moves towards the leading edge of the aerofoil.

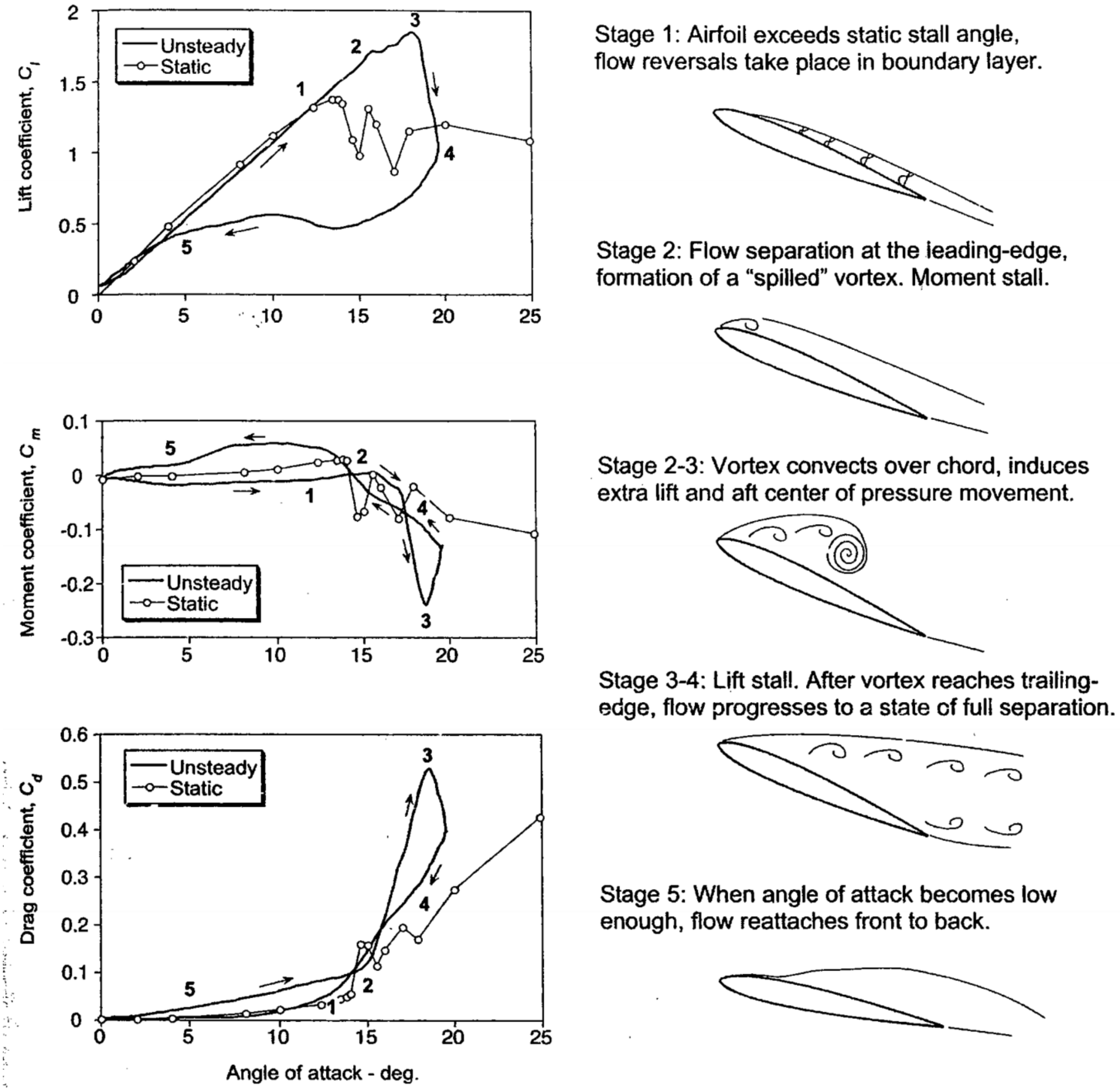

Stage 1: Airfoil exceeds static stall angle, flow reversals take place in boundary layer.

Stage 2: Flow separation at the leading-edge, formation of a "spilled" vortex. Moment stall.

Stage 2-3: Vortex convects over chord, induces extra lift and aft center of pressure movement.

Stage 3-4: Lift stall. After vortex reaches trailing-edge, flow progresses to a state of full separation.

Stage 5: When angle of attack becomes low enough, flow reattaches front to back.

Figure 2.13. The stages of dynamic process, adapted from [46]

STAGE 2: the lift coefficient increased further passed the static stall angle also with the flow reversal having considerably moved to the leading edge causing flow separation while the moment coefficient reduced in value further away from this point due to moment coefficient stall.

STAGE 2-3: the vortex increased in size and convects over the aerofoil surface with an attendant increased in the lift until the maximum lift is attained and also the movement of the pressure gradient towards the trailing edge.

STAGE 3-4: sudden drop in lift coefficient as a result of a lift stall at the maximum angle of attack is seen, and with the vortex at the trailing edge, the flow is fully separated from the aerofoil surface while vortices are being shed into the wake.

STAGE 4-5: with the reduction in angle of attack, onset of flow reattachment is initiated, although there is delay reattachment due to interaction with the shed vortices, until the angle of attack is low enough for the subsequent reattachment of the flow fields to the aerofoil surface. The reattachment starts from the leading edge and move down the trailing edge.

Through the use of PIV and CFD flow visualisation techniques, the dynamic stall phenomenon will be implemented in this investigation for the study of the blade chord influence, on the aerodynamics and performance of VAWTs. This would be achieved by comparing the changes in the dynamic stall of the blade chords with torques, the coefficient of lift and drag, hence the effects of physics of flow on the aerodynamics and performance of VAWT, at the various tip speed ratios will be shown later on in the thesis.

2.2.6 Summary

The parameters that can influence the performance of VAWTs and the conflicting revelations from various investigations have been shown. Since a single parameter can affect VAWT performance, the ability of the designer to make appropriate choice of the individual parameters is required so the end product can meet the customer expectations. In addition to improving the performance and aerodynamics of the VAWT, are also longevity and aesthetics, all of which must be given due considerations before a final design is made. Therefore, it is normal to make reasonable compromises in some aspects of the VAWTs while trying to meet the set targets. However, while the reasons behind some important decisions made in this thesis based on available literature regarding some of the parameters have been justified, the gaps in the literature which this thesis is intended to explore, some of which have been shown, are summarised in section 2.4.

2.3 VAWT Investigative Methods and Application

The numerous methods of investigating the performance of VAWT are classified into two broad categories; experimental and numerical methods. While both methods can be used to study VAWT by varying the parameter under investigation, as shown in the previous sections, there are a number of similarities and difference in these methods, which will be shown at the end of this section. Meanwhile, the methods and their applications in various studies by other authors are examined below.

2.3.1 Experimental Methods

Experimental methods is limited by the huge capital cost requirements, an array of diverse technical skills, time constrains, operational know-how, and a number of physical and environmental parameters that can influence measurements. Despite these shortcomings, it is acclaimed the most reliable method of investigation, and can be carried out by either field tests or wind tunnel tests. The Sandia National Laboratories (SNL) of the USA and the National Research Council (NRC) of Canada have been the foremost in the development of wind machines, and have led in this regard.

Sandia National Laboratories in 1974 started its VAWT experiments on 5m curved bladed Darrieus turbine in an open field and later added the 17m and the 2m turbines. The field tests were focused on the:

- Determination of the performance of the 5m, 17m, and the 2m turbines system while also varying the number of blades from 2 to 3.
- Determination of appropriate cambered section blades on 5m VAWT
- Determination of an appropriate blade mounted accelerometer on the 17-m VAWT
- Suitability of drag brake on the 5m VAWT

- Influence of blade welds and joints on the performance of 5m VAWT

However, the inability to control environmental factors to achieve an ideal state encouraged the use of a wind tunnel to investigate the blade section characteristics, parametric performance and wake measurements on 2m VAWT. The implementation of their findings appeared to have set the pace of the modern day technology and further research in VAWT.

2.3.1.1 Performance and Aerodynamics

Recently, Dabiri [47] compared the power density of wind farms with HAWTs on one hand and VAWT on the other through field experiments conducted at 7m/s. He utilised six 10m tall x 1.2m diameter VAWTs, while three of the turbines rotated in a clockwise direction the other three rotated in a counter clockwise direction with appropriate spacing between the VAWTs.

$$WPD = \frac{PF(1-L)}{(\pi/4)(SD)^2} \qquad 2.3$$

The performance of the VAWTs was measured and, the calculated power density using Equation 2.3 was compared to the power density of HAWT if they were to be sited in the same area size. The results showed about 10 times higher power density per square metre in favour of the VAWT over the HAWT because, the close spacing of the turbine improved the vertical flux of kinetic energy which is enhanced by the level of turbulence near the ground [48]. With further research and reassessment, it is obvious from the findings that, the VAWT can compete favourably with the already established HAWT.

Fiedler and Tullis [49] investigated the effects of blade offsets and pitch effect on a high solidity VAWT by comparing the performance of the preset pitch of ± 3.9° and $\pm 7.8^{\circ}$ configurations against that of zero pitched configuration. Their results showed about 29% increase in performance for the toe-out configuration while the peak tip speed ratio at which maximum power is attained is maintained. Judging from the literature, efforts are being made to increase the performance efficiency of VAWT while at the same time reducing the rotor blade chord hence cost of production, so the study could be seen as a mere academic exercise unless it is extended to lower solidity VAWT at which better power efficiency can be achieved. A similar study but with variable pitch control by Kiwata et al [50], also corroborated the results of Fiedler and Tullis. The justification for the need of the investigation and the presentation of the study were clear and orderly but the complexity of the design and extra operational requirements is not justified, not to mention the consideration of a high solidity VAWT (drag force type) which the authors saw as a drawback and recommended the construction of a larger scale to further evaluate the design.

Bravo et al [51] tested a full scale 3.5 kW VAWT at the NRC 9m x 9m low speed wind tunnel in Ottawa. The VAWT was tested at a range of 6 to 16m/s wind speed at irregular intervals. Although, the results bear a good resemblance of a typical power curve, technical details preceding the results are omitted so repeating the experiment elsewhere would require further information.

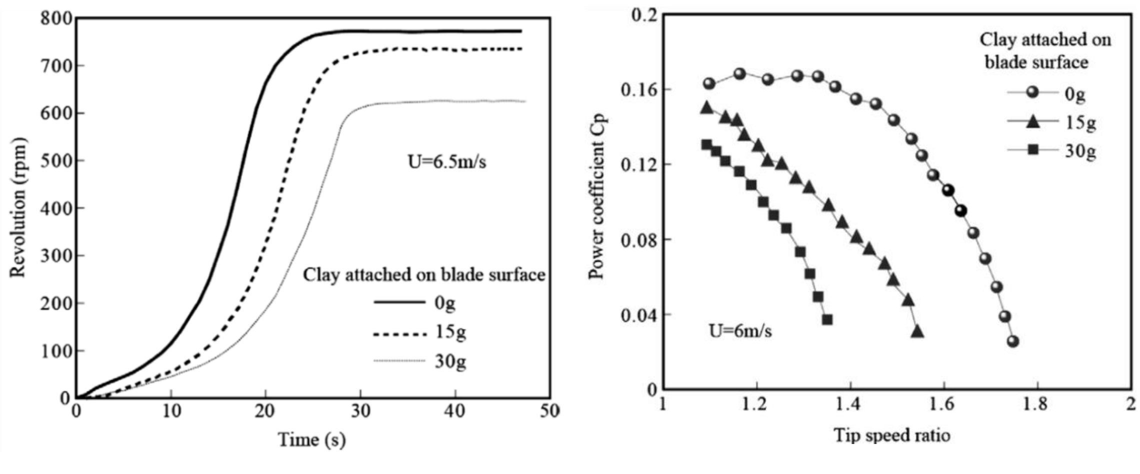

a. Change in revolution at 6.5-m/s b. Change in power coefficient

Figure 2.14. The effects of attachment on the performance of VAWT [52]

The scale and the level of revolutions attained can determine the useable power that can be generated by the VAWT. Operational VAWTs in the fields are usually subjected to harsh weather condition which alters their performance from the design conditions. To ascertain the degree of deviation from the desired output of VAWT due to the harsh weather condition effects, Li et al [52] experimentally tested the effects of attachment on VAWT in a wind tunnel by using clay to mimic ice on the blade, due to its suitability based on the physical characteristics. While the tests were in two folds; effects of attachment on VAWT rotation versus time and the effects of attachment on VAWT power coefficient versus tip speed ratio, the tests were conducted at a regular interval of 0.5m/s ranging from 5m/s to 7m/s.

The effects of the attachment showed (Figure 2.14) a remarkable decrease in both the revolution and the power coefficients. Also the performance of the VAWT decreases with increases in the weight of the attached clay. Although, the results from this investigation seems to contradict those of the surface roughness investigations of Dodd et al [4] and Ashwill [37], but with further tests to reveal the stalling of the blades resulting from the attachment, it could be seen as an improvement over these earlier studies.

Edwards [39] carried out a comprehensive experimental investigation into the fundamental aerodynamics of VAWTs. Edwards [39] designed and commissioned a three-bladed VAWT of NACA0022 profile with solidity of 0.34 which he used in investigating the influence of blade stall on the performance and aerodynamics of VAWTs. By developing a new performance measurement technique, “the spin-down method” [53], the VAWT performance was measured over a wide range of tip speed ratios at various wind speeds at the Sheffield University low speed, open suction wind tunnel. Consistency was observed in the resulting performance curves of the VAWT at the various wind speed tests, with the curves tending to converge at higher tip speed ratios signifying the VAWT performance becoming Reynolds number independent. Also negative trough was seen at lower tip speed ratios which explain the self-starting inability of the VAWT.

Recently, Danao et al [54] adopted “the spin down method” in the investigation into the influence of unsteady wind on the aerodynamics and performance of the same VAWT, which was the first experiment of its kind and a comprehensive study into VAWT performance in an unsteady wind conditions. The study revealed that the unsteady CP does not follow the steady performance path but cut across the steady CP curves due to the fluctuation of the performance with changing wind speeds (Figure 2.15), which is an improvement in the unsteady performance curves that was also shown in CFD results [55], over the earlier findings of McIntosh and Scheurich of similar investigations in which vortex models were used. Also, the study revealed no effects of small amplitudes on the cycle CP. While large fluctuating amplitudes are seen to reduce the CP, the mean λ that is lower than λ at which peak performance is attained showed hysteresis in the CP curve whereas higher λ do not.

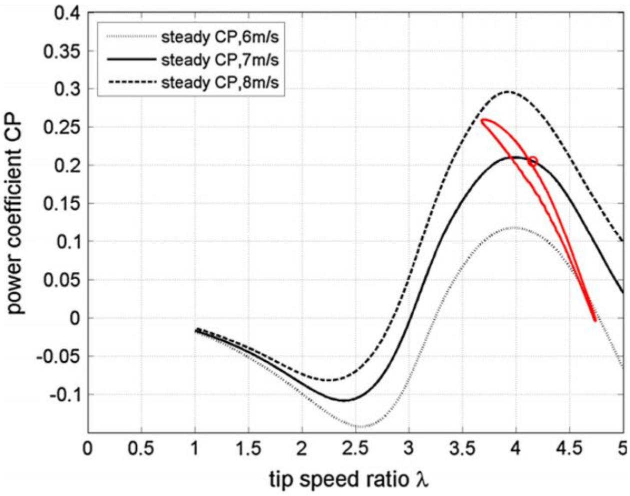

Figure 2.15. Comparison of unsteady wind performance versus steady wind performance [54].

In continuation of research into VAWT at the Sheffield University and also with the confirmation of the suitability of the VAWT performance measurement technique developed by Edwards [39], the spin down method is adopted in this thesis to further, experimentally investigate two VAWT configurations of different solidity, by altering the blade chords, at various wind speeds and blade Reynolds numbers.

2.3.1.2 Particle Image Velocimentery and Flow Physics

The experimental methods have been extended to measurements and visualisation of the velocity flow fields around the rotor blade to capture the dynamic stall phenomenon, while the blade is in motion. Tests have been conducted on one-, two- and three- bladed VAWT configurations using Laser Doppler Velocimentry (LDV) measurement techniques in a water tunnel by Brocheir et al [56], Particle Image Velocimentry (PIV) measurement techniques in a water tunnel by Fujisawa and Shibuya [44] and also PIV flow visualisation and measurements in a wind tunnel by Simao-Fereira et al [57]. Notable is the works of Fujisawa and Shibuya that, not only revealed the two pairs of shed vortices in one blade's cycle, but also the shedding of vortices being influenced by the tip speed ratios and the reference which most recent flow measurements and visualisations are compared. While Fujisawa and Shibuya conducted their tests on a single bladed VAWT at a low Re = 3000 by injecting dye in the water tunnel to aid flow visualisations and PIV measurements, Simao-Fereira [57] conducted their tests on a one-bladed rotor in a wind tunnel, at Re = 50,000 and 70,000 and also validated a 2D CFD model at $\lambda = 2$.

In a similar investigation conducted at the Sheffield University, Edwards [39] and Danao [55] have extended the flow visualisation and PIV measurement to a three bladed VAWT of $\sigma = 0.34$ with tests conducted at λ = 2, 3 and 4 at the corresponding blade Re = 40,000, 60,000 and 80,000. The measurements were also extended to cover the 360° azimuth positions at a regular interval of 10° except for a few positions that were not measured due to view obstructions resulting from the wind tunnel location and support structures.

Furthermore, the extensive visualisation and PIV measurement campaign by Edwards [39] and Danao [55] not only provided penetrating insights into the detailed dynamic stall phenomenon but also yielded revelations which hitherto has not been found in the earlier researches. For example;

- The onset and evolution of flow field reattachment in the upwind section of the rotation and the delayed reattachment of flow field to blade surface beyond 180° azimuth position.
- The onset and evolution of flow field separation, shedding of vortices and subsequent reattachment of the flow field to the blade surface in the downwind section of the rotation at the various λ.

All the studies involving visualisations and PIV measurements are only focused on the understanding of the fundamental aerodynamics of VAWT at the various λ tested. Therefore, in furtherance of the understanding of dynamic stall and its effects on the aerodynamics and performance of VAWT, the flow visualisation and PIV measurement campaign in this thesis is applied in relation to the experimentally measured VAWT performance to explain the changes in aerodynamics and performance resulting from altering of the blade chord at the various λ in which comparison of the two configurations is made.

2.3.1.3 Summary

Experimental methods have been used in the investigation into the performance and aerodynamics of VAWT, and with the improved technology, efforts have recently been made in visualisation and measurements of the flow physics around the rotor blade to further the understanding of VAWT. Although experimental test conditions are idealised so experimental performance may not be achieved in real life, they can be used to explain the cause and effects and also seen as the benchmark which the accuracy of the results from other investigative methods are verified. So, despite the limitations arising from the enormous resources needed for experimental investigations, it is still being widely used in VAWT studies. A comparison of all the investigative methods is presented in table 2.1.

2.3.2 Numerical Modelling

The numerical modelling of VAWT is aimed at making the mathematical representation of a problem to carry out a comprehensive investigation at comparably low cost. Usually, various configurations can be created and tested in a wide range of test conditions without going through the rigours associated with experimental designs. Numerical modelling can solve problem either by discretization or iteration and the computing of the solution does not terminate in a few steps. By setting a convergence criteria, it starts from an initial guess and progressed towards a solution through successive approximations until the solution is converged. Numerical modelling does not give an exact solution to a problem but get closer and closer by each successive iteration, depending on the problem, it could take several hours, and even weeks to simulate a practical problem. However, there are mathematical models that can be very fast even when applied to solve complex problems.

Unlike the experimental methods, the level of skills and resources required are less, while the timing, planning and management are also less, but, the accuracy of the solutions of numerical modelling are verified against available experimental data. While there are differences in the application codes / software, the suitability of the created grid that is used for the iteration can vary from one individual to another so the need for validation of numerical results is not only important but necessary. The application of the numerical modelling in VAWT can be achieved in two ways, either by momentum or vortex methods or by Computational Fluid Dynamics (CFD) modelling.

2.3.2.1 Momentum and vortex Methods

In the following subsections, a review of the literature of momentum and vortex modelling of the VAWT is detailed. A sequence of the evolution of the various models applied to VAWT research is made while pointing out the deficiencies and improvements of the preceding and succeeding models.

2.3.2.1.1 Momentum Models

The first application of the momentum theory in VAWT research was by Templin [20], he applied the single stream tube model in modelling the performance characteristics of the rotor. Figure 2.16 (a) presents an example of a simple single stream tube including the turbine represented as an actuator disc within which the momentum equation is solved. The deficiency of this model is caused by the following assumptions made:

- The flow velocity is uniform throughout the stream tube domain so the fluid in the domain is homogenous and incompressible.
- There is no frictional drag from the blades and the stream tube boundary.
- The blades are infinite in number, and also in length since the actuator disc is 2D.
- The lift force over the disc and rotor area is uniform irrespective of the angle of attack.
- The wake behind the rotor is non-rotating therefore uniform.
- The pressure across the disc is constant so there is no change in velocity across the disc.
- The far upwind static pressure and far downwind static pressure of the rotor is equal to the undisturbed ambient static pressure.

With these assumptions which has been revealed as uncharacteristic of VAWT flow, the single stream tube model, could not accurately predict the performance of the VAWT especially at the lower tip speed ratios where the occurrence of blade stall is predominant.

The shortfall of the single stream tube model was improved by Strickland [22] through the implementation of the multiple stream tube model which extended the model boundary resulting in the division of the flow through the domain into many independent stream tubes shown in Figure 2.16 (b) and discussed in section 2.2.2. Despite some of the improvements, the multiple stream could not always predict the performance of the VAWT accurately when compared to experimental data because the loading of the blade in the downwind section is not considered due to some of the assumptions of the single stream tube that are retained.

Paraschivoiu [58] developed the double multiple stream tube model version, to correct the deficiency encountered with the multiple stream tube model. The model incorporated the differences in the upwind and downwind sections rotation through the division of each stream tube into two halves of upwind and downwind respectively (Figure 2.16 (c)). With an additional disc at the downwind section signifying a secondary induction factor, the turbine interacts with the wind twice in one cycle at the upwind and the downwind passes. And also solve the two equations based on conservation of momentum and, aerodynamic force coefficients (lift and drag) and the free stream wind velocity twice for the upwind and the downwind sections of the rotation so the predictions are more accurate compared with the multiple stream tube. However, the predictability of experiment data and dependence on external data, by the model was still seen as a problem.

2.3.2.1.2 Vortex Models

These are flow models that incorporate the influence of vorticity in the wake of the blades while computing the velocity field around the VAWT and within the fluid domain. Bound vortex filaments are used to represent the rotor blade, and the regular shedding of span wise vortices from the trailing edge affects the strength of the bound vortex which changes with time.

The locally computed angle of attack and relative velocity are considered as well as the external aerofoil lift, drag and moment coefficient data set in the determination of the strength of the shed vortices, while the Biot-Savart law is applied to calculate the induced velocity that results from shedding of vortices. Also the free stream velocity and the induction of all the shed vortex filaments are included in determining the flow velocity.

The vortex models that were first introduced by Larsen [59], and followed by the models developed by Fanucci and Walters [60], Wilson [61], and later Holme [62] are based on similar principles and assumptions:

- The models considered a small range of angle of attack so could not be used to analyse blade stall.
- The analysis of the blade load cannot be extended to highly loaded rotors
- The models are used to represent 3D problems but are 2D.

In continuation of his research, Strickland [63] developed an improved vortex model which included the capability of modelling 3D effects, free wake and dynamic stall phenomenon. Although the results from the vortex models were an improvement over those of the momentum models, the vortex model could not accurately predict the real performance of VAWT as the results deviated from experimental results especially at the higher solidity due to the inability of the vortex model to accurately predict the stalling characteristics around a VAWT blade. The lack of consistent experimental data availability in some of the cases tested was also seen as a drawback in the comparison of the model's and experimental results.

Recently, McIntosh et al [64] developed a 2D free vortex model that can model and compute VAWT problems in a few minutes, which was applied in the investigation of the unsteady power output of a VAWT that operates within a fluctuating free stream while also examining the assumptions of the direct relation of tip speed ratio to wind speed. They tested a three bladed VAWT of NACA0012 profile with solidity of 0.25 and an aspect ratio of 20. The study revealed that power out from VAWT is influenced not only by the tip speed ratio but also by the increases in the aerodynamics torque that result from an accelerated free stream and the interaction between the turbine and its wake.

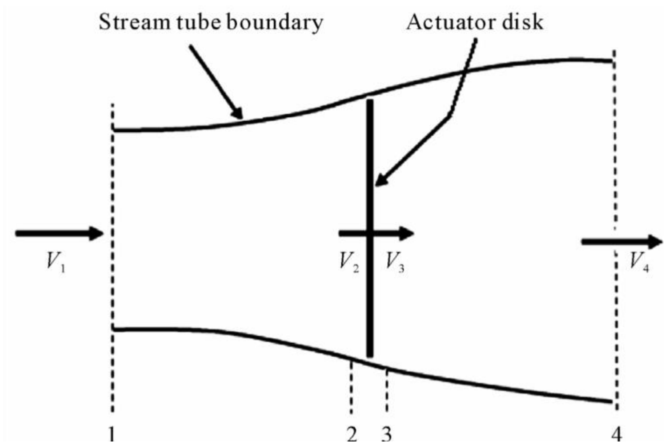

a. Single stream tube

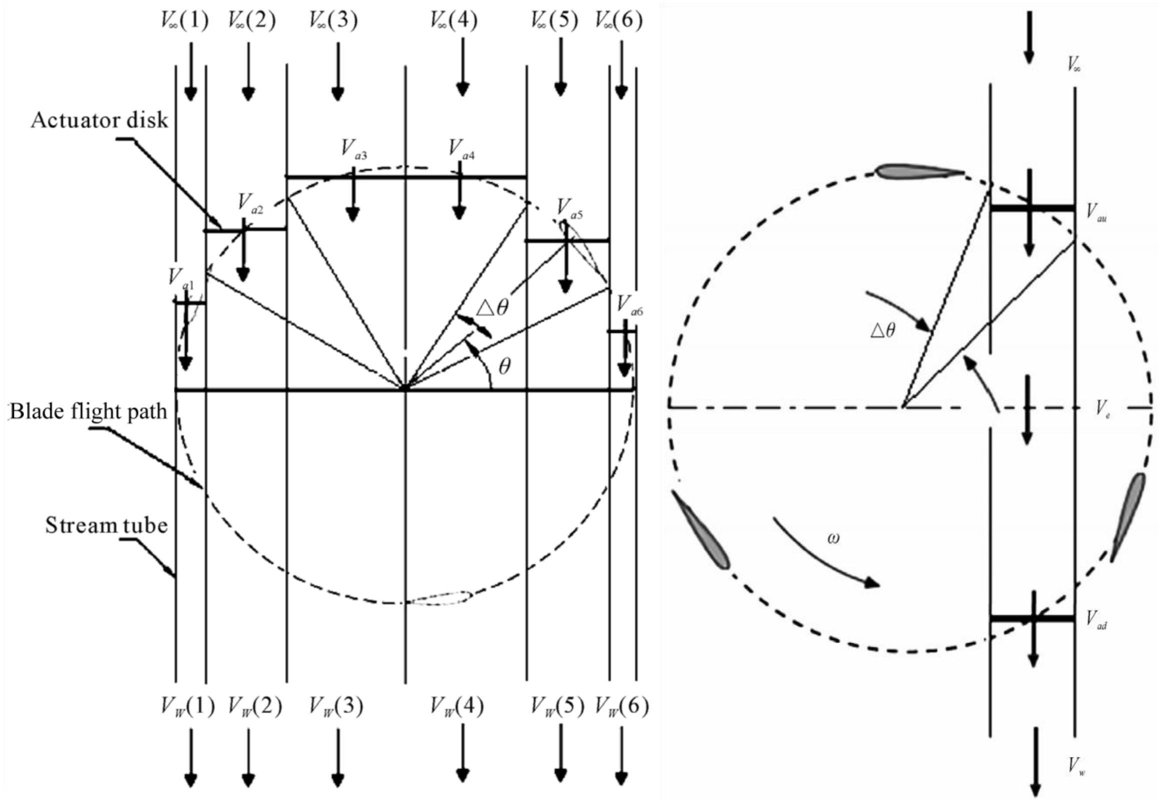

b. Multiple stream tube

c. Double multiple stream tube

Figure 2.16. Illustrations of momentum models [65]

Scheurich et al [66] also used a vortex model to simulate the aerodynamic performance and wake dynamics of a VAWT by implementing Brown's vortex transport model (VTM). By incorporating dynamic stall model into the VTM, the results from the simulation compared well with those of the experimental data of similar VAWT. However, Scheurich et al [66] noted the inability of the VTM to model experimental data accurately in their previous studies, citing the non-inclusion of a dynamic stall model as the reason, which further confirms the weakness and inconsistency of the vortex models.

Following on from the shortfalls of the momentum and vortex model's inability to model the VAWT aerodynamic, performance and flow physics within reasonable accuracy without being tailored, this method of investigation is not used in this thesis.

2.3.2.1.3 Summary

The momentum and vortex modelling methods were used by the early researchers in their attempts to reasonably predict and measure the performance of VAWT. This aroused the interest of various individuals and organisations in support of the improvement and advancing of the VAWT technology, which has led to the development of numerous models some of which have been presented here in a chronological order of their capabilities, and also provided some insight into the aerodynamics and performance of VAWT. These methods of modelling are seen to suffer from their inability to accurately simulate complex problems and also to give reasonable insight into the flow physics around the rotor and the wake despite the huge efforts that has been invested. This call for a more flexible, accurate and better modelling tool to overcome the shortfalls seen with the use of the momentum and vortex methods of modelling.

2.3.2.2 Computational Fluid Dynamics Methods

The development of CFD and its subsequent application into research in VAWTs has considerably reduced most of the inadequacy of the momentum and vortex modelling. The use of the CFD software has equally been enhanced by advances in computational hardware so the benefits derived from CFD is all comprising. The benefits of CFD are not limited to its application in the evaluation and optimisation of design and performance to solve the problems of existing VAWT, but it can also be used to create and visualised a virtual prototype of a VAWT that give insight into the design and performance which may not be possible with other methods. It also has the flexibility by which the design can be altered to test various desired conditions for analytical purposes. CFD also has the capability of calculating aerodynamic forces on blades so does not rely on external data set for further analysis which can be seen as a major advantage over the momentum and vortex models reviewed earlier. Following on is a review of some of the studies into VAWT in which CFD was adopted as the investigation method.

2.3.2.2.1 Aerodynamics and Performance

In a bid to enhance the aerodynamics and performance of the VAWT, Mohamed [67] tested five series of both symmetric and non- symmetric aerofoil shapes (20 aerofoils) after a convincing argument that in spite of the numerous studies in VAWT, the best aerofoil and an accurate simulation of the Darrieus turbine has not been realised up to now. The investigation revealed the suitability of S-1046 aerofoil at a lower $\sigma = 0.1$ over the conventional NACA symmetrical aerofoils. Although the purpose of the study and the presentation fit into modern researches in VAWT, the grid resolution especially on the trailing and the leading edges, and also the compromisingly low number of node density of the model are poor. This has caused the 2D CFD model's to unable to correctly determine the aerodynamic forces hence the under prediction of the experimental data. So, the revelation from the study may be subjective.

McLaren et al [68] investigated a 2D small scale H-type three bladed VAWT with CFD. The performance of the VAWT was tested over a wide range of blade speed ratios from the dynamic stall region through the peak power production region and to the viscous effects region. The model was verified by comparing the lift coefficients from the simulation results of a static

NACA0012 aerofoil to experimental data. The SST k-w was chosen as the most suitable turbulence model based on the validation and subsequently used in the study. The results from the study are consistent with the solidity results of Templin [20] and equally compared well with the high solidity results of Mays and Holmes [24]. To account for the 3D components which are not simulated with 2D, a correction factor was considered and applied.

Amet et al [69] also employed CFD in the investigation of a 2D H-type 2 bladed VAWT with the aim of analysing the dynamic stall of VAWT. A good resemblance was shown in their model's verification against Laneville and Vittecoq [70] experiment data. The lift and drag coefficients of the computed results versus those of the experiment's data showed a similar trend with a discrepancy of over prediction of the experimental results. The refined k-w Kok turbulence model by [71] was adopted for the simulations while tests were conducted at the extremes $\lambda = 2$ and $\lambda = 7$. They differentiated water and air Darrieus VAWTs based on associated stalling characteristics. An insight into the flow physics of the VAWT was also attempted by the plots of velocity vector isocontours and relative streamlines. Pairs of counter clockwise vortices were observed shed from the blade, which, when the occurrence is high, cause negative performance and flatten the hysteresis loop of the lift and drag curve. Their observation is consistent with the findings in the literature.

Untaroiu et al [72] also used the CFD method to investigate the self-starting capability of a wind tunnel scale VAWT, they used the standard $k-\varepsilon$ to simulate 2D and 3D models of a three bladed VAWT. The CFD models were verified against experimental data of the Durham turbine [73]. While the 2D model over predicted the experimental results the 3D model under predicted the results. Although the result of the validation is consistent with the observations of Howell et al [29], the inability of the $k-\varepsilon$ turbulence model to accurately model the blade's near-wall was adduced as the main reason for the poor predictions. Therefore, blended turbulence model with the ability to model near wall and transitional effects was recommended while also downplaying 3D modelling, since the gains do not justify the efforts, cost and the computation time invested.

Iida et al [74] adopted the CFD in their investigations into the unsteady flow and aerodynamic performance around a VAWT. The Large Eddy simulation was used to simulate the flow over a three bladed VAWT with NACA018 profile. While there was no CFD model verification and validation, they observed low divergence of flow and lower dynamic stall at the high λ and the reverser was observed at the lowest λ.

With the flexibility and the acceptability of CFD as a good research tool, based on the level of accuracy of the results it can offer, especially when properly used, it is being adopted in this thesis to further the investigation into the VAWT due to the cost implications of not being able to get all the necessary data through an experimental process only.

2.3.2.2.2 CFD Model Verification and Validation

Verification and validation is a quantitative assessment aimed at establishing the credibility of results obtained from numerical simulations by comparing preliminary results against accurate standard results which in most cases are experimental in nature. The practice when faithfully carried out, with good understanding of the application software by the user, could eliminate or reduced to a tolerable level, the conflicting results from the investigations available in the literature. Following on is a review of literature whose authors have or attempted to validate their models, noting the importance of the exercise.

Raciti Castelli et al [75, 76], and Howell et al [29] made separate attempts at validating their CFD models against wind tunnel measured data. The validation was purely a comparison exercise where only one turbulence model was compared with measured wind tunnel power coefficient and there was no comparison of the physics associated with the flow. So the privilege of being able to make a choice of an appropriate turbulence model from the verification and validation was not created.

Howell et al [29] conducted their experiments at the University of Sheffield low speed wind tunnel using a three bladed VAWT of NACA0022 profile. Solidity and surface roughness were tested at varying λ and realistic wind speeds. The data obtained from the experiment was compared with the simulation results of the 2D and 3D CFD models (Figure 2.17). Although an encouraging insight into the understanding of VAWT performance in relation to the tested parameters was achieved, the process that led to the selection of the RNG $k-\varepsilon$ turbulence model is not scientific since the generalised characteristics of the RNG $k-\varepsilon$ were used as the yardstick. Raciti Castelli et al [75, 76] conducted their experimental measurements at the "Politecnico di Milano" in Milan–Bovisa low turbulence wind tunnel where the power coefficients of the three bladed VAWT with NACA0021 profile was obtained over λ that ranges between 1.0 to 3.5 inclusive at 9m/s. The experimental data and the results of the 2D CFD model simulation using the enhanced wall treatment $k-\varepsilon$ Realisable turbulence model were compared, again, the choice of the turbulence model was based on available information from the CFD software documentation.

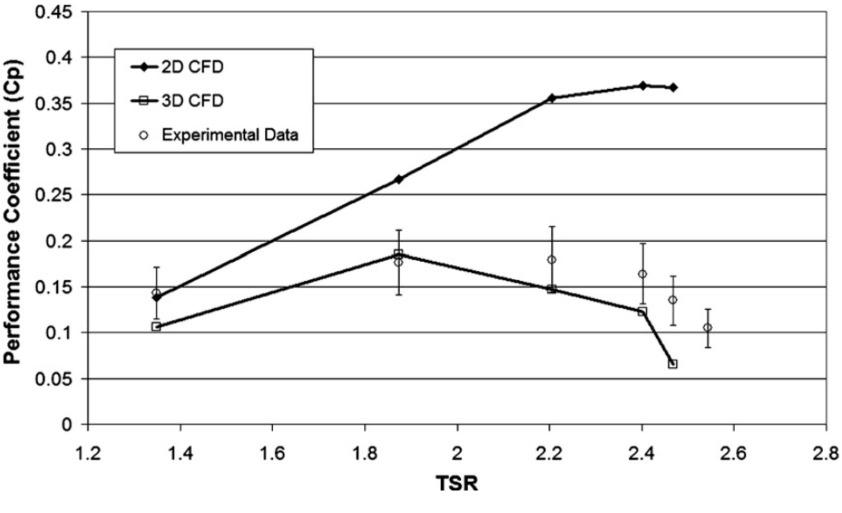

Figure 2.17. Verification and validation of 2D and 3D models [29]

Similar trends in the performance curve were obtained from both the experimental data and the turbulence modelling but the 2D CFD model over predicted the experimental results in both studies, while, for the Howell et al [29], the 3D model under predicted the experimental results at the higher tip speed ratios. Due to the recurrent 2D CFD models over predicting of experimental performance data and the much effort, cost and computational resources needed for 3D modelling without the assurance of achieving perfect agreements with experimental force data in most cases, Simao-Ferreira et al [45] investigated the suitability of using flow visualisation for the verification and validation of 2D CFD VAWT model. They simulated dynamic stall on a single bladed VAWT of NACA0015 profile using one laminar and two turbulence models. The experimental flow conditions of an earlier PIV visualisation and measurements by Simao-Ferreira et al [77] were simulated at $\lambda = 2$ to achieve the aim. From their findings the following assertions were made:

- One equation turbulence model is unsuitable for simulating the stall dynamic of a 2D Darrieus turbine in dynamic stall especially at the lower tip speed ratio
- The three models tested showed similar average forces over the upwind half rotation but with totally different vortices development and shedding, hence, comparing the power coefficients of experiments and CFD model only for verification and validation purposes is not enough. A judgement based on the performance comparison only can be misleading in most cases.
- Comparing the flow physics of experiments and CFD models can achieve better verification and validation results of the rotor aerodynamics, since the flow field can give total and penetrating insights into the interaction between the blade and the wind speed which determine the level of forces attained by the blade at each azimuth position.

In recognition of the Simao-Ferreira et al [45] revelations Edwards et al [53] implemented a thorough verification and validation campaign in their investigation, which is seen as the first proper and complete validation of a VAWT CFD model. First, a list of turbulence model was narrowed down by simulating the wind tunnel flow conditions of a pitching aerofoil study conducted by Lee and Gerontakos [78], because in absence of VAWT data the pitching aerofoil data is closest to VAWT, then the forces and flow structures of the models were compared with the experimental data as shown in Figures 2.18 and 2.19 respectively for the complete validation.

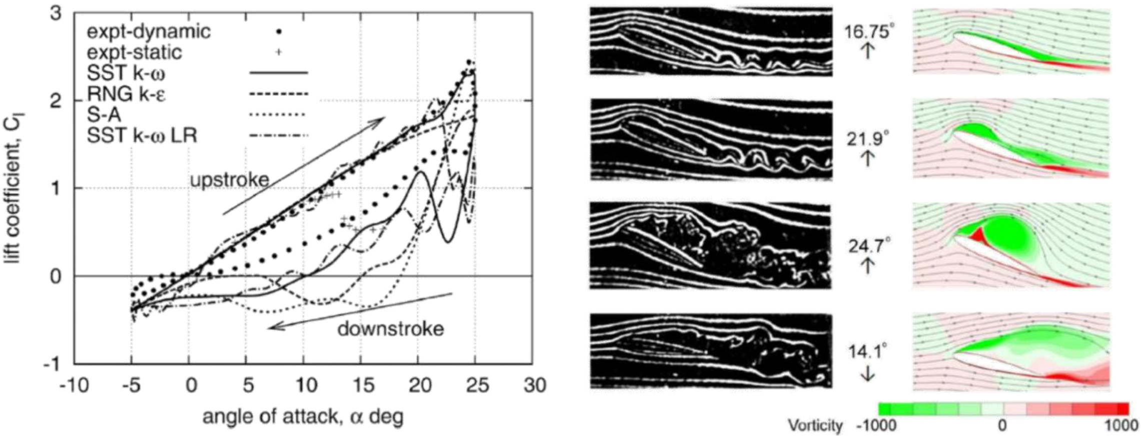

a. Force prediction b. Flow prediction

Figure 2.18. . Verification and validation by comparing a) pitching aerofoil and turbulence models' forces, b) pitching aerofoil and $k-\omega$ SST model flow features [53].

Edwards et al [53] revealed the $k-\omega$ SST as the most suitable turbulence since it was the best available model that predicted both the forces and flow features of the pitching aerofoil experimental data. Second, the wind tunnel experimental conditions of a three bladed VAWT comprising NACA0022 profile conducted at the Sheffield University was also simulated using the $k-\omega$ SST turbulence model.

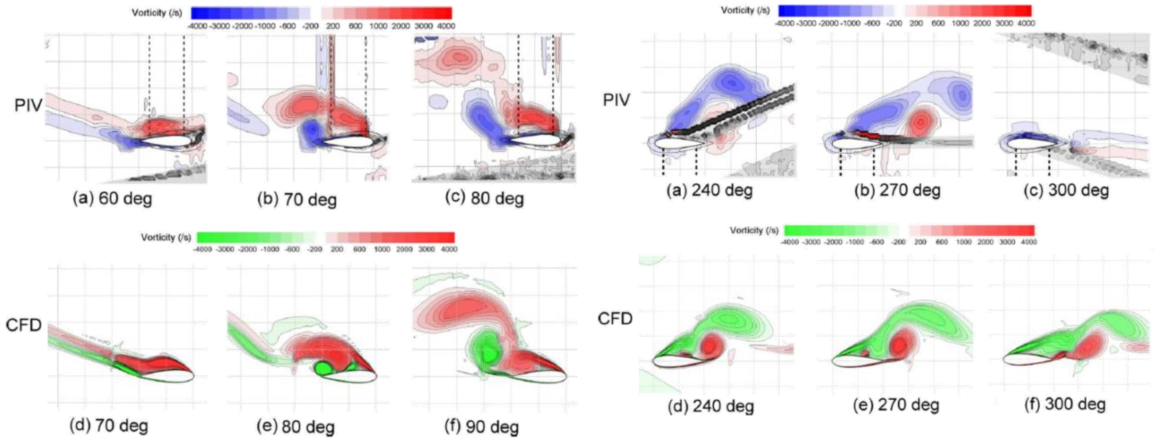

a. Upwind section b. Downwind section

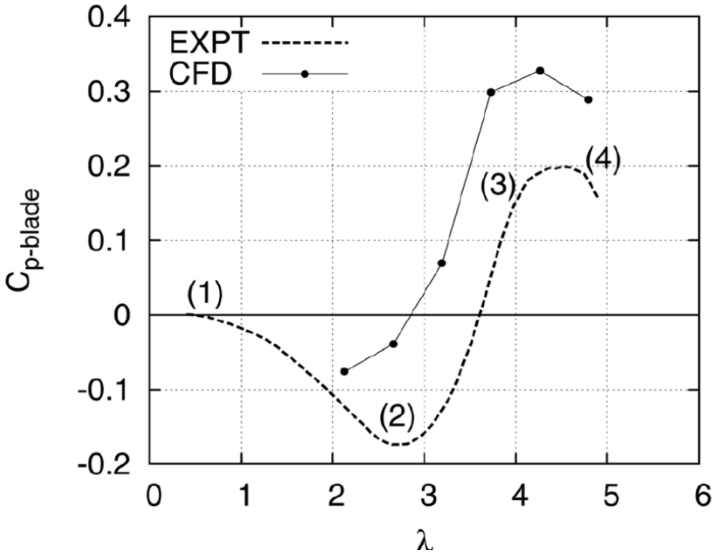

c. Power curves

Figure 2.19. Verification and validation by comparing a) PIV and CFD upwind vorticity plots of a blade , b)) PIV and CFD downwind vorticity plots of a blade, c) Experiment and CFD power coefficient.

A close similarity in trend was observed in the power curves comparison but the 2D CFD model's recurrent over prediction of experimental results was also observed, while the CFD vorticity plots lagged behind the PIV measurements by a phase difference of about 10° in the upwind section of the rotation due to the inability of the turbulence model to accurately model flows within the transitional low Reynolds numbers region. Overall, the prediction of the experimental results by the $k-\omega$ SST was seen as being satisfactory, and hence was adopted, for further simulations in the study despite the little discrepancies observed. Similarly the $k-\omega$SST was also used by [10, 68, 69], in their studies.

Recently, Danao and Howell [79] through further investigations in which the transitional SST turbulence model was considered due to its better ability to model Reynolds numbers operating within transition Reynolds numbers region, the discrepancies earlier observed in Edwards et al [53] study was improved on.

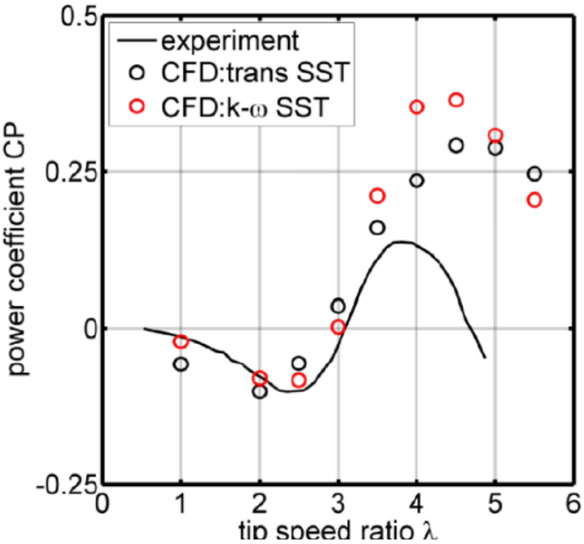

Figure 2.20. Verification and validation of forces [67].

The 10° phased difference seen between the CFD (k-ω SST model) and the PIV data was not seen with the implementation of the Transitional SST model, and also a better prediction of the VAWT performance was observed (Figure 2. 20). However, the prediction of the two turbulence models appear to converge at λ = 5.5 indicating the assumption of fully turbulence characteristics by the Transitional SST model.

In this thesis a similar verification and validation procedure that was carried out by Edwards et al and later by Danao and Howell would be adopted to justify the choice and accuracy of the chosen turbulence model for the CFD investigation. Also to establish that the CFD model can be used for further study to complement the results obtained from the experimental tests.

2.4. Summary

The various methods applied in VAWT investigation have been presented and also their applications in various studies. The summary of the investigative methods is detailed in Table 2.1. A number of performance dependent parameters that can influence the aerodynamics and performance of VAWTs has been reviewed and the decisions made in some related aspects of this thesis have been placed into context. The literature review has equally exposed knowledge gaps in the investigation of VAWTs, some of which this study intends to fulfil:

- Current understanding of the influence of solidity on the aerodynamics and performance of VAWTs has been limited to the number of blades, with only a few but not exhaustive study of the blade chords. Even with the number of blades, the performance of VAWTs has been classified based on a single performance point and the nature of the slopes associated with the performance curves without detailed explanation of why such differences existed. Using the flow physics, the forces and the power coefficients, a detailed investigation into the influence of the blade chord on the aerodynamics and performance of VAWTs will be accomplished in this thesis by linking the performance prediction to the flow physics and the forces to show a good picture of the aerodynamics.
- Current understanding of the influence of Reynolds number on the aerodynamics and performance of VAWT has also been limited to varying the wind speed and again, without an exhaustive discussion of why performance changes, the aerodynamics and performance of the VAWT is seen to change with changes in Reynolds numbers. By altering the blade chord the VAWT Reynolds number is also varied so detailed explanation into the influence of Reynolds number on the performance of VAWTs will equally be provided in this thesis.
- Most of the studies have been conducted with one investigative method, either numerical or experimental. Where an attempt is made

at using two methods, the studies are limited to the fundamental aerodynamics and performance of VAWTs. In this study, experimental and computational fluid dynamics methods will be used for the investigations, to establish the validity of the research presented in this thesis. While the experimental method is the main method, the CFD method will complement the results obtained from the experimental investigative method.

- All the PIV visualisation and measurement studies have been limited to the fundamental understanding of the dynamic stall phenomenon. The best attempts made so far in the application of the knowledge gained from the PIV measurements are in the validation of CFD models. In this study, in addition to using the PIV images acquired from PIV measurements in the validation of the CFD models, the PIV images will also be used in explaining the performance differences caused by altering the blade chord (solidity) and changes in Reynolds numbers.

Investigative Method	Main features	Speed and Accuracy of Results	Cost	Limitations
Experimental Methods	- Divided into laboratory and field experiments. - Allows the precise control of parameters including confounding variables. - Allows conclusions with far more certainty to be made. - Allows explanations of cause and effect - Ideal conditions are assumed in laboratory experiments - Usually follow a standardised procedure so repeatable - Field experiment is difficult to control	Slow with very accurate results especially when the right skills and equipment are deployed.	Requires huge financial resources, materials, skills and human efforts so very high financial involvement is required.	- Due to the high cost involved the range of VAWT parameters tested is very narrow. - It is not possible to control all the environment variables so error margins are usually accommodated. -Tests are usually conducted in wind tunnels in the laboratory. - Measured performance is not achieved in real life situations.
Momentun and Vortex modelling methods	- Based on a Glauert's actuator disc theory which is improved on, in the formation of other mathematical models. - Each stream tube has its own actuator disc in the multiple stream tube model. - Each stream tube has two actuator discs; one at the upwind and downwind in the double multiple stream tube model. -Vortex models compute velocity induction based on both-Savart law and, - Flow solvers using bound vortex filaments. -Free vortex model is capable of simulating unsteady wind, and the Vorticity transport model can also simulate unsteady wind conditions.	Very fast but with less accurate results	Low financial involvements required	- Flow field around the blade cannot be modelled - Depends on external static aerofoil data - No standard procedure is observed. - Results must be validated against experimental data - Usually cannot accurately predict experimental results.
CFD modelling methods	- Excellent pre-preprocessing abilities. - Physical modelling ability is flexible and available wide range of turbulence models can be tested in the various fluid medium. - Capable of simulating flows involving dynamic stalls. - Solves RANS and URANS equations and offer multiple solvers. - Provide for post-processing of simulated results. - Good user interface, and user-support group hence very user friendly.	Moderate speed but with accurate results than can match well with experimental results	High financial involvements required.	- Requires fair knowledge and expertise - Requires large input of information. - Due to its standard procedure, it requires time to solve a simple problem. - results are also validated against experimental results.

Table 2.1. Summary of VAWT investigative methods

Chapter 3

Methods

3.1 Introduction

The details of the procedure used in the acquisition of experimental performance data, particle image visualisation and measurements, and computational fluid dynamics model development are presented in this chapter. First, the wind tunnel facility (test cell), the VAWT model and measurement apparatus, and the VAWT performance measurement method are discussed. Second, the description and discussion of the PIV measurement method that included the PIV equipment, setting verification, data processing and discussion of results sample.

Finally, the process leading to the development of the CFD models used in all the simulations in this investigation is presented detailing the general features of the model: the inner rotating domain, the outer stationary domain, multiple meshes, and the inlet and outlet conditions. Also, parametric studies into the number of node densities and time step size are discussed to explain the reasons behind the choice of some of the model's features adopted in this thesis.

It is noteworthy that most of the facilities used for the investigations presented in this thesis already existed and were developed by Edwards [39] and Danao [55] who were more senior PhD students to the author in the same research group.

3.2 The Wind Tunnel

The wind tunnel which is used as the test cell in this study is shown in Figure 3.1. It is a low speed, open-circuit and suction type wind tunnel facility designed, built and commissioned by the Mechanical Engineering Department of the University of Sheffield. The wind tunnel is 8.5m in length and it comprises of five sections namely: the flow settling, flow contraction, working, and diffuser and fan sections. The flow settling section is at the tunnel inlet where the flow is intercepted with a flow straightening 10 x 100mm honeycomb. Larger scale structures in the flow are broken down for a smoother flow through the honeycomb and the two fine meshes further downstream of the flow. The fine mesh is 1mm x 1mm in size and produces small-scale turbulence that helps to further even-out the flow. After the fine mesh there is a short settling section that allows the dissipation of turbulence and non-uniformities in the flow before the flow enters the contraction section. The contraction section accelerates the flow through a three dimensional 6:25:1 contraction cone.

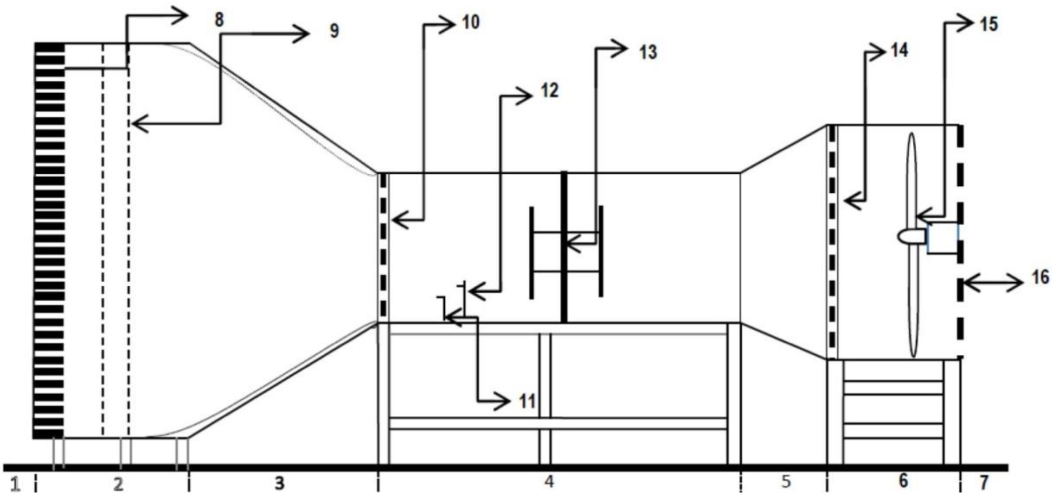

Figure 3.1.University of Sheffield open-circuit wind tunnel.

Legend

1 Inlet
2 Flow settling section
3 Flow contraction section
4 Working section
5 Diffuser section
6 Fan section
7 Outlet
8 Honeycomb
9 Fine mesh
10 2”x2” turbulence grid
11 Pitot tube
12 Hot wire
13 VAWT rig
14 Safety mesh
15 Axial fan
16 Outlet safety mesh

The working section is next to the contraction section. A turbulence grid is installed at the end of the contraction section, which is also the inlet of the working section. Varying the size of the turbulence grid allows the user to have control over the turbulence intensity in the working section. The 0.025 x 0.025m grid at the inlet generates 1% turbulence intensity at the VAWT test position. The working section is the test section where virtually all measurements and model observations are carried out. It contains the VAWT model placed at 1.8m from the working section inlet, reference hot-wire and pitot tube are located towards the inlet of the working section to set and monitor the wind tunnel flow speed. Towards the end of the test section is a 0.025m x 0.025m safety mesh to screen particles from the fan. The diffuser section followed the working section closely. This section decelerates the flow with minimum distortion after the 1.2m from the axis of VAWT position.

The fan is controlled by a frequency drive that allows accurate setting of the fan speed in revolution per minute (RPM) and has a speed limit of just over 900rpm. Theoretically, the fan maximum speed is equivalent to wind speed approximately 25m/s which corresponds to 70,000 Reynolds number based on wind speed. In consideration of the shear stress, deflection of the blades due to aerodynamic forces and other safety reasons, the fan was run at a maximum speed of 9m/s (Re_C = 24,000) for the entire experiments. Beyond the fan section is the flow outlet, where there is also a 0.025 x 0.025m safety grid installed at the outlet to screen particles and prevent human contact with the axial fan.

3.3 Wind Tunnel VAWT Models

Two VAWT models were used in this study. Straight three-bladed VAWT rotor was adapted for the experiment after a review of literature on number of blades effect on the performance on VAWT in chapter two. Considering the cost of blade manufacture and mechanical stability of VAWT also, the three-bladed VAWT was considered as most appropriate. The geometry of an existing three-bladed VAWT model at the University of Sheffield was adopted for the study. The existing VAWT geometry has a central shaft of 0.027m that runs across the wind tunnel test section from top to bottom. The rotor shaft is positioned 1.8m from the upwind and 1.2m downwind. There are two hubs rigidly attached to the centre shaft, with provisions for the attachment of the support arms that connects the blades to the centre shaft. The blades are 0.35m further away from the centre shaft when attached to the support arms, and, in addition to the existing VAWT, a new configuration was created with different blade chord but with the same support arms and central shaft for easy comparison of their performance.

The two sets of blades and the entire rotor are made of aluminium and are of NACA0022 profile. The blades of the existing VAWT that has been used in two previous PhD studies have 0.04m chord lengths, $\sigma = 0.34$ and AR = 15, while the blades of the additional rotor have 0.03m chord length, $\sigma = 0.26$ and AR = 20. The blades are 0.6m in length and are attached to the shaft via the two support arms at ¼ and ¾ blade length. The low drag support arms are made of NACA0026 profile with a chord length of 0.03m. The same support arms were used for all the experiments.

3.4 VAWT Performance Measurement Apparatus

A number of different apparatus was required for the conduct of the VAWT experiments. The description of the apparatus used in the determination of VAWT performance is presented in this section. It includes the start-up apparatus that drives the turbine and provide the needed power to start-up, and also the measurement apparatus which is divided into the apparatus used in the preliminary measurements that preceded the main measurements and those used in the main measurements as well.

3.4.1 Start-up Apparatus

The start-up mechanism was used to aid the starting of the VAWT's models due to the inherent non-self-starting characteristics that are typical of lift-based VAWTs especially the small-scaled models of this nature. The non-starting capabilities of lift based small VAWTs have been attributed to the negative performance region of the power curve at low λ. This prevents the VAWTs from self-starting [80]. The start-up system provides the required power to overcome the inertia and bring the rotation of the rotor to the appropriate λ and Reynolds numbers where positive performance of the VAWTs can be maintained. A 250W DC motor was combined with an electromagnetic clutch and both devices were installed at the top of the rotor rig. The clutch enables the control of the motor which can be used to disengage the motor when the needed speed has been attained.

Figure 3.3 shows the motor, clutch and the coupling to the rotor shaft. The clutch control is independent of the rotor hence when necessary the clutch can efficiently disengage the motor from the rotor shaft. This operational flexibility is useful for the VAWTs power measurements without the clutch interference and also in situations where the VAWT RPM is required constant especially during PIV experiments when the λ is at the lowest performance region.

3.4.2 Measurement Apparatus

Two types of measurements were carried out during the experiments. These are the preliminary measurements and the main measurements. The preliminary measurements preceded the main measurements, and involved the reading of room temperature from digital thermometer, ambient atmospheric pressure from mercury barometer and the calibration of a

DANTEC type 55P16 Constant Temperature Anemometer (CTA) hot-wire. A very sensitive Furness control type micro-manometer (FC0510) was also used in the CTA hot-wire calibration.

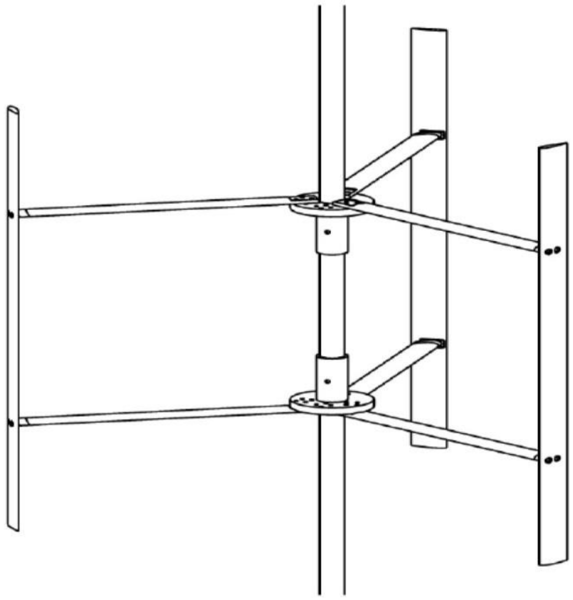

(a) 3D view

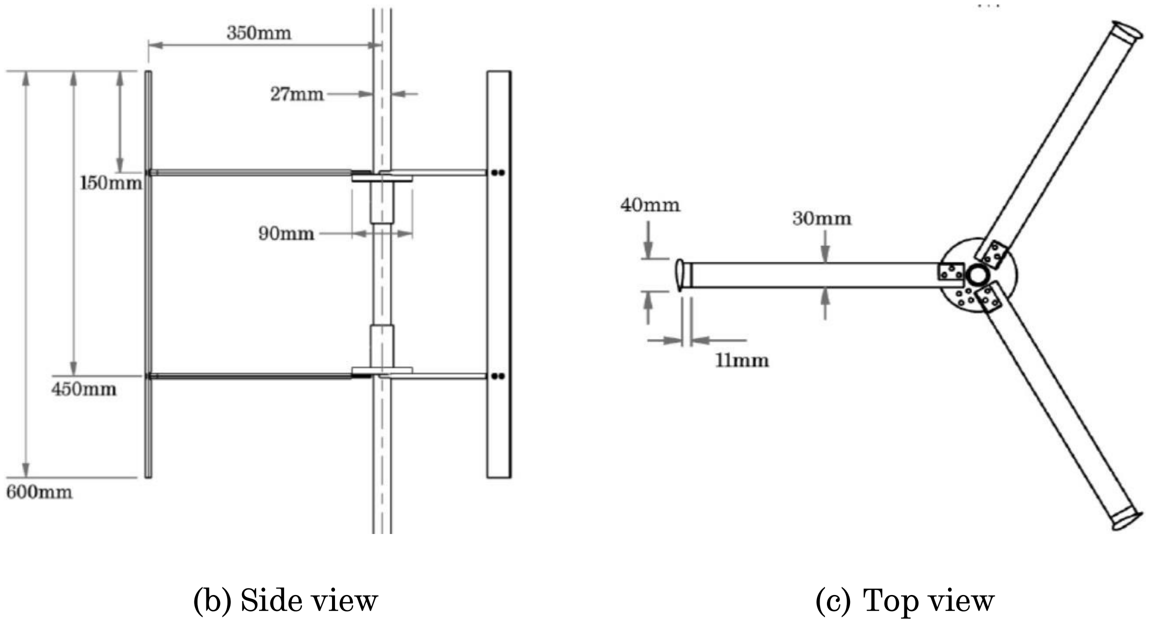

(b) Side view

(c) Top view

Figure 3.2. VAWT rotor assembly [39].

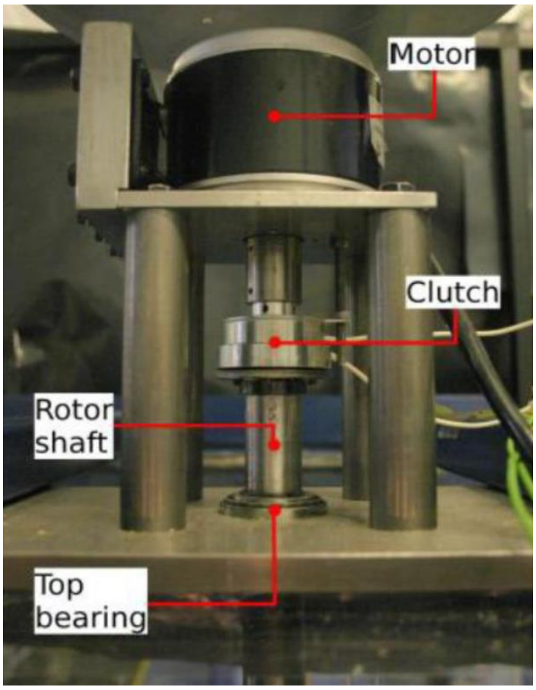

Figure 3.3. Start-up mechanism [39].

The hot-wire calibration was necessary because it characterises the flow field for the actual and precise measurement of wind speeds [81, 82]. After the hot wire calibration, the wind tunnel velocity profile and turbulence intensity was measured by traversing the pitot tube across the wind tunnel width and also the hot wire probe from the inlet position of the working section to the location of the VAWT. This was to determine the uniformity of the velocity profile and the turbulence intensity decay between the inlet of the working section and the VAWT position.

An Avago optical encoder ''AEDA-3300-TAM'' was used to measure the rotational velocity. This optical encoder is capable of giving 3000 pulses per revolution. A LABVIEW program counts the frequency of the pulses. The optical encoder measured the rotational velocity by connecting the encoder output to a standard personal computer through a National Instruments BNC 2090 connector block, and also connecting BNC 2090 connector block to a compatible PCI-6220 data acquisition card. Figure 3.4 shows the assembly for the measurement of the rotational velocity. The assembly is coupled to the bottom of the shaft and supported indirectly by the bottom of the wind tunnel.

The torque of the VAWT was not directly measured due to the experimental design; hence it was indirectly calculated from the basic relationship between it, angular acceleration and inertia as expressed in Equation 3.1.

$$T = I\xi \tag{3.1}$$

An appropriate measure of brake torque that depends on the test wind speed was applied at the higher positive performance region of the VAWT to prevent the rotor from over speeding, since over speeding of the rotor can cause structural failures and other safety issues especially, if the designed speed limit is exceeded. Figure 3.4 shows the Magtrol hysteresis brake 'HB-140-M2" of 1Nm load maximum capacity incorporated in the main measurement assembly for this purpose. The Magtrol hysteresis brake would interact magnetically when current is passed through it causing the needed braking torque.

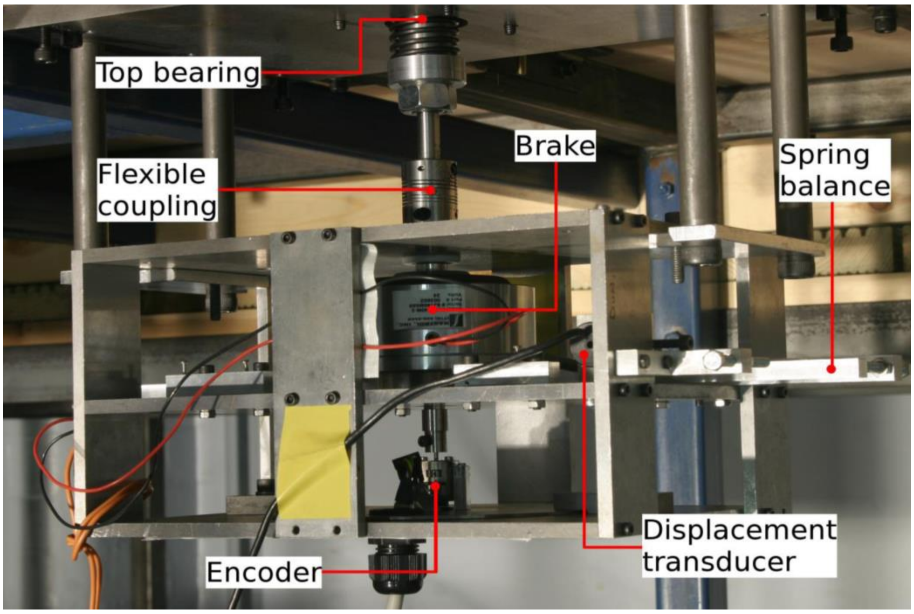

Figure 3.4. Main measurement assembly [39].

The applied brake torque T_{app} by the Magtrol hysteresis is independent of the rotational speed of the VAWT and would produce a constant brake torque for a particular experiment, irrespective of the operating settings of the rotor. The value of the applied torque T_{app} is a necessary data for the computation of other parameters that were not measured directly. The brake was fixed on a spring balance so a Sangamo DC "DFG/2.5" miniature displacement transducer that measures the linear displacement of the core and is coupled to a 155mm radius lever arm from the centre of the brake. The voltage of the transducer is linearly proportional to the displacement, so irrespective of the spring balance rotational movement, a complete stroke of the displacement transducer renders the rotational displacement linear which gives the value of the applied torque with an observed maximum error of ±0.01Nm [39] at the lowest wind speed where the brake is applied.

3.5 Performance Measurement Method

The procedure followed in the conduct of the VAWT performance measurements is presented in the following sections. It includes the calibration of the Constant Temperature Anemometry (CTA) hot-wire, velocity profile measurements and turbulence intensity of wind tunnel determination, and VAWT power coefficient measurements. Also a discussion of the results sample is presented.

3.5.1 Calibration

Calibration of the measuring devices was important for accurate, consistent and reliable measurements in the main experiments. By the calibration of the Constant Temperature Anemometer hot-wire the coefficients of the constants of the King's Law equation needed as an input for data logging and monitoring of wind speed during the entire period of the experiments are determined. In-situ calibration method was employed as in [83, 84] and a DANTEC type 55P16 Constant Temperature Anemometer (CTA) hot-wire was used in measuring the wind velocity in the wind tunnel for the entire experiments. The T_{app} Sangamo DC "DFG/2.5" miniature displacement transducer "DFG/2.5" was previously calibration by [55].

The hot-wire calibration was conducted at the start of the experimentation on a daily basis during the entire period of the tests. This ensured unfailing and accuracy of measured data. Also relevant coefficients that are dependent on atmospheric pressure and temperature that vary with the weather conditions were equally obtained, for the hot-wire calibration. The calibration tests were carried out at a range of wind velocity measurements, in which the main experiments were conducted. The wind velocity has a lower limit of 3 m/s and upper limit of 10 m/s at an interval of 1m/s.

The wind tunnel axial fan was run at a constant speed for each particular test. Differential pressure readings from the micro-manometer at the fastest data logging frequency of I Hz and voltage readings of the hot-wire at the lowest frequency of 100Hz were recorded for 30 seconds for each test. These were the same data logging frequencies used for the main experiments. The averages of these readings combined with the reference temperature and pressure values from the thermometer and barometer, which were used to obtain the density, were included in computing the coefficients of Kings Law equation in Equation 3.2 popularly used for the hot wire anemometry [85], based on the least-squares curve fitting.

$$E^2 = A + B.U^n \qquad 3.2$$

Where:

E : hot-wire voltage

A, B, n = constant coefficients

U : wind velocity

The Figure 3.5 shows result samples of the hot-wire calibration. Figure 3.5 (a) is a plot of wind velocity versus data logging time. The wind speeds are constant as time varies between 5s and 30s for all the wind speed conditions tested. The unsteadiness observed between 0 and 5s is due to the initial poor response of the micro-manometer data logging, to changes in wind speed settings which settled beyond 5s.

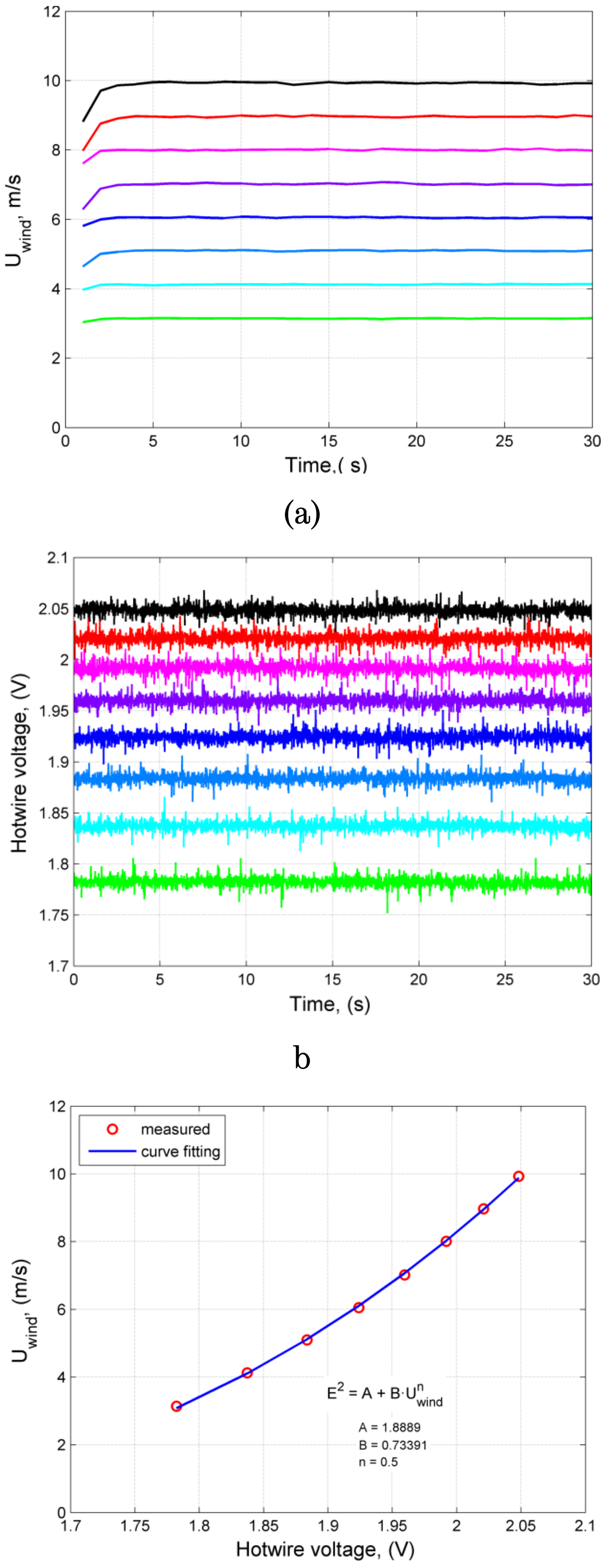

(a)

b

(c)

Figure 3.5. Hot-wire calibration: a) wind speed versus time, b) hot-wire voltage versus time, c) wind speeds versus hot-wire voltage.

Figure 3.5 (b) is a plot of the hot-wire voltage versus data logging time; the amplitude of fluctuating voltage is orderly and repetitive as the wind speed varies from zero to 30s. This shows that the hot-wire response is good and can be used for reliable measurements, and Figure 3.5 (c) is the curve fitting of the calculated wind speed and plot of the measured wind speed versus the hot-wire voltage. A good match between the measured and the calculated curve fitting is shown so the hot-wire measurements can be relied upon for the main experimentation.

3.5.2 Velocity Profile and Turbulence Intensity Measurement

The University of Sheffield wind tunnel has honey comb at the inlet and two fine meshes that strengthen and even out the flow before being intercepted by the turbulence grid at the inlet of the working section. To ascertain the level of the velocity fluctuation across the working section of the wind tunnel, a velocity profile test was conducted.

A pitot tube was transverse across the wind tunnel working section, at a regular interval of 0.1m within 0.5m from the rotor axis in the both X, horizontal directions without the VAWT running. The wind tunnel fan was set to run at a 295rpm all through the experiments. At each measurement position, changes in pressure (ΔP) were read with the micro-manometer at the fastest data logging frequency of 1Hz, and thereafter the velocity was calculated for each position using Equation 3.5 that combines the Bernoulli equation (Equation 3.3) which relates pressure and velocity, and the ideal gas law (Equation 3.4). The calculated velocity profile was seen uniform across the wind tunnel except the immediate distance from tunnel walls which is due to the no-slip condition effects. A maximum difference of 0.06m/s between the highest and the lowest calculated velocity is observed. This is within tolerable experimental error margins and since the VAWT blades are 0.25m and 0.3m from the side walls in the X and Y directions respectively, the effects of the non-uniformity of velocity on the VAWT performance at the immediate side walls could be negligible. Therefore, the wind tunnel condition is considered good for the study.

$$\Delta P = \frac{1}{2}\rho V^2 \qquad 3.3$$

$$\rho = \frac{P}{RT} \qquad 3.4$$

$$V = \sqrt{\frac{2(\Delta P)RT}{P}} \qquad 3.5$$

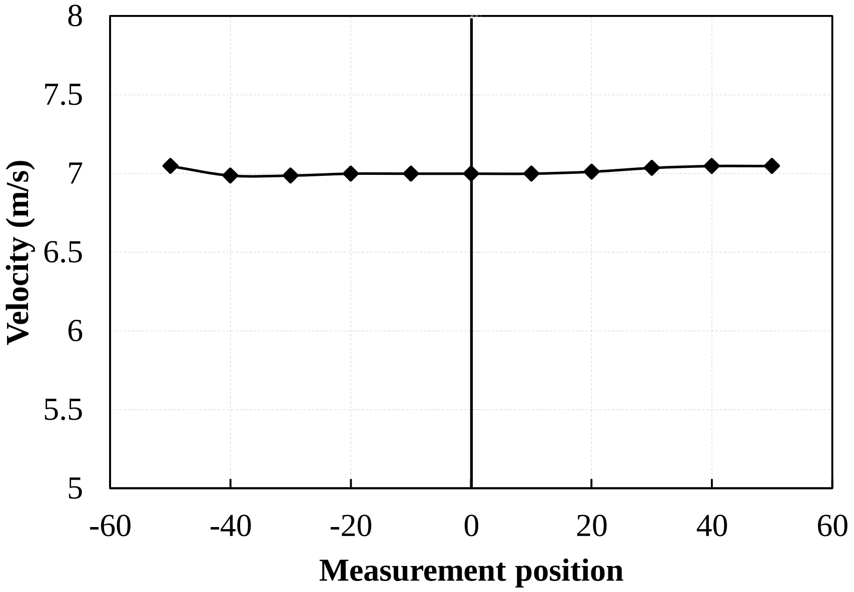

Figure 3.6.Velocity profile across the wind tunnel.

A follow up study that was aimed at ascertaining the level of eddies and noise in the wind tunnel flow was also conducted by [55]. The study determined *Tu* which is also used in the boundary conditions setting for correct simulation of the wind tunnel VAWT and domain conditions in Computational Fluid Dynamics. Through the use of Equation 3.6 that defined turbulence intensity, the flow turbulence in the tunnel was measured at the various positions.

$$Tu = \frac{u'}{U_{mean}} \qquad 3.6$$

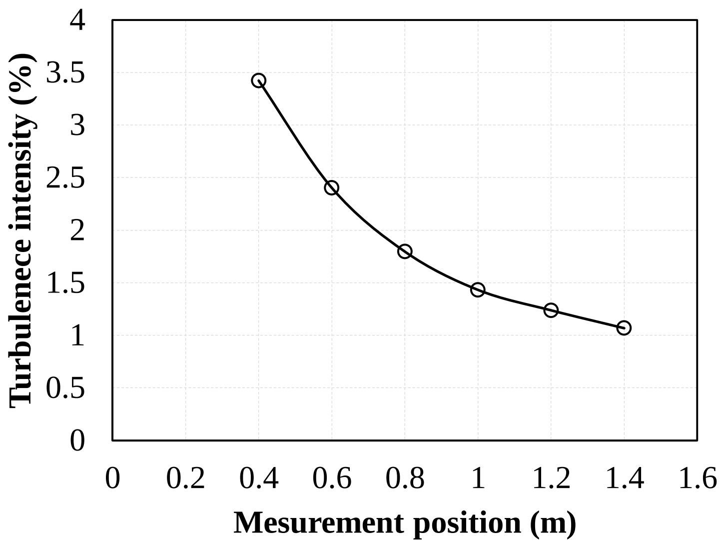

Figure 3.7. Turbulence intensity decay in the wind tunnel [55].

A preliminary test without the VAWT running shows a fairly constant *Tu* = 3.5% across the wind tunnel which confirmed the earlier velocity profile tests. Although, the *Tu* = 3.5% shows there are eddies and noise in the wind tunnel, the wind tunnel was considered suitable for experimentation. Since, with the VAWT running, turbulence decay was observed. The hot-wire probe was traversed at an interval of 0.2m from the working section inlet to the possible closest position to the VAWT blade. The Figure 3.7 shows a plot of wind tunnel turbulence intensity versus the measurement position. An initial turbulence intensity of 3.42% at a position of 0.4m away from the working section turbulence grid was observed. This decayed to 1.06% at the closest position to the VAWT's blade.

3.5.3 Power Coefficient Measurement

The VAWT's blade performance was measured using the 'spin down' method, a VAWT performance measuring technique developed by Edwards [39]. The method involves the spinning down of the rotor from a high rotational speed while the angular velocity and time is monitored through an optical encoder. The instantaneous acceleration is then computed by equation 3.7.

$$\xi = \frac{\omega_2 - \omega_1}{t_2 - t_1} \qquad 3.7$$

For each test wind speed, the rotor is spun twice to determine the performance of the VAWT. The first spinning down of the rotor is aimed at determining the resistive torque of the rig and it involves spinning the rotor down without the blades attached. The resistive torque (T_{res}) is a measure of the system resistance caused by mechanical friction, bearings and the support arm's induced drag. Since the blades are not attached to the rotor during the resistive torque tests, brake was not applied irrespective of the wind speed test condition, because significant power is not generated that can cause over speeding of the rotor. The T_{res} is computed after the test by Equation 3.8.

$$T_{res} = I_{rig}\xi \qquad 3.8$$

Where: I_{rig} is rotational mass moment of inertia of the rotor without blades.

With the blades attached, a second spinning down test is conducted again to determine the overall performance of the VAWT based on the blade torque. The blade torque is mostly of interest since the study involves the investigation of two VAWT configurations with different blade chords and also for comparison with the CFD models where only a 2D slice of the blade is simulated. For the C = 0.04m and σ = 0.34 VAWT model, the brake was applied at wind speeds greater than 6.5m/s while for the C = 0.03m and σ = 0.26 VAWT model, the brake was applied at wind speeds greater than 7.5m/s. The application of the brake was necessary to prevent the VAWT from cut-in, a situation where positive power is generated, so the turbine no longer spins down. At all the tested wind speeds, the blade torque is computed by using Equation 3.9, the applied torque, T_{app} = 0 for cases in which brake power was not applied. Other details of the development and verification of the spin down method are found in [39].

$$T_B = I_{rig}\xi - T_{res} - T_{app} \qquad 3.9$$

I_{rig} : rotor mass moment of inertia with the blades attached.

The power coefficient of the VAWT based on the blade torque was obtained using Equation 1.7 after computing the T_B from the spin-down tests. Figure 3.8 shows result samples of the two VAWT configurations at 8m/s wind speed obtained from the performance measurements. A negative and positive performance region is clearly shown in the two plots implying that the VAWTs are absorbing power at the tip speed ratios that lie within the negative region and generating power at the higher tip speed ratios within the positive performance region. While the negative region of $C = 0.04$m VAWT with $\sigma = 0.34$ spanned from $\lambda = 1$ to 3.75, that of the $C = 0.03$m with $\sigma = 0.26$ ranges from $\lambda = 1$ to $\lambda = 3.9$. The $C = 0.04$m and $\sigma = 0.34$ attained a low $CP = -0.061$ at $\lambda = 2.3$ while the $C = 0.03$m with $\sigma = 0.26$ attained a low $CP = -0.14$ at $\lambda = 3$.

At the positive performance region, the $C = 0.04$m VAWT with $\sigma = 0.34$ attained a higher peak $CP = 0.325$ at a lower comparable $\lambda = 3.75$ while the $C = 0.03$m VAWT with $\sigma = 0.26$ attained a lower peak $CP = 0.15$ at a higher comparable $\lambda = 3.75$. The resulting measurements compared well with other studies in which the spin down procedure was used (is shown in chapter five). The method was adopted for the performance measurements at other wind speed conditions also presented and discussed in greater details in chapter five.

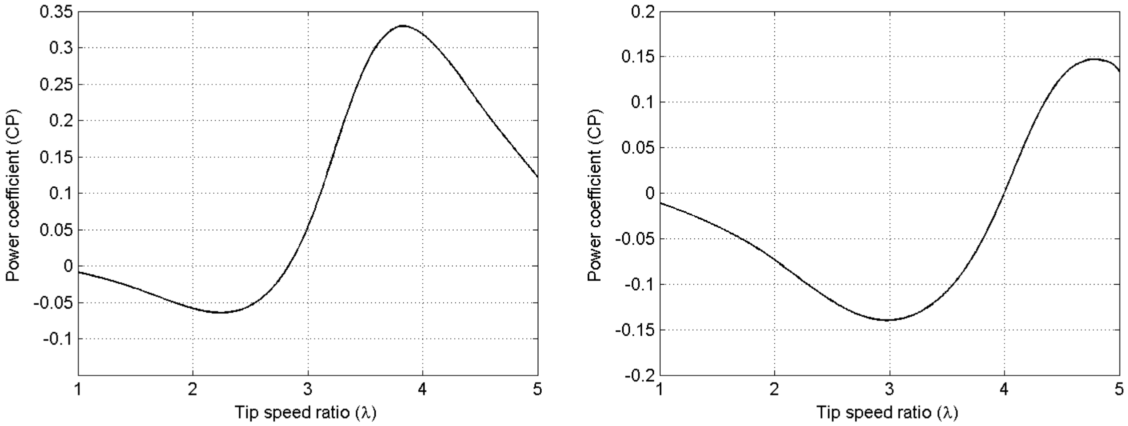

a. b.

Figure 3.8. Power coefficient measurement at 8m/s: a) C = 0.04, b) C = 0.03m.

The VAWT models used in this study are not dynamically similar to real world VAWT because of the difference in the Reynolds numbers. The real word

VAWT operates at relatively higher Reynolds numbers compared to the very low Reynolds numbers the VAWT models operate in in this study. However, the CP- λ curves are similar in shape with three distinct regions: the dynamic stall, the peak power and the viscous effects regions. Therefore, the understanding gained in this is applicable to real world VAWTs.

3.6 Particle Image Velocimentery (PIV) Method

PIV method is a technique with which the instantaneous flow velocity within the required "field of view" (FOV) are visualised and measured through the introduction of particles of very small diameter to the fluid stream. The buoyant particles in the fluid stream that are illuminated by a laser sheet are assumed to faithfully follow the fluid velocity, and with the particle being very small in size, several particles are seen and captured within the illuminated FOV by using a sensitive camera. Basically, the flow velocity is measured as a ratio of displacement and time interval for the group of particles within the FOV.

A light sheet source is required to illuminate the field of view that contain the particles while the camera captures two images of the illuminated particles in the FOV. The time interval between the two images determines the accuracy of the cross correlation between a pair of images, so the smaller the time interval is, the better is the time estimation of the velocity.

3.6.1 PIV Equipment

Considering the required equipment for PIV experiment, PIV measurements can be described as a quantitative and non-intrusive method that combines seed particles, light source and charge couple device (CCD) digital cameras to accurately visualise and measure the flow field under investigation. The PIV system at the Sheffield University is mainly composed of the following:

- Tracer particle generator.
- A pulsed light sheet source.

- A camera that is synchronised with the laser, and
- Image acquisition and processing software.

One of the objectives of the study in this thesis is to use the PIV system to visualise and measure the flow around a VAWT blade of the two configurations being investigated at different wind speeds and λ. To aid the analysis of the changes in blade chord on the performance and aerodynamics of VAWT. The details of the PIV system at the University of Sheffield are presented in the following sections.

3.6.1.1 Tracer Particle Generator

Six-jet Atomiser of model 9306A was used for the generation of the tracer particles for the PIV measurements. It contains a purpose built-in pressure regulator, pressure gauge, dilution system and one to six atomiser jets so particle concentration and output are easily controlled (Figure 3.9). The Six-jet Atomiser was used for generating small particles of approximately the 2μm diameter size from olive oil based on verified settings from preliminary tests conducted and presented in subsequent sections.

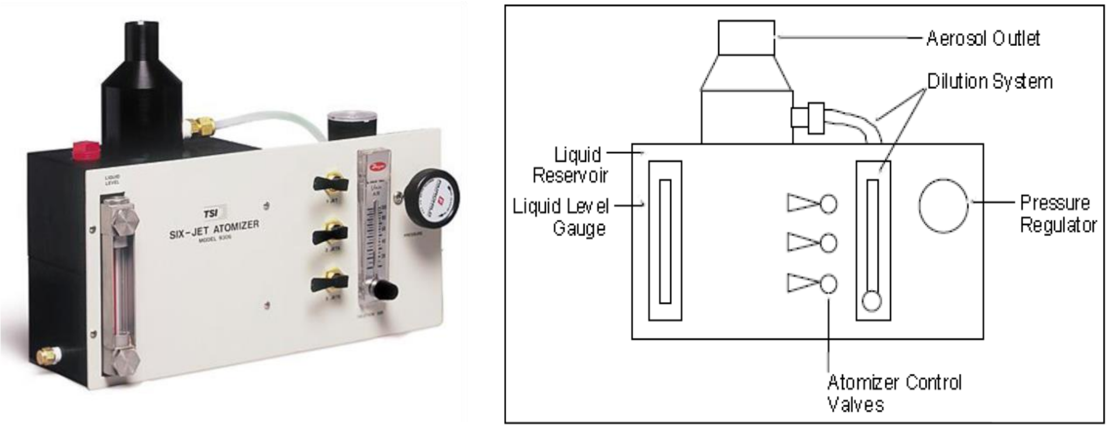

a. b.

Figure 3.9. Model 9306A six-jet atomiser: a) picture, b) outline drawing [86]

The flow field velocity around a blade is measured based on the motion of the particles so it is important that the particles accurately follow the fluid motion.

One of the methods of determining the accuracy with which the tracer particles follow the fluid motion is by estimating the settling velocity of the particles in relation to the fluid motion. This is achieved by assuming that the Stokes law of drag in Equation 3.10 [87] is applicable.

$$v_s = \frac{2gR_p^2\left(\rho_p - \rho_f\right)}{9\mu_f} \qquad 3.4$$

The tracer particles are adjudged suitable if the settling velocity is insignificant when compared to the actual fluid velocity. Using Equation 3.10 the settling velocity of the particle was estimated to be 0.0001m/s which are very negligible when compared to the 6 and 8 m/s wind speeds at which the PIV tests were conducted in this study. This implies that the particles would follow the fluid motion faithfully without deviating from the fluid streamlines even during periods of rapid changes in flow direction as a result of flow separation.

3.6.1.2 Pulsed Light Sheet Source

Dantec Litron Nano–S–65 Nd:YAG laser (Figure 3.10 (b)) was used to provide the light sheet. It can provide light pulses at very short duration while emitting light at a maximum energy level of 65mJ per pulse and at 520nm wavelength. Over the short period of time, two laser flashes are emitted by the lasers while the repetition frequency varies from a very low 5Hz up to 15Hz. The laser also contains a cylindrical lens nob that extended away from the laser through which the laser sheet thickness and focal length can be set, which makes it very flexible and adaptable to PIV testing.

3.6.1.3 Camera Synchronised with the Laser

A 4megapixel (CCD) camera of 2048 x 2048 pixel sensor resolution of 70% QE (Figure 3.10 (b)) was used to capture the position of the particles in the FOV that was illuminated by the laser sheet. A Nikon AF Micro-Nikkor 60mm f/2.8D lens was attached to the camera for improved performance.

The captured images corresponding to the two flashes are thereafter used to derive the fluid motion through cross-correlation. A Dantec software is installed on a computer which also provided control over a Dantec timing unit via a National Instruments PCI 6602 timer board. A combination of the software and the BNC cables enabled the synchronisation of the laser and camera as shown Figure 3.10 (c). The procedure observed for the synchronisation of the laser and camera involved the alignment of the laser and the camera, triggering the camera at two different time intervals, transfer of data from the camera to the PIV computer and adjusting the time order to start the process again until satisfactory performance is achieved. The additional channel in the encoder was used to achieve the synchronisation that gave the syncing of the trigger to the passing of a specific blade in the FOV. Once synchronised, many of the components of the PIV were time coordinated.

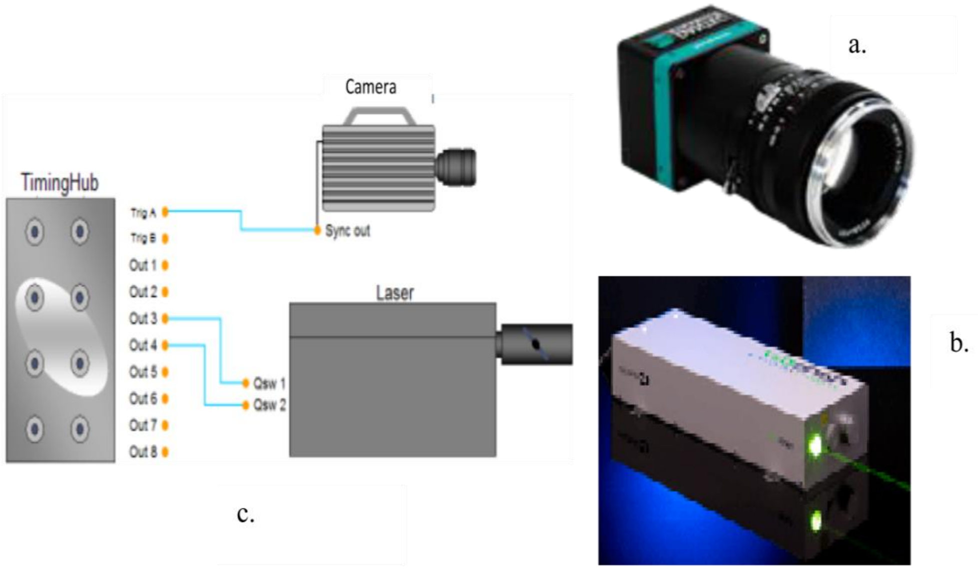

Figure 3.10. PIV equipment: a) Camera, b) Laser and C) Synchronisation [88].

3.6.1.4 Image Acquisition and Processing Software

The synchronisation of the camera and the laser, capturing and recording of images, and the initial processing of the recorded images is facilitated by the use of the Dantec Dynamic studio v3. 30 software via a National Instrument PC1 – E 1427 DAQ card. Thereafter, the final processing to obtain the desired vortices around the blade was achieved by the use of other applicable software. Result samples are shown in the latter part of this chapter.

3.6.2 PIV Experimental Set-up and Test Cell

The set-up of the PIV equipment for the campaign is as shown in Figure 3.11. The camera and the laser are perpendicular in alignment. Reflection is also reduced with the camera aligned in the perpendicular plane of the image. A marked disc with the main 36 azimuth angles representing the 360° of a full rotation at 10° intervals are attached to the camera rig and the VAWT encoder so the camera and the VAWT can be rotated to various angles within reasonable accuracy.

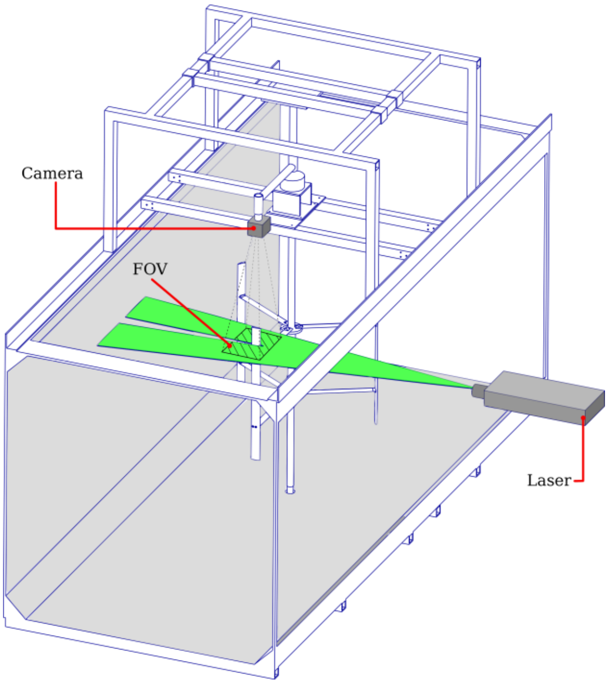

Figure 3.11. The PIV set-up and test cell at the University of Sheffield [39].

The laser position is moved around to retain the initial set alignment at the desired azimuth angle being tested. The camera was positioned radially such that the blade was centred in the camera view and also the chord line parallel to one edge of the FOV. The seeding generator generates the small buoyant particles upstream, in front of the wind tunnel. The open suction low speed wind tunnel with 1.2 x 1.2 m^2 working section (Figure 3.1) was the test cell. The transparent sides of the tunnel were covered with non-transparent blinds for safety of personnel in the laboratory, while the experiment is being conducted.

3.6.3 Blade Surface Treatment

Surface reflection can be caused by the emitted light from the laser and also the material which the blade is made of. Therefore the intensity of emitted light from the laser, and the image filtering devices used to limit these effects are a major concern during PIV experiments. Even with the camera position and the intensity of the laser appropriately set, reflection from the surface of the blade could still pose a serious problem since proper setting and alignment of the camera and the laser only reduces the level of reflection from the blade surface. Therefore, it is very necessary to treat the blade surface to achieve a tolerable level of reflection that cannot damage the camera and as well as having an insignificant impact on the accuracy of the results.

The VAWT blades being made of aluminium have their surfaces highly reflective even at very low laser intensity. In order to reduce the surface reflection in the current study, the blade surface was treated following the procedure detailed in [89]. A thin layer of body filler was applied to the surface of the blade and allowed to dry for about 2 hours. The body filler was then sanded with about #200 grit sandpaper, thereafter, a thin layer of matte black was sprayed on the surface of the blade. The blade was allowed to dry for several hours and inspected using a small microscope to ascertain the uniformity of the applied matte black. Upon satisfactory results, and in addition to the coat of the matte black paint, a thin layer of Dykem steel red paint was applied and again, allowed to dry for several hours. The Dykem steel red paint is suitable because it contains Rhodamine so has the characteristics of being able to absorb wavelengths that is close to 530nm which is near the wavelength of the laser used in this investigation. Health and safety rules and regulations regarding the use of paints in the laboratory were strictly adhered to during the blade surface treatment.

3.6.4 Verification of Test Settings

The process of selection of an appropriate test conditions for the main PIV experiment in this study was by systematically conducting several tests, while the parameter being verified is gradually changed until a satisfactory condition is attained. This was aimed at justifying the suitable test condition selected which is very necessary following research tradition. It is important to note that all the settings cannot be simultaneously tested, and there were no guidelines that suggest the order of importance of one setting over the other since several settings conditions are required, so the order of the verification was purely the author's discretion.

Earlier laser sheet thickness and height of the laser sheet with respect to the blade position used by Edwards [39] and Danao [55] are adopted for this study without further verification since the justification regarding these settings are convincing enough and will not change irrespective of changes in test wind speeds. The details of the various settings verified are presented in the following sections.

3.6.4.1 Seeding Concentration

The accuracy of PIV measurements is highly dependent on proper seeding, because the right seeding density is important to capture complicated flow details especially in the recirculation or separation zone. To achieve this, seeding must be uniformly distributed and be of the required concentration. The six-jet atomizer was run between 4 to 12 minutes inclusive at an interval of 4 minutes and the same number of images was recorded in each of the tests. The numerical data were analysed based on the correlated vectors.

Figure 3.12 shows the effects of varying the seeding time on the correlated vectors. At the lowest seeding time of 4 minutes, very high number of vectors were poorly correlated hence the number of the rejected vectors is very high. This is confirmed in Figure 3.12 (b) as 5.4% of the total number of vectors is poorly correlated which is almost double the 3% tolerable level. With increases in seeding time, a rapid reduction is seen in the number of poorly correlated vectors.

3.0% of vectors are rejected at 8 minutes seeding while at 12 minutes seeding time, only 2.6% of vectors are poorly correlated. In consideration of time and small differences between the poorly correlated vectors at 8 and 12 minutes, 8 minutes seeding time, was adopted for all the PIV testing presented in this study.

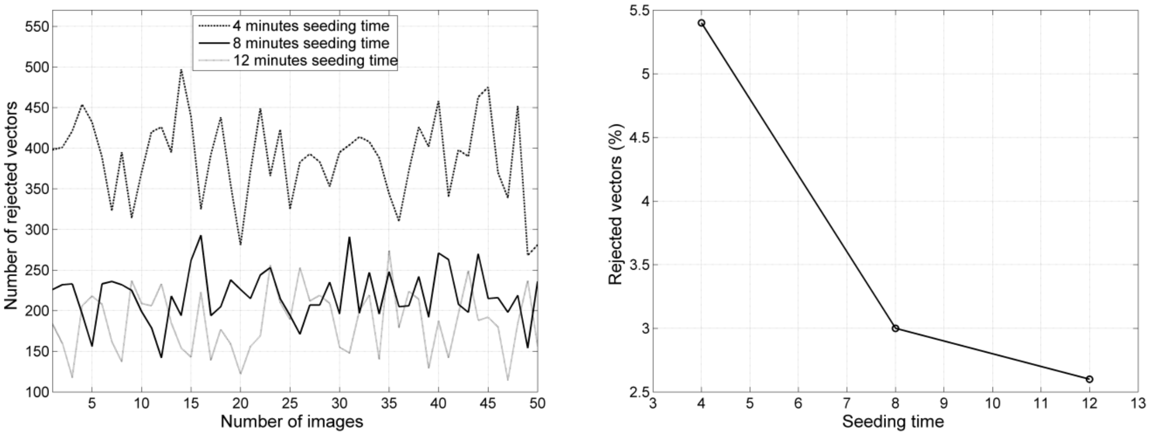

a. Rejected vectors per image b. Percentage of rejected vectors

Figure 3.12. The effects of seeding time on rejected vectors.

3.6.4.2 Laser Power

The intensity of the light sheet is directly related to the laser power. At the maximum laser power, the laser can emit highly concentrated light beams. For safety reasons, and also to prevent the camera sensors from being damaged due to too high light sheet intensity, different levels of the laser power were tested to find a suitable power level. Images were acquired from 70% - 100% range of the laser power at 10% intervals. The tests were conducted at 8 minutes seeding time.

The data were analysed based on the quality of the correlation. The number of poorly correlated vectors fluctuates within a median of 1400 at 70% power level (Figure 3.13 (a)) which is unarguably very high. At 80% laser power level a sharp drop to a median of 420 poorly correlated vectors is seen which also reduced further to a median of around 200 with further increases of the laser power to 90 and 100%.

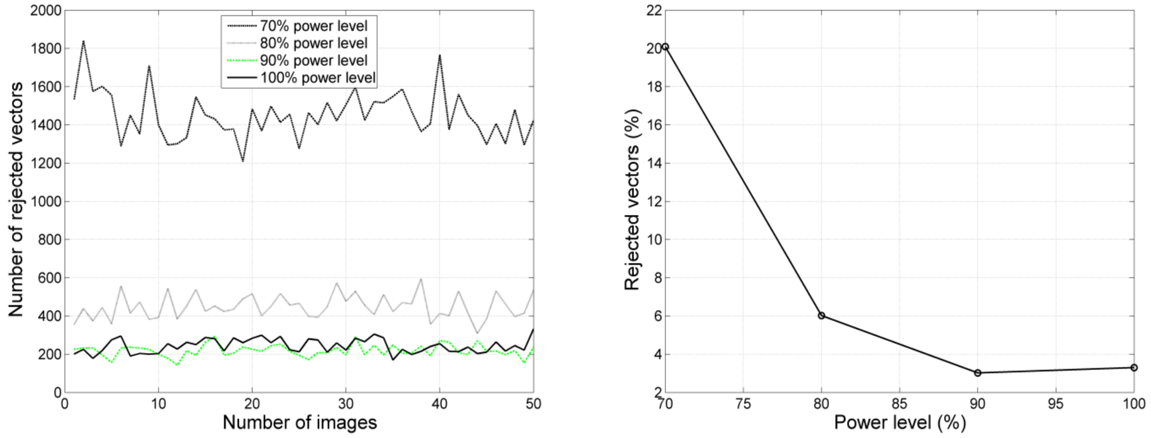

a. Rejected vectors per sample b. Percentage of rejected vector

Figure 3.13. The effects of laser power level on rejected vectors.

Figure 3.13 (b) also shows similar trend but in percentages. An insignificant difference of <0.025% between the poorly correlated vectors is observed at 90 and 100% laser power. The 90% laser power level is adopted for this study since the rejected vectors are within 3% at this power level. This is slightly altered within ±5% when the azimuth angle being tested is causing the blade to be very close to the wind tunnel side walls, either closer to the laser or further away. When the blade is closer to the laser, the intensity of the light sheet at the 90% laser power is decreased so the laser power is reduced while the reverse is the case when the blade is further away.

3.6.4.3 Time Between Pulses

The default 5Hz setting of the acquisition frequency was adopted for this study so it was necessary to determine the appropriate time between laser pulses to capture a pair of images. Because the time between pulses must be sufficient enough to accommodate the first and the second laser pulses come to an end of the exposures of the images so that both the slow and fast moving particles are captured within the interrogation window. The timing was varied from a low 7.5µs to a highly 60µs inclusive. The poorly correlated vectors at 60µs fluctuate around a median of 1457 (Figure 3.14 (a)) corresponding to 20% (Figure 3.14 (b)) which is very high. The high number of rejected vectors is due to the inability of the camera to properly capture images of the fast moving particles, implying that longer time between pulses does not favour accurate PIV measurements.

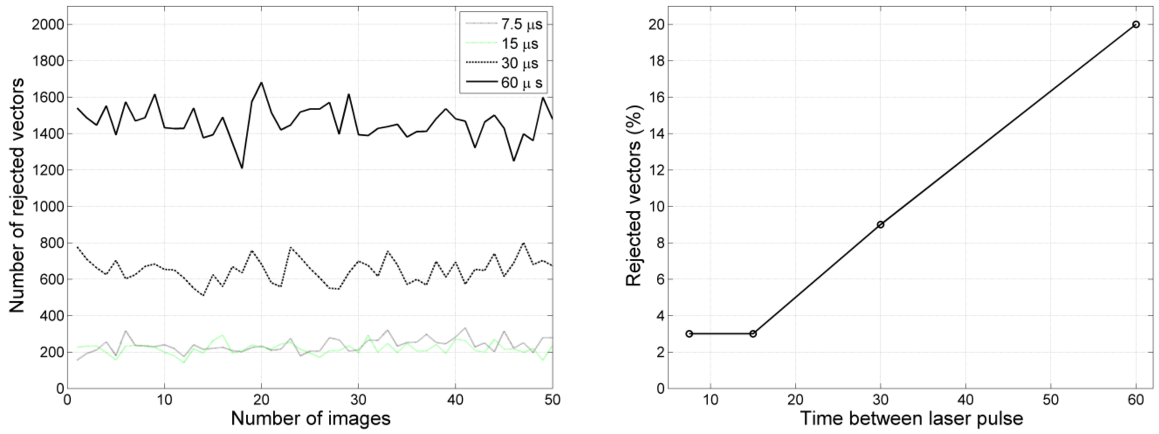

a. b.

Figure 3.14. The effects of time between laser pulses on correlated vectors: a) number of rejected vectors versus numbers of samples, b) percentage of rejected vectors versus time between laser pulses.

At 30µs the number poorly correlated vectors fluctuate within a median of 654 which corresponded to 9% of rejected vectors. This again indicated that 30µs is still too high, since the camera is unable to correctly capture all the particles within the interrogation window. Insignificant differences in the number of poorly correlated vectors are observed at 7.5µs and at 15µs. While the poorly correlated vectors fluctuate around a median of 232 at 7.5µs, and a fluctuation around 216 is seen at 15µs with corresponding rejected vectors at 3% in both cases. Thus, signifying a small time interval between laser pulses is needed for accurate PIV visualisations. For this study 15µs was therefore chosen for the PIV testing, which also corresponded to the time between pulses used by Ferreira et al [90] and Edwards [39].

3.6.4.4 Number of Images

The number of samples was also systematically studied for an appropriate number of samples to be chosen for the accuracy of measured data, and also to save time during the actual testing and the period of the analysis of acquired data. 25 to 100 inclusive samples at an interval of 25 image samples were tested. Poorly correlated vectors were high at the lower number of samples and reasonable low at 50 samples and above (Figure 3.15)

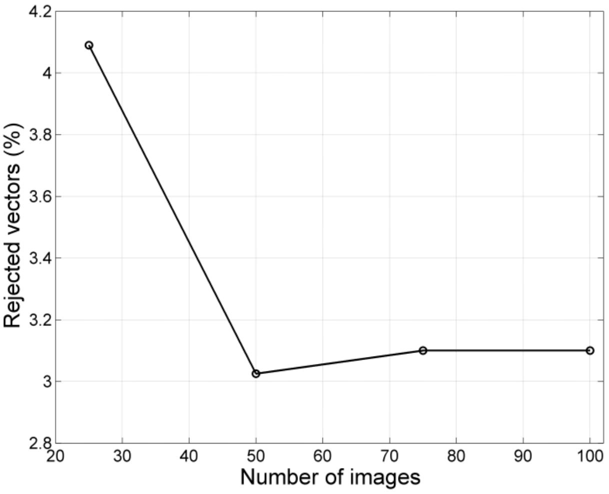

Figure 3.15. The effects of number of samples on correlated vectors.

For the PIV investigation presented in this thesis, 50 samples were chosen for all the testing. Which drastically reduced testing and data processing time when compared to the 100 samples adopted by Edwards [39] in his investigations.

3.6.5 Testing and Image Acquisition Procedure

At the start of tests each day, the atmospheric pressure and temperature are read from the mercury barometer and thermometer. Since, the temperature of the outside and inside of the wind tunnel are read, the average of the two temperatures is computed while the mercury barometer reading is converted to standard pressure unit before the values are keyed into a labview programme that was initially used for the "spin down" tests.

The wind tunnel fan and later followed by the VAWT testing rig are made to start running while a minimum of 10 minutes is allowed for warming up to attain a steady performance level. This was followed by the seeding of the room for 8 minutes through the Six-jet Atomiser positioned upstream of the wind tunnel before the actual testing. With the synchronisation and the alignment of the camera and the laser at 90^o blade angle having been achieved previously, 50 images are acquired for each blade angle usually starting from 90^o.

The positions of the camera and the VAWT rig are manually rotated to a new angle for each subsequent azimuth angle to be tested, through the attached discs, while the laser is wheeled to a new corresponding and perpendicular position to the camera. The marked floor for the various azimuth angle position made the adjustment of the laser position easier for repeated tests. To maintain the same level of particle concentration, the seeding of the room during the tests is repeated every 30 minutes or when the seeding concentration on the screen is observed low.

It was possible to measure above 20 azimuth angle positions around the blade usually at 10^o intervals which gave a widespread record of the complete rotation. The camera view was obstructed by the wind tunnel and camera rig support structures, hence, it was not possible to visualised at 20°, 30°, 150°, 160°, 200°, 210°, 330°, and 340 azimuth angles. A few other angles viewed had incomplete information due to the shadow region of the blade. The tests were conducted for the VAWT configuration with $C = 0.04$ m at 6 m/s at $\lambda = 2.5$, $\lambda = 3$, $\lambda = 4$ while the second VAWT configuration was tested at 6 and 8 m/s, and also at the corresponding λ.

3.6.6 Image Evaluation and Data Analysis

This section presents the logical sequence followed in the analysis and processing of the visualised and measured PIV data. It involves image masking, cross correlation, moving average validation and vector statistics. A sample of the acquired raw data is presented in Figure 3.16, it shows the FOV with an approximate area of 135mm x 135mm, the flow direction, seeded particles, reflecting blade surface, support arm and shadow region.

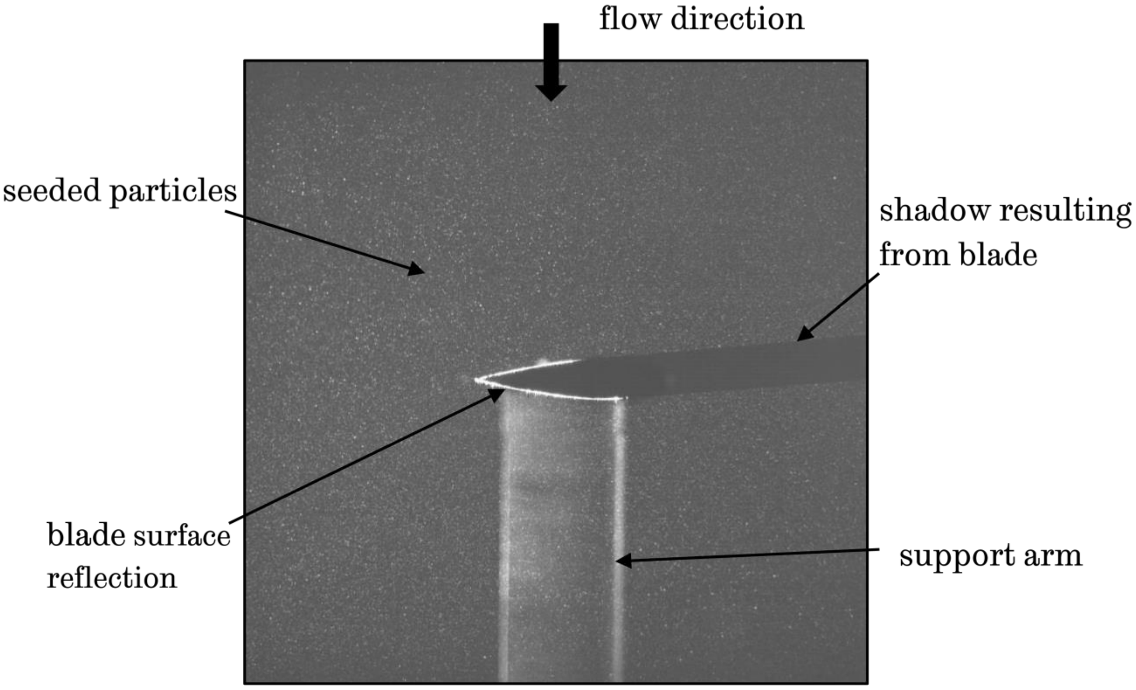

Figure 3.16. Raw PIV data at a 90° azimuth angle and 6m/s in the FOV.

3.6.6.1 Image Masking

Masking of images enables the removal of unwanted areas in the raw image by carefully defining the regions that are of no interest and applying the masking which eventually cut out the data in the defined region (Figure 3.17). This was the first step employed in the analysis of the acquired data, since, it was necessary to mask out the near blade invalid region due to the reflection and the shadow region caused by the blade. The vectors within these regions could be poorly correlated when further processed without being masked out.

3.6.6.2 Correlation of Image

Image correlation is aimed at determining the distance the particles have moved during the time between pulses of the laser and thereafter translate the distance moved into a velocity measure. The Equation 3.5 relates particle velocities and displacements [91].

$$u_p = \frac{d_p}{M_p \Delta t} \qquad 3.5$$

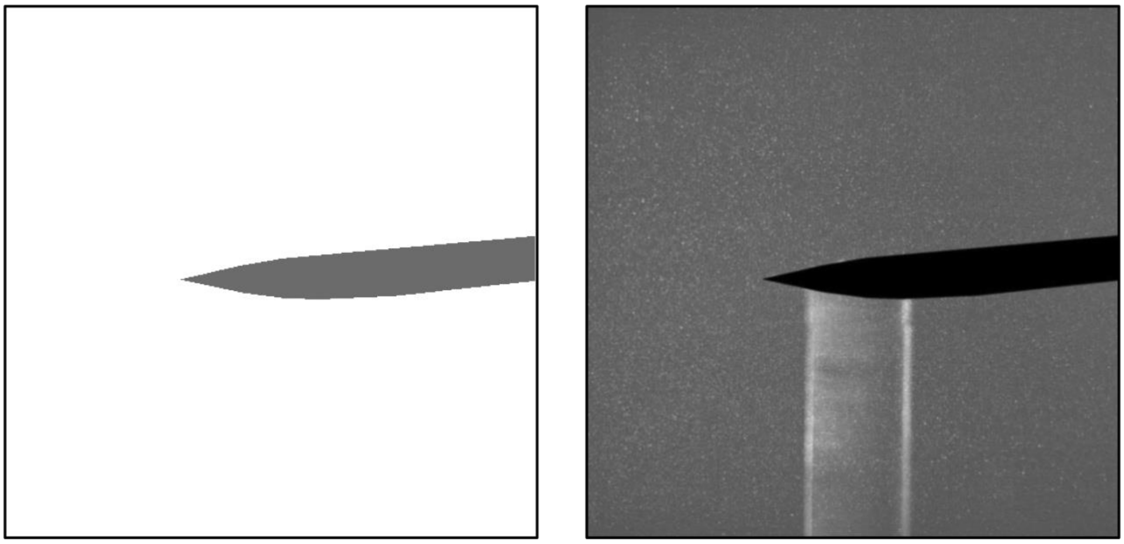

Figure 3.17. Masking of image: a) defined masked region, b) applied mask.

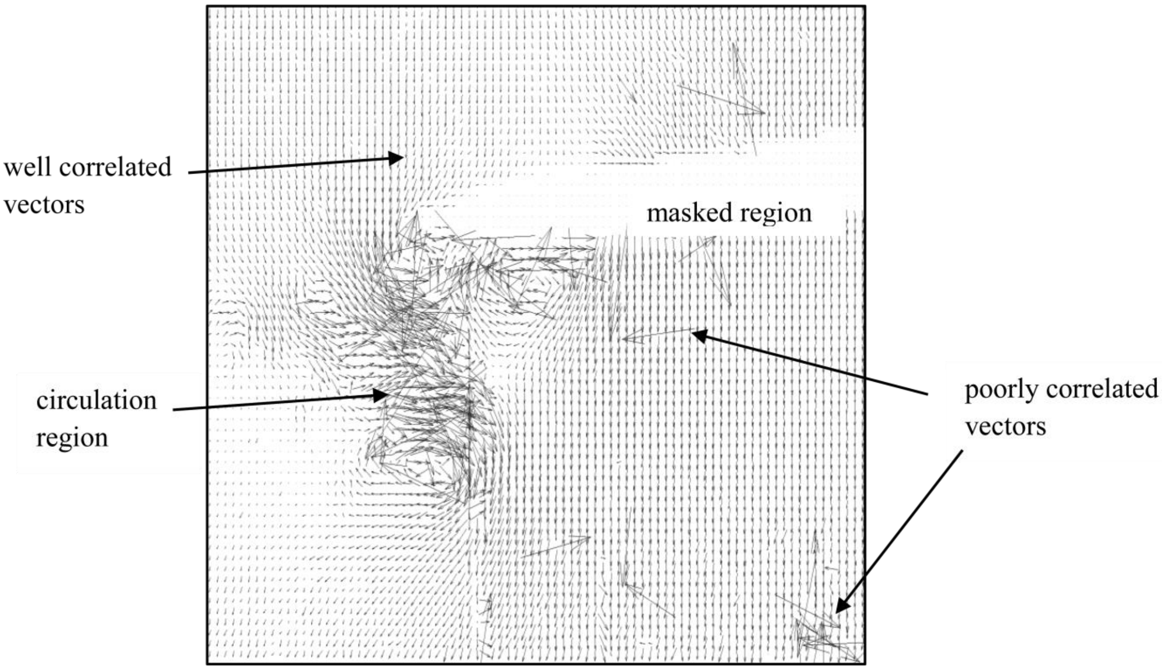

Figure 3.18. Zoomed-in sample of cross-correlated vectors of a single pair of image.

Basic cross-correlation of images used by [92] was adopted for this study. The cross-correlation function is calculated on small interrogation areas, which result in one vector map from a double frame image per interrogation window that make up the full FOV vector map containing 2048 X 2048 pixels. 32 x 32 pixel interrogation window with an overlap of 25% at 0 x 0 pixel distance to second correlation area was adopted for the cross-correlation. A result sample is shown in Figure 3.18 with the important characteristic features indicated.

3.6.6.3 Moving Average Validation and Vector Statistics

The moving average validation, which was applied after the cross-correlation of the images, certifies vector maps by the comparison of velocity of each vector with the average velocity of the vectors in a close defined vicinity of the interrogation window. A reasonable estimate of the true velocities is achieved by replacing the vectors whose velocities deviate too much from the average velocity of the vectors in the defined vicinity.

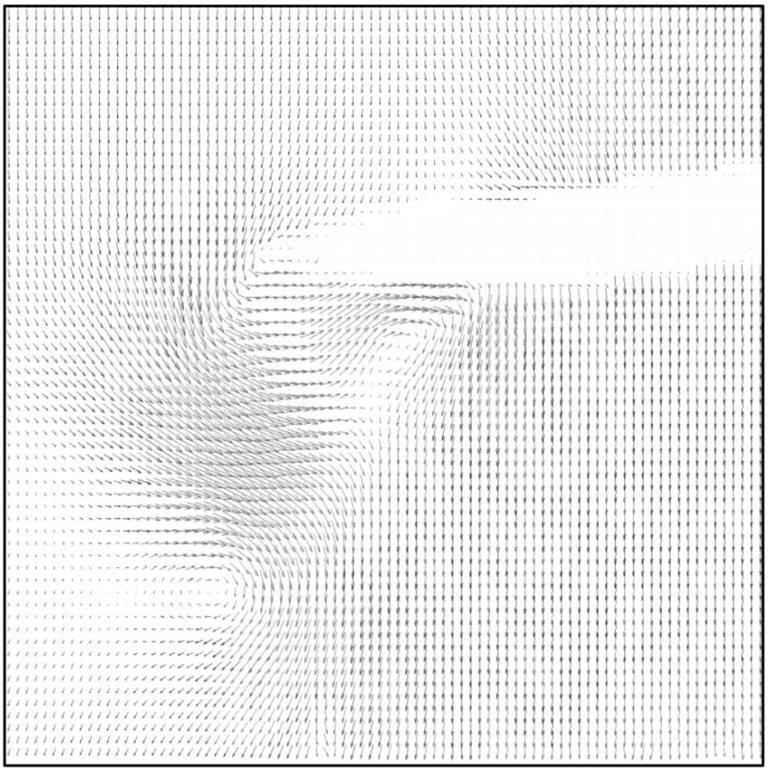

Figure 3.19. Zoomed-in map of vectors statistic of all image samples.

A 3 x 3 moving average validation window was applied which help to filter and reduce the number of poorly correlated vectors to minimum value.

Thereafter, vector statistics being a vector arithmetic analysis method which enabled the calculation of the mean velocity vector of all the ensembles in all the number of samples was implemented. This method can provide a mean of the velocity vectors of all the samples and also produce a vector map of the samples in one image which can facilitate the application of other software in the further processing of the data (Figure 3.19).

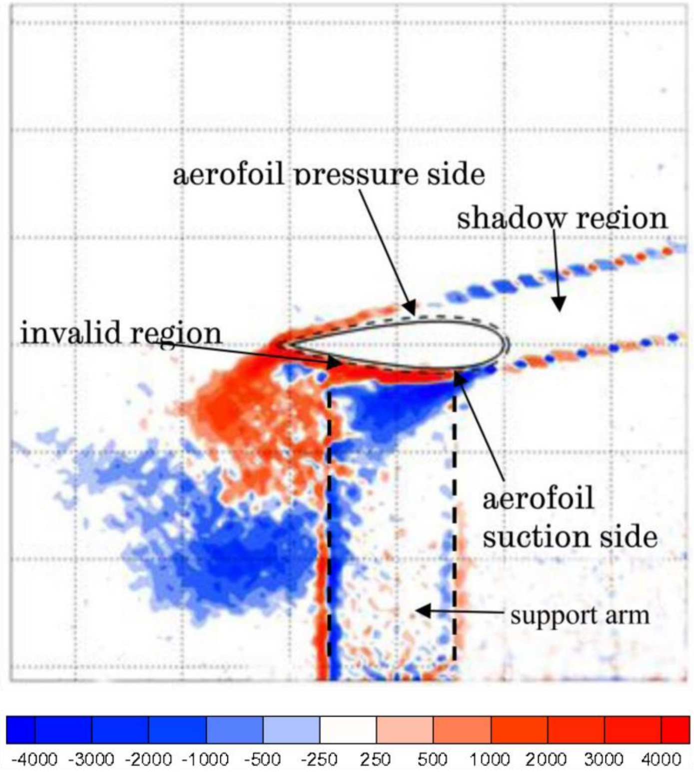

Figure 3.20. Sample of vorticity plot of the vectors statistics at 6m/s, θ=90o, C = 0.04m.

Another processing software was used to further process the acquired two dimensional PIV data to obtain the desired vorticity plots. Vorticity was used to show the flow circulation based on literature and also because it can best describe the clockwise and anti-clockwise movements of the seeded particles in the flow around the VAWT blade over velocity streamlines by relating particle circulation in the interrogation windows to the FOV area. For a 2D PIV FOV plane, Equation 3.6 [93] defines particle circulation and vorticity.

$$\text{vorticity}(\zeta) = \frac{\text{circulation}(\Gamma)}{\text{area}} = \frac{\partial v}{\partial x} - \frac{\partial u}{\partial y} \qquad 3.7$$

Figure 3.20 presents a sample of vorticity plot with an imported NACA0022 aerofoil which is of the same chord length with the VAWT blade on which the PIV measurements is conducted. The scale of the vorticity contours ranges from -4000 to 4000. This scale is used in all the investigations including those of the CFD plots.

3.7 Computational Fluid Dynamics Method

The process involved in the development and selection of the CFD model features used in this study is outlined in this section. A detailed description of the model features such as the boundary conductions including the inlet and outlet, the mesh around the blade chord and also the rotating and stationary domains meshes is presented. Then, parametric studies of time step size, and the number of node density, that enable choice of appropriate features of the model is also presented. Earlier domain side wall distance studies by Danao [55] based on a similar VAWT scale is adopted in this study since the same wind tunnel test cell which the CFD investigations is aimed at complementing is used for both studies.

3.7.1 CFD Solver

The numerical investigations presented in this thesis have been conducted with the commercial CFD package, Ansys Fluent 12.1. The Fluent 12.1 code solves the fluids governing equations through a finite volume method. The flow is incompressible so a fully unsteady pressure-based coupled solver was selected and all the spatial discretization terms were set to second order [94]. The solution control was set at a courant number of 200 that was high enough to save computational time while allowing reliable convergence. The turbulence intensity was set to $Tu = 8\%$ at the inlet, with a turbulence viscosity ratio of $\mu_t/\mu = 14$ that enable the decay of the turbulence intensity to $Tu = 1\%$ at the immediate region of the blade following the turbulence intensity experimental results. The computation of the solution in the flow domain was initialized using the inlet conditions.

3.7.2 CFD Model Development

Relevant literature has shown that a VAWT model and the domain could be represented by a two-dimensional CFD model since it can reliably provide penetrating insights into the understanding of the performance, aerodynamics and flow characters of VAWTs. With the right model created, a 2D model can also be used to investigate the parameters that limits and enhance VAWT performance. VAWT models with infinite length of the blades and aspect ratios are basically 2D in nature. The additional benefit of reduced computational time which the 2D model offers over the 3D model and also the assertions of [72], that the results of the 3D model do not justify the resource requirements in the use of 3D models in VAWT investigations, a 2D model was developed for this study, while the 3D model is left out for future works.

A 2D CFD model was used to represent the wind tunnel experiments VAWT and domain (Figure 3.21). Gridgen meshing software and techniques were used to mesh the entire domain in a systematic process. First, the blade shape was defined by importing the NACA0022 profile coordinates, then the aerofoil sizes (chord lengths) used for the investigation were defined. Based on the parametric studies detailed in the later sections, the near blade and the entire mesh surrounding blades including the extent of the boundaries were defined.

The created 2D model contains two main domains; the rotating inner and the stationary outer domain. The rotating circular inner domain rotates while the stationary outer domain does not. There is a sliding mesh interface boundary that connects the two sub-domains, the interface is far enough away from the blade to avoid problems.

Each of the blades was meshed with 400 nodes. A node sensitivity study was carried out to determine an appropriate node density in section 3.7.3.2, and to resolve the stall affected region properly, each of the three aerofoils contained in the rotating domain is embedded in an O-type mesh of 60 layers (Figure 3.22), such that the refined O-type mesh remained with the blades as the rotating inner sub-domain rotated relative to the stationary outer sub-domain. The same 400 node density was retained for the immediate mesh surrounding the O-type mesh (Figure 3.24).

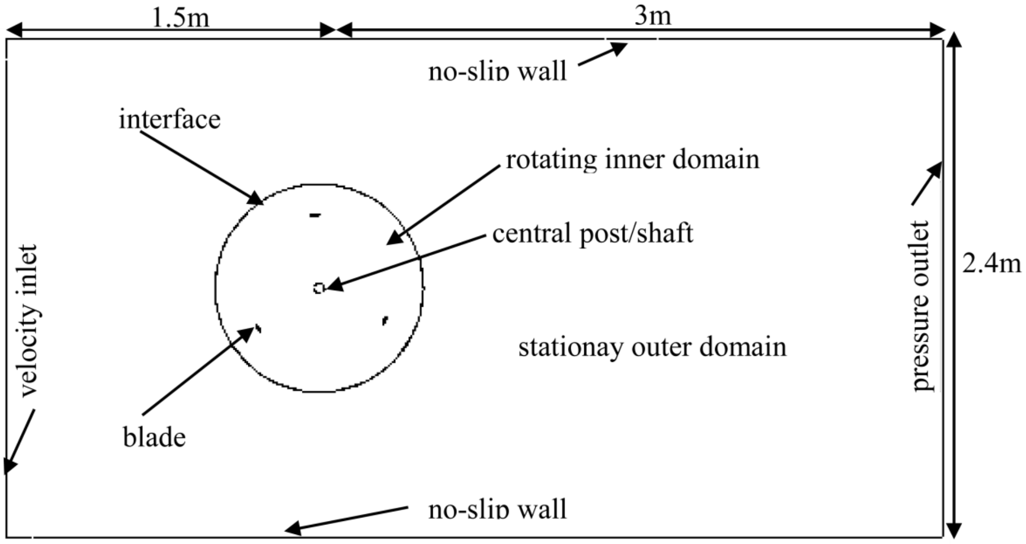

Figure 3.21. The boundaries and features of the 2D CFD model.

The nodes are concentrated but equally at both the leading and trailing edges for good capture of the flow physics (Figure 3.23). The sharp trailing edge is rounded (Figure 3.23 (c)) with an insignificant radius/chord ratio which has no effects on the results. The 60- layer O-type mesh around the aerofoils is inflated from the blade surface while the remaining rotating domain mesh is generated from the O-type mesh. The entire domain contains fully structured meshes and the boundary layer around the blades has a first cell height of 1e-05m which gives a range of $0.8 \leq y^{+} \leq 5$ and an average of less than one from the flow solutions. The angle skew-ness of the mesh was reduced to 0.6 by using the meshing software smoothing algorithm .

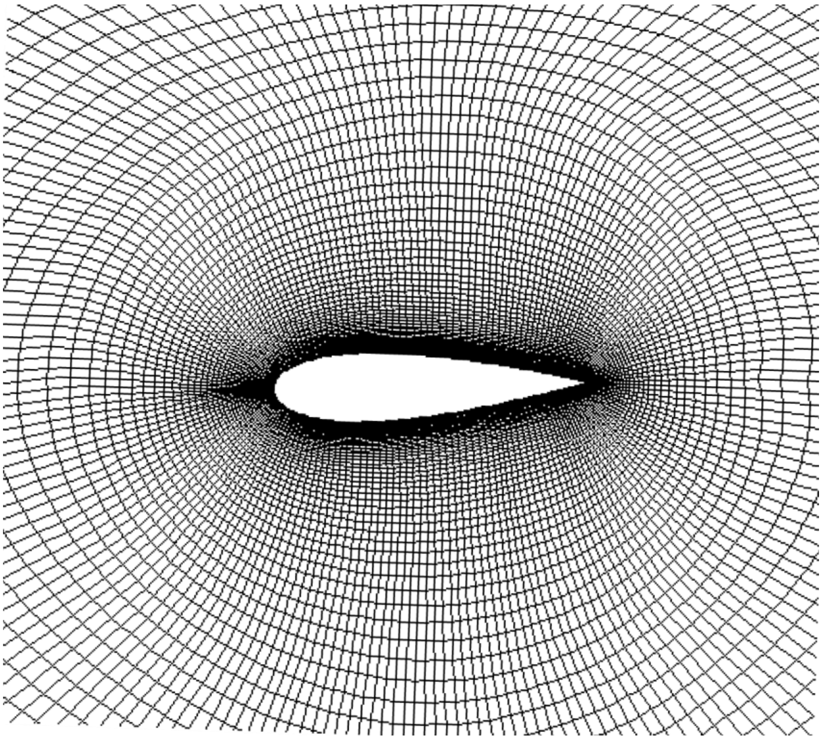

Figure 3.22. The near blade and O-type mesh around an aerofoil.

The stationary outer domain was coarsely meshed with 100 nodes only, while the maximum length cell was set to the length size of the smaller chord to reduce computation time (Figure 3.25). The coarseness of the mesh in the stationary domain was not considered an issue since the pattern of the developed wake is not within the scope of the study presented in this thesis. So the effects of the presence of a steal matting grid of 2” x 2” and a shuttle mechanism, that can generate gusty wind when needed, behind the VAWT axis in the actual wind tunnel set-up on wake development was not considered.

The VAWT axis of rotation are set at 1.5m from the velocity inlet boundary. Although in the actual experimental set up, the VAWT axis is 1.8m away from the velocity inlet boundary, the velocity within 0.3m difference was considered to be still influenced by contraction of the wind speed in the wind tunnel, hence the 1.5m distance of the VAWT axis from the inlet boundary is considered appropriate. A turbulence intensity of 8% was set at the inlet which is expected to decay as observed in the experiments.

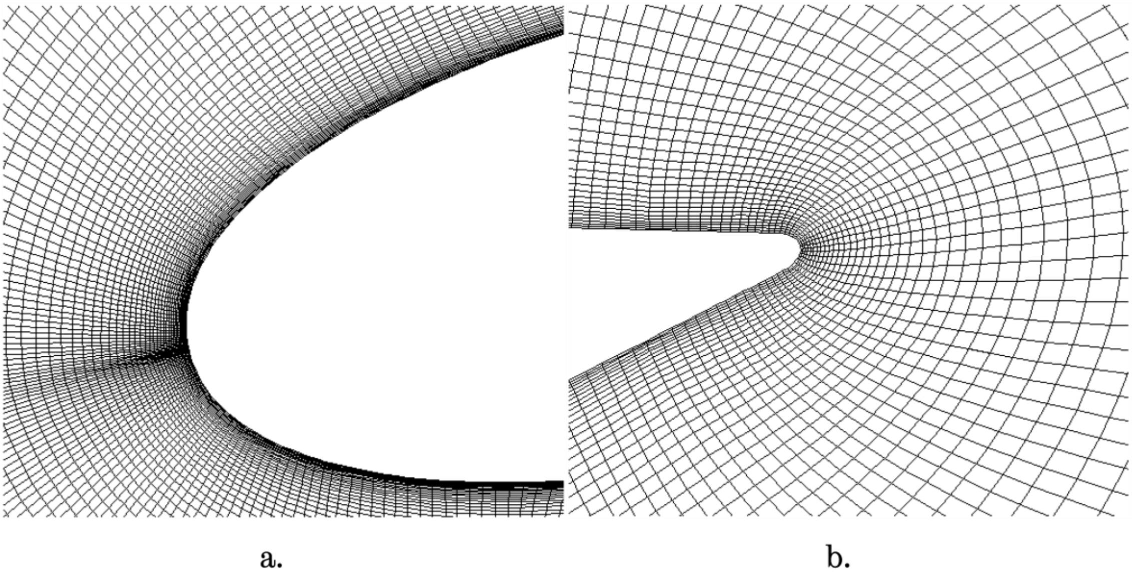
a.

b.

Figure 3.23. The clustered mesh around: a) the leading edge, b) the Trailing edge.

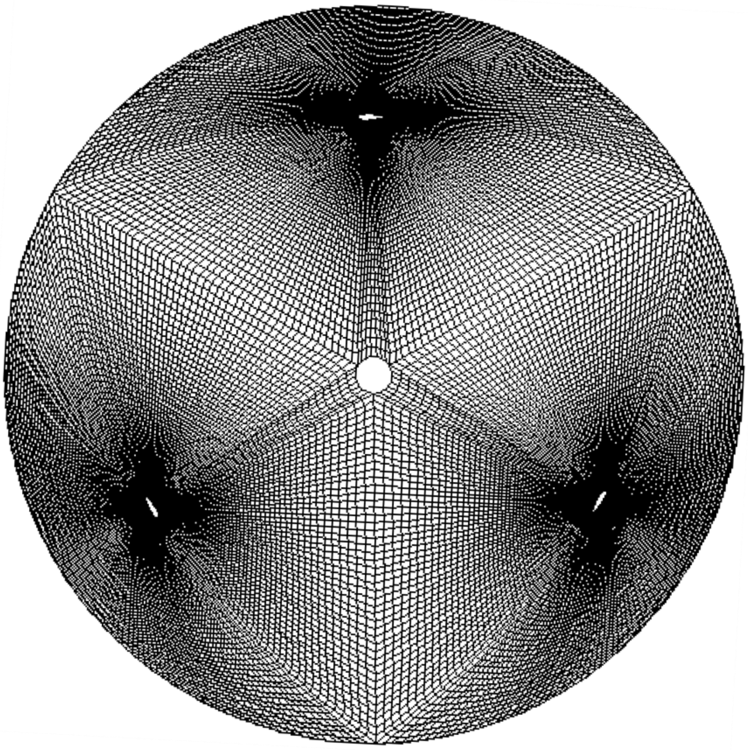

Figure 3.24. The rotating inner domain mesh.

The outlet boundary was defined as pressure outlet and set at a distance of 3m equivalent to the actual distance of the wind tunnel fan from the VAWT axis of rotation. The set 3m distance is considered appropriate to ensure that the wake development is not terminated prematurely despite Danao [55] revelation that no appreciable changes in torque was observed when the outlet boundary, $d_o \geq$ 2m from the VAWT axis. Also, There was no additional computational time due to the increase in outlet distance from the VAWT axis based on preliminary tests. The side walls were defined as no-slip wall and set at 1.2m apart from the VAWT axis of rotation.

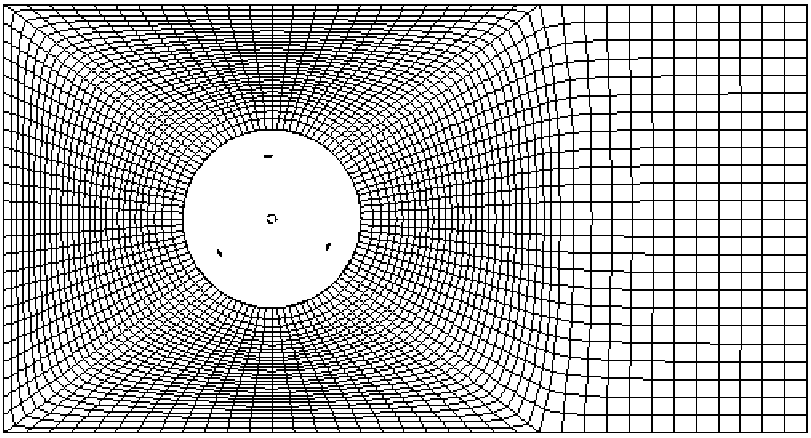

Figure 3.25. The stationary outer domain mesh.

The 1.2m distance of the side walls from the VAWT axis was adopted since it equals the blockage ratio of the actual 3D wind tunnel setup and also in agreement with the sidewall investigation by Danao [55] on a similar VAWT model in the same wind tunnel. For this study, the effects of blockage on the performance of the VAWT were left out for future investigation.

Having created the CFD model based on the parametric studies conducted in section 3.7.3, the model was tested to ascertain its suitability for the investigation presented in this thesis. First, the chord with C = 0.04m was tested at λ = 2.5, which the overall average performance was observed to be in the negative region, and at λ = 4 which the performance is in the positive region. Secondly, the chord with C = 0.03m was also tested at the same λ the bigger chord was tested. In all the test cases the time convergence of the variables was monitored by setting convergence criteria of variable drop to less than 1x10^{-6}. Also the simulation was made to run up to ten rotations in each test to ensure reasonable periodic convergence.

Figure 3.26 presents plots of torque versus the number of rotation of one blade, at the two λ tested for C = 0.04m. The peaks of upwind and downwind torques are irregular for the first four cycles. Regularity in the torque peaks is seen after the fourth rotation and for the last three cycles, a close match in the upwind torque peaks and downwind ripples is seen. A maximum difference of less than 0.6% in the average torque of the last three cycles for λ = 2.5 and 0.45% for λ = 4 is observed.

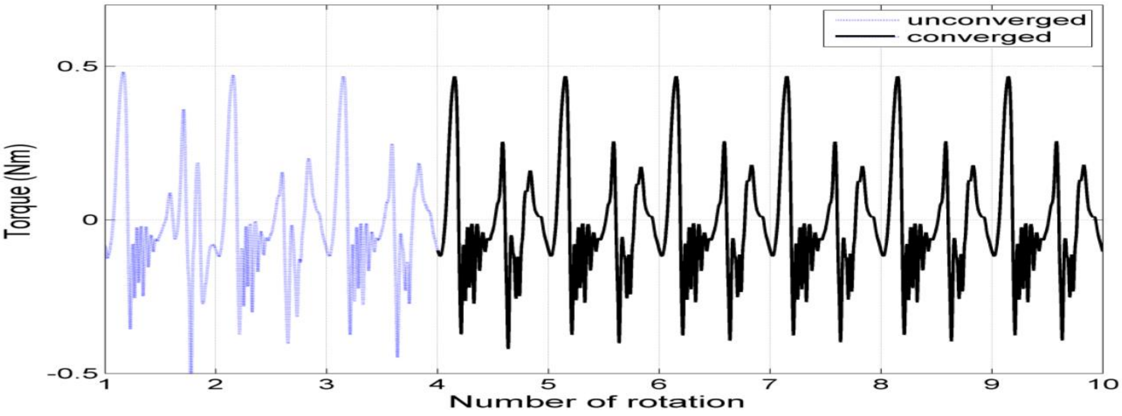

a.

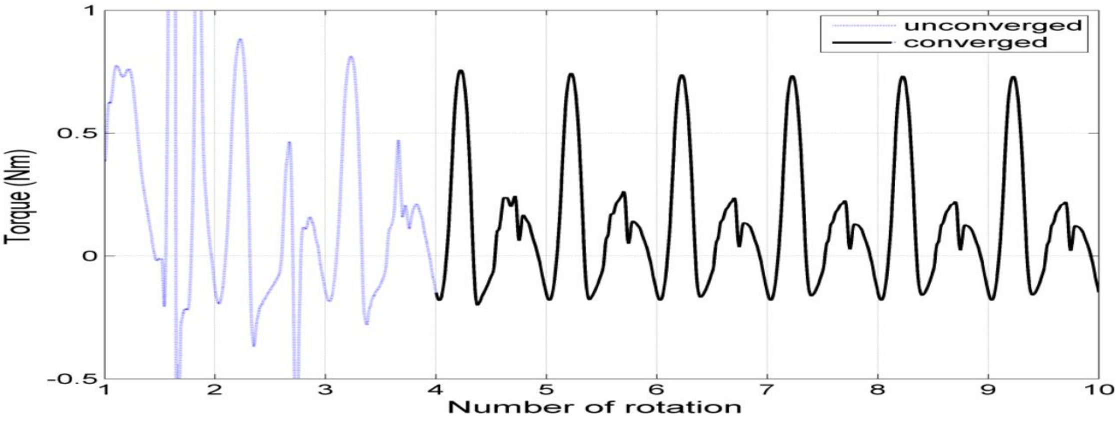

b.

Figure 3.26. Torque ripple of one blade for ten rotations C =0. 04m: a) λ = 2.5, and b) λ = 4.

Similar observations are equally seen in the C = 0.03m tests at the two λ despite irregularities in the downwind ripples that extend beyond the fourth cycle at λ = 4 (Figure 3.27). While the maximum difference in the average torque of the last three cycles is around 0.64% at λ = 2.5, it is approximately 0.5% for λ = 4. Implying that, the two models are suitable for the investigation although further tests will be conducted to validate the models by comparing their power coefficient and flow physics versus experiment data later in chapter four.

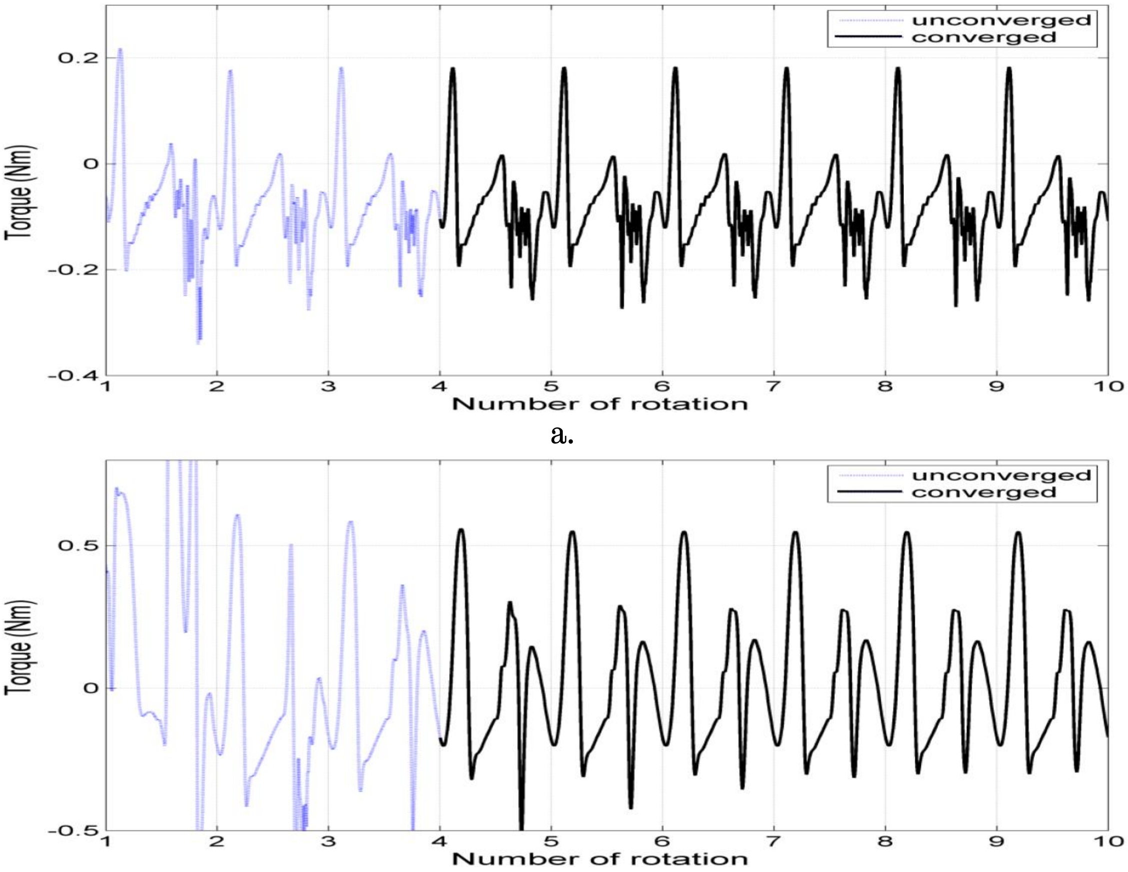

a.

b.

Figure 3.27. Torque ripple of one blade for ten rotations C =0. 03m: a) λ = 2.5, and b) λ = 4.

3.7.3 Parametric Studies

The parametric studies conducted that enabled appropriate choice of the model features made is presented in the following sections. It includes the time step size and number of node density studies. All the parametric studies are conducted at a low $\lambda = 2.5$, since settings at lower λ are more sensitive to changes in parameters, it is more difficult to achieving convergence and also susceptible to higher occurrence of dynamic stall [74].

3.7.3.1 Time Step Size

Unsteady simulation is time dependent so good choice of the time step size is important to ensure proper VAWT simulation. Since the VAWT rotates within an axis the choice of the time step size was based on the time (δt) equivalent to some defined VAWT rotational displacement along the azimuth. Four different degree equivalent time step sizes were tested. The lowest tested δt was equal to a $\delta t = 0.25^o$ and was multiplied by 2 to get $\delta t = 0.5^o$, $\delta t = 1^o$, and $\delta t = 2^o$. The four δt's were tested at a low $\lambda = 2.5$ which was considered to be within the low tip speed ratio region where the occurrence of blade stall is predominant. Selecting an appropriate time step size at the lower λ, with converged solutions, indicates convergence at the higher λ can be achieved.

Figure 3.28 presents the plots of the time step size study. In the upwind section, a negligible variation is seen between the finer δt's indicating a good agreement in the predicted torque. The maximum torque was attained at around $\theta = 45^o$ at all the δt's with the highest $\delta t = 2^o$ deviating most. Between $\theta = 60^o$ and 135^o stalling characteristics of the blade is predicted at all the δt's with significant deviation between the two lower δt's and the two higher δt's. In the downwind section around $\theta = 240^o$ $\delta t = 0.25^o$ (the lowest time step size) is seen to deviate most, indicating over prediction of the torque while $\delta t = 1^o$ and 2^o attained $T_B = 0.048$Nm. The $\delta t = 0.5^o$ is the midpoint between the lowest and the two higher tested δt's.

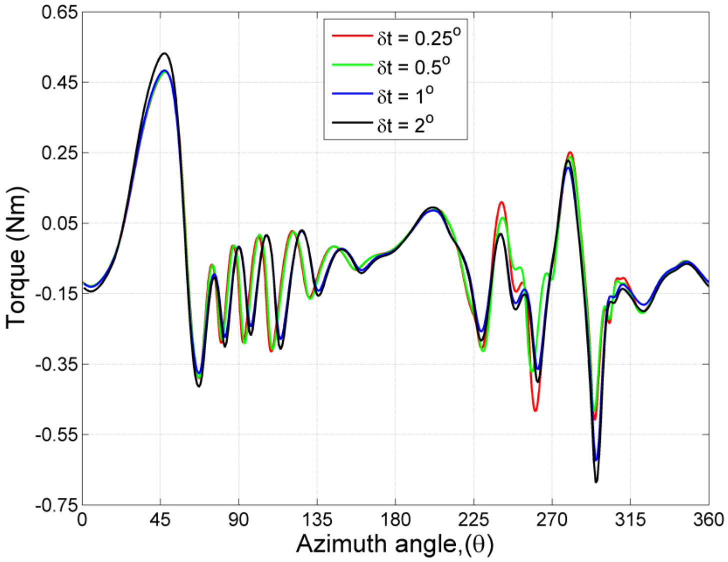

Figure 3.28. Time step size at various azimuth rotation (δt) at λ = 2.5, C = 0.03m.

In terms of ΔCP attained, all the δt's attained negative coefficient of performance with a maximum ΔCP = - 0.0028 between the δt's. Since sufficient time resolution is required for accurate simulations in this study, without increasing computational time unnecessarily and as well as avoiding convergence problems with the use of lower time step, δt = 0.5° has been chosen and adapted for all the modelling runs in this study.

3.7.3.2 Mesh Sensitivity

The number of node density was considered very important since it dictates the coarseness and fineness of the mesh so can affect the accuracy of the aerodynamic forces generated on the blade surface. To reduce errors caused by a poor mesh quality, a comprehensive study was conducted in which a wide range of node densities was tested following the guidelines of [95, 96]. Notable in these grid refinement guidelines is, that the number of the successive grid should be increased by doubling the number of the preceding grid.

Four node densities, spread around the aerofoil surface in each of the test cases, were tested at λ = 2.5. The blade torque for one full rotation and for each of the node densities was computed and compared as was done in the previous time step size studies. Figure 3.29 shows the effects of change in node density on a blade torque. Obviously, significant difference can be seen in the toque ripples both at the upwind and the downwind section of the rotation between the four node densities tested.

All the node points attained maximum torque at $\theta = 60^{\circ}$ with negligible difference seen between the three lower densities, whereas the highest node density attained 32% higher blade torque. At the stall angle around $\theta = 90$ and azimuth angles between $\theta = 110^{\circ}$ and 170° where the generation and the shedding of vortices is predominant, the 800 node density trailed behind the other three node densities. Thus, indicating that the effects of shedding of vortices are felt most at a higher node density in this region. While the T_B attained at 100 node density is higher in this region those of 200 and 400 node densities are closely matched. Between $\theta = 180^{\circ}$ and 300° the performance of all the four nodes is seen to change repeatedly intersecting and crossing over one another, until $\theta = 315^{\circ}$ where visible difference is seen again with the 800 nodes deviated from the other node densities.

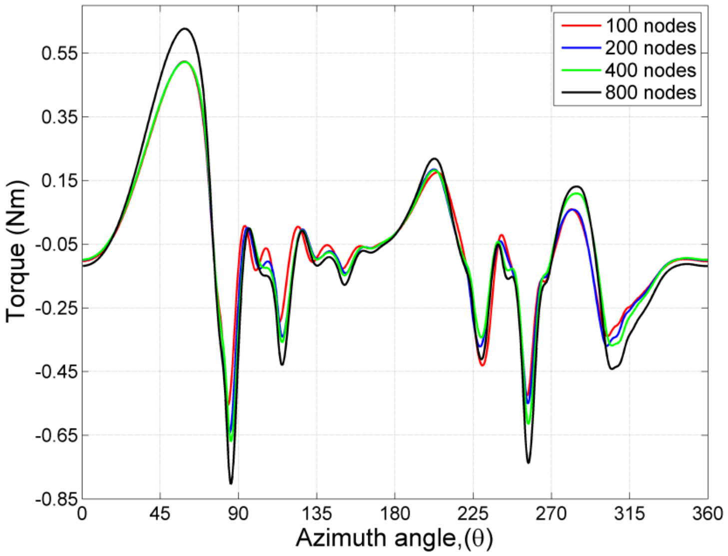

Figure 3.29. The effects of varying node densities on blade torque at $\lambda = 2.5$, C = 0.04m.

Comparing the effects of node density based on average torque attained, the 800 node density attained T_B = -0.063Nm followed by 200 node density with a T_B = -0.055Nm, then the 400 node density with a T_B = - 0.053Nm and the 100 node density that attained a T_B = -0.049Nm. A maximum ΔT_B = -0.014Nm is observed between all the node densities and a minimum ΔT_B = -0.002Nm is observed between 200 and 400 node densities. Following the insignificant difference that exits between the 400 and 200 node densities, and also not compromising on the total number of cells for the entire domain while avoiding convergence problems that may result with the use of higher node density, 400 node density was adopted as the appropriate number of node density for this study.

Chapter 4

Turbulence Modelling and CFD Model Validation

4.1 Introduction

This chapter presents the details of the turbulence modelling and the validation of the two CFD models used in this thesis. First, the turbulence modelling in which a turbulence model list of five candidates was compared to a static aerofoil coefficient of lift experimental data is presented and discussed. Second, the turbulence model that best predicted the aerofoil lift coefficient and an additional Transition SST model are compared to the power coefficients of a VAWT experimental data at various tip speed ratios and wind speeds to confirm the suitability of the developed 2D CFD models for this investigation.

Finally, the same two turbulence models that were compared with the VAWT experimental data by comparing their forces were also compared with the VAWT PIV data for the selection of an appropriate turbulence model since force validation alone is not enough yardstick for the selection of a good turbulence model.

4.2 Turbulence Modelling

A static aerofoil study was conducted to test a list of turbulence models to initially reduce the candidate list of turbulence models available for this investigation. This was achieved by comparing the coefficients of lift from the various turbulence models tested with the experimental data of Sheldhal and Klimas [97]. A NACA0012 aerofoil profile was simulated at a Reynolds number of $1.35\text{x}10^5$, similar to the conditions in which the experiment was conducted. The simulated aerofoil is 0.15m long and was meshed with a fully structured O-type grid with 1000 nodes over the surface, a result of an initial node sensitivity study conducted using a static aerofoil.

The nodes were concentrated at the leading and the trailing edges to enhance its sensitive to changes in flow conditions. The cells extend from the surface of the blade at a growth rate of 1.1. Although the $\mathrm{k}-\varepsilon$ model use wall function which requires y^+ that ranges between 30 and 100, a first cell height that yielded a $y^+ \leq 1$ was implemented for all the models. Therefore the $\mathrm{k}-\varepsilon$ models are not appropriately implemented for this case. The total number of cells is approximately 180,000. An appropriate time step size equivalent to $0.1C/U_\infty$ was used based on a free stream wind velocity of 13.67m/s that corresponded to the chord Reynolds number of $1.35\text{x}10^5$. The turbulence intensity of 0.8% was set and a pressure based unsteady second order was selected. The time step convergence was monitored by setting convergence criteria of residual drop to $1\text{x}10^{-6}$. The simulations were initialised to compute from far field and also set to run for 400 time steps at 50 maximum iterations per time step. For all the turbulence models tested the coefficient of lift was monitored while the angle of attack was varied from $\alpha = 0^o$ to $\alpha = 15^o$.

The different turbulence models tested in the static aerofoil study are the one equation fully turbulent Spallart-Almaras (S-A) model and four other two equation fully turbulent models, which are the Standard $\mathrm{k}-\omega$, SST $\mathrm{k}-\omega$, Realisable $\mathrm{k}-\varepsilon$ and RNG $\mathrm{k}-\varepsilon$. The S-A has been designed for wall-bounded flows and reliably in simulating boundary layers that are subjected to adverse pressure gradient especially in the aerospace, but suffers from the disadvantage of not being able to accurately predict the decay of homogeneous and isotropic turbulence. Also the S-A is less sensitive to numerical errors arising from mesh quality when compared to the $\mathrm{k}-\omega$ and $\mathrm{k}-\varepsilon$ turbulence models.

The $\mathrm{k}-\varepsilon$ turbulence models are an improvement on the S-A due to their sensitivity to numerical errors that can result from mesh quality and also are two equation models that determine the turbulent viscosity and length scale independently while solving the transport equations. The $\mathrm{k}-\varepsilon$ models differ from each other in the manner in which the turbulence viscosity is calculated, the turbulent diffusion of the k and ε, and also the method involved in the generation and destruction of the ε terms in the equation. But, they suffer from the disadvantage of not being able to accurately simulate near wall boundary layers so cannot provide adequate flow details when required.

The $\mathrm{k}-\omega$ turbulence models are other important models which have gained recognition in engineering applications of recent. They are also two equation models that solve the transport equation to calculate the turbulent viscosity and the length scale independently. The Standard $\mathrm{k}-\omega$, is an improved model over the $\mathrm{k}-\varepsilon$ models for being able to simulate the near wall but also cannot be relied upon in the prediction of far field flows. This drawback was corrected by Menter [98], through the inclusion of additional terms, in the Standard $\mathrm{k}-\omega$ turbulence model equation, that accounted for the intermittency and the transition onset criteria which produced the SST $\mathrm{k}-\omega$. The SST $\mathrm{k}-\omega$ can accurately predict flows within the near wall regions as well as the far field. This has made it one of the most sort after turbulence models in engineering applications.

The result of the static aerofoil study is presented in Figure 4.1. At $\theta = 0^{\circ}$ all the tested turbulence models accurately predicted the experimental results.

Away from $\theta = 0^{o}$ up to $\theta = 2^{o}$, the accurate prediction is maintained except for the Standard $k-\omega$ that is seen to clearly under predict the experimental results by around 20%. The under prediction of the experimental results, by the Standard $k-\omega$ is seen to continue even beyond $\theta = 13^{o}$ where the peak coefficient of lift is attained in the experiments. While the under prediction of the experimental results is seen with the Standard $k-\omega$, the Spallart-Almaras is obviously seen to over predict the results by around 7% at $\theta = 5^{o}$. The over prediction continue also even beyond $\theta = 13^{o}$. The over prediction of the results by the Spallart-Amaras turbulence model is expected since its applicability is better in flows with high pressure gradients which this study is far below, considering the blade chord's Reynolds number.

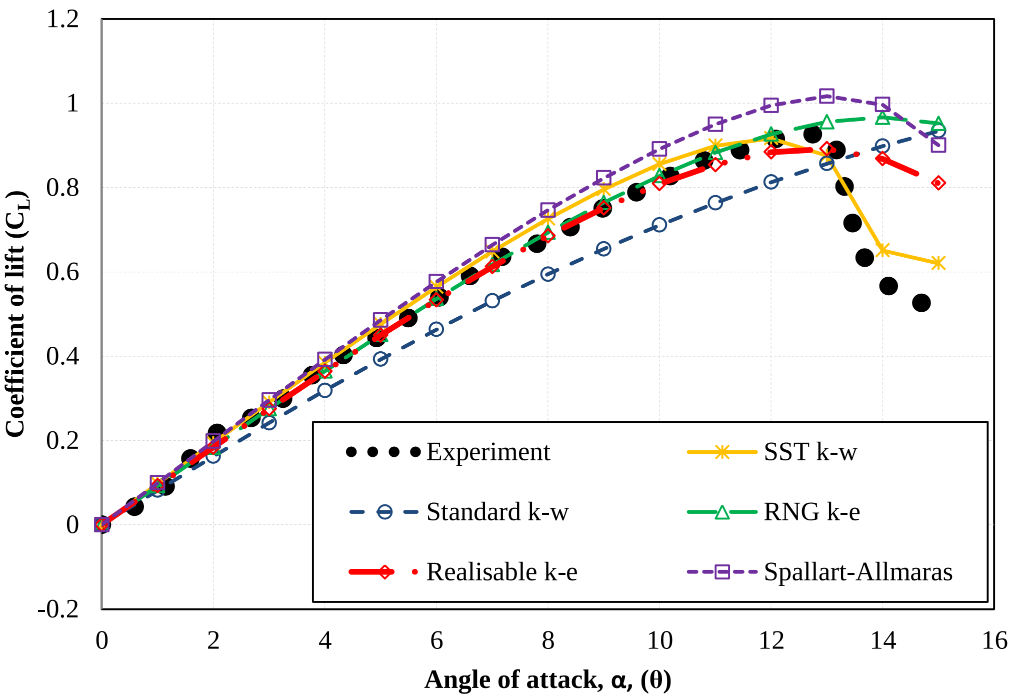

Figure 4.1. Coefficient of lift versus angle of attack for five turbulence models.

The two $k-\varepsilon$ turbulence model closely matched the experimental results until $\theta = 12^{o}$, despite the inappropriate y^{+} implemented for these models, at which point, the Realisable $k-\varepsilon$ is seen to drop off by around 0.5%. This deviation is also seen to increase with further increase in the angle of attack.

The RNG $k-\varepsilon$ closely matched the experimental results until the peak lift coefficient is attained at $\theta = 13^{o}$, further away from this angle of attack, the RNG $k-\varepsilon$ is seen unable to predict the experimental data. After the peak $C_L = 0.95$ is attained, a drop in the lift coefficient is seen in the experiment which all the turbulence models are unable to predict except the SST $k-\omega$. Although the SST $k-\omega$ over predicted the experimental results by a maximum of 7% at $\theta = 9^{o}$ and under predicted the peak C_L also, it captured the trend of the C_L versus α plot of the experimental result better than the rest of the turbulence models tested so the SST $k-\omega$ is considered the best model, although the Transition SST model was not tested in the static aerofoil study, of the turbulence models tested in the static aerofoil study. The SST $k-\omega$ is therefore chosen for further comparison with the VAWT experimental data at the appropriate Reynolds numbers for the CFD model validation purposes.

4.3 Model Validation

The developed CFD models adopted for this study, based on the settings and parametric study presented in chapter three is compared with the experimentally acquired VAWT data of similar scale. This is a follow up of the static aerofoil study since the flow characteristics surrounding the static aerofoil are not the same with that of a VAWT. For a good choice of turbulence model and proper validation campaign, the developed CFD VAWT models are compared with the author's experimental data of a VAWT of equal scale. The comparison included the power coefficient and the flow physics to ensure that the developed CFD models can actually simulate the VAWT performance and flow physics correctly. The correct simulation of VAWT performance aerodynamics and flow physics will be achieved by adopting the turbulence model that compared best with the experimentally measured data. The validation of the power coefficient and flow physics is detailed in the following sections.

4.3.1 Power Coefficient

The power coefficient CP_{cfd} obtained from the VAWT simulation using the Transition SST and the fully turbulent SST $k-\omega$ being the most appropriate turbulence model for the static aerofoil study, are compared against the experimentally measured CP of a VAWT on the same scale. The Transition SST turbulence model has the attributes of accurately predicting flows within transition region. Since the Reynolds numbers under which the experimental data are obtained and the simulations were conducted are within the transition region, the inclusion of the Transition SST as one of the turbulence model candidates is necessary.

The power coefficients are compared at two wind speeds for the two CFD models developed for this study over a wide λ range of 1.5 to 5 at an interval of 0.5. The C = 0.04m (σ = 0.34) VAWT model's CP are compared at 6m/s being the lowest wind speed used in this investigation while the C = 0.03m (σ = 0.26) VAWT model's CP are compared at 8m/s being the highest wind speed adopted for this investigation.

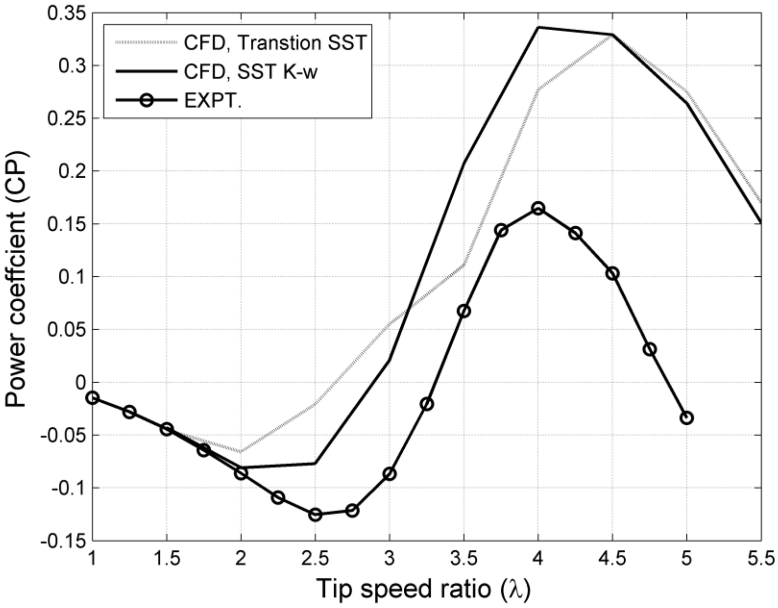

Figure 4.2. Comparison of CP curves at 6m/s, C = 0.04m.

It is shown in Figure 4.2 that the Transition SST and the fully turbulent SST $k-\omega$ turbulence models over predicted the experimental CP at all the tip speed ratios except at λ = 1.5 where the convergence of the three curve is seen. On the low λ region, negative performance is seen in the curves up to λ = 2.7 where the Transition SST model deviated and started attaining positive performance which peaked at CP = 0.325 at λ = 4.5 and drop off beyond this point. The fully turbulent SST $k-\omega$ is seen with a deeper negative trough that tend to follow the experimental curve but deviated between λ = 2.5 and λ = 3 from the experiment, but the SST $k-\omega$ is seen in the positive performance region while also being closer to the experimental curve. The fully turbulent SST $k-\omega$ maintained a steady rise until a peak CP = 0.34, higher than the peak CP attained by the Transition SST, is attained at = 4, and thereafter dropped off gradually showing a wider peak power region when compared to the narrower peak power region of the Transition SST.

Notable in the peak performance region of the curves in Figure 4.2, is that the Transition SST is closer to the experiment than the fully turbulent SST $k-\omega$. Between λ = 3.5 to λ = 4.5 the Transition SST is closest to the experimental curve signifying better prediction in this region than the fully SST $k-\omega$ model. The peak performance region is usually of more importance to the designer considering the economic returns that is associated with wind turbines harvesting wind in the urban environments.

At λ = 4.5 and beyond the difference in the performance between the two turbulence model is seen negligible. The curves are seen to converge at λ = 4.5 and with little separation as they move further down with an increase in the tip speed ratios. From the Figure 4.2, the prediction of the experimental results by the two turbulence models show that, the experiment is best predicted by the Transition SST at the peak power region while the fully turbulent SST $k-\omega$ best predicted the performance of the lower λ including the negative performance region. To further test the consistency in the prediction of experimental performance, by the developed CFD models and the two turbulence models in predicting the VAWT experimental data, and also to justify the choice of an appropriate turbulence model, another comparison of the same turbulence models with the experimental VAWT data of the C = 0.03m (σ = 0.26) was carried out. Figure 4.3 shows a comparison of the power coefficient of the two turbulence models against the experimental data at the various λ. A similar trend seen in Figure 4.2 is equally observed.

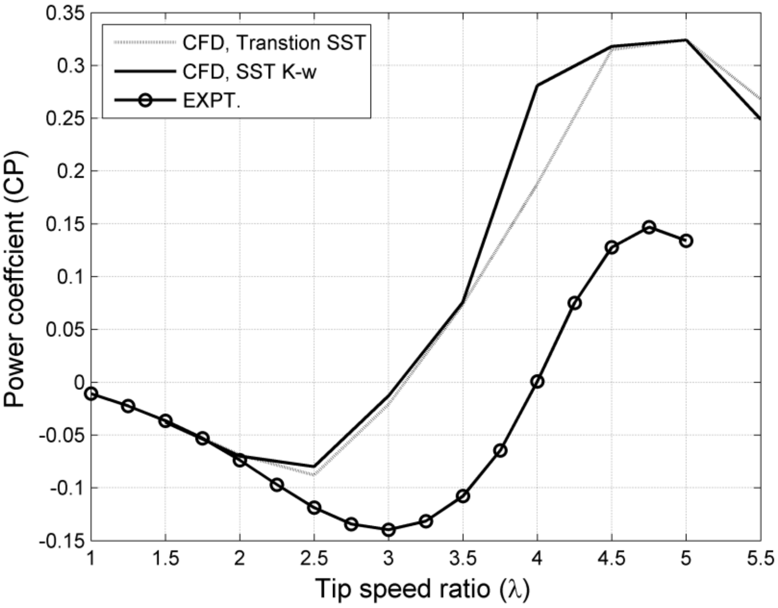

Figure 4.3. Comparison of CP curves at 8m/s, C = 0.03m.

The performance curves are seen in both the negative and the positive performance regions with the experiment presenting a deeper negative tough. Between λ = 1.5 and λ = 2 the two turbulence models accurately predicted the experimental data. Beyond λ = 2 and up to λ = 3.5 the CP of the fully turbulent SST $k-\omega$ and that of the Transition SST are closely matched while maintaining consistent gap away from the experiment. Away from λ = 3.5, the fully turbulent SST $k-\omega$ is significantly deviated from the experiment and also from Transition SST, again, implying and confirming the better capability of the Transition SST over the fully turbulent SST $k-\omega$ as previously observed in the C = 0.04m VAWT. At λ = 5 the two turbulence models attained the same maximum CP = 3.25 indicating that the Transition SST can become fully turbulent at higher Reynolds numbers.

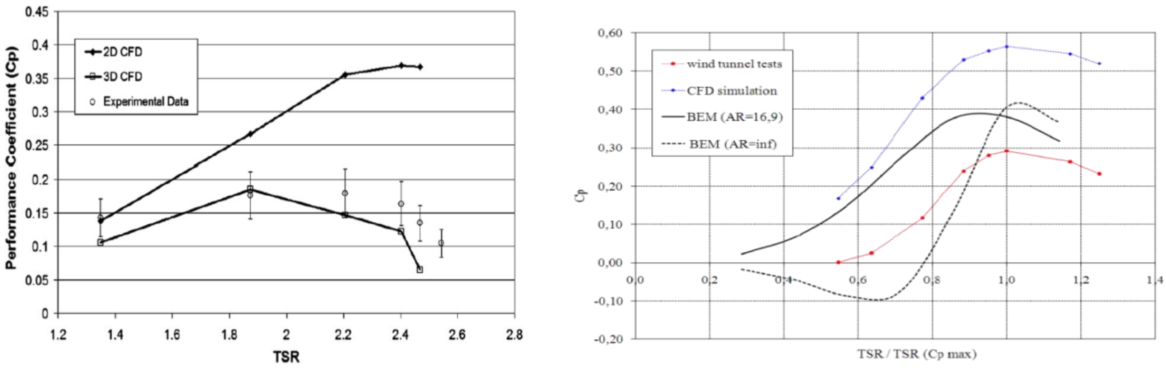

a. Howell et al [29]

b. Rasciti Castelli et al [76]

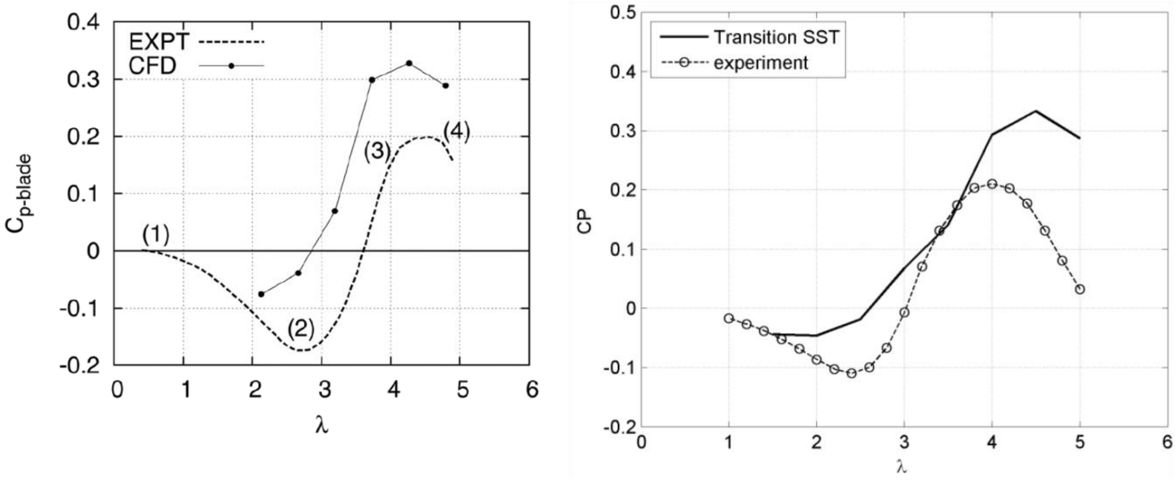

c. Edwards et al [53]

d. Danao et al [54, 99]

Figure 4.4. Validation of 2D and 3D CFD models using experimental data in the literature.

There is consistency in performance of the two turbulence models tested as shown in the figure 4.2 and 4.3 which confirms the suitability of the developed CFD model for the rest of the investigation. Over prediction of the experimental data is seen in the two Figures (4.2 and 4.3), this is due to the two dimensional nature of the CFD models developed that are being compared to 3D experimental data. The over predictions of the experimental data by the CFD models have also been observed by a number of authors available in the literature. Howell et al [29] compared both 2D and 3D CFD models, in which Realisable $k-\varepsilon$ was used, with experimental data on a similar VAWT scale (Figure 4.4a). Over prediction of the experimental data by the 2D CFD model at all the tip speed ratios and the under prediction of the experimental data by the 3D CFD model at the higher tip speed ratios were observed.

In a similar study by Rasciti Castelli et al [76] in which the Realisable $k-\varepsilon$ was also used, and that of Edwards et al [53], the experimental data were over predicted by a 2D CFD model (Figure 4.4 (b and c)). While the Danao et al [54, 99] study although, showed good prediction at some tip speed ratios because of the Transition SST model used, it equally over predicted the experimental data in most of the tip speed ratios (Figure 4.4 (d)). Common in all these studies is the higher over prediction of experimental data at higher tip speed ratios by the 2D CFD models. The 2D CFD models over prediction of experimental data observed in all these studies has been adduced to the effects of infinite blade span of the 2D CFD models and the finite blade span and support arm effects of the 3D experimental VAWT. Tip vortices shed by the 3D models are the main reasons for the difference in performance observed between the 2D and 3D models, since the shed tip vortices induced drag lead to the reduction of overall performance. All these studies compared well with the power coefficient validation campaign presented in this investigation.

4.3.2 Flow Physics

The comparison of the flow physics of the two CFD turbulence models against the PIV measured data was the second and last part of the validation campaign. This is aimed at justifying the choice of the CFD turbulence model that best compared well with the experimental data since the changes in the flow physics influence and determines the performance of VAWT at the various tip speed ratios, so the power coefficient validation alone is not sufficient for the choice of an appropriate CFD turbulence model. First, the flow physics of the two turbulence models is compared at $\lambda = 2.5$ and $\lambda = 4$ with PIV data for the C = 0.04m ($\sigma = 0.34$) VAWT at various azimuth positions. The chosen tip speed ratios corresponded to the λ at which the minimum and maximum CP is attained in Figure 4.2. Second, the flow physics of the two turbulence models is compared at $\lambda = 3$ with PIV data for the C = 0.03m ($\sigma = 0.26$) VAWT. The comparison is made only at λ= 3, which is the λ at which the minimum CP is again attained, for brevity.

4.3.2.1 Flow Fields at $\lambda = 2.5$, C = 0.04m

Figure 4.5 shows the plots of vortices around a blade for the Transition SST, SST $k-\omega$ and the PIV experiments. At $\theta = 70^o$, a separation bubble is seen in the PIV indicating an onset of blade stall. The onset of the stall is equally seen in the Transition SST and the SST $k-\omega$. While the formation of the separation bubble is seen more advanced for the Transition SST, it is delayed in the SST $k-\omega$.

At $\theta = 80^o$, the flow structure seen in the PIV is better captured by the Transition SST. The LEV vortex is fully developed and being pushed away from the surface of the blade by the development of the TEV which is seen at the formative stage in the PIV and the Transition SST. Whereas, the LEV has increased in size and still attached to the surface of the blade due to the delayed development of the TEV in the SST $k-\omega$ signifying delayed stalled.

At $\theta = 90^o$, in the PIV, the first LEV developed detaches from the blade surface which is followed by the formation of a second separation bubble, while the roll up of the TEV has advanced. This is well captured by the Transition SST but with the development of the TEV being more advanced. About 10^o phase lag behind the PIV is seen with the SST $k-\omega$. At $\theta = 130^o$, a resemblance is seen in the two CFD turbulence models showing detachment and shedding of pairs of vortices which is equally seen in the PIV implying that the PIV data are well captured by the two turbulence model at this azimuth position.

At $\theta = 290^o$, shedding of vortices and the onset of flow reattachment to the blade surface is seen in the PIV while the Transition SST and SST $k-\omega$ have their flow attached to the blade surfaces. At $\theta = 300^o$ all the flow fields, including that of the PIV are attached to the blade surface. Overall the Transition SST is a better choice judging from the better capture of the PIV than the SST $k-\omega$ at some of the azimuth positions. The best performance can be adduced to the ability of the Transitional model in capturing the flow transition from the start until $\theta = 130^o$ when the flow became turbulent.

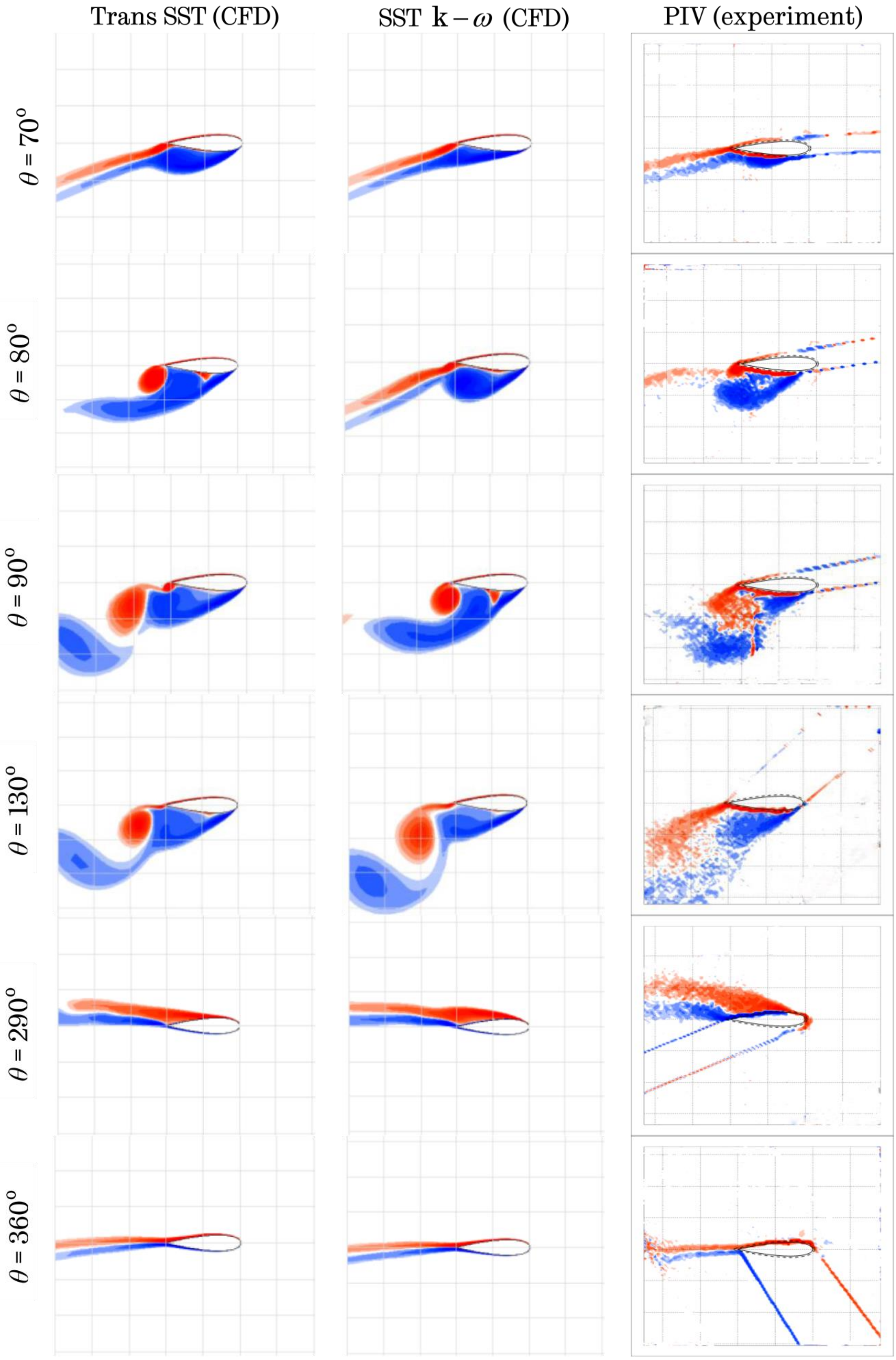

Figure 4.5. Vorticity plots of flow fields around a blade at 6m/s for various azimuth angles, $\lambda = 2.5$, C = 0.04, $\sigma = 0.34$.

4.3.2.2 Flow Fields at λ = 4, C = 0.04m

The flow structures at λ = 4 are very different from those of λ = 2.5. This could be due to the differences in the Reynolds numbers which the blade sees at the two λ. It can also be seen that the occurrence of stall is higher in the previous λ where the flow features of the two CFD models were compared with the PIV than at the λ = 4. As shown in the Figure 4.6, the flow fields are attached to the blade surfaces in virtually all the azimuth positions in the Transition SST, SST $k-\omega$ and also in the PIV, except at $\theta = 140^o$.

At θ = 140^o, pairs of LEV and TEV vortices are seen being developed in the PIV, The Transition SST showed better prediction than the SST $k-\omega$ although the size of the vortex seen in the PIV is larger. Overall, judging from the flow structures at this λ, it is difficult choosing one turbulence model over the other since predictions of the PIV flow features, by the two turbulence models are similar in most azimuth positions due to the turbulence nature of the flow at the higher Reynolds numbers, so the transition region could not be well captured at the 10^o interval used between azimuth positions.

4.3.2.3 Flow Fields at λ = 3, C = 0.03m

In this section the flow physics of the two turbulence models is compared against the PIV of the VAWT with the smaller blade chord at λ = 3 and at 8m/s to further test which of the models can best capture the flow fields around the VAWT blades. Figure 4.7 shows the vortices plots of the flow field around the blade at various azimuth angles and the two turbulence models are compared against the PIV.

At θ = 70^o, the onset of the development of separation bubble is seen in the PIV. This is well captured in the Transition SST model in which the development of the separation bubble is obviously seen bigger by the thickening of the boundary layer, while the fully turbulent SST $k-\omega$ is seen delayed with the insignificant formation of the separation bubble on the suction side of the aerofoil.

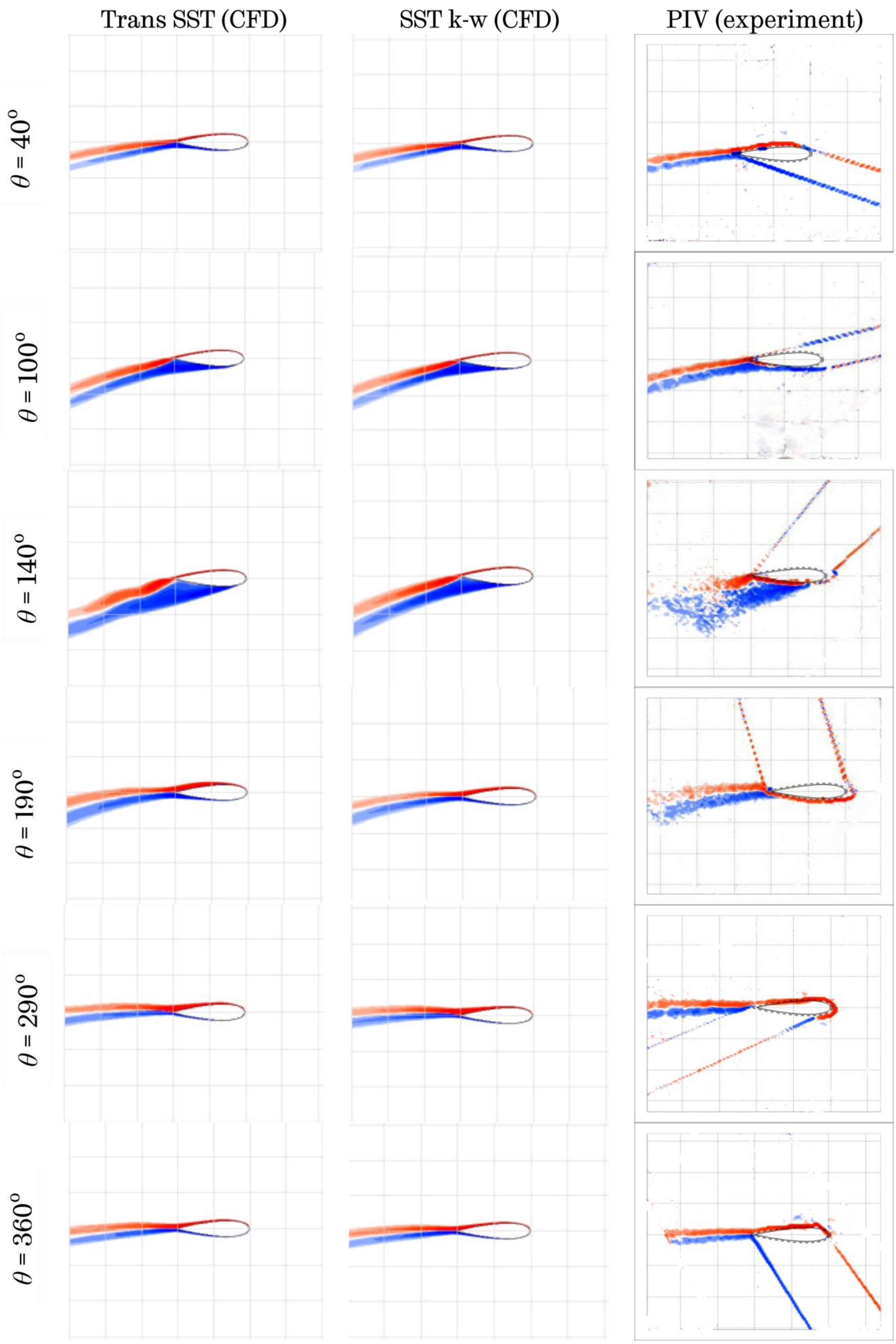

Figure 4.6.Vorticity plots of flow fields around a blade at 6m/s for various azimuth angles, $\lambda = 4$, $C = 0.04$, $\sigma = 0.34$.

At θ = 80°, the LEV is fully developed, and the TEV formation has also advanced. LEV is also being pushed away from the blade by the development of the TEV. This is equally better captured in the Transition SST than in the fully turbulent SST $k-\omega$. While the separation bubble has developed into a LEV and the development of the TEV has advanced in the Transition SST, the formation of the separation bubble is seen in the formative stage in the fully turbulent SST $k-\omega$ with no sign of the formation of the TEV. This implies that the flow field of the fully turbulent SST $k-\omega$ lags behind that of the PIV with more than 10°.

At θ = 90°, flow separation, detachment of the boundary layers from the blade surface and shedding of a pair of vortices are seen in the PIV and also in the Transition SST with both the LEV and the TEV stretched away from the blade. The blade is seen stalled in the fully turbulent SST $k-\omega$ indicating a phase difference of more than 10° between the flow field of the PIV and the fully turbulent SST $k-\omega$ flow field.

In the downwind section of the rotation, similarities are seen in the flow fields of the PIV and the two turbulence models. At θ = 290°, an onset of flow reattachment is seen in the PIV which is well captured by the Transition SST and also by the fully turbulent SST $k-\omega$. The reattachment of the flow is seen to continue at θ = 310° and complete reattached flow to the blade surface is seen at θ = 360° in the PIV. This is equally well captured in the two turbulence models. Overall, the Transition SST model is a better turbulence model than the SST $k-\omega$ for this study since it was able to capture the flow transition from the start up to θ = 90°.

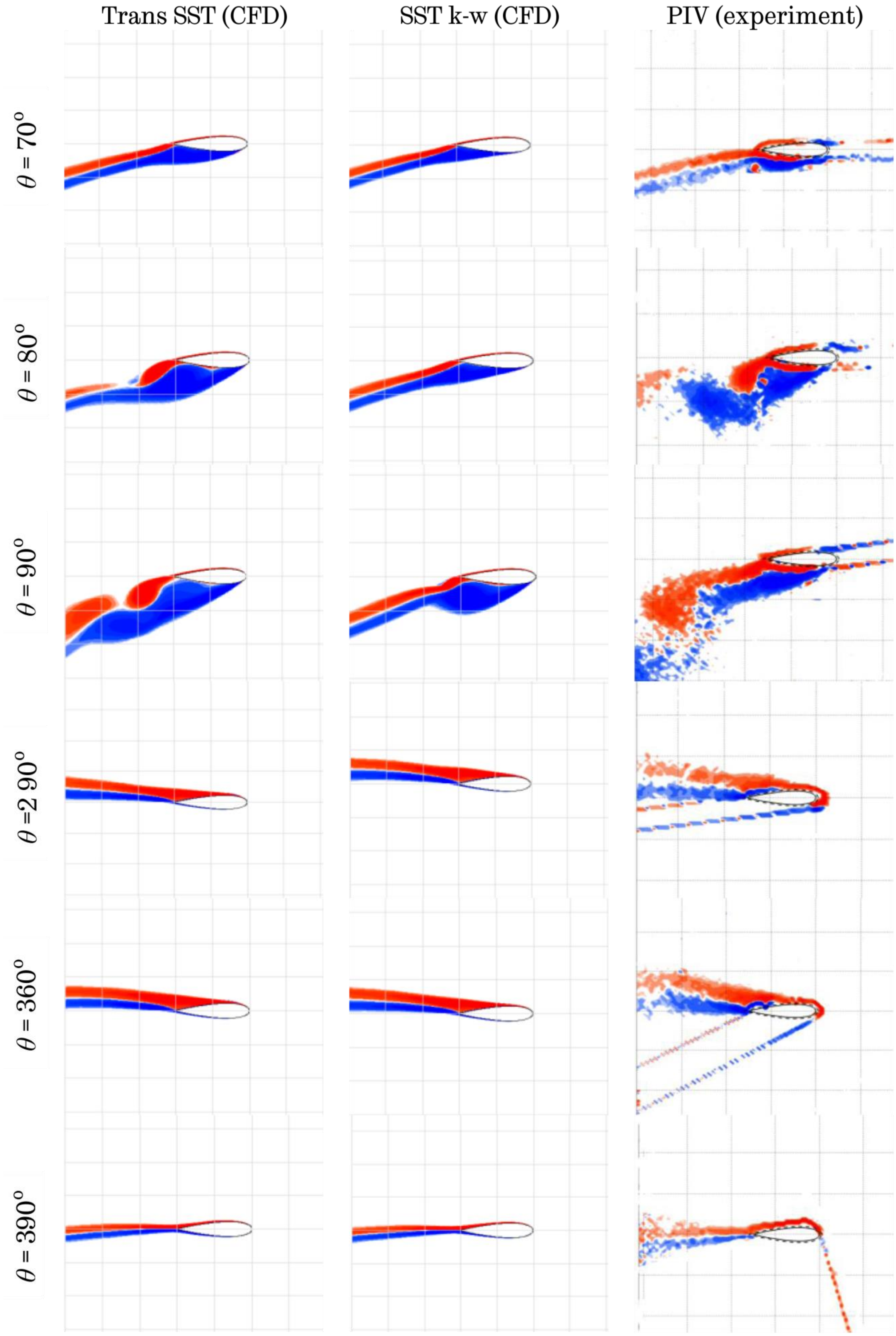

Figure 4.7. Vorticity plots of flow field around a blade at 6m/s for various azimuth angles, λ = 3, C = 0.03m, σ = 0.26.

4.4 Summary

The turbulence modelling exercise in which five models were tested against experimental data of a NACA012 static aerofoil has shown that the SST $k-\omega$ turbulence was the most appropriate model of the five candidates tested. A further comparison of the SST $k-\omega$ and Transition SST with experimental power coefficient data of the VAWT showed a better prediction at the lower λ by the SST $k-\omega$ while the Transition SST prediction at the higher λ is better for the C = 0.04 VAWT. The force validation of the C = 0.03m VAWT showed the two turbulence model attaining the same CP at the λ = 1.5 to λ = 3.5. Beyond this λ, the Transition SST showed a better prediction than the SST $k-\omega$.

The flow physics validation especially at the λ = 2.5 and λ = 3 for the two VAWT configurations also showed the Transitional SST as the better turbulence model since it best captured the PIV features in most of the azimuth positions compared in the upwind section of the flow than the fully turbulent SST $k-\omega$. Judging from the force and flow physics validations, the Transition SST turbulence model is adopted as the most appropriate model for the CFD modelling presented in this study.

Chapter 5

Experimental Results

5.1 Introduction

Chapter five presents results of the experimental investigation into the performance, flow visualization and PIV measurements of the two small-scaled wind tunnel VAWTs (with different σ) model at the University of Sheffield wind tunnel. It details the fundamental performance and aerodynamics based on power coefficient versus TSR, and PIV vorticity flow field measurements. One blade each of the two VAWTs was investigated for the PIV measurements assuming the vorticity flow fields around a blade are the same for all the three VAWTs' blades at the same azimuth position and wind speeds. The last sections present the performance and flow physics analysis of the effects of varying blade chords (solidities) on VAWTs at different Reynolds numbers (the same wind speed) and at the same Reynolds numbers (different "matching Reynolds numbers" wind speeds) based on blades' chord.

5.2 Performance of VAWTs

The aerodynamics advantages of one VAWT machine over another can be judged by comparing their power coefficients (CP). Since, CP can define how much power in the wind is extracted by the wind turbines. It is employed in this investigation to evaluate the performance of the two VAWTs. The CP over a wide range of λ is presented and discussed for the two VAWTs under investigation.

5.2.1 Power Coefficient Determination

The coefficient of power was determined for the two VAWT models by the "spin down" test procedure detailed in chapter 3. The spin down tests were conducted for eight wind speeds ranging from 5.5m/s to 9m/s at an interval of 0.5m/s. For each test, the time and revolution per minute of the VAWTs were recorded and all other steps as contained in the "spin down" test procedure were followed to obtain the performance coefficient.

5.2.1.1 Blade Chord = 0.03m ($\sigma = 0.26$)

Figure 5.1 shows a plot of CP versus λ for all the spin down tests for the VAWT with $C = 0.03$m ($\sigma = 0.26$) and it can be seen that the CP varies considerably with changes in wind speed and λ. Between $\lambda = 1$ and $\lambda = 3.8$ the performance of the VAWT for all the tested wind speeds is in the negative region implying the turbine is absorbing power rather than generating power. For wind speeds 5.5m/s, 6m/s, 6.5m/s and 7m/s, the VAWT performance is completely in the negative region at all the λ. At 7.5m/s, it is observed that the VAWT attained a peak $CP = 0$ at $\lambda = 4.75$ and begins to fall below zero beyond $\lambda = 5$. Also the wind speeds above 7.5m/s have their CP – λ curves at the higher λ in the positive performance region. The 8m/s CP – λ curve has its positive performance region between $\lambda = 4.3$ and 5 and, the 8.5m/s wind speed has its positive performance region between $\lambda = 4.1$ and 5, while the 9m/s wind speed performed positively between λ = 3.82 and λ = 5. The VAWT thereafter attained a maximum CP = 0.151 at λ = 4.75 at the tested maximum 9m/s wind speed.

Figure 5.2 shows a plot of wind speed versus λ. It is seen that there are decreases in the tested wind speeds during the experiments, especially at the start. This deviation from the set wind speed is due to blockage effects resulting from the VAWT while in operation and also solid blockage caused by the blades in the upwind half of the rotation. Energy extraction from the wind by the VAWT also causes a decrease in the tested wind speed. Comparing Figures 5.1 and 5.2, it can be seen that the λ with higher CP in Figure 5.1 corresponded to the λ with a more noticeable decrease in wind speed in Figure 5.2 and the λ with the lower CP also corresponded to the λ with leaser drops in wind speeds. This confirmed energy being extracted from the wind by the VAWT as one of the reasons for the observed deviation.

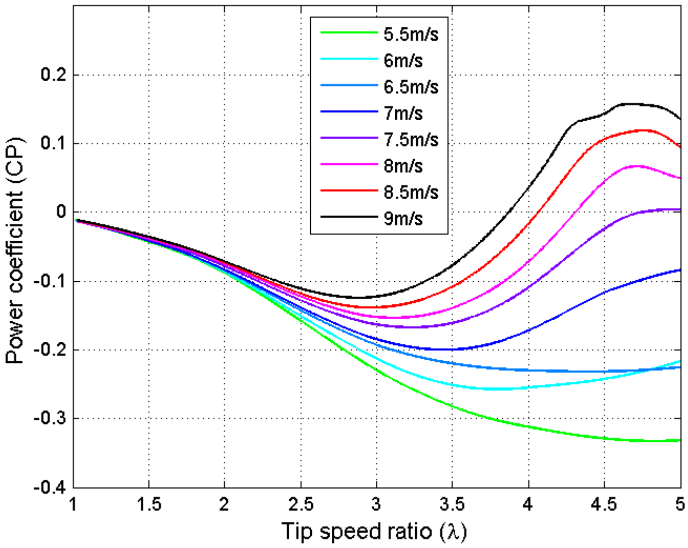

Figure 5.1. The power coefficient versus tip speed ratio for all spin down tests, C = 0.03m, σ = 0.26.

The deviations from the set wind speed can influence the overall performance of the VAWT, and to compare the experimental results with those obtained from CFD in a steady wind condition is considered mis-normal in the author's opinion. So, these deviations from the set wind speeds were corrected through an interpolation of the data set of the spin down tests for 5.5m/s – 9m/s to achieve comparable steady performances. The desired wind speeds for this investigation ranges from a minimum of 6m/s to a maximum of 8m/s, and despite the drop in the wind speeds, the desired wind speeds are within the resulting data set of all the spin down tests conducted.

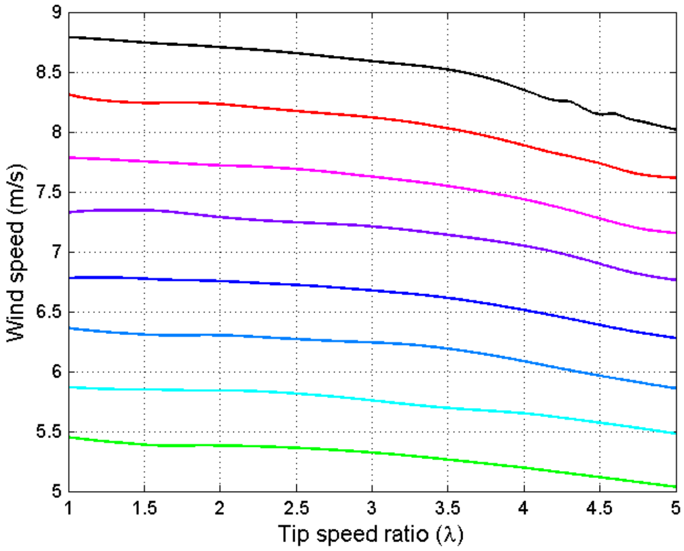

Figure 5.2. Decreases in wind speed for all the spin down tests, C= 0.03m, σ = 0.26.

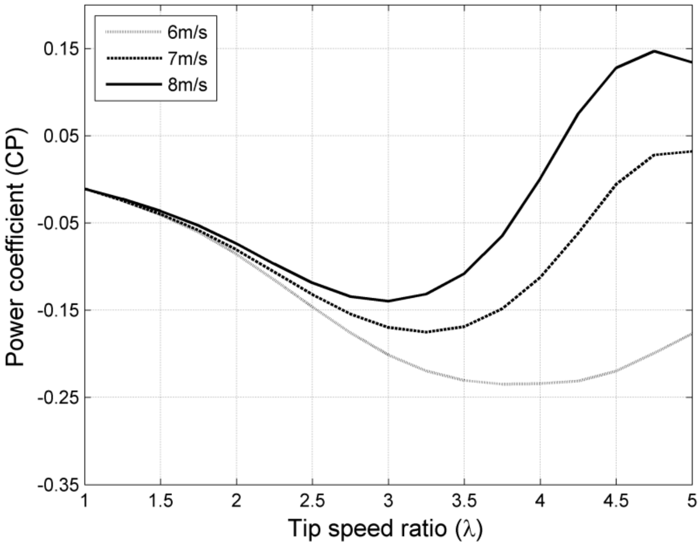

Figure 5.3. Interpolated Power coefficient versus tip speed ratio, C= 0.03m, σ = 0.26.

The interpolated performance curves for the steady performance are presented in Figure 5.3. When compared to the data set in Figure 5.1, the maximum value of the interpolated CP for the 8m/s case is higher at 0.147 than the non-interpolated case. This difference is due mainly to the non-interpolated case having operated at a lower wind speed of 7.76m/s at the start of the test and wind speed of 7.22m/s at the end of the test. These wind speeds are clearly far below 8m/s set wind speed. Similar differences are also observed between the interpolated and non-interpolated curves for the 7m/s and 6m/s cases. The deviations from the set wind speeds are corrected by the interpolation which results in higher CP over the non-interpolated CP, since a steady state performance is assumed for the interpolation

5.2.1.2 Blade Chord = 0.04m (σ = 0.34)

The spin down tests were also conducted for the VAWT with C = 0.04m (σ = 0.34) at the same conditions (wind speeds) that the VAWT with C = 0.03m blade was tested. Figure 5.4 presents the non-interpolated and interpolated plots of CP versus λ and also the decreases in the wind speed for all the spin down tests. Unlike the observed performance of the VAWT with C = 0.03m blade, the negative region is narrower and span from λ = 1 to λ = 2.7 for the highest tested wind speed and the VAWT recorded positive CP between λ = 3.75 and λ = 4.4 for all the tested wind speeds (Figure 5.4 (a)). At the lowest wind speed, the VAWT attained a peak CP = 0.046 at λ = 4. As the wind speed is increased at the regular interval of 0.5m/s, the peak CP also increased correspondingly until the VAWT attained a maximum of CP = 0.34 at the corresponding λ = 3.75. Convergence of the CP curves at higher tested wind speeds and, a shift of the peak CP towards lower λ with increases in wind speeds is also observed. The observed convergence and shift of the peak CP, with further increases in wind speed, suggest that the VAWT performance can be independent of Reynolds numbers effects if the wind speed were increased further.

There is also decreased in the wind speeds during the tests as was previously observed in the VAWT with C = 0.03m cases. Figure 5.4 (b) shows the decreases in wind speeds for all the spin down tests due to blockage. Although the pattern of the decreases in wind speed for the two VAWTs at the start and end of each test shown in Figures 5.2 and 5.4(b) are similar, there are noticeable differences from λ = 4.5 and up to λ = 2.5 between the drop in wind speeds of the two VAWTs. These observed differences can be attributed to the difference in the blade's chords (solidities) of the two VAWTs. With the increase in the blade's chord resulting in increase in solidity; solid blockage and energy extraction also increase for the tested cases.

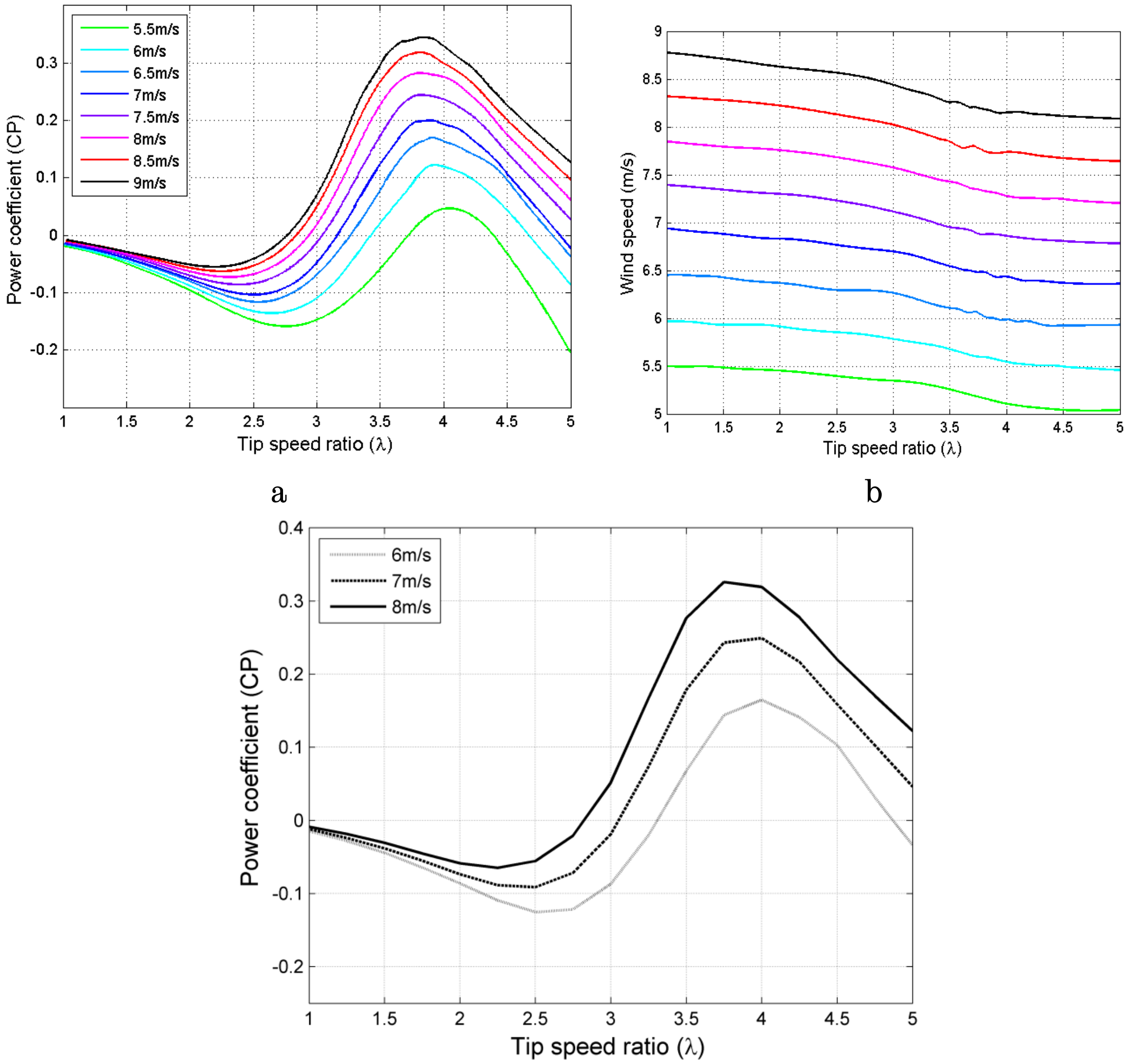

a

b

c

Figure 5.4. Performance of VAWT with C = 0.04m, σ = 0.034 a) non interpolated data set showing CP versus λ, b) decreases in wind speeds for all the spin down tests, c) interpolated CP versus λ.

Convergence is also seen in the interpolated CP – λ curves (Figure 5.4 (c)) as is observed in the data set. Similar to C = 0.03m VAWT, the interpolated CP is higher than the CP of the non-interpolated data set due to the reasons explained earlier. At the highest interpolated wind speed of 8m/s, the VAWT attained a maximum of CP = 0.326 at the corresponding λ = 3.75 whereas the maximum CP attained by the VAWT at the same 8m/s wind speed in the non-interpolated data set is 0.28 at the same λ = 3.75. At the negative performance region, a minimum CP = -0.065 for the interpolated 8m/s is recorded as against the minimum CP = -0.08 for the non-interpolated case. However, there are similarities in the performances of the two VAWTs under investigation; the effects of Reynolds number are shown clearly in both cases as the CP increase with an increase in wind speed, convergence of the performance curves and shift of the peak CP towards lower λ at higher wind speeds is present in both cases. The negative performance region is also obvious in both cases.

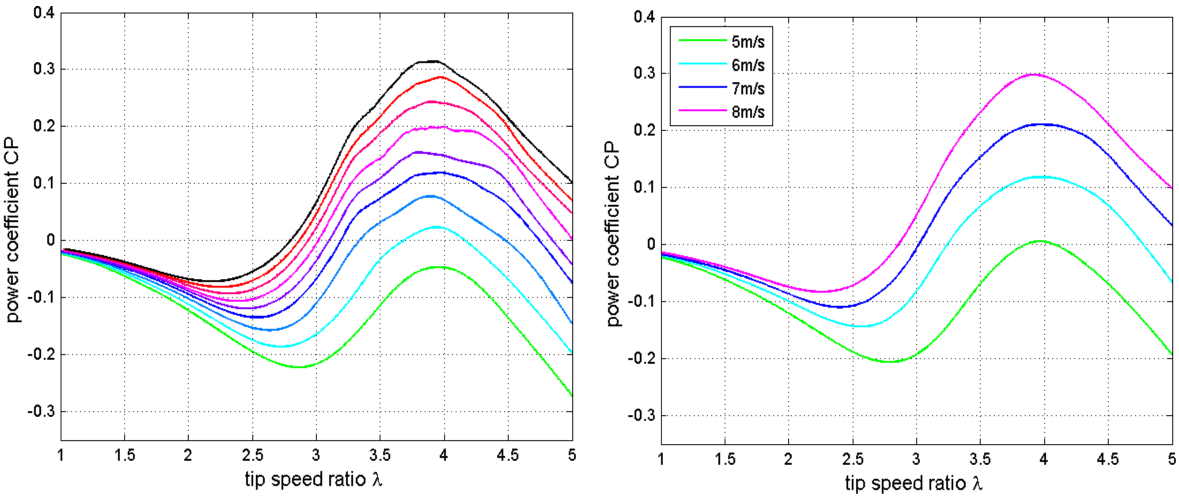

a. b.

Figure 5.5. CP –λ curves for spin down test: a) actual CP – λ curves for all tests, b) interpolated CP – λ curves for steady wind speeds [1].

The results are consistent with the works of Danao [55] and Edwards[39]. They have also shown (Figures 5.5 and 5.6) increases of CP with an increase in wind speed, convergence of the CP – λ curves at the higher winds and a negative region (dead band) at the lower λ. The dead band was equally observed by [13, 14, 18] in their studies.

The insignificant difference in CP observed between Figures 5.4 (c) and 5.5 is due to system error arising from replacements of some machine parts. Mentioned by Danao [55], the data set in Figure 5.6 were not interpolated to achieve steady state performance so the differences in the CP are expected. Despite these differences, the performance trend in the three studies is very similar. A discussion of the effects of solidity due to the changes in the blade chord of the two VAWTs is left until later in the chapter.

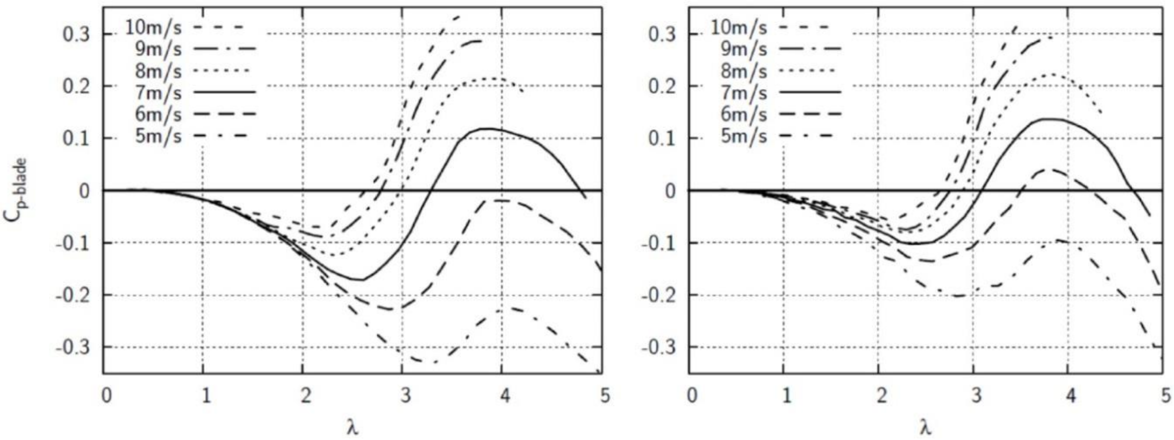

a. b.

Figure 5.6. Spin down test at different turbulence intensity levels showing the effects of Reynolds number: a) Tu = 0.4%, b) Tu = 1% [2].

5.3 Flow Field Visualization and PIV Measurements

The flow fields around the two VAWTs at various blade azimuth positions were visualized and measured with PIV. Atomized olive oil was injected into the airstream at the inlet of the wind tunnel, with a Six-Jet Atomizer, served as the tracer particle, a Dantec Litron Nano–S–65 Nd:YAG laser that emits 65mJ per pulse at 520nm illuminated the FOV, and a Flow Sense CCD camera of 2048 by 2048 pixel resolution captured the flow fields around the blade in the FOV. The synchronization of the camera and laser are made possible by the use of DynmicStudio 3.24 software.

The PIV measurement experiments were conducted on the VAWTs with C = 0.04m at 6m/s at 10° intervals around the 360° rotation of the VAWT for three λ = 2.5, 3 and 4 based on the peculiarity of the dynamic stall associated with these λ and the corresponding CP of the VAWTs. The azimuth positions for which the experiments could not be conducted was due to viewing restrictions caused by the laser position, since the laser could only be used on one side of the wind tunnel.

The experiments were conducted for the VAWT with C = 0.03m (σ = 0.26) at the same wind speed, λ and azimuth positions, and also for a higher wind speed of 8m/s and at λ = 2.5 and 3 at similar azimuth positions. The experiments for the higher λ = 4 at 8m/s could not be conducted due to safety reasons as the operating RPM exceeded that of the design limit of the rig. The flow field visualization and PIV measurements were designed to examine the four stages of the dynamic stall phenomenon: 1) Start of formation of the separation bubble on the inner surface (suction side) of the blade, 2) Leading Edge Vortex (LEV) build-up on the inner surface of the blade, 3) Detachment of LEV from the blade's surface and build-up of Trailing Edge Vortex (TEV) and 4) Detachment of TEV and shedding of a pair of LEV and TEV. Also to investigate how the stall phenomenon affects flow field aerodynamics around a blade with changes in λ, and, VAWTs performance with changes in blade chords and Reynolds numbers.

5.3.1 Blade Interaction with 6m/s Wind Speed, C = 0.03m (σ = 0.26)

The development of the dynamic stall phenomenon of the C = 0.03m, σ = 0.26 VAWT, as it interacts with wind speed at 6m/s is presented and discussed in the following sections. It details the onset, growth of the vortex, separation of flow, shedding of vortices and reattachment of the flow to the surface of the blade at λ = 2.5, 3 and 4 and at various azimuth positions.

5.3.1.1 Flow Fields at λ = 2.5

Figure 5.7 shows the z-vorticity flow fields of PIV measurements for different azimuth positions at 6m/s and at λ = 2.5. It is seen that the flow field is fully attached to the blade surface as the rotation of the blade starts from $\theta = 0^o$ up to $\theta = 50^o$ (Figure 5.7(a)). At $\theta = 60^o$ (Figure 5.7(b)) the blade is stalled with the

Leading Edge Vortex (LEV) fully developed and, the formation of Trailing Edge Vortex (TEV) had progressed to a stage it has started to push away the LEV from the blade's surface. The roll up of the TEV is completed and the LEV detaches from the blade's surface; shedding of irregular pair of LEV and TEV is also seen at $\theta = 70^{o}$ (Figure 5.7 (c)). The blade is in the post stall stage at $\theta = 90^{o}$ (Figure 5.7(d)), with the flow field separated from the blades' surface, shedding of regular pair of vortex continued until $\theta = 100^{o}$ (Figure 5.7(e)) where the flow field is seen to be fully separated. Away from $\theta = 100^{o}$, in the second half of the upwind section of the rotation, the dynamic stall (in the post stall stage), flow separation and shedding of a pair of vortices continued with an onset of flow reattachment observed at $\theta = 140^{o}$ (Figure 5.7(f)). At $\theta = 170^{o}$ (Figure 5.7(g)) it is seen that the shedding of the pair of vortex has become random, the width of the LEV and TEV also have decreased while the reattachment of the flow field to the blade surface had advanced considerably.

Further in the downwind part of the rotation at $\theta = 260^{o}$ (Figure 5.7(h)), the flow is seen to be completely separated and also shedding of a pair of vortices with the length of the LEV more than two chord length. The flow separation from the blade's surface, shedding of the pair of vortices and gradual reattachment of flow to the blade surface continued up to $\theta = 310^{o}$ (Figure 5.7(i)) and beyond $\theta = 320^{o}$ (figure 5.7(j)) until $\theta = 360^{o}$ (figure 5.7(k)) where the flow is seen to be completely attached to the blade surface.

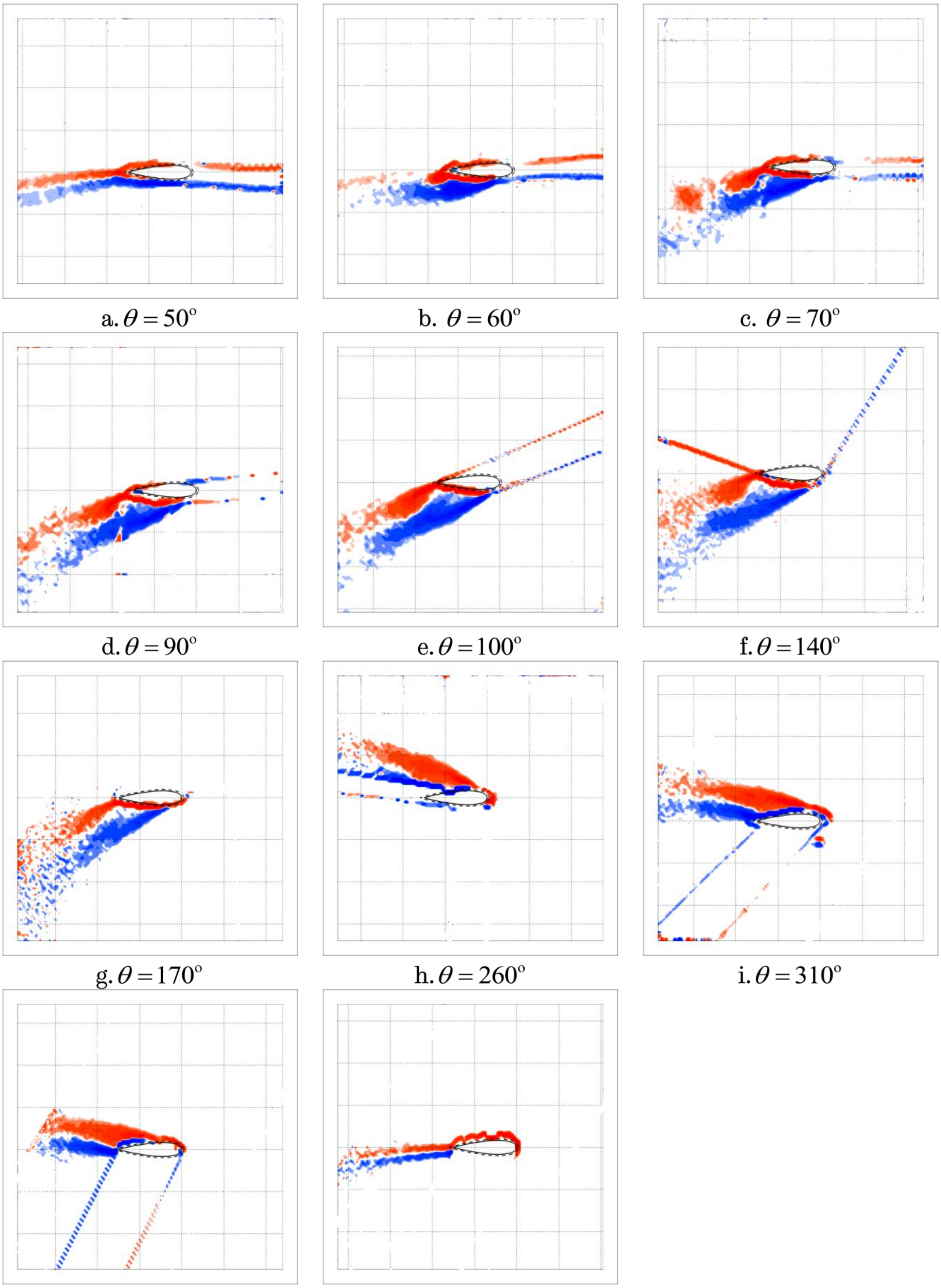

a. $\theta = 50^{\circ}$ b. $\theta = 60^{\circ}$ c. $\theta = 70^{\circ}$

d. $\theta = 90^{\circ}$ e. $\theta = 100^{\circ}$ f. $\theta = 140^{\circ}$

g. $\theta = 170^{\circ}$ h. $\theta = 260^{\circ}$ i. $\theta = 310^{\circ}$

j. $\theta = 320^{\circ}$ k. $\theta = 360^{\circ}$

Figure 5.7. Z-vorticity flow fields of PIV measurements at 6m/s for different azimuth positions, λ = 2.5, Chord = 0.03m.

5.3.1.2 Flow Fields at λ = 3

Figure 5.8 shows z-vorticity flow fields of PIV measurements for different azimuth positions at 6m/s and at λ = 3. It is seen that the flow is fully attached to the blade surface as the rotation of the blade starts from θ = 0° up to θ = 60° (Figure 5.8(a)) which is different from the λ = 2.5 where an onset of the blade stall was initiated θ = 60°. At θ = 70° (Figure 5.8(b)) a LEV has developed with size approximately one and half chord length, and the formation of TEV is at the initial stage of development. The roll up of the TEV is seen to have been completed causing both the LEV and TEV to be fully detached from the blade's surface; also shedding of LEV and subsequent convection of the shed vortex downstream of the flow while the onset of TEV shedding is also observed at θ = 80° (Figure 5.8(c)). The blade is in the post stall stage at θ = 90° (Figure 5.8(d)) with the flow fully separated from the blades' surfaces and shedding of vortices in pairs is also seen, this was equally observed in the λ = 2.5. This continued until θ = 100° (Figure 5.8(e)) where the pair of vortex shed is very regular and the flow field is seen to be fully separated.

Past θ = 100° in the second half of the upwind rotation, the flow separation and shedding of a pair of vortices continued with the onset of flow reattachment observed at θ = 140° (Figure 5.8(f)). At θ = 170° (Figure 5.8(g)), it is seen that the shedding of the pair of vortex still continued, while the reattachment of the flow to the blade surface had advanced with the width of the LEV and TEV also observed to have decreased.

The blade having past the upwind section and further in the downwind part of the rotation at θ = 260° (Figure 5.8(h)), the LEV is seen to be completely separated from the blade's surface with LEV more than two chord length of the aerofoil and also being shed. Flow separation, shedding of pairs of vortices and the gradual reattachment of the flow to the blade surface continued up to θ = 310° (Figure 5.8(i)), and beyond θ = 320° (Figure 5.8(j)) until θ = 350° (Figure 5.8(k)) where the flow is seen to be completely attached to the blade surface.

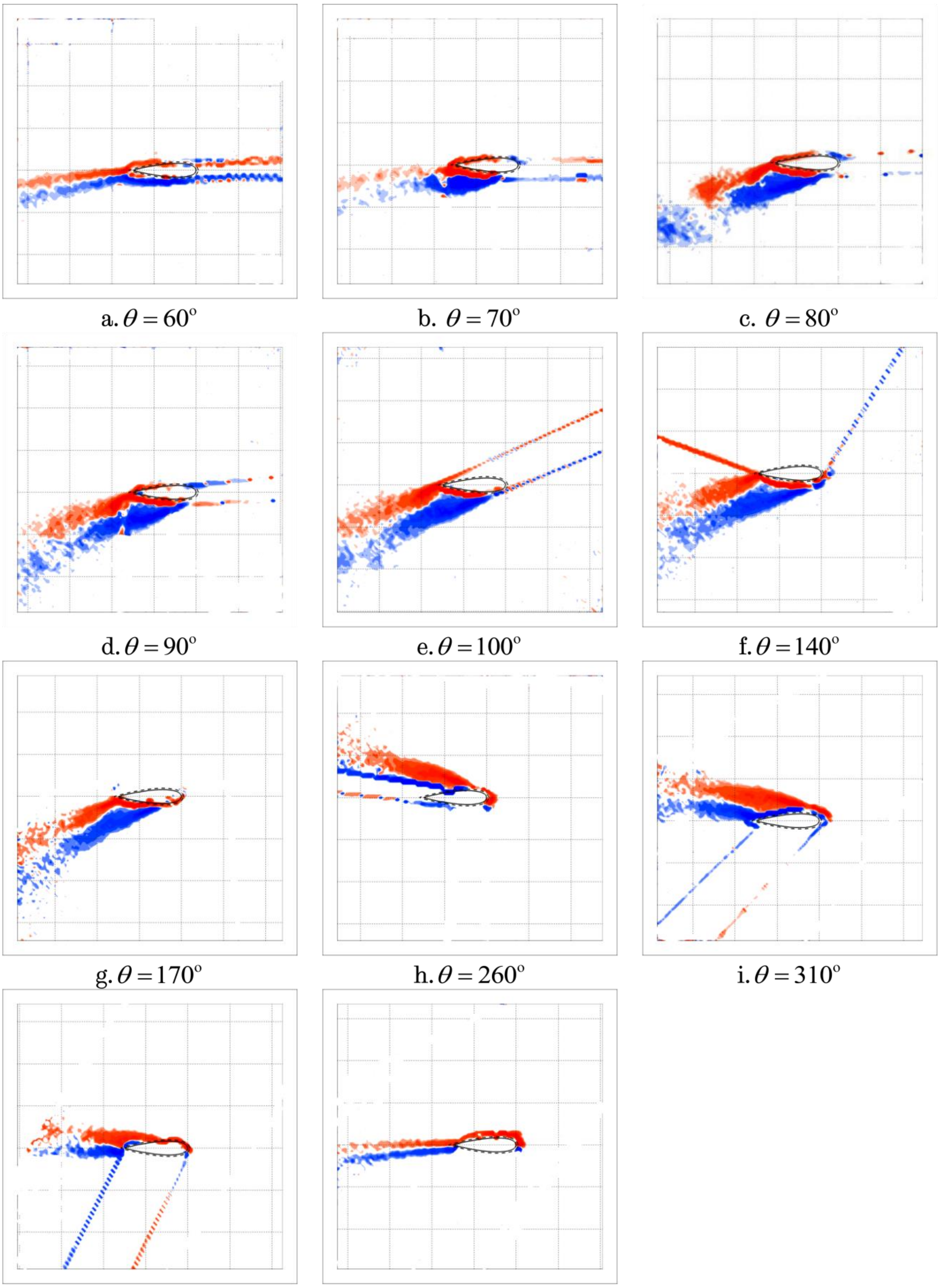

a. $\theta = 60^{\circ}$ b. $\theta = 70^{\circ}$ c. $\theta = 80^{\circ}$

d. $\theta = 90^{\circ}$ e. $\theta = 100^{\circ}$ f. $\theta = 140^{\circ}$

g. $\theta = 170^{\circ}$ h. $\theta = 260^{\circ}$ i. $\theta = 310^{\circ}$

j. $\theta = 320^{\circ}$ k. $\theta = 350^{\circ}$

Figure 5.8.Z-vorticity flow fields of PIV measurements at 6m/s for different azimuth positions, $\lambda = 3$, Chord = 0.03m.

5.3.1.3 Flow Fields at λ = 4

Figure 5.9 shows the z-vorticity flow fields of PIV measurements for different azimuth positions at 6m/s for λ = 4. It is seen that the flow is fully attached to the blade surface as the rotation of the blade starts from θ = 0° up to θ = 80° (Figure 5.9(b)) indicating a delay in the onset and blade stall at this λ when compared to the earlier two λ in which shedding of vortices was observed to have started θ = 80°. At θ = 90° (Figure 5.9(c)) the blade is stalled, the LEV has developed with size approximately one chord length and the TEV is observed to be at the initial stage in its development. The start of the roll up of the TEV with increase in size while pushing away the LEV from the blade's surface is observed at θ = 100° (Figure 5.9(d)). Fully separated flow from the blade surface and shedding of a pair of vortex is seen to have started at θ = 110° (Figure 5.9(e))

Away from θ = 110° (Figure 5.9(e)) in the second half of the upwind section of the rotation, with the dynamic stall process of the blade already in the post stall stage similar to the observed dynamic stall at λ = 2.5 and 3, flow separation and shedding of a pair of vortices continued with the onset of flow reattachment observed at θ = 140° (Figure 5.9(f)). At θ = 170° (Figure 5.9(g)), it is seen that the shedding of the pair of vortices still continued while the reattachment of the flow to the blade surface had also advanced with the width of the LEV and TEV observed to have also decreased.

Further away in the downwind part of the rotation at θ = 260° (Figure 5.9(h)), the LEV is separated from the blade surface confirming that dynamic stall phenomenon occurs two times in one full blade's rotation cycle, which was also observed at λ = 2.5 and 3. The LEV is seen to be completely separated from the blade's surface with size more than two chord length of the aerofoil and also being shed. Flow separation, shedding of a pair of vortices and speedy reattachment continued until θ = 290° (Figure 5.9(i)) and beyond. At θ = 310° (figure 5.9(j)) and θ = 320° (figure 5.9(k)) the flow is seen to be completely attached to the blade's surface.

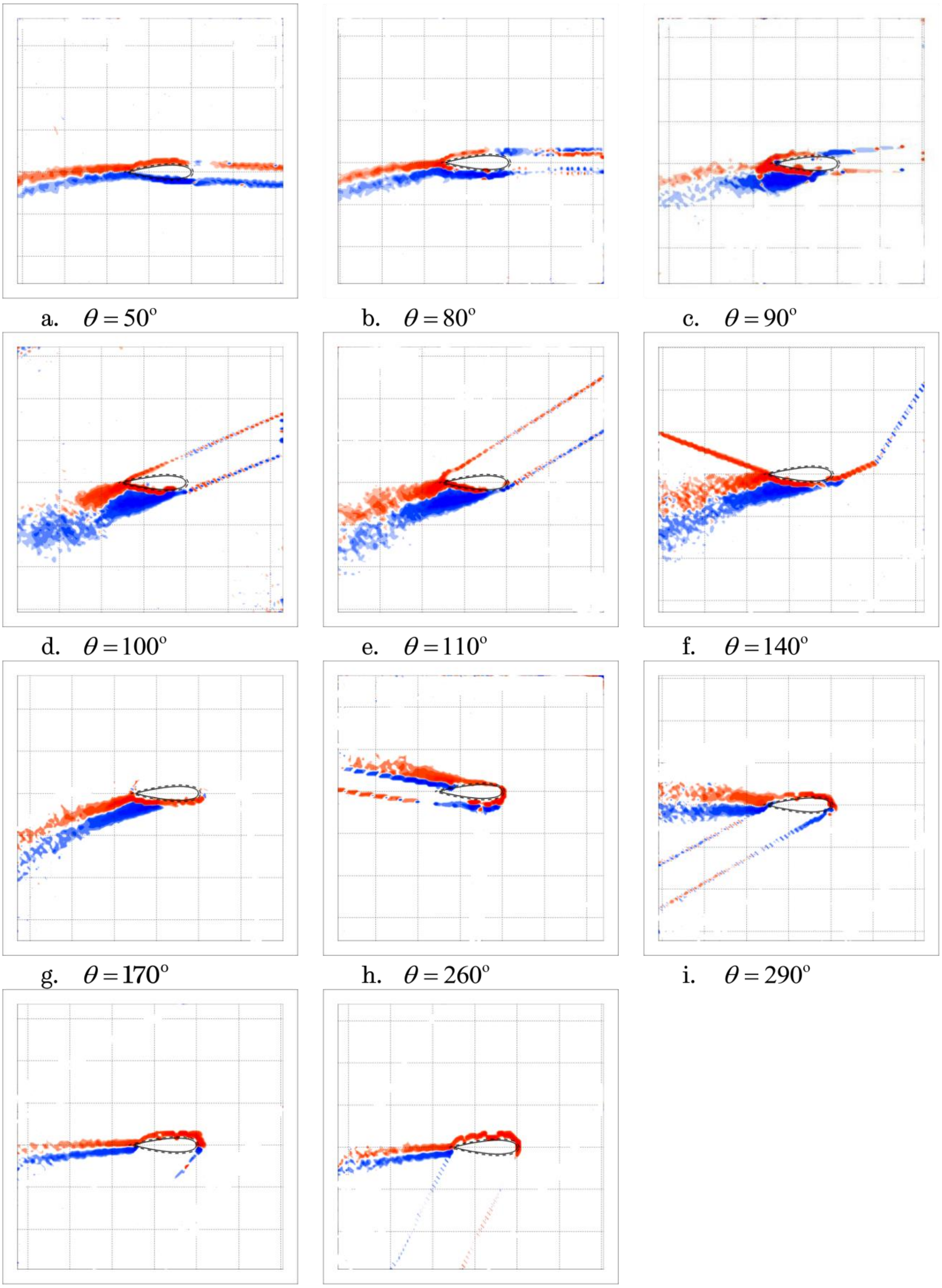

a. $\theta = 50^{\circ}$

b. $\theta = 80^{\circ}$

c. $\theta = 90^{\circ}$

d. $\theta = 100^{\circ}$

e. $\theta = 110^{\circ}$

f. $\theta = 140^{\circ}$

g. $\theta = 170^{\circ}$

h. $\theta = 260^{\circ}$

i. $\theta = 290^{\circ}$

j. $\theta = 310^{\circ}$

k. $\theta = 320^{\circ}$

Figure 5.9. Z-vorticity flow fields of PIV measurements at 6m/s for different azimuth positions, λ = 4, Chord = 0.03m.

5.3.2 Blade Interaction with 8m/s Wind Speed, C = 0.03m ($\sigma = 0.26$)

In the following sections the nature of the development of the dynamic stall process is presented for the C = 0.03 VAWT blade. The interaction of the blade with the wind speed of 8m/s is different from the previous case presented so the details of the onset and blade stall, flow separation and detachment of the boundary layer from the blade surface, shedding of vortices and the eventual reattachment of the flow to the blade surface at $\lambda = 2.5$ and 3 at the various azimuth positions is discussed.

5.3.2.1 Flow Fields at $\lambda = 2.5$

Figure 5.10 shows z- vorticity flow fields of PIV measurements for different azimuth positions at 8m/s and $\lambda = 2.5$. The flow field is seen completely attached to the blade surface as the rotation of the blade starts from $\theta = 0^o$ up to $\theta = 50^o$ (Figure 5.10(a)). The beginning of the formation of LEV separation bubbles is seen on the inner surface of the blade at $\theta = 60^o$ (Figure 5.10(b)). At $\theta = 70^o$ (Figure 5.10(c)) the blade is deep stalled and also the formation of the TEV has advanced, and rolled up with an enlarged size which has pushed away the LEV from the blade's surface causing the LEV to be detached from the blade surface.

The length of the TEV and the LEV continue to increase more than the chord length of the blade. While a pair of vortices are being shed, the TEV shed vortices of diameter approximately the length of the blade chord is observed being convected downstream away from the blade at $\theta = 80^o$ (Figure 5.10(e)). The flow separation and shedding of a pair of vortices continued until the LEV and TEV are seen to be approximately equal in length and width at $\theta = 140^o$ (Figure 5.10(f)) The size of the LEV and TEV decreasing in width, and the LEV closer to the blade's surface for reattachment of the flow to the blade surface is observed $\theta = 180^o$ (Figure 5.10(g)). The flow field is seen not fully reattached to the blade surface even at the midway of the VAWT rotation which suggests a delay in reattachment of the flow to the blade surface.

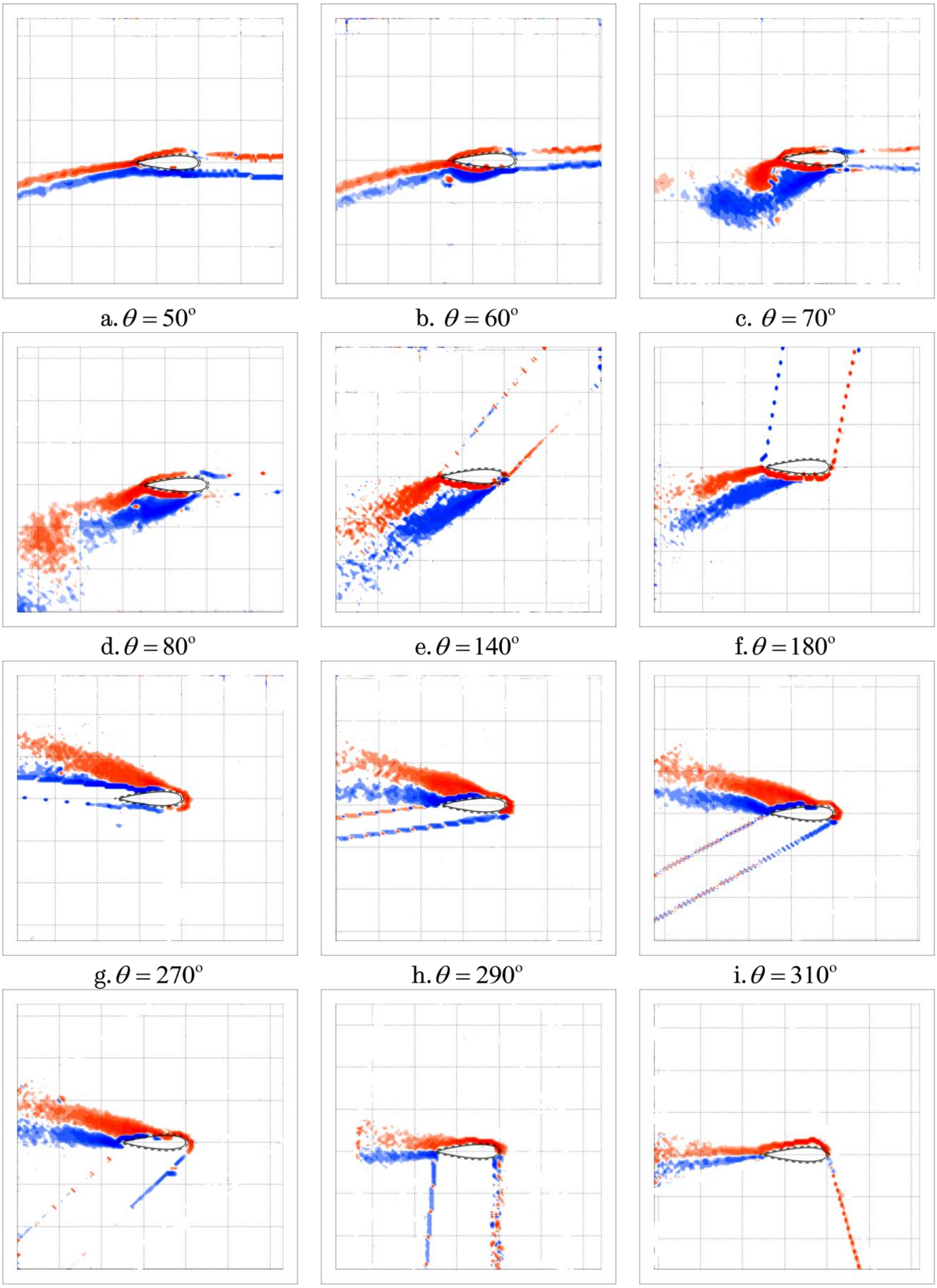

a. $\theta = 50^{\circ}$ b. $\theta = 60^{\circ}$ c. $\theta = 70^{\circ}$

d. $\theta = 80^{\circ}$ e. $\theta = 140^{\circ}$ f. $\theta = 180^{\circ}$

g. $\theta = 270^{\circ}$ h. $\theta = 290^{\circ}$ i. $\theta = 310^{\circ}$

j. $\theta = 320^{\circ}$ k. $\theta = 350^{\circ}$ m. $\theta = 360^{\circ}$

Figure 5.10. Z-vorticity flow fields of PIV measurements at 8m/s for different azimuth positions, λ = 2.5, Chord = 0.03m.

Further away in the downwind part of the rotation at $\theta = 270^{o}$ (Figure 5.10(g)), the flow is seen to be completely separated and also the shedding of vortices with the length of the LEV more than two chord length of the aerofoil is observed. At $\theta = 290^{o}$ (Figure 5.10(h)) the flow separation and a pair of vortices shedding continued with the onset of flow reattachment. The reattachment continued through Figures 5.10 (i, j and k) until $\theta = 360^{o}$ (Figure 5.10(m)) where the flow is seen to have been completely attached to the blade's surface.

5.3.2.2 Flow Fields at λ = 3

Figure 5.11 shows z- vorticity flow fields of PIV measurements for different azimuth positions at 8m/s and $\lambda = 3$. It can be seen that the flow field is fully attached to the blade surface as the blade starts to rotate from $\theta = 0^{o}$ up to $\theta = 60^{o}$ (Figure 5.11(a)). At the midway of the aerofoil chord, the beginning of LEV separation bubble formation is seen to have started on the suction side of the blade at $\theta = 70^{o}$ (Figure 5.11(b)) unlike the previous $\lambda = 2.5$ in which the development of the separation bubble started earlier, at $\theta = 60^{o}$. At $\theta = 80^{o}$ (Figure 5.11(c)) The TEV has formed and rolled up with an enlarged size which has pushed away the LEV from the blade causing the LEV to be completely detached from the blade surface. The length of the TEV and the LEV continued to increase more than the chord length.

The flow is fully separated from the blade surface and a pair of vortices are being shed at $\theta = 90^{o}$ (Figure 5.11(d)) while the LEV and TEV have increased in width which was also observed in the $\lambda = 2.5$ at $\theta = 80^{o}$. Further away in the second half of the upwind section of the rotation, at $\theta = 100^{o}$ (Figure 5.11(e)), the cyclic rolling up of the TEV has disappeared with both the LEV and the TEV completely stretched out away from the blade surface. The flow is separated from the blade's surface and shedding of a pair vortices continue beyond $\theta = 140^{o}$ (Figure 5.11(d)) where the intensity of shedding is still seen to be regular but, with the onset of flow reattachment and the reduction of the LEV and TEV sizes.

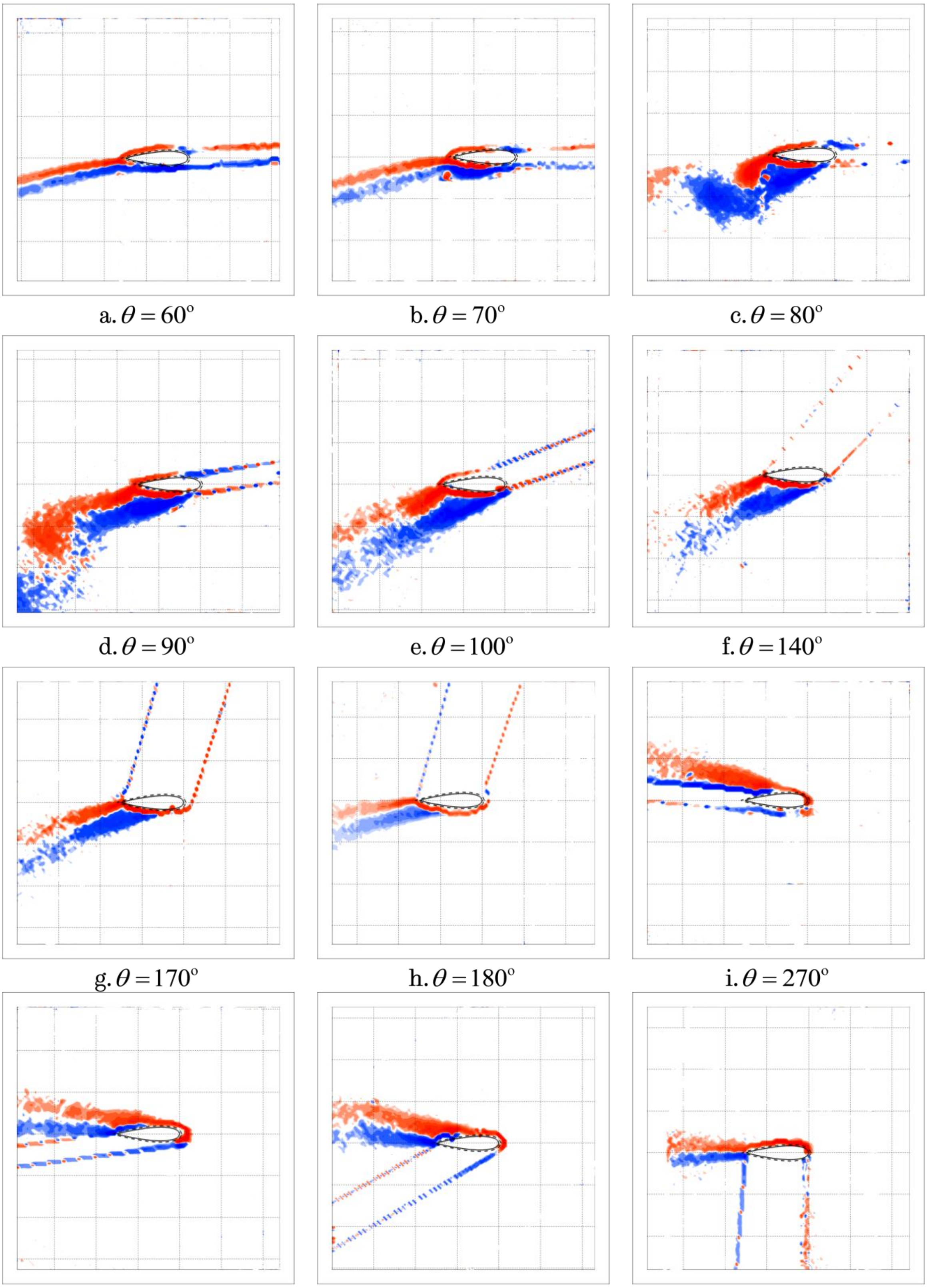

a. $\theta = 60^\circ$ b. $\theta = 70^\circ$ c. $\theta = 80^\circ$

d. $\theta = 90^\circ$ e. $\theta = 100^\circ$ f. $\theta = 140^\circ$

g. $\theta = 170^\circ$ h. $\theta = 180^\circ$ i. $\theta = 270^\circ$

j. $\theta = 290^\circ$ k. $\theta = 310^\circ$ m. $\theta = 350^0$

Figure 5.11. Z-vorticity flow fields of PIV measurements for different azimuth positions at 8m/s and λ = 3, Chord = 0.03m.

The flow reattachment has progressed significantly at θ = 170° (Figure 5.11(g)) and, the LEV and TEV has also reduced in size considerably. The reattachment continued after midway of the rotation, similar to the flow fields at $\lambda = 2.5$. In the first half of the downwind section of the rotation cycle, it is seen that the flow is completely separated from the blade's surface and a pair of vortices are being shed at θ = 270° (Figure 5.11(i)). The flow separation from the blade surface and vortices shedding is observed up to θ = 290° (Figure 5.11(j)), and beyond θ = 290° the flow reattachment is observed. The reattachment of the flow continued further away from θ = 310° (Figure 5.11(k)) and is seen to have fully attached to the blade's surface at θ = 350° (Figure 5.11(m)) earlier than was observed in the flow fields at $\lambda = 2.5$.

5.3.3 Blade Interaction with 6m/s Wind Speed, C = 0.04m ($\sigma = 0.34$)

The resulting dynamic stall phenomenon from the interaction of the C = 0.04, $\sigma = 0.34$ VAWT with wind speed at 6m/s is presented in the following sections. Also, the onset, development of the vortex, separation of the flow, shedding of vortices and reattachment of the flow to the surface of the blade at $\lambda = 2.5$, 3 and 4 and at various azimuth positions are discussed.

5.3.3.1 Flow Fields at $\lambda = 2.5$

Figure 5.12 shows the z-vorticity flow fields of PIV measurements for different azimuth positions at 6m/s and $\lambda = 2.5$. Completely attached flow to the blade surface is observed as the blade starts to rotate from θ = 0° up to θ = 60° (Figure 5.12 (a)). The onset of LEV separation bubble development is seen on the suction side of the blade at θ = 70° (Figure 5.12 (b)). At θ = 80° (Figure 5.12 (c)) the blade is stalled and the onset of detachment of the LEV from the blade surface at the trailing edge is observed. The start of a trailing edge vortex (TEV) development is also seen though, at a formative stage.

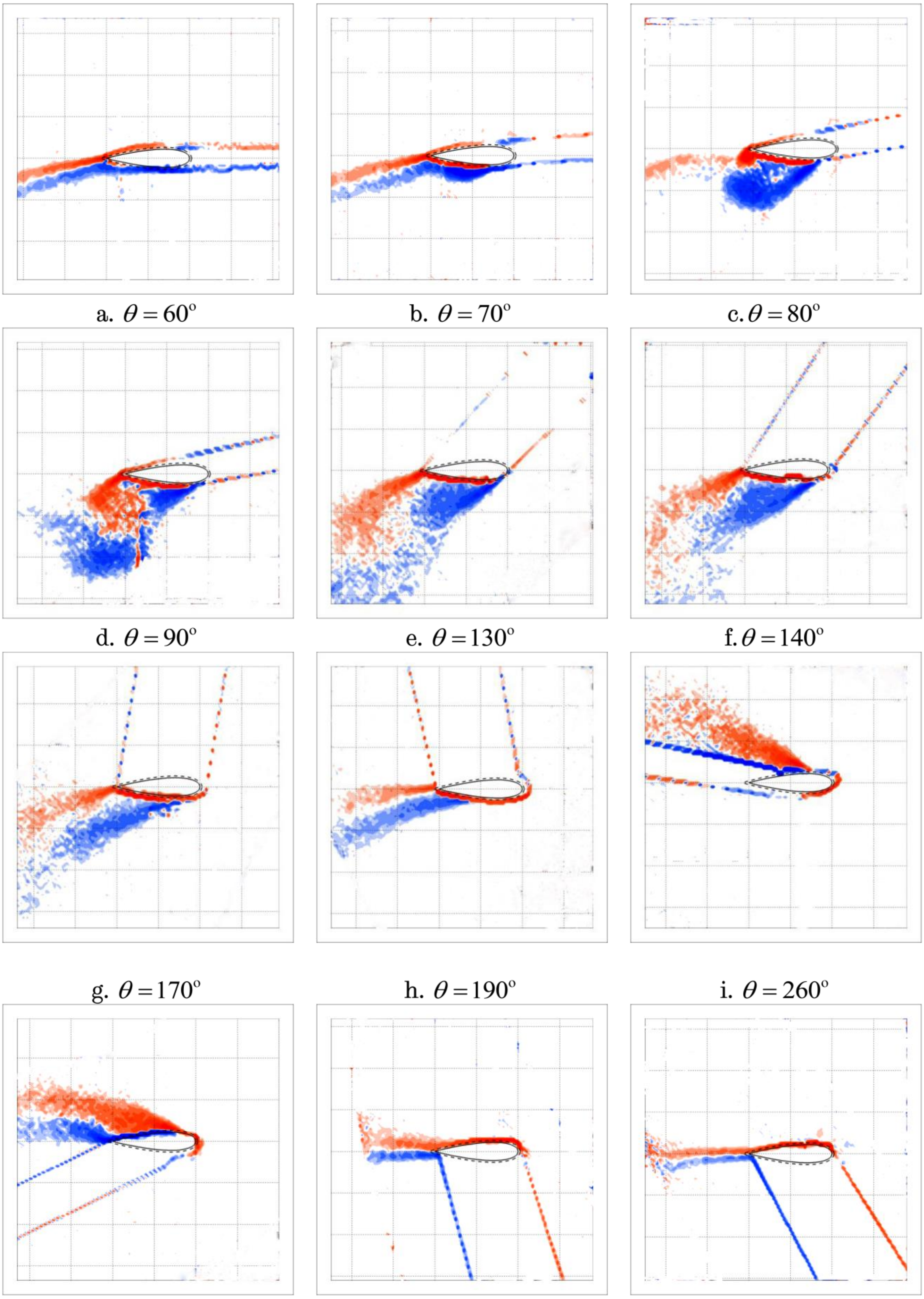

a. $\theta = 60^{\circ}$ b. $\theta = 70^{\circ}$ c. $\theta = 80^{\circ}$

d. $\theta = 90^{\circ}$ e. $\theta = 130^{\circ}$ f. $\theta = 140^{\circ}$

g. $\theta = 170^{\circ}$ h. $\theta = 190^{\circ}$ i. $\theta = 260^{\circ}$

j. $\theta = 290^{\circ}$ k. $\theta = 350^{\circ}$ m. $\theta = 350^{\circ}$

Figure 5.12. Z-vorticity flow fields of PIV measurements for different azimuth positions at 6m/s and λ = 2.5, Chord = 0.04m.

At $\theta = 90^{o}$ (Figure 5.12 (d)) the TEV starts to roll up with the increase in size while pushing away LEV from the blade's surface causing the LEV to be completely detached from the blade surface. The length of the TEV and the LEV continued to increase more than the chord length of the blade until shedding of the pairs of vortices is seen at $\theta = 130^{o}$ (Figure 5.12 (e)).

Thereafter, the blade is seen to be under a regime of shedding of a pair of vortices while both the length and width of the LEV and TEV is different, and the onset of flow reattachment to the blade surface is observed at $\theta = 140^{o}$ (Figure 5.12 (f)). While the shedding of a pair of vortices and also the reduction in size of the TEV and the LEV are observed, the LEV is seen at a quarter chord length of the blade. The LEV is also closer to the blade's surface for the continuation of the flow implying the flow reattachment had advanced at $\theta = 170^{o}$ (Figure 5.12 (g)). The flow continued to be separated from the blade surface even halfway of the VAWT rotation and beyond $\theta = 190^{o}$ (Figure 5.12 (h)) indicating a significant delay in reattachment of the flow.

The flow reattachment is seen to be considerably delayed even at $\theta = 190^{o}$ but stays for a very short period at this stage before the flow reattaches to the blade surface afterward. With the blade in the downwind part, the LEV is observed to form on top of the aerofoil surface while the TEV is formed below the aerofoil surface.

At $\theta = 260^{o}$ (Figure 5.12 (i)) the LEV is fully separated from the aerofoil surface and also being shed. The separation and shedding of a pair of vortices continue even after $\theta = 290^{o}$ (Figure 5.12 (j)) where the onset of flow reattachment is observed. The flow reattachment progressed faithfully through $\theta = 350^{o}$ (Figure 5.12 (k)) and is seen to have completely attached to the blade surface at $\theta = 360^{o}$ (Figure 5.12 (m)) without delay.

5.3.3.2 Flow Fields at $\lambda = 3$

Figure 5.13 shows the z- vorticity flow fields of PIV measurements for different azimuth positions at 6m/s at $\lambda = 3$, It is shown that the flow is fully attached to the blade surface as the blade starts to rotate from $\theta = 0^{o}$ up to $\theta =$

70^o (Figure 5.13 (a)), different from the flow fields at $\lambda = 2.5$ in which the onset of separation bubble was seen at $\theta = 70^o$. At the midway of the chord, the beginning of a separation bubble formation is seen to have started on the suction side of the blade at $\theta = 80^o$ (Figure 5.13 (b)).

At $\theta = 90^o$ (Figure 5.13 (c)) the separation bubble has grown into a dynamic stall vortex or leading edge vortex (LEV) with the same length as the blade chord and the LEV width at the trailing edge approximately half chord length, which is similar to the developed LEV at $\theta = 80^o$ at the previous $\lambda = 2.5$. While the LEV is seen still attached to the blade's suction surface at $\theta = 90^o$, the trailing edge vortex (TEV) development is in the formative stage.

At $\theta = 100^o$ (Figure 5.13 (d)) the TEV starts to roll up and with the increase in size it pushes away the LEV from the blade's suction surface. This caused the LEV to completely detach from the blade surface which is similar to $\theta = 90^o$ in the previous $\lambda = 2.5$ flow fields. The first pair of vortices has been shed and the formation of a new pair has started also at $\theta = 100^o$. The flow is under a full regime of flow separation from the blade surface and the shedding of pairs of vortices, also the LEV and the TEV are different in size at $\theta = 120^o$ (Figure 5.13 (e)).

Further away, the flow separation from the blade surface and the pair of vortices shedding continued but with a reduction in the size of the TEV. The LEV and TEV are stretched out away from the blade surface. The LEV is approximately two chord length while the TEV is about one chord length. Also an onset of reattachment is observed at $\theta = 140^o$ (Figure 5.13f).

The reattachment of the flow to the blade surface continued and very visible with the width of both the LEV and TEV having reduced considerably. Even after the midway of the VAWT rotation the flow is obviously still separated from the blade surface and reattaches after $\theta = 190^o$ (Figure 5.13 (g)). The delay in the reattachment to the blade surface was also observed at the previous $\lambda = 2.5$.

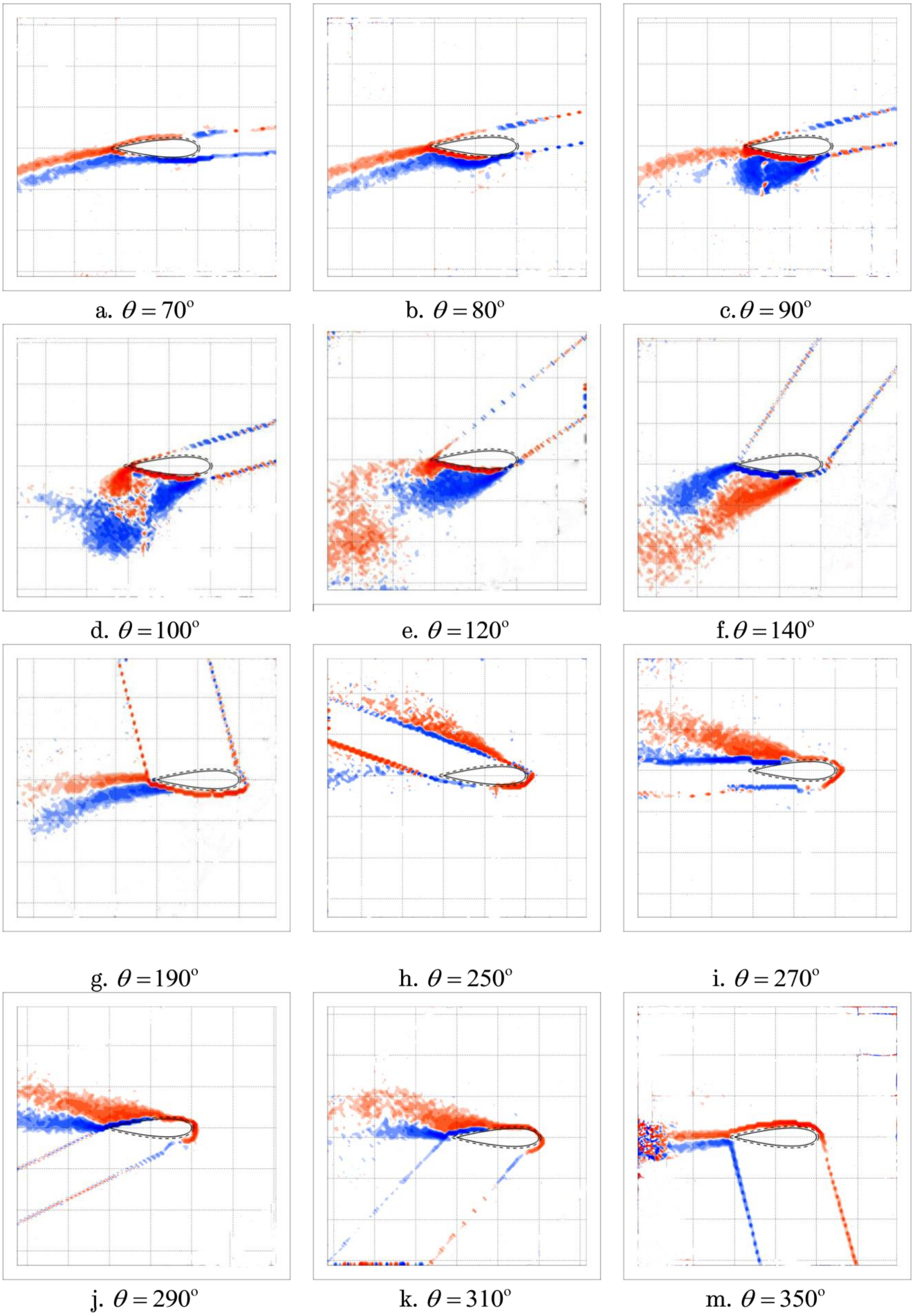
a. $\theta = 70^{\circ}$
b. $\theta = 80^{\circ}$
c. $\theta = 90^{\circ}$
d. $\theta = 100^{\circ}$
e. $\theta = 120^{\circ}$
f. $\theta = 140^{\circ}$
g. $\theta = 190^{\circ}$
h. $\theta = 250^{\circ}$
i. $\theta = 270^{\circ}$
j. $\theta = 290^{\circ}$
k. $\theta = 310^{\circ}$
m. $\theta = 350^{\circ}$

Figure 5.13. Z-vorticity flow fields of PIV measurements for different azimuth positions at 6m/s and λ = 3, Chord = 0.04m.

After midway of the rotation, with the VAWT blade at the downwind section of the rotation, a swoop of the pressure and suction surfaces is observed with the LEV formation on top of the aerofoil surface while the TEV developed below the aerofoil surface. However, the delayed flow reattachment to the blade surface stayed briefly at this stage of the flow, and at θ = 250° (Figure 5.13 (h)) the LEV completely detaches from the blade surface and shedding of a pair of vortices is also observed with the onset of flow reattachment which progressed through θ = 270° (Figure 5.13 (i)) and is seen to have completely attached to the blade's surface at θ = 350° (Figure 5.13 (m)). Unlike the flow field in the upwind section of the rotation in which delay reattachment of the flow to the blade surface was observed, the flow reattachment is not delayed, but rather the flow reattachment to the blade surface is earlier than was previously observed in the flow fields at λ = 2.5.

5.3.2.3 Flow Fields at λ = 4

Figure 5.14 shows z-vorticity plots of PIV images for different blade angles for λ = 4. The flow is very different at this λ since the onset of the blade stall development is significantly delayed at the upwind section of the rotation. At the start of the rotation from θ = 0° and up to θ = 100° (Figure 5.14 (a)) the flow field is fully attached to the blade surface and the attachment of the flow to the blade surface is seen to continue until θ = 120° (Figure 5.14 (c)) where the formation of the separation bubble at the mid chord length of the suction side of the aerofoil is seen. At similar azimuth position, θ = 120° in previous two flow fields at λ = 2.5 and 3 already discussed, the shedding of vortices had commenced.

Further away at θ = 130 (Figure 5.14 (d)) the separation bubble is seen to have developed into LEV with length slightly longer than the blade chord. The TEV is also seen at the early stage of its development. The LEV is fully separated from the blade's surface and has increased in length while the TEV has also developed. The shedding of a pair of vortices is also observed at θ = 140° (Figure 5.14(e)).

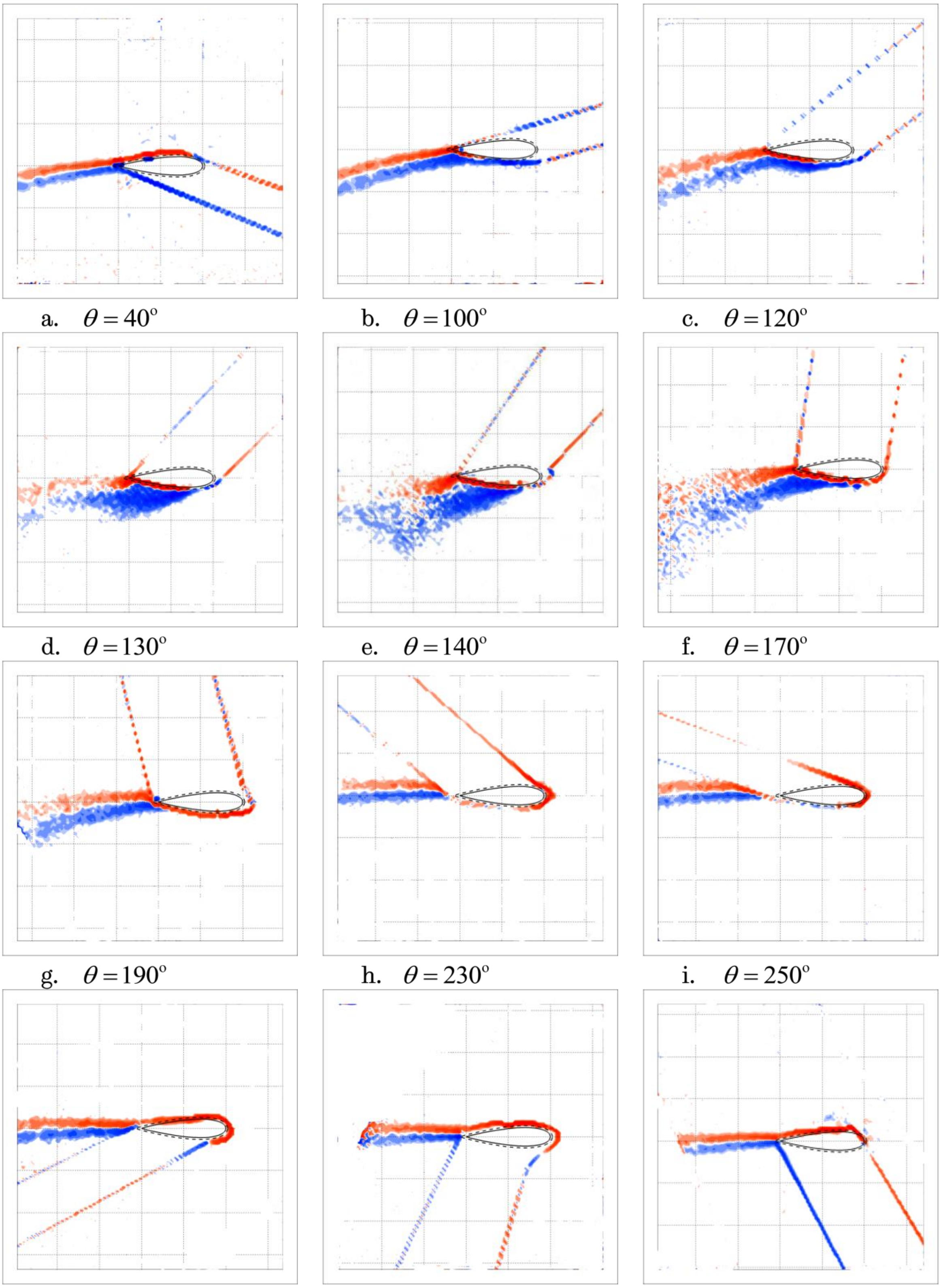

a. $\theta = 40^{\circ}$

b. $\theta = 100^{\circ}$

c. $\theta = 120^{\circ}$

d. $\theta = 130^{\circ}$

e. $\theta = 140^{\circ}$

f. $\theta = 170^{\circ}$

g. $\theta = 190^{\circ}$

h. $\theta = 230^{\circ}$

i. $\theta = 250^{\circ}$

j. $\theta = 290^{\circ}$

k. $\theta = 320^{\circ}$

m. $\theta = 360^{\circ}$

Figure 5.14. Z-vorticity plots from PIV images snapped at 6ms at different azimuth positions, $\lambda = 4.0$, Chord = 0.04m.

At $\theta = 170^{\circ}$ (Figure 5.14 (f)) the flow field separation and pairs of vortices being shed continued but with the onset of flow reattachment to the blade surface, similar to the λ 2.5 and 3. The LEV is seen at a quarter chord of the blade from the leading edge of the aerofoil. The flow reattachment is delayed after midway of the rotation as seen at $\theta = 190^{\circ}$ (Figure 5.14 (g)) and also as was previously shown at λ = 2.5 and 3.

At the downwind section of the rotation the flow is seen attached at most azimuth positions of the rotation in Figure 5.14 (h, I, j, k, m). It is noteworthy that the flow separation and vortices shedding at this λ started late, especially in the upwind section of the rotation, and the occurrence of dynamic stall is very low compared to the previous λ = 2.5 and λ = 3 cases in which the occurrence of blade stall dominated the flow. In the downwind section of the rotation the flow was attached to the blade at virtually all the azimuth positions unlike was also observed in the previous two cases.

5.4 Performance and Flow Fields at Different Reynolds Numbers

The performance and the flow features of the two VAWT configurations at different Reynolds numbers (based on Equation 1.3) are compared in this section. The comparison of the CP of the two configurations is based on 8m/s, 7m/s and a reference 6m/s wind speeds. The flow fields visualization and PIV measurements at three λ (2.5, 3 and 4) discussed in the previous sections are used to explain the observed differences in the CP. The Reynolds numbers discussed in this chapter are based on the wind speed the VAWT's blade sees while in operation, so it is dependent on the blade chord and λ. Table 5.1 shows the Reynolds numbers of the two VAWTs at 8m/s for various λ. The Reynolds numbers of C = 0.03m ranges from 16,800 to 84,000 for the corresponding minimum and maximum λ while that of the VAWT with C = 0.04m ranges from 22,400 to 112,000 for the corresponding minimum and maximum λ compared.

	Reynolds number								
λ	1	1.5	2	2.5	3	3.5	4	4.5	5
C = 0.03m	16800	25200	33600	42000	50400	58800	67200	75600	84000
C = 0.04m	22400	33600	44800	56000	67200	78400	89600	100800	112000

Table 5.1. Shows the Reynolds number of the two VAWT configurations at 8m/s for the various λ

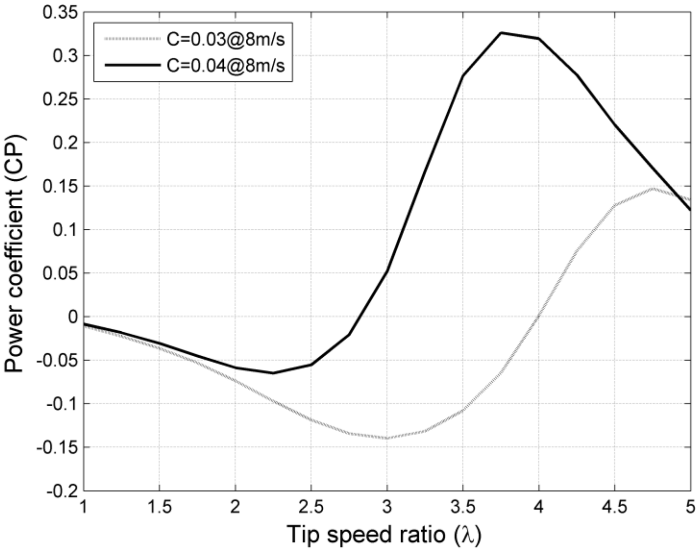

Figure 5.15. Shows power coefficient versus tip speed ratio for two VAWT configurations at 8m/s wind speed.

Figure 5.15 shows the CP of the two VAWTs at various λ for 8m/s wind speed. The VAWT with C = 0.03m (σ = 0.26) attained a maximum CP = 0.14 at λ = 4.75 and minimum CP = -0.14 at λ = 3, with a wider negative power region that run between λ = 1 and 3.9 while the VAWT with C = 0.04m (σ = 0.34) attained a maximum CP = 0.326 and a minimum CP = -0.065 at the corresponding λ = 3.75 and 2.25, with a smaller negative power region that ranges from λ = 1 to 2.75. The differences in the performance of the two VAWTs are due to the chord length of the blades and the resulting solidities and Reynolds numbers.

For consistency, the performances of the two VAWT configurations were also investigated at 7m/s and 6m/s wind speeds at similar λ. The Reynolds numbers at which the experiments were conducted are presented in tables 5.2 and 5.3 for the two VAWT configurations at various λ.

	Reynolds number								
λ	1	1.5	2	2.5	3	3.5	4	4.5	5
C = 0.03m	14700	22050	29400	36750	44100	51450	58800	66150	73500
C = 0.04m	19600	29400	39200	49000	58800	68600	78400	88200	98000

Table 5.2. The Reynolds number of the two VAWT configurations at 7m/s for the various λ.

Figure 5.16 presents the CP versus λ of the two VAWT configurations at 7m/s and 6m/s wind speeds. The performance trend of the VAWT configurations observed in Figure 5.15 is also observed in Figure 5.16. The VAWT with C = 0.03m (σ = 0.26) has lower maximum CP values, wider negative power regions while the VAWT with C = 0.04m (σ = 0.34) has higher maximum CP values and smaller negative power regions. It is also observed that the performance of the two VAWT configurations, are Reynolds number dependent as increases in wind speed had corresponding influences on the CP values at all the λ. From the observed features of the two VAWTs in Figures 5.15 and 5.16, it is not only obvious but also evidently seen that the performance trend of the two VAWTs is very consistent with changes in wind speeds (indirectly, Reynolds number) and λ.

	Reynolds number								
λ	1	1.5	2	2.5	3	3.5	4	4.5	5
C = 0.03m	12600	18900	25200	31500	37800	44100	50400	56700	63000
C = 0.04m	16800	25200	33600	42000	50400	58800	67200	75600	84000

Table 5.3. The Reynolds numbers of the two VAWT configurations at 6m/s for various λ.

Further investigations were carried out to understand and explain the observed differences in the performance of the two VAWTs by using the flow fields visualization and PIV measurements obtained at λ = 2.5, 3 and 4 for 6m/s wind speed. The VAWTs' performances at 6m/s wind speed was adopted as the reference case because it is the lowest wind speed the VAWTs can be compared and also distinct and important flow features of the two VAWTs blades can be seen at this wind speed than at the other higher wind speeds.

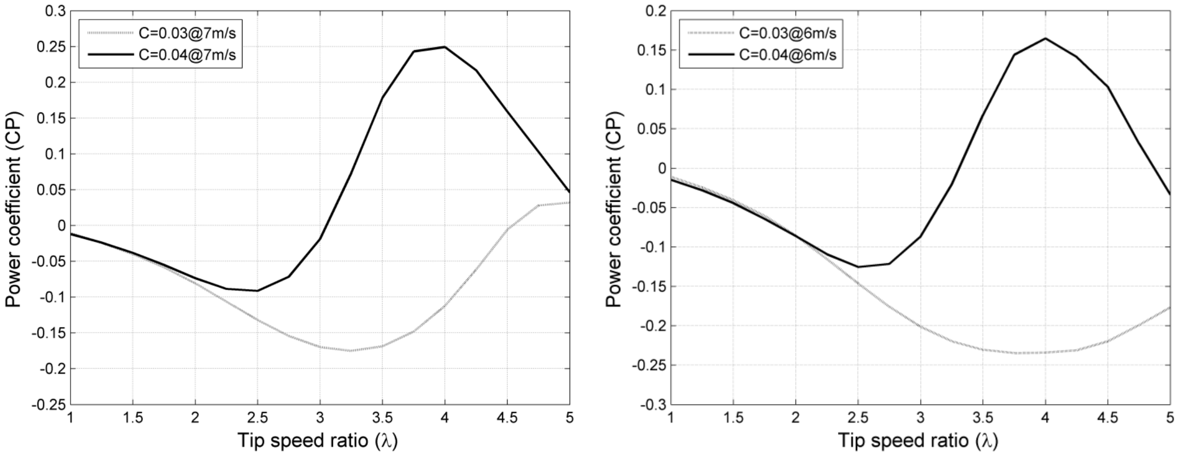

a. b.

Figure 5.16. Compares power coefficient versus tip speed ratio for two VAWT configurations: a) 7m/s wind speed, b) 6m/s wind speed.

The three λ are chosen based on; (a) at λ = 2.5, a clear difference in the CP of the two VAWTs is seen starting from the low λ for the three wind speeds, (b) λ = 3 is approximately the mean λ the tests were conducted and (c) λ = 4 is the corresponding λ at which the VAWT with C = 0.04m (σ = 0.34) attained its maximum CP at 6m/s wind speed and, also close to this λ, the VAWT with C = 0.03m attained its minimum CP at 6m/s wind speed.

5.4.1 Description of Power Coefficients and Flow Fields at λ = 2.5

The VAWT with C = 0.03m (σ = 0.26) attained a CP = -0.146 while that of C = 0.04m (σ = 0.34) attained a CP = -0.125 at λ = 2.5. The difference in the CP values for the two VAWT configurations is approximately 17% in favour of the VAWT with C = 0.04m. Figure 5.16 (b) also shows that the C = 0.03m curve is dropping to lower CP values away from λ = 2.5 towards λ = 3, while the C = 0.04m attained its minimum CP at λ = 2.5 therefore, further away towards λ = 3 there are increases in the CP values. The differences observed in the CP of the two configurations would be explained by the introduction of the PIV measurement data to provide penetrating insights into the flow aerodynamics at λ = 2.5.

Figure 5.17 shows the flow fields visualization and PIV measurements for the two VAWTs blades. The flow structures at $\theta = 60^o$, $\theta = 70^o$ and $\theta = 80^o$ are chosen for the comparison because the occurrence of the onset of stall, blade stalled and flow separation from the blade surface is higher at these angles. At $\theta = 60^o$ the C = 0.03m is stalled with the LEV seen fully developed on the inner surface of the blade and still attached to the blade's surface while the TEV is observed forming and increasing in size. At this stage of the dynamic stall cycle, the C = 0.03m experiences an abrupt increased in the lift. Whereas C = 0.04m has the flow still attached to the blade's surface, so it still experience a steady increase in lift, this is explained in details later in chapter six.

Further away at $\theta = 70^o$, the LEV fully detaches from the blade's surface, the TEV roll up is complete and fully stretched away from the blade's surface and a pair of LEV and TEV is being shed for C = 0.03m. The C = 0.03m is in the post-stall stage characterized by the reduction in power. Whereas for the C = 0.04m, the stall is being initiated by the formation of the separation bubble on the inner surface of the blade seen by the thickening of the boundary layer.

At $\theta = 80^o$ the LEV and TEV is seen completely detached and a pair of vortices is being shed, the loss of lift would continue far beyond $\theta = 90^o$ until midway of the rotation ($\theta = 180^o$) for C = 0.03m as detailed in Table 5.4. Whereas, the C = 0.04m is stalled with the LEV fully developed but still attached to the blade surface, and the TEV is seen in the formative stage beginning to push away the LEV from the blade surface. A sudden increased in lift force is experienced by the C = 0.04m blade at this stage of the dynamic stall cycle. The flow field vorticity at other azimuth positions for C = 0.04m and C = 0.03m compared are summarized in Table 5.4.

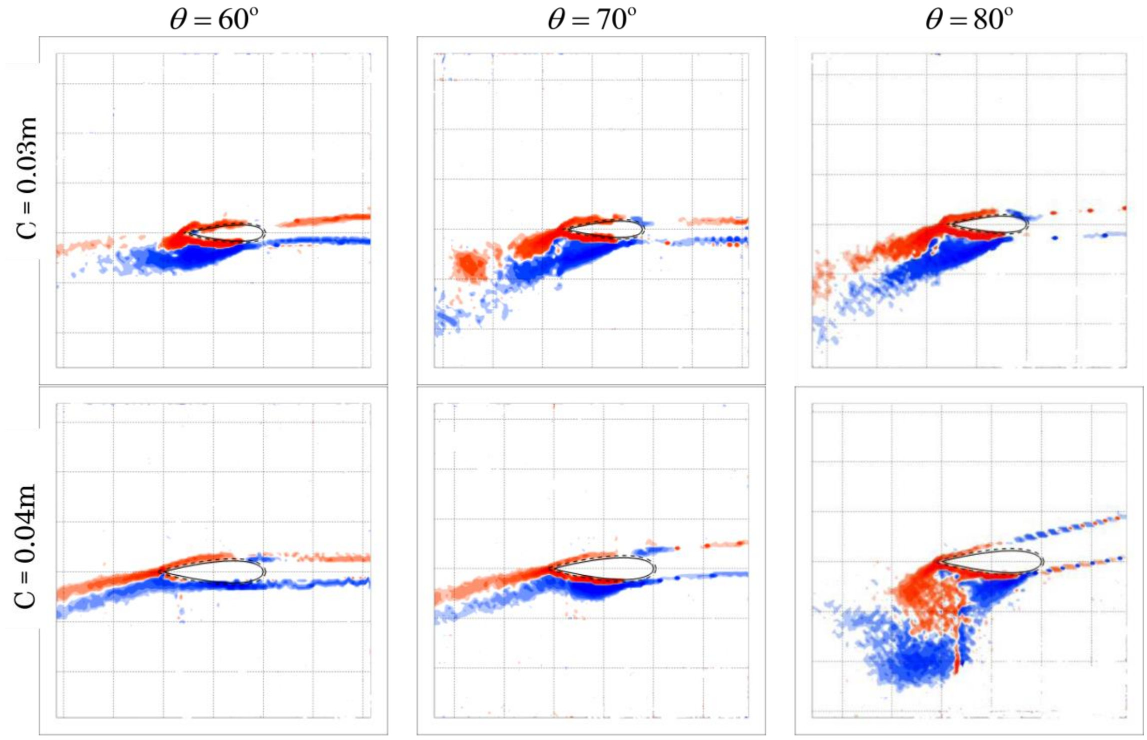

Figure 5.17. Z-vorticity plots of PIV images of two chords at $Re_{0.03m}$ = 31,500, $Re_{0.04m}$ = 42,500 and different azimuth position of the upwind section, λ = 2.5.

On the downwind section of the rotation the flow features and vorticity flow fields of the two blades began to bear similarities. Although, the dynamic stall phenomenon occurs twice in one revolution of the VAWTs, the pre-stall and stall stages were not properly captured by the PIV at the start of the downwind half of the rotation due to the obstructed camera view, by the support structure of the wind tunnel, shadow region of the blades at some azimuth positions and insufficient space around the wind tunnel so the use of the laser was restricted to one side of the wind tunnel. However, the number of blade's azimuth positions visualized and measured with the PIV is adequate for the investigation.

Azimuth	C = 0.03m (σ = 0.26) , V = 6m/s	C = 0.04m, (σ = 0.34), V = 6m/s
$\theta = 0^{o}$	The flow is fully attached to the blade's surface	The flow is also seen completely attached to the blade's surface as observed in C = 0.03m
$\theta = 50^{o}$	The flow is still attached to the blade's surface.	The flow is still attached to the blade's surface.
$\theta = 60^{o}$	The blade is stalled, LEV has been formed and being pushed away from the blade's surface due to the formation of the TEV that has progressed.	The blade is still in the pre-stall stage with the flow observed to be fully attached to the blade's surface.
$\theta = 70^{o}$	The blade has advanced in the stall process. The LEV is being pushed away from the blade's surface by the roll up of the TEV.	Blade stall is being initiated with the formation of LEV separation bubble at the suction side of the blade's surface.
$\theta = 80^{o}$	The roll up of the TEV is complete and stretched out. The flow is separated from the blade's surface and pairs of vortices are being shed.	The blade is stalled with the formed LEV about the length of the blade's chord. The TEV formation and roll up have also commenced while the LEV is being pushed away from the blade's surface.
$\theta = 90^{o}$	Separation of the flow from the blade surface and also shedding of a pair of vortices continued.	The blade is in the post stall stage. The LEV is completely pushed away from the blade's surface by the roll up of the TEV.
$\theta = 130^{o}$	Separated, detached flow and shedding of a pair of vortices continued.	The flow is fully detached from the blade surface and shedding of pairs of vortices is also observed to have started.
$\theta = 140^{o}$	The flow is separated from the blade's surface and shedding of a pair of vortices is seen. The onset of reattachment of the flow is also seen.	The flow is separated from the blade's surface and shedding of a pair of vortices continued. The onset of flow reattachment is also observed.
$\theta = 170^{o}$	The flow reattachment has advanced considerably. A pair of vortices is still being shed.	Like the C = 0.03m, the flow reattachment has advanced significantly and the shedding of vortices continued.
$\theta = 180^{o}$	Delayed reattachment of the flow to the blade's surface is observed.	Reattachment of the flow to the blade's surface is delayed as also observed in C = 0.03m.
$\theta = 190^{o}$	The reattachment of the flow to the blade's surface is significantly delayed.	The reattachment of the flow field is also observed to be delayed even after midway of the rotation.
$\theta = 260^{o}$	The blade is in the post stall stage with the LEV fully detached from the blade's surface and also being shed.	It is also observed that the blade is in the post stall stage with the LEV fully detached from the blade's surface and also being shed.
$\theta = 290^{o}$	Detached flow from the blade's surface, shedding of a pair of vortices and the onset of flow reattachment to the blade's surface is observed.	Separated flow, the shedding of a pair of vortices and the onset of flow field reattachment to the blade's surface is also seen.
$\theta = 320^{o}$	The flow reattachment to the blade's surface is seen to have advanced.	It is also observed that the flow reattachment to the blade's surface has advanced.
$\theta = 360^{o}$	The flow is seen to be fully attached to the blade's surface.	Also it is observed that the flow is fully attached to the blade's surface.

Table 5.4. Differences and similarities in flow field aerodynamics of the two VAWT configurations at λ = 2.5 and $Re_{0.03m}$ = 31,500, $Re_{0.04m}$ = 42,500.

Figure 5.18 compares flow fields of the two VAWTs blades at the downwind section of their rotation. At θ = 260° both the C = 0.03m and C = 0.04m blades are in the post stall stage of the dynamic stall cycle. Their LEV is fully separated from the blade's surface and also being shed, and due to the bigger size of C = 0.04m larger vortices are seen at comparable azimuth positions around it than the smaller vortices seen around C = 0.03m. At θ = 290° the LEV and TEV are detached from the surface of the two blades, shedding of a pair of vortex and onset of flow reattachment are observed. The blades are in the post-stall stage of the dynamic stall cycle characterized by reduction of lift and, at θ = 350° the flow fields are seen attached to the surfaces of both blades.

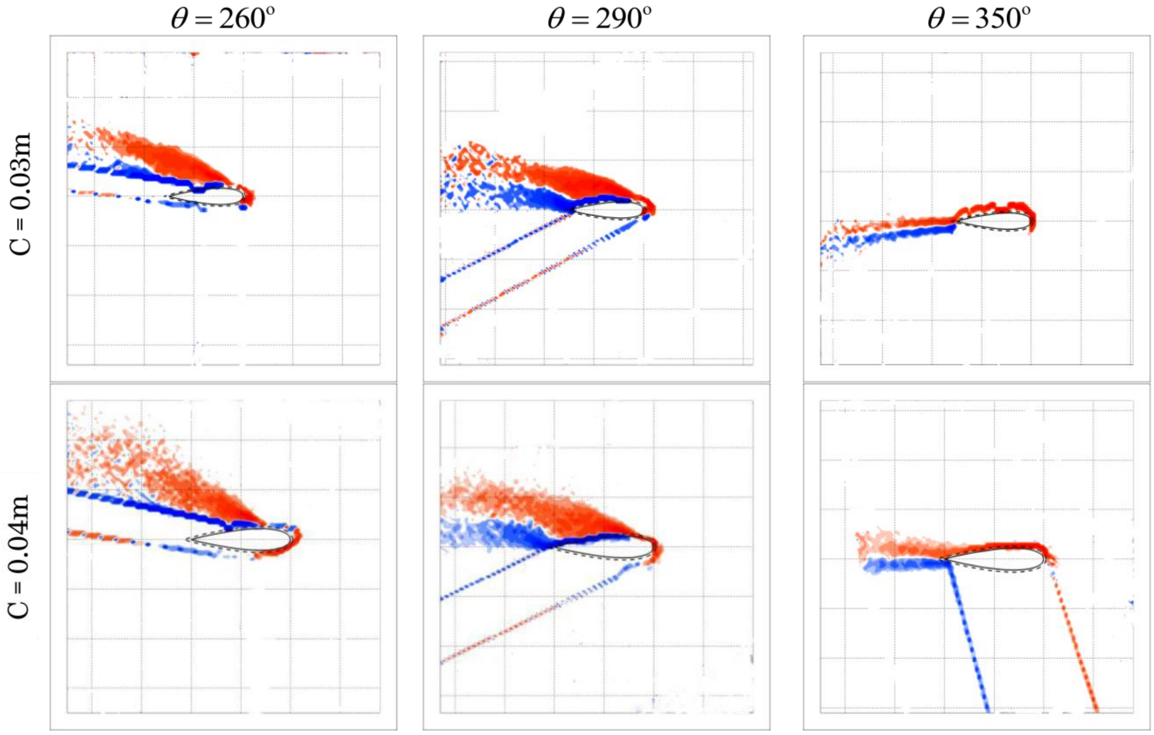

Figure 5.18. Shows z-vorticity plots of PIV images of two chords at $Re_{0.03m}$ = 31,500, $Re_{0.04m}$ = 42,500 and different azimuth position of downwind section rotation, λ = 2.5.

The flow physics of the two VAWT blades as compared in Figures 5.17 and 5.18, and also in Table 5.4 have shown distinct features that can influence VAWTs performance. Too early start to the dynamic stall process has been shown to have unfavourable effects on the overall performance of VAWTs. This is due to the follow-on effects of early detachment of the flow fields from the blade's surface, shedding of mature regular pair of vortices and conversely, inability of the blade to sustain the lift force especially when in the post-stall stage. The dynamic stall process started very early for the VAWT with C = 0.03m. At θ = 60^{o} the blade was already stalled and before θ = 70^{o} pairs of vortices were being shed, whereas the VAWT with C = 0.04m is seen stalled only at θ = 80^{o} with the LEV even still attached to the blade's surface. A phase difference of more than 20^{o} is observed of which, indisputably, can cause a significant difference in performance. The similarities in the flow fields observed in the downwind section of the flow may not have impacted on the performance so as to undermine the advantage gained by the C = 0.04m in the upwind section. Because the two blades are in the post-stall stage, and at these azimuth positions the blades interact with their own wake and the wake of the shaft, and also the blades would see lower velocity magnitude due to the solid blockage caused by the blades in the upwind section hence lower power is generated, so the advantage gained by the bigger blade is maintained. This explains the superior performance of C = 0.04m VAWT with σ = 0.34 over the VAWT with C = 0.03m (σ = 0.26) at λ = 2.5, as seen in Figure 5.16 (b).

5.4.2 Description of Power Coefficients and Flow Fields at λ = 3

The CP of the VAWTs at λ = 3 in the Figure 5.16 (b) is different. The C = 0.03m VAWT with σ = 0.26 attained CP = -0.203 while C = 0.04m (σ = 0.34) VAWT attained CP = -0.087 resulting in a superior difference of 133.3% in favour of C = 0.04m. Based on the performances attained by the two configurations, the CP of the two VAWT configurations is seen in the negative performance region at λ = 3. The observed difference in the CP is further investigated using the flow field visualization and PIV measurements obtained to explain the flow aerodynamics and performance of the two blades at this λ.

The flow field visualization and PIV measurements of three azimuth positions for the two blades at θ = 60^{o} , θ = 70^{o} and θ = 80^{o} are shown in Figure 5.19. The three azimuth angles are the corresponding angles where the occurrence of blade stalled is predominant. The flow field around both blades is seen completely attached to the blade surfaces at $\theta = 60^{o}$. Thus, the two blades are in the pre-stall stage of the dynamic stall cycle which is usually accompanied by a steady increase in lift. As the blades advance to $\theta = 70^{o}$ azimuth position the C = 0.03m is stalled, the LEV was formed on and still attached to the inner side of the blade's surface and the roll up of the TEV is in the formative stages, whereas the flow around C = 0.04m blade is fully attached to the blade surface. At these stages of the dynamic stall the C = 0.03m blade would experience a sudden increase in the lift force, while the C = 0.04m would maintain a steady increase in its lift force, see chapter six.

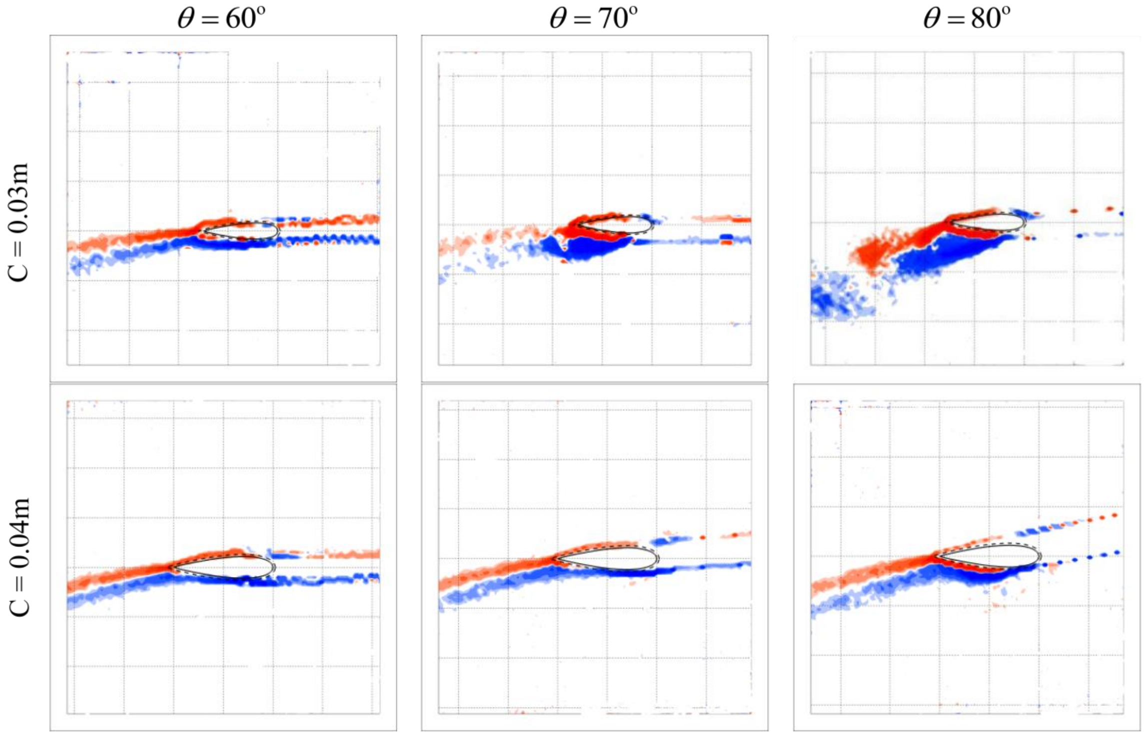

Figure 5.19. Z-vorticity plots of PIV images of two chords at $Re_{0.03m}$ = 37,800, $Re_{0.04m}$ = 50,400 and different azimuth positions in the upwind section, $\lambda = 3$.

At $\theta = 80^{o}$ the C = 0.03m had advanced in the dynamic stall process with the LEV and the TEV detached from the blade's surface, also a pair of LEV and TEV in different sizes are being shed. The early detached of the flow and the shedding of the vortices from the surface of the C = 0.03m blade results in a reduction of lift force hence, lower the overall performance of the VAWT.

Azimuth	C = 0.03m (σ = 0.26) , V = 6m/s	C = 0.04m (σ = 0.34), V = 6m/s
$\theta = 0^o$	The flow is fully attached to the blade's surface	The flow is also seen completely attached to the blade's surface as observed in C = 0.03m
$\theta = 60^o$	The flow is still attached to the blade's surface	Also the flow is still attached to the blade's surface.
$\theta = 70^o$	The blade is stalled. LEV has been formed on the suction side of the blade's surface and still attached. The TEV is in the formative stages.	The flow is observed to be fully attached to the blade's surface.
$\theta = 80^o$	The blade is also in the stall stages, the flow is fully separated from the blade's surface and a pair of vortices is being shed.	The blade is in the pre stall stage with the start of the formation of LEV separation bubble seen at the suction side of the blade's surface.
$\theta = 90^o$	The flow completely detaches from the blade's surface, a pair of vortices is being shed	The blade is stalled with the LEV attached to the blade's surface and the TEV is also seen in its early stages of formation.
$\theta = 100^o$	The flow field separation, shedding of regular pair of vortex continued, and also the downstream convection of the shed LEV is also observed.	The blade is in the stall stage with the LEV being pushed away from the blade surface by the roll up of the TEV.
$\theta = 120^o$	The flow separation and shedding of a pair of vortices continued.	The first pair of the LEV and TEV formed has been detached and shed and the formation of the second pair of LEV and TEV has started. The shed pair of vortices from the blade's surface is observed to vary in size.
$\theta = 140^o$	The flow is separated from the blade's surface and shedding of a pair of vertices is seen.	The flow is separated from the blade's surface and shedding of a pair of vortices continued. The onset of flow reattachment is observed.
$\theta = 170^o$	The flow reattachment has advanced considerably. A pair of vortices of equal sizes is being shed.	Like the C = 0.03m, the flow reattachment has advanced significantly and the shed vortices are equal in size.
$\theta = 190^o$	The reattachment of the flow to the blade's surface is significantly delayed.	The reattachment of the flow is also observed to be delayed even after midway of the rotation.
$\theta = 250^o$	The LEV is seen to form on the top side of the blade and also separated from the blade's surface. The LEV is being shed.	The LEV is separated from the blade's surface. The LEV is formed on the top side of the blade while the formation of the TEV is on the bottom side of the blade.
$\theta = 260^o$	The blade is in the post stage stage, detached flow from the blade's surface and shedding of the LEV is observed.	It is also observed that the flow is separated from the blade's surface; both the LEV and TEV is being shed.
$\theta = 290^o$	Detached flow, shedding of pairs of vortices and the onset of flow reattachment to the blade's surface is observed.	Separated flow, the shedding of a pair of vortices and the onset of flow reattachment to the blade's surface is also seen.
$\theta = 310^o$	The flow reattachment to the blade's surface and shedding of a pair of vortices is observed.	The flow reattachment to the blade's surface continued with the pair of vortex shedding seen to be irregular and less vigorous due to the advancement of the flow reattachment to the blade's surface.
$\theta = 350^o$	The flow is seen fully attached to the blade's surface.	It is also observed that the flow is fully attached to the blade's surface.

Table 5.5 The differences and similarities in flow fields aerodynamics of the two VAWT configurations at λ = 3 and $Re_{0.03m}$ = 37,800, $Re_{0.04m}$ = 50,400.

At the same blade position, the C = 0.04m blade had just advanced into the stall stage with the LEV separation bubble still in the formative stages on the suction side of the blade, giving an advantage of further increase in lift force of the blade and overall better performance of the VAWT with the bigger chord. These observed differences continued into the second half of the upwind section, and even further in the rotation as detailed in Table 5. 5. The distinct differences observed between the cases in the upwind section are not present in the downwind section of the rotation, rather close similarities in the flow fields of the two blades are seen. Figure 5.20 compares the vorticity and PIV measurements of the two VAWT's blades at the downwind section of the rotation. At θ = 260° the LEV is separated from both blades and also being shed. The LEV for the C = 0.04m is bigger than that of the smaller blade. The two blades are also in the post stage of the dynamic stall cycle. Reattachment of the flow fields to the blades' surfaces had advanced at θ = 310° and, further down at θ = 350° the flow fields around the two blades are completely reattached to the blade's surfaces.

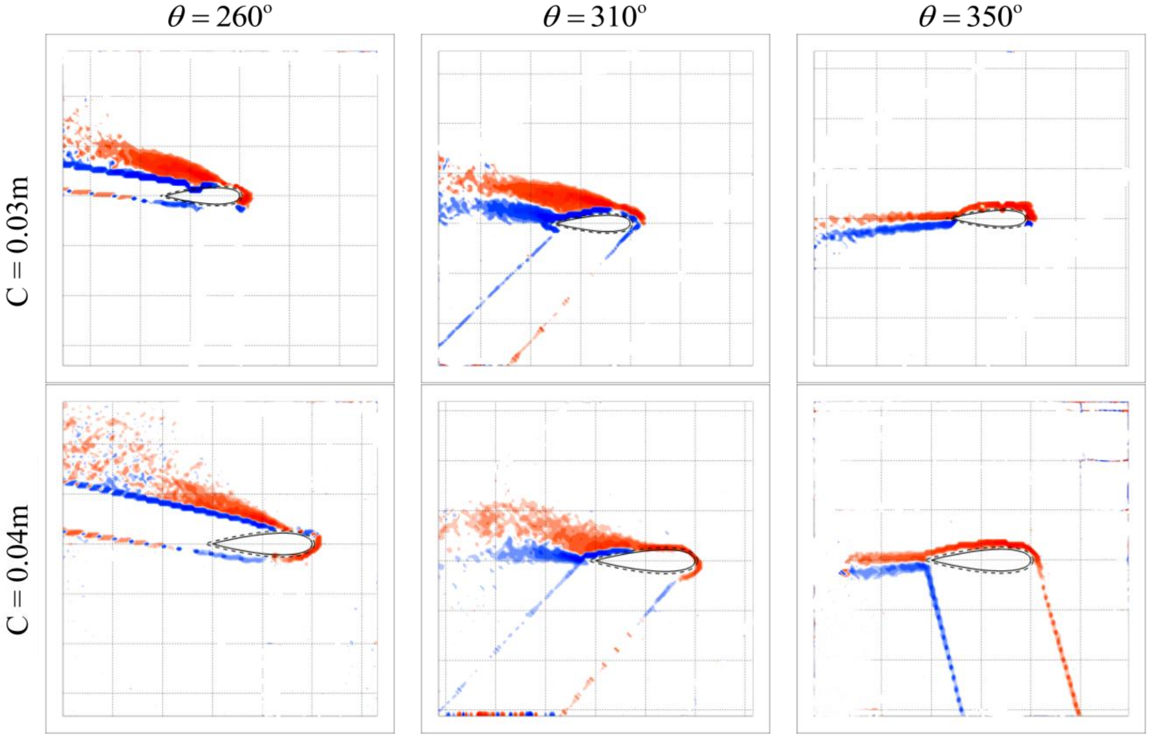

Figure 5.20. Z-vorticity plots of PIV images of two chords at $Re_{0.03m}$ = 37,800, $Re_{0.04m}$ = 50,400 and different azimuth positions in downwind section, λ = 3.

The azimuth position at which the dynamic stall process began is seen to have greatly influenced the overall performance of the two VAWT configurations. The dynamic stall process for C = 0.03m started earlier and the blade was stalled at $\theta = 70^o$. A pair of vortices was already being shed at $\theta = 80$ whereas the dynamic stall of C = 0.04m blades started late, the onset of the separation bubble formation was seen only at $\theta = 80^o$, this show a phase difference of more than 15^o. Subsequently, the TEV formation, a detachment of flow from the blade's surfaces and shedding of vortices are delayed well into the second half of the upwind section of the rotation with the lift force being sustained longer for the C = 0.04m blade. This explains why the VAWT with C = 0.04m and σ = 0.34 performed better in Figure 5.16 (b) than that of C = 0.03m (σ = 0.26) at λ = 3.

5.4.3 Description of Power Coefficients and Flow Fields at λ = 4

The performance at this λ is very distinctive as the CP attained by the two VAWT configurations are obviously different with a larger gap than what was seen at the previous λ = 2.5 and λ = 3. The C = 0.03m VAWT attained a low CP = -0.234 while, the C = 0.04m attained its maximum CP = 0.165. Auspiciously, λ = 4 corresponded approximately to the λ at which the C = 0.03m VAWT attained its minimum CP, while it also corresponded to the λ at the C = 0.04m VAWT attained its peak CP. As clearly seen in Figure 5.16 (b), an enormous difference of over 200% separates the CP of the two VAWT configurations in favour of the C = 0.04m VAWT with σ = 0.34. This massive difference in the CP is further investigated to understand the aerodynamics of the flow physics and performance by employing the visualized flow fields and the PIV measurements around the blades at this λ.

Figure 5.21 compares the flow fields and the PIV measurements of the two blades at the upwind section for $\theta = 80^o$, $\theta = 90^o$, $\theta = 100^o$ azimuth positions at which the occurrence and development of dynamic stall are observed. The flow fields are seen attached to the surfaces of the two blades at $\theta = 80^o$, this is a distinctive feature associated with VAWT at the medium and high tip speed ratios especially where maximum power is attained. While the C = 0.03m blade stalled at θ = 90° the flow of C = 0.04m blade is still fully attached even after θ = 100°.

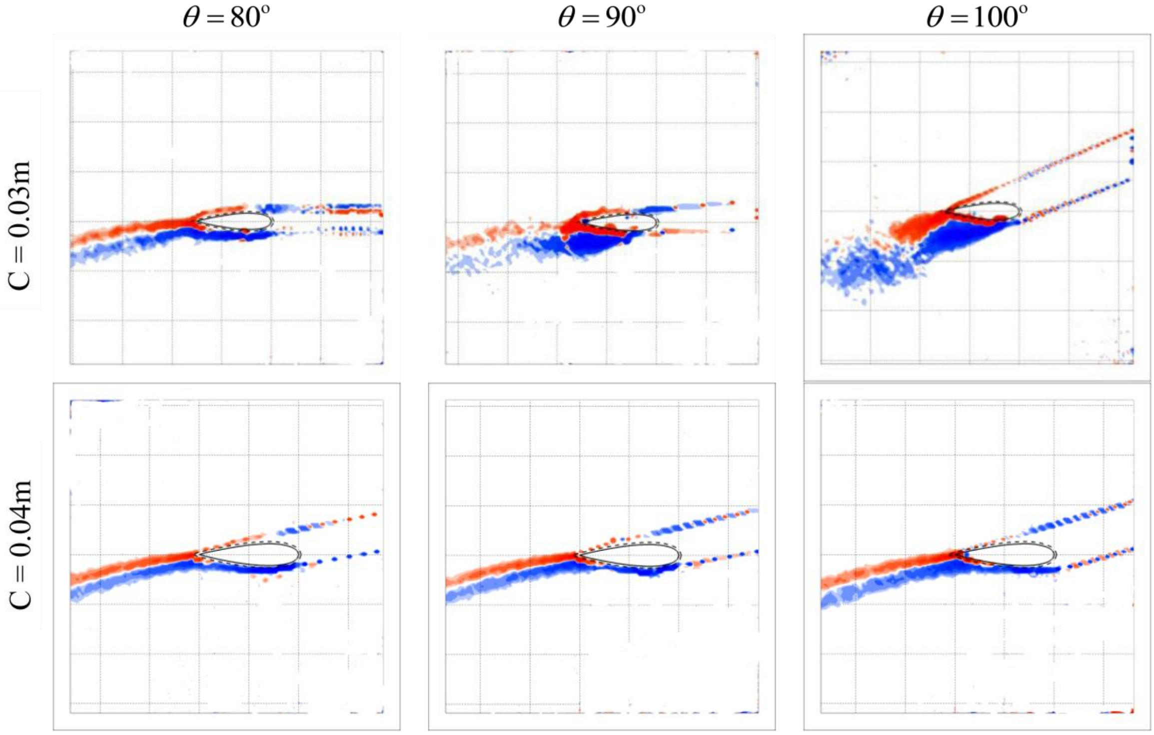

Figure 5.21. Z-vorticity flow fields and PIV measurements of two chords at $Re_{0.03m}$ = 50,400, $Re_{0.04m}$ = 67,200 and different azimuth positions for upwind section, λ = 4.

The attached flow to the C = 0.04m blade from θ = 0° up to θ = 100° show that the lift is gained as well as sustained all through the first half and into the second half of the upwind section of the rotation. This signifies, during this period, high levels of power is being extracted from the wind by the VAWT, whereas the C = 0.03m blade had its LEV being convecting away from the blade's surface and the roll up of the TEV had also advanced. At this stage, the C = 0.03m had begun to lose lift, hence loss of power. Table 5.9 detailed the flow field's aerodynamics around the two blades at the other azimuth positions.

As was observed in the upwind section, distinct differences between cases are present in the downwind section of the rotation. The flow features are mostly attached to the C = 0.04m blade surface for all the azimuth positions investigated but, all the stages of the dynamic stall are present on the surface of the C = 0.03m blade for the azimuth positions visualised (Table 5.6). At $\theta = 290^{\circ}$ the LEV and TEV pairs are being shed and also the onset of reattachment of the flow to the blade's surface is seen (Figure 5.22).

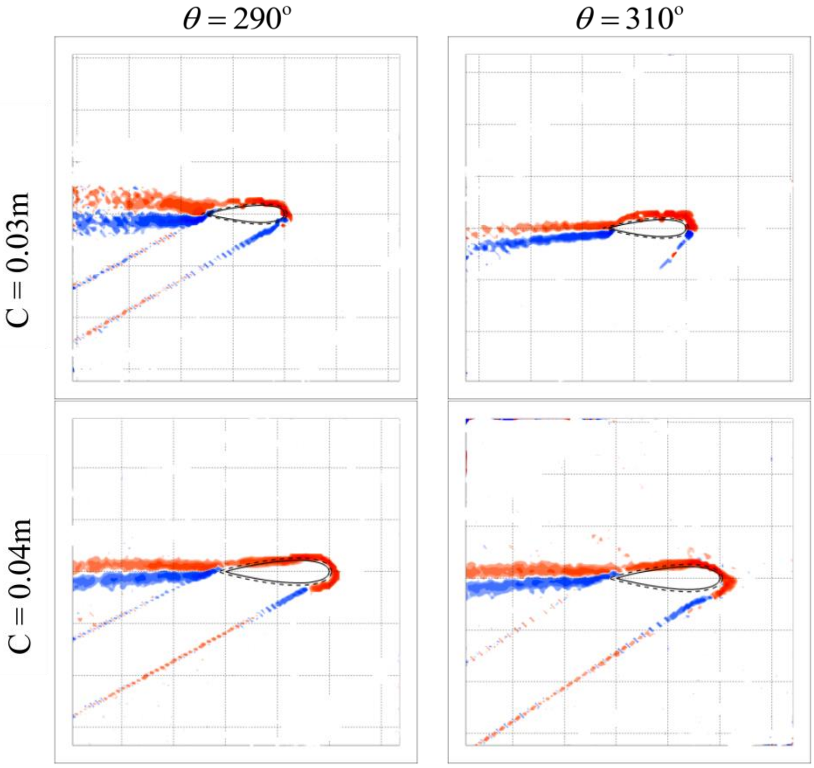

Figure 5.22. Z-vorticity plots of PIV images of two chords at $Re_{0.03m}$ = 50,400, $Re_{0.04m}$ = 67,200 and different azimuth positions in the downwind section, $\lambda = 4$.

The C = 0.04m blade has its flow fully attached to the blade's surface. Although the two blades are in the early part of second half of the downwind section of the rotation, the C = 0.03m is in the post stall stage with the effects of loss of lift, while the C = 0.04m blade is already in the pre-stall stage which is characterized by the gain in and sustained lift. However, the flow is seen to be fully attached to the C = 0.03m blade's surface only at $\theta = 310^{\circ}$.

Azimuth	C = 0.03m (σ = 0.26) , V = 6m/s	C = 0.04m (σ = 0.34), V = 6m/s
$\theta = 0^{\circ}$	The flow is fully attached to the blade's surface	The flow is also seen completely attached to the blade's surface as observed in C = 0.03m
$\theta = 80^{\circ}$	The flow is still attached to the blade's surface	Also the flow is still attached to the blade's surface.
$\theta = 90^{\circ}$	LEV has been formed on the suction side of the blade's surface and still attached. The TEV is in the formation stage. The blade is stalled	The flow is observed to be fully attached to the blade's surface.
$\theta = 100^{\circ}$	The blade is in the post stall stage. The LEV is being pushed away from the blade's surface while the TEV formation has advanced.	The flow is fully attached to the blade's surface.
$\theta = 120^{\circ}$	The flow completely detaches from the blade's surface, a pair of vortices is being shed	The start of the formation of separation bubble is seen at the suction side of the blade.
$\theta = 130^{\circ}$	The flow completely detaches from the blade's surface; pairs of vortices are being shed.	The LEV has been formed and attached to the blade's surface. The blade is stalled.
$\theta = 140^{\circ}$	The flow is separated from the blade's surface and shedding of a pair of vortices continued and the onset of the flow reattachment is also observed.	The LEV is pushed away from the blade's surface by the roll up of the TEV. The blade is in the post stall stage.
$\theta = 170^{\circ}$	The flow reattachment has advanced considerably. A pair of vortices is still being shed.	The flow is separated from the blade's surface, shedding of pair of vortices is also observed.
$\theta = 190^{\circ}$	The reattachment of the flow to the blade's surface is almost complete.	Like in C = 0.03m the reattachment of the flow field to the blade's surface is almost complete.
$\theta = 230^{\circ}$	Not available.	It is observed that the flow field is fully attached to the blade's surface.
$\theta = 250^{\circ}$	The blade is in the post-stalled stages, flow detached from the blade's surface and shedding of the LEV from the top of the aerofoil is observed to continue.	It is observed that the flow is fully attached to the blade's surface.
$\theta = 260^{\circ}$	The blade is stalled, flow detached from the blade's surface and shedding of the LEV from the top of the aerofoil is observed to continue.	It is observed that the flow is fully attached to the blade's surface
$\theta = 290^{\circ}$	The blade is stalled, flow detached from the blade's surface and shedding of a pair of vortices and onset of flow reattachment is observed.	It is observed that the flow is fully attached to the blade's surface
$\theta = 320^{\circ}$	The flow fully attached to the blade's surface.	It is observed that the flow is fully attached to the blade's surface.

Table 5.6. Differences and similarities in flow fields aerodynamics of the two VAWT configurations at λ = 4 and $Re_{0.03m}$ = 50,400, $Re_{0.04m}$ = 67,200.

It is obvious that performance of the two VAWT configurations at this λ is strongly influenced not only by the flow physics but also by the blade chord. Although the two configurations operate at the same wind speed, they see different Reynolds number due to the differences in their blade chords. The C = 0.03m blade is operating within the Reynolds number range that can cause a deep stall of the blade and also zero- lift drag that is being experienced by the blade. For the C = 0.04m blade the reverse is the case, the Reynolds number is above the stall level so, maximum power is being extracted. This explains the enormous difference in the VAWTs CP at λ = 4 in Figure 5.15 (b).

5.5 Performance and Flow Fields at the Same Reynolds Numbers

This section details the description of the performance and flow characteristics of the two VAWT configurations at the same Reynolds numbers by comparing their power coefficients at various λ, and also comparing their visualized flow fields and the PIV measurements at λ = 2.5 and 3. Table 5.7 compares the Reynolds numbers of the two configurations at which the experimental investigations were conducted at the various λ. The Re ranges from a low value of 16,800 to a high value of 84,000 corresponding to the minimum and maximum λ for the VAWTs with C = 0.03m and C = 0.04m. The Re is based on the blade's speed and chord.

	Reynolds number								
λ	1	1.5	2	2.5	3	3.5	4	4.5	5
C = 0.03m, 8m/s	16800	25200	33600	42000	50400	58800	67200	75600	84000
C = 0.04m, 6m/s	16800	25200	33600	42000	50400	58800	67200	75600	84000

Table 5.7. The Reynolds numbers for the two VAWT configuration at various λ.

Figure 5.23 compares the performance of the two VAWTs at various tip speed ratios. The performance of the VAWT configuration with C = 0.03m has a wider negative trough that starts from λ = 1 to 4 and a positive power region that starts from λ = 4 to λ = 5, it attained a peak CP = 0.147 at the corresponding λ = 4.75 and lowest CP = - 0.14 at a corresponding λ = 3. The VAWT with C = 0.04m has a narrower negative trough spanning from λ = 1 to λ = 3.3 and a positive power region that is between λ = 3.5 and 4.75, it attained a maximum CP = 0.165 at a corresponding peak λ = 4 and minimum CP = - 0.125 at the corresponding λ = 2.5. The negative trough in the CP – λ curves makes it difficult for self-start-up of the VAWT. An equivalent force is required to overcome the torques within the negative band for the VAWT to operate within the desired positive power production region.

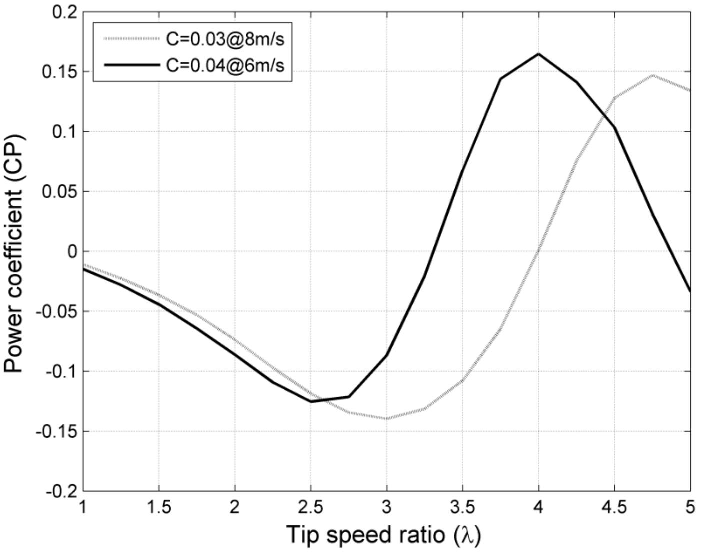

Figure 5.23. The CP versus λ for two VAWT configurations at the same Reynolds numbers (Table 5.7).

5.5.1 Description of Power Coefficients and Flow Fields at λ = 2.5

The power coefficients of the two VAWT configurations at λ = 2.5 are in the negative performance region. It is shown in Figure 5.23 that a 0.5% difference exists between the power coefficients of the two VAWT configurations indicating that the performance at λ = 2.5 is similar (the same) since 0.5% is within acceptable experimental error margin (Appendix 1). It is observed also that the curve of C = 0.03m is moving down to lower CP values as it moves away from λ = 2.5 towards λ = 3 where the minimum CP is attained whereas that of C = 0.04m progresses upward from λ = 2.5 to higher CP values.

The similarity in the performance of the two VAWT configurations at this λ are further investigated using the flow field visualization and PIV measurements obtained at the λ = 2.5. Figure 5.24 compares the z – vorticity flow fields of the two VAWTs blades at similar azimuth positions in the upwind section of rotation. At $\theta = 60^{\circ}$, blade stall is being initiated by the formation of the LEV separation bubble on the inner side of the blade surface for C = 0.03m whereas the flow field is seen attached to the blade surface for the C = 0.04m.

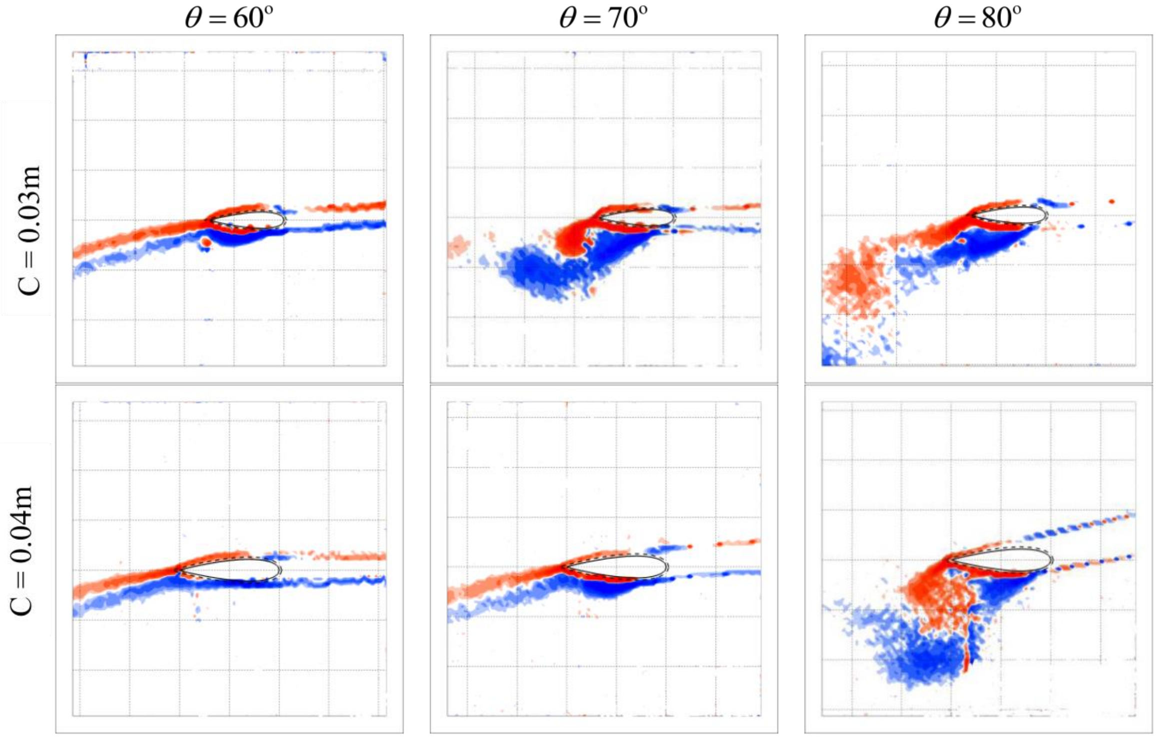

Figure 5.24. The z-vorticity flow field of PIV measurements of two chords at Re = 42,000 and different azimuth positions for upwind section, λ = 2.5.

Further away to $\theta = 70^{\circ}$, the blade experienced deep stalled with the LEV seen detached from the blade's inner side of C = 0.03m due to the formation of the TEV that is already at an advanced stage, while the onset of stall is being initiated by C = 0.04m with the formation of the LEV separation bubble at the inner surface of the blade. At this azimuth position, the C = 0.03m would gain sudden increase in lift that impact positively on the overall performance, nonetheless the lift for C = 0.04m would continue to increase steadily.

Towards the end of the first quadrant of the rotation at $\theta = 80^{\circ}$, the blade for C = 0.03m is already shedding LEV and TEV, and is in the post stall stage characterized with dominant drag force and reduced lift force. It is apparent that C = 0.03m blade would loss lift and gain an increased in drag with the attendant effects of lowered CP of the VAWT. Contrary to the flow field around C = 0.03m blade, the blade of C = 0.04m is stalled with the LEV seen attached to the inner surface of the blade while the TEV is in the formation stage. At this stage, the blade experiences a sudden increase in lift force, though for a very brief period, until the start of detachment of the LEV and TEV from the blade's surface with abrupt reduction in lift (see chapter six).

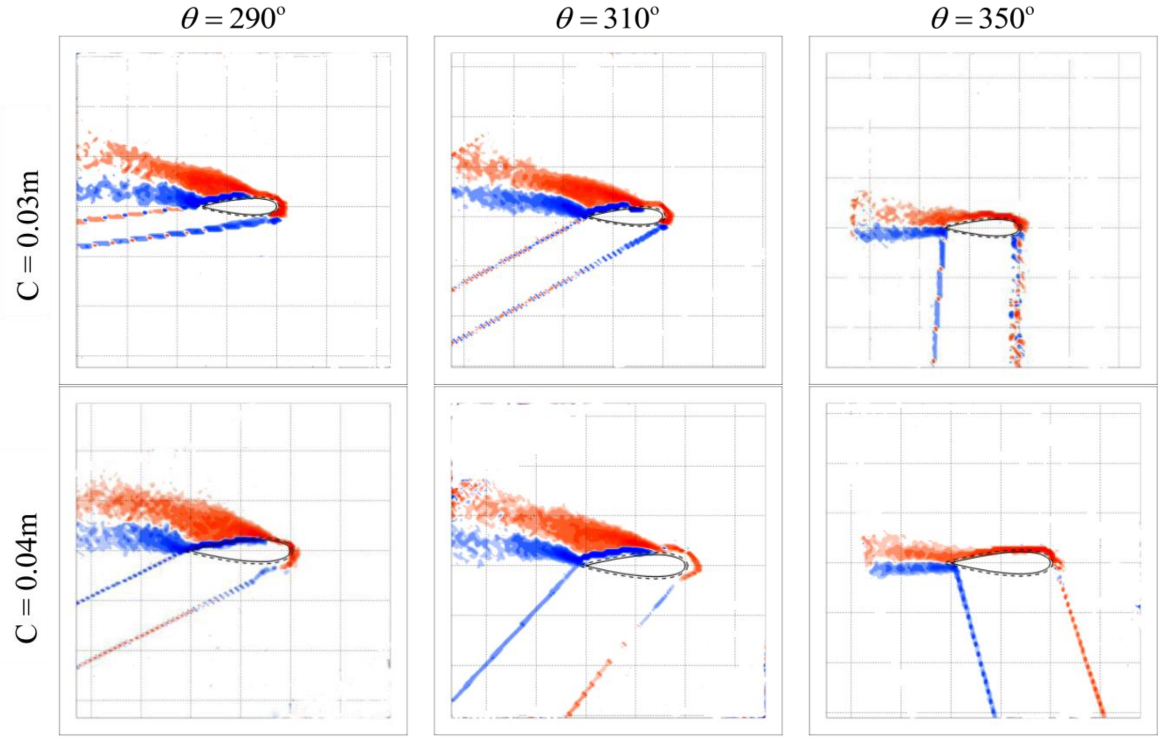

Figure 5.25. The Z-vorticity flow fields of PIV measurements of two chords at Re = 42,500 and different azimuth positions in the downwind section, $\lambda = 2.5$.

These differences in the flow field continued and also some observed similarities at various other azimuth angles detailed in Table 5.8. Figure 5.25 compares z-vorticity for the downwind section of the rotation. It is seen that the flow field for the two blades bear some similarities as there are no significant differences except for the lager vortex structures of the blade of C = 0.04m. It is also observed that the LEV and TEV of the two blades are detached from the blade's surfaces and a pair of vortex is being shed at $\theta = 290^o$. The two blades are in the post-stall stage where drag force is dominant. At $\theta = 310^o$, reattachment of the LEV on the two blade's surface had progressed significantly and the flow fields are seen attached at $\theta = 350^o$.

It is shown in Figures 5.24 and 5.25 and Table 5.8 that the performance of the two VAWT configuration at $\lambda = 2.5$ is strongly influenced by the flow fields around the blades that is why the performance are the same despite the differences in the solidities. The blade with C = 0.03m stalled at a lower (before $\theta = 70^o$) azimuth angle and also the LEV and TEV are detached completely from the blade's surface in the first half of the upwind section rotation.

The vorticity being fully developed due to the early stalling of the blade before $\theta = 70^o$ led to early shedding of pairs of vortices which is seen at $\theta = 140^o$. Whereas, the blade with C = 0.04m stalled at a higher azimuth angle (after $\theta = 80^o$) and the flow detachment is seen after $\theta = 90^o$. The shedding of a pair of vortices was virtually suppressed until around $\theta = 170^o$ when reattachment of the LEV to the blade's surface has advanced considerably because the dynamic stall process started quite late. The flow features are seen with close similarities towards the end of the rotation in the downwind part. The available energy content in the wind for the C = 0.03m VAWT is higher than the available energy content for the C = 0.04m VAWT hence the impact of the predominant dynamic stall experienced by the smaller blade was undermined resulting in the two VAWT configurations attaining similar performance. This explains the similarities in the power coefficients attained by the two configurations at $\lambda = 2.5$.

Azimuth	C = 0.03m (σ = 0.26) , V = 8m/s	C = 0.04m (σ = 0.34), V = 6m/s
$\theta = 50^{o}$	The flow is attached to the blade's surface	The flow is attached to the blade's surface.
$\theta = 60^{o}$	Development of the LEV separation bubble is seen on the suction side of the aerofoil	The flow is still attached to the blade's surface.
$\theta = 70^{o}$	The blade is stalled with the LEV being pushed away from the blade surface by the rolling up of the TEV.	The blade is in the pre-stall stage. Although the formation of the LEV separation bubble is seen on the suction side of the blade's surface.
$\theta = 80^{o}$	The blade is stalled. The flow is separated from the blade's surface and pairs of vortices are being shed.	The blade is stalled but the LEV is attached to the blade's surface and the TEV formation is also seen at its early stage of formation.
$\theta = 90^{o}$	The flow separation and shedding of pairs of vortices continued.	The blade is in the post stall stage, with the LEV completely pushed away from the blade surface by the roll up of the TEV.
$\theta = 130^{o}$	The flow separation and shedding of pairs of vortices continued.	The flow is fully detached from the blade surface and shedding of pairs of vortices is observed to have started.
$\theta = 140^{o}$	The flow is separated and shedding of vortices is seen.	The flow is separated from the blade's surface and shedding of pairs of vortices continued. The onset of flow reattachment is also observed.
$\theta = 170^{o}$	The flow reattachment has advanced considerably with pairs of vortices is still being	Like the C = 0.03m, the flow reattachment has advanced significantly and the shed vortices is regular in .
$\theta = 180^{o}$	Delayed reattachment.	Reattachment is delayed as also observed in C = 0.03m
$\theta = 190^{o}$	Reattachment is significantly delayed. The LEV is formed on the top of the aerofoil while the TEV is formed at the bottom of the aerofoil based on the swoop of the suction and pressure surfaces.	Similar to C = 0.03m the flow reattachment is significantly delayed. The LEV is formed on the top of the aerofoil while the TEV is also seen to have formed at the bottom of the aerofoil based on the swoop of the suction and pressure surfaces.
$\theta = 240^{o}$	The blade is seen to be post-stalled with the LEV completely detached from the blade's surface because of the roll up and increase in size of the TEV.	The blade is post-stalled as in C = 0.03m but the roll up of the TEV has been completed and both the LEV and TEV fully detach from the blade surface also irregular of vortex is being shed.
$\theta = 260^{o}$	The flow is separated from the blade surface; the LEV is seen being shed.	The flow is also separated from the blade surface with the LEV being shed.
$\theta = 270^{o}$	The flow separation from the blade's surface continued and shedding of a pair of vortices continues	The flow is still separated and shedding of a pair of vortices continues
$\theta = 290^{o}$	The flow separation from the blade's surface and shedding of a pair of vortex continued, also the onset of flow reattachment is observed.	Like in C = 0.03m, the flow separation from the blade's surface and shedding of a pair of vortices continued, and also the onset of flow reattachment
$\theta = 360^{o}$	The flow field is completely attached to the blade's surface.	Also the blade is completely attached to the blade's surface.

Table 5.8 Differences and similarities in flow fields aerodynamics of the two VAWT configurations at λ = 2.5 and Re = 42,000.

5.5.2 Description of Power Coefficients and Flow Fields at λ = 3

Figure 5.23 shows the CP of the two VAWT configurations at λ = 3 in the negative region. The VAWT with the larger chord attained a CP = -0.0869 while the VAWT with the smaller chord attained a CP = -0.14. The differences in the CP between the two VAWTs at this λ is around 61% in favour of the VAWT with C = 0.04m. The CP - λ curve of the C = 0.04m is moving upward towards the positive performance region from λ = 3, while that of the VAWT with C = 0.03m has the curve at its foot, although, away from this λ, it is also moving towards higher CP values. To understand the reasons behind the differences in the performance between the two VAWT configurations, the flow field visualization and PIV measurements obtained at λ = 3 are again used for further investigation. Figure 5.26 compares z – vorticity flow fields of the two VAWTs blades at the similar azimuth positions in the upwind section of the rotation.

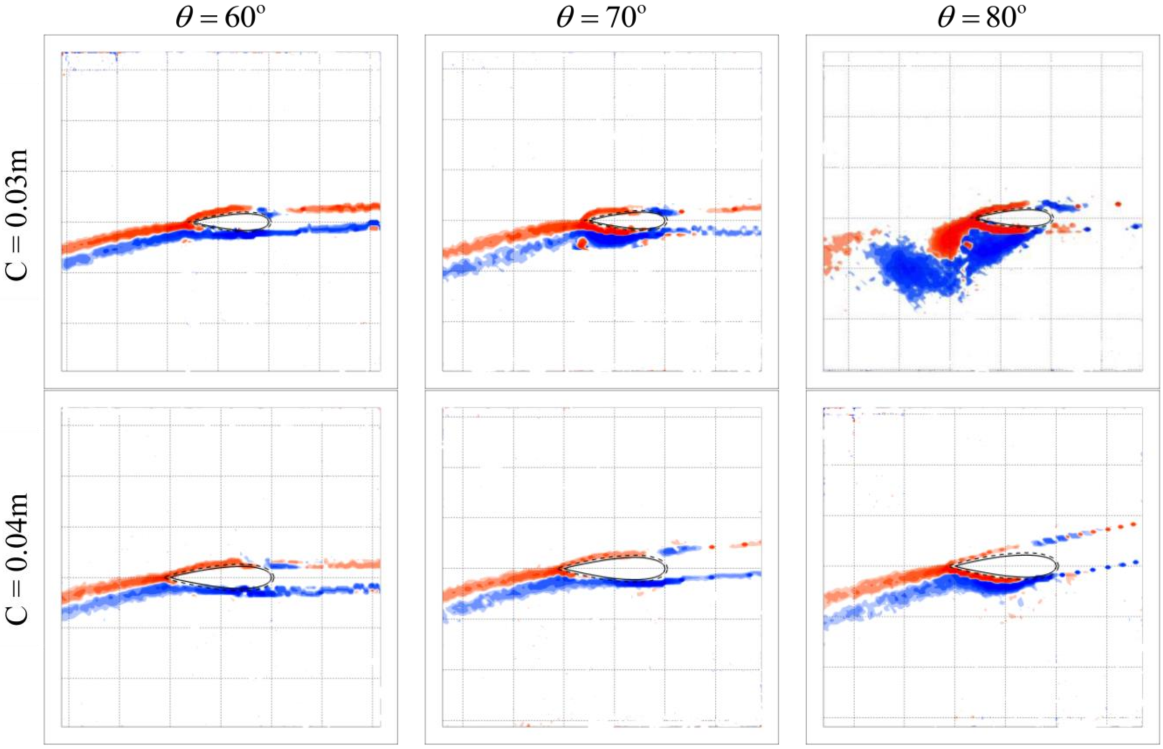

Figure 5.26. Z-vorticity flow fields of PIV measurements of two chords at Re = 50,400 and different azimuth positions in the upwind section, λ = 3.

At $\lambda = 60^{o}$ the flow around the two blades is fully attached to the blade surface. this means that C = 0.03m and C = 0.04m are in the pre-stall stage of the dynamic stall cycle and also that the lift force is dominant (see chapter six). The start of dynamic stall is observed by the formation of the separation bubble on the inner side of the VAWT with C = 0.03m at $\theta = 70^{o}$, whereas the flow field around C = 0.04m is still fully attached to the blade's surface.

At $\theta = 80^{o}$, the LEV has developed and it is seen being pushed away from the blade's surface by the roll up of the TEV whose formation has advanced for the C = 0.03m. Obviously the blade is deep stalled, and the resultant sudden lift gained would drop to lower values. In contrast to the vorticity flow field around C = 0.03m, the flow field around C = 0.04m is seen attached to the blade's surface with the initiation of blade stall. Clearly, the two blades have a phase difference of more than 10 degrees, since they are operating at the same Re, the difference in the blade's chord, hence the solidity is solely responsible for the performance differences being observed. Detailed comparison of the vorticity flow fields around the two blades at other various blade's azimuth positions are presented in Table 5.9. Further away in the first half of the downwind section of the rotation, the flow features of the two blades are similar as observed in Figure 5.19. The flow fields are characterized by the detachment of the LEV and the TEV from the blade's surfaces, and also shedding of a pair vortices continued with the onset of flow field reattachment to the blade's surfaces at $\theta = 290^{o}$. The blades are in the post-stall stage of the dynamic stall cycle and usually at this stage, the drag force is dominant as a result there is reductions in the lift force. This negatively impact on the overall performance of the VAWTs. At $\theta = 310^{o}$ the LEV reattachment to the blade surface for the chords had advanced considerably and later on at $\theta = 350$ the flow fields are seen attached to the surface of the two blades. The performance and flow fields around the blades of the two VAWT configurations at $\lambda = 3$ are quite distinct although some similarities are observed in their flow fields at few blade's azimuth angles (Table 5.9).

Azimuth	C = 0.03m (σ = 0.26) , V = 8m/s	C = 0.04m (σ = 0.34), V = 6m/s
$\theta = 0^{o}$	The flow is fully attached to the blade's surface	The flow is also seen completely attached to the blade's surface as observed in C = 0.03m
$\theta = 60^{o}$	It is observed the flow is still attached to the blade's surface	The flow is still attached to the blade's surface.
$\theta = 70^{o}$	The formation of LEV separation bubbles is seen at the suction side of the blade's surface.	The flow is observed to be fully attached to the blade's surface.
$\theta = 80^{o}$	The blade is in the stall stages with the LEV being pushed away from the blade's surface by the roll up of the TEV.	Blade stalled is being initiated with the formation of LEV separation bubble at the suction side of the blade surface.
$\theta = 90^{o}$	The roll up of the TEV is complete and stretched out. The flow field is separated from the blade's surface and pairs of vortices are being shed.	The blade is stalled. The LEV is attached to the blade's surface and the TEV is also seen at its early stage of formation.
$\theta = 100^{o}$	Flow separation from the blade's surface and shedding of a pair of vortex continued.	The blade is in the stall stages with the LEV being pushed away from the blade surface by the roll up of the TEV.
$\theta = 120^{o}$	Flow separation from the blade's surface and shedding of a pair of vortices continued.	The first pair of the LEV and TEV formed has been detached and shed and the formation of the second pair of LEV and TEV has started. The shedding of pairs of vortices from the blade's surface continues.
$\theta = 140^{o}$	The flow is separated and shedding of a pair of vortices is seen. The onset of reattachment of the flow is also seen.	The flow is separated from the blade's surface and shedding of pair of vortex continued. The onset of flow field reattachment is also observed.
$\theta = 170^{o}$	The flow field reattachment has advanced considerably. Pairs of vortices are still being shed.	Like the C = 0.03m, the flow reattachment has advanced significantly and the shed vortices is continues.
$\theta = 180^{o}$	Delayed reattachment of the flow to the blade's surface is observed.	Reattachment of the flow to the blade's surface is delayed as also observed in C = 0.03m.
$\theta = 190^{o}$	The reattachment of the flow to the blade's surface is significantly delayed.	The reattachment of the flow is also observed to be delayed even after midway of the rotation.
$\theta = 230^{o}$	Not available.	The flow is attached. The LEV formed on the top side of the blade while the formation of the TEV is formed on the bottom side of the blade.
$\theta = 270^{o}$	Detached flow, from the blade's surface and shedding of the LEV is observed.	It is also observed that the flow is separated from the blade's surface, both the LEV and TEV is being shed.
$\theta = 290^{o}$	Detached flow, shedding of pairs of vortices and the onset of flow reattachment to the blade's surface is observed.	Separated flow, shedding of pairs of vortices and the onset of flow reattachment to the blade's surface is also seen.
$\theta = 310^{o}$	The flow reattachment to the blade's surface and shedding of pairs of vortices is observed.	The flow reattachment to the blade's surface continued with the pair of vortices shedding and also the onset of flow reattachment to the blade's surface.
$\theta = 350^{o}$	The flow is seen fully attached to the blade's surface.	It is also observed that the flow is fully attached to the blade's surface.

Table 5.9. Differences and similarities of flow fields aerodynamics of the two VAWT configurations at λ = 3 and Re = 50,400.

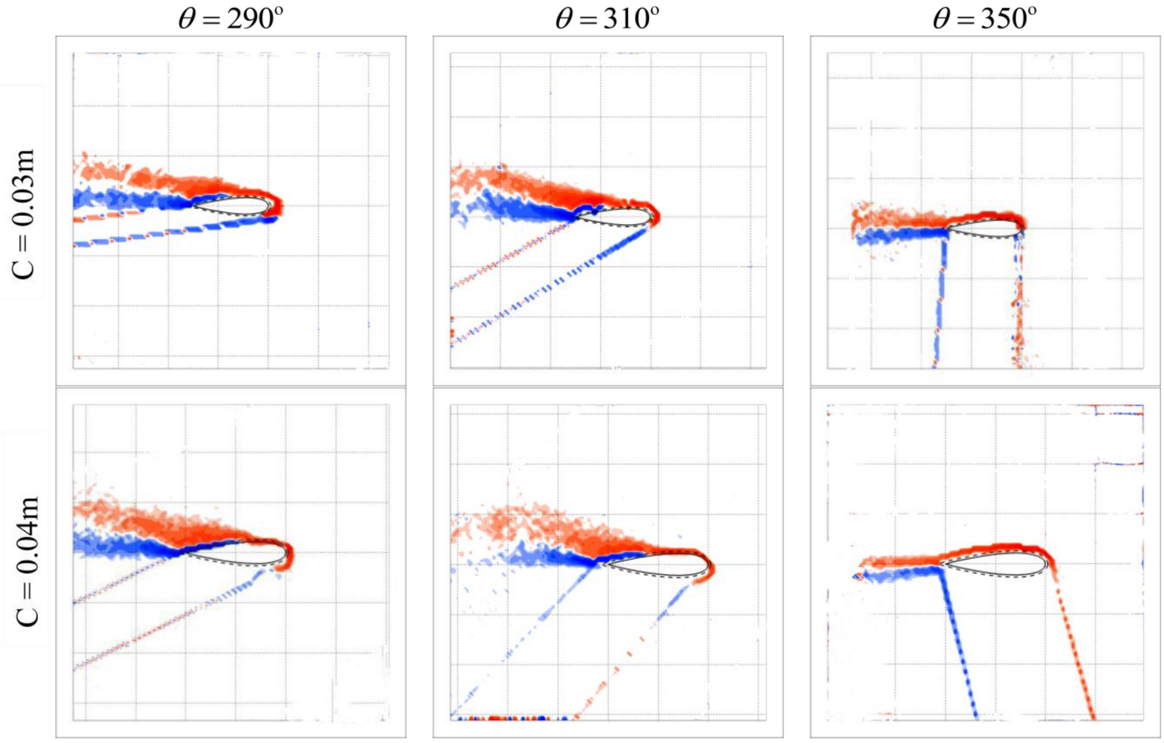

Figure 5.27. Z-vorticity plots of PIV images of two chords at Re = 50,400 and different azimuth positions in the downwind section, λ = 3.

It can be inferred from Figures 5.26 and 5.27 that the CP of the VAWT configurations is again swayed by the flow physics exhibited by the blades. The blade size and azimuth position also are seen to have influenced the development of the dynamic stall phenomenon. The dynamic stall process for C = 0.03m VAWT started around $\theta = 70^{\circ}$ and stalled before $\theta = 80$ whereas that of C = 0.04m VAWT started late, and even at $\theta = 100^{\circ}$ the LEV was still being pushed away from the blade's surface, this show a phase difference of around 20°. Consequently, the detachment of the flow fields from the blade's surface and shedding of pairs of vortices are delayed well into the second half of the upwind section of the rotation with the attendant effects of the lift force being sustained longer. This explains why the VAWT with C = 0.04m performed better in Figure 5.15 than that of C = 0.03m at λ = 3.

5.6 Comparison of Results with Literature

The power measurements of the VAWT compared well with the two previous experimental studies conducted at the university of Sheffield by Edwards [39] and Danao [55] and, also with the studies of Baker [13] and McIntosh [18]. These four studies observed a well-defined negative band at the lower λ region of the CP –λ curve. The Baker's studies focused on self-starting capabilities of VAWT and he showed that reasonable Reynolds numbers at the lower λ can improve performance while reducing the dead band and further recommended forward tilting of the blade relative to the axis of the VAWT as well as fixing the blade at a positive yaw to minimize the dead band, hence improved the self-starting capabilities of VAWT. McIntosh asserted that lower stall angle can increase the depth of the negative dead band especially for the low Reynolds' number aerofoils. All these agree well with the present study.

The flow visualization and PIV measurements of the flow field around the Darrieus rotor by Fujisawa and Takeuchi[92], at a lower Reynolds number, captured the dynamic stall phenomenon and also observed shedding of two pairs of vortices in one rotation of the blade. Simao-Fereira [100] showed the development of the LEV and subsequent shedding of LEV followed by shedding of TEV in the upwind section of the blade's rotation. These two studies are in agreement with the comparably improved results obtained from the flow visualization and PIV measurements of the two VAWTs' blades in this study. The author has also clearly shown the distinct dynamic stall phenomenon stages, (pre-stall, stall and post-stall) corresponding to the flow separation, detachment of the boundary layer, shedding of a pair of vortices both at the upwind and downwind sections of a blade's rotation which are to a very high degree in agreement with Edwards [39] and Danao [55] investigation's results. The difference being, this investigation was conducted at different wind speeds, with an additional rotor and smoothing was not applied to the processed PIV data. Kirk [14] in his thesis, studied the effects of varying Reynolds numbers on the dead band of a VAWT with momentum method over a wide range of Reynolds numbers. With decreases in the Reynolds numbers, He observed a deepening of the dead band and narrower peak power region of the CP – λ curve, hence lower CP. These were not only observed in this investigation, but it has been determined that the blade's azimuth position at which the dynamic stall process begins has influenced the overall performance of the VAWT. This also corroborates the Baker's [13] assertion that lower stall angle can induce negative dead bands in thinner aerofoil sections or at lower Reynolds numbers. The results of this investigation also corroborate Marini et al [101] findings that VAWT CP increases with increase in Reynolds numbers, although he tested a cylindrical VAWT at a higher Reynolds number, the principle of operation is similar so these results can be compared. Migliore's [32] experimental investigation into the flow curvature effects on the Darrieus turbine blade aerodynamics opined that premature blade stall can impact negatively on turbine efficiency and power extraction, this also concurs well with the results obtained in this investigation. As shown, a too early start of blade stall in the rotation cycle has reduced VAWT overall performance at all the lower λ tested in this study.

5.7 Summary

The major contributions this investigation has revealed with the use of the "spin down" method and, the flow field visualization and PIV measurement technique, are summarized as follows:

- The performance of vertical axis wind turbines is λ and Reynolds numbers dependent especially when the wind machines operate at low or at a transition range of Reynolds numbers. At lower Reynolds numbers a negative performance region is seen at the lower λ. This hinders the self-starting capability of the VAWT. This negative dead band is observed in the CP - λ curves of the two VAWTs with the C = 0.03m (σ =0.26) having shown wider negative band resulting from the effects of chord size and solidity. This negative band is seen to decrease in both cases as the wind speed is increased from 5m/s to 9m/s.

- Blade chord has shown significant impact on the performance of the two VAWT configurations. Decreases in the blade chord initiate a wider negative band, hence a reduction in lift and power extraction. An increase in the blade chord causes the narrowing of the negative band. At the positive performance region, increased blade chord reduces the peak power region while decreased blade chord increase the peak power region of the curve. At 8m/s wind speed the VAWT with C = 0.04m(σ = 0.34) attained a maximum CP = 0.326 while C = 0.03m (σ = 0.26) attained a maximum CP = 0.146 .
- The onset of the blade stall, a detachment of flow from the blade's surface, shedding of a pair of the vortices, and reattachment of flow to the blade's surface have been shown to be highly dependent on λ, the blade chord and Reynolds numbers. For 6m/s wind speed the C = 0.03m blade stalled at $\theta = 60^o$ for $\lambda = 2.5$, at $\theta = 70^o$ for $\lambda = 3$ and at $\theta = 90^o$ for $\lambda = 4$ while the C = 0.04m (σ = 0.34) blade stalled at $\theta = 80^o$, at $\theta = 90^o$ and at $\theta = 130^o$ at the corresponding λ. This show that for the smaller blade chord and lower λ the stall process is earlier than for the bigger blade chord and higher λ.
- It has been shown that the performance of the two VAWTs with different blade chords when compared at the same wind speed and λ, is influenced by Reynolds numbers resulting from the blade chords and also the azimuth position the stall processes of the two blades are initiated. Early stall is seen to be associated with small blades so cannot sustain lift long enough on the blade surface which can lead to lower CP. Whereas the bigger chord experienced late stall which provided an advantage of increases in, and sustained lift with the attendant increases in CP. When the two VAWT configurations were compared at different and the same Reynolds numbers, the blade chord (solidity) and the dynamic stall process determined the performance of the VAWTs. In both cases, the C = 0.04m (σ = 0.34) attained the better performance in the positive performance regions of the CP – λ curves compared.

Chapter 6

Computational Fluid Dynamics Results

6.1 Introduction

The computational fluid dynamics investigations into the influence of blade chord and Reynolds number on the performance of a VAWT are presented and discussed in this chapter. First, the variation of the power coefficient versus the tip speed ratio at three wind speeds at which simulations were conducted is presented for the two VAWT configurations under investigation. Second, the variation of angle of attack and relative velocity in relation to the three tip speed ratios are presented and explained. Thereafter, the influence of changes in tip speed ratios on the force and flow physics on the two VAWT configurations are examined in great details at λ = 2.5, 3 and 4 at the relevant wind speeds.

Third, the performance of the two VAWT configurations is compared at the different and the same Reynolds numbers, based on their force, non-dimensional coefficients of lift and drag, and also the flow physics at the corresponding λ. Lastly, a comparison of some of the revelations with relevant literature is discussed before a summary of the major revelations and contributions to knowledge is presented and explained.

6.2 Blade Chord = 0.03m (σ = 0.26)

The plots of CP_{cfd} versus λ of three wind speeds for the VAWT with C = 0.03m is presented in Figure 6.1. The CP_{cfd} - λ curves vary considerably with changes in wind speed in a similar manner seen in the experimental results (Figure 5.1) except for the higher power coefficients attained. The high performance is due to the 2D CFD model results being compared to a 3D experimental data which differences are already explained in chapter 4. A negative CP band that spanned between λ = 1.5 and λ = 3.2 is seen for all the wind speeds, and the negative band increases with decreases in the wind speed since the VAWT's performance is Reynolds numbers dependent.

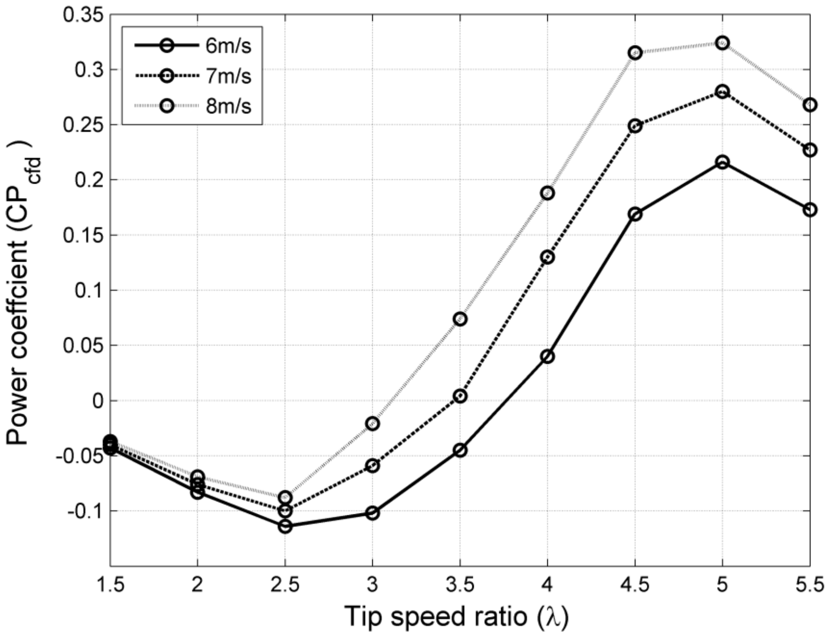

Figure 6.1.Compares CPcfd versus λ of three wind speeds for C = 0.03.

The VAWT attained a maximum CP_{cfd} = 3.25 at $\lambda = 5$, at the highest tested wind speed of 8m/s, and a minimum CP_{cfd} = -0.12 at $\lambda = 2.5$ at the lowest tested wind speed of 6m/s. For a particular wind speed, the performance of the VAWT is also seen to vary with changes in λ. The reasons behind the variations will be discussed in the subsequent sections of this chapter.

6.3 Blade Chord = 0.04m (σ = 0.34)

Figure 6.2 presents the plots of CP_{cfd} versus λ of the three wind speeds for the second VAWT with C = 0.04m and σ = 0.34. Although the CP_{cfd} - λ curves also vary considerably with changes in wind speed in a similar manner observed with the C = 0.03m (σ =0.26) VAWT, a higher CP_{cfd} is attained at all the tip speed ratios at the comparable wind speeds. Also, a narrower negative band is seen and maximum CP_{cfd} are attained at lower λ while the curves drop off earlier.

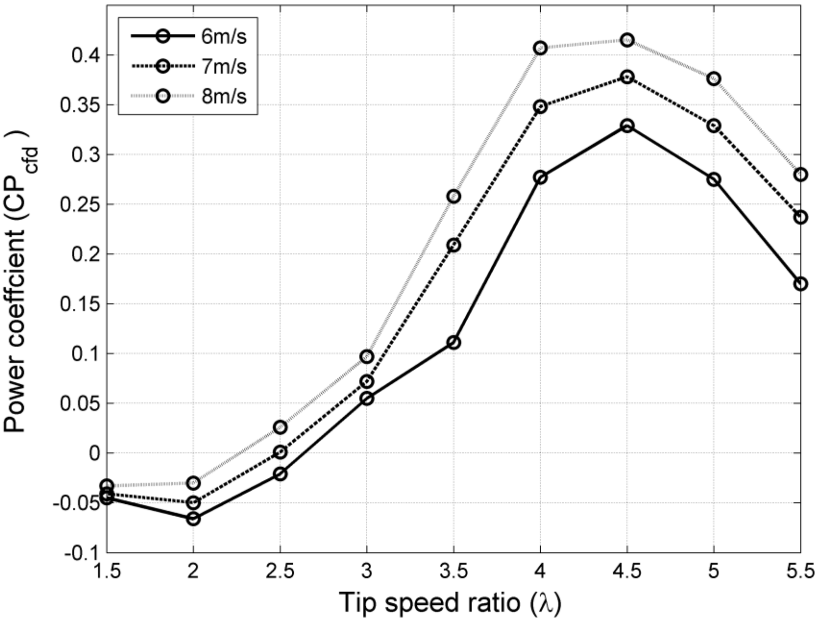

Figure 6.2. Compares CPcfd versus λ of three wind speeds for C = 0.04.

These differences are investigated later in sections 6.5 and 6.6 in this chapter. The negative CP band spanned between λ = 1.5 and λ = 2.6 for all the wind speed, and also increases with decreases in the wind speed. The VAWT attained a peak

CP_{cfd} = 4.12 at the λ = 4.5 at the highest wind speed of 8m/s and also attained a minimum CP_{cfd} = -0.65 at λ = 2 also at the lowest wind speed of 6m/s. For a particular wind speed, the performance of the VAWT is also seen to vary with changes in λ due to the resulting changes in Reynolds numbers, angle of attack and relative velocity.

6.4 Angle of Attack and Relative Velocity

The aerodynamics and performance of the VAWT can be seen to highly depend on the tip speed ratio. The tip speed ratios influence the VAWT performance and aerodynamics by determining the angle of attack and the relative velocity of the air onto the VAWT blades. At a high tip speed ratio, based on geometrical angle considerations, the maximum value of angle of attack attained is low at the upwind section of the rotation and increases correspondingly with decreases in the tip speed ratio (Figure 3 (a)). This variation reverses at the downwind section of the rotation. The α = 0 at the start, midway and also at the end of the rotation is due to the inclination of the blade relative to the wind stream.

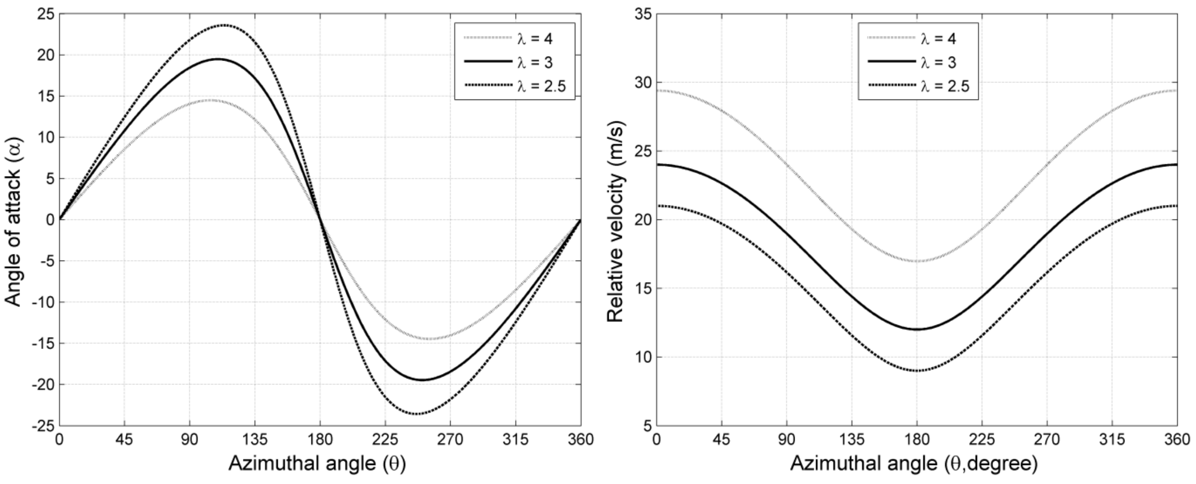

a. b.

Figure 6.3. Compares the influence of the tip speed ratio on VAWT aerodynamics, a) angle of attack versus azimuth angle, b) relative velocity versus azimuth angle.

Away from the start point and depending on the λ, the α increases until it reached a maximum between $\theta = 100^o$ and 135^o in the second half of the upwind section of the rotation and drop to zero at $\theta = 180^o$ and lower negative values in the downwind section. The decreased continued until a minimum is attained and thereafter increased to zero at $\theta = 360^o$. The relative velocity increased with increases in the tip speed ratios at both sections of the rotation (Figure 3 (b)). These variations of angle of attack, relative velocity versus azimuth angle for the three tip speed ratios under investigation can impact positively or negatively on the forces and blade stall of a VAWT.

6.5 Influence of λ on Force and Flow Physics

Earlier in chapter five, the power coefficient of VAWT has been shown to depend on the dynamic stall phenomenon and also the dynamic stall pattern has equally been shown to depend on λ. In this following sections the influence of λ on the forces and flow physics is being examined in greater details to complement the discussions presented in chapter five since data on blade forces were not measured in the experiment campaign.

6.5.1 Blade Chord = 0.03m ($\sigma = 0.26$) at 6m/s

The CFD flow features having closely matched with the PIV measurements and visualizations, with observed similar features in the onset of LEV and TEV development, vortex shedding, onset and flow fields' reattachment to the blade's surface. It is possible with the results from CFD to determine how changes in λ can affect the forces and flow physics of a VAWT. At $\lambda = 2.5$, the blade stalled at $\theta = 60^o$ and is accompanied with a loss of about 35% in T_{lift} between the stalled azimuth angle and $\theta = 50^o$ (onset of stall azimuth angle) where the blade attained the highest T_{lift} (Figure 3 (a)) in the upwind section of the rotation. A drop in the T_B is seen at the corresponding azimuth angle whereas only about 2.34% increase in the T_{drag} was gained. Beyond $\theta = 60^o$ there is a decrease in the T_{lift}, while increases are seen in both the T_{drag} and the T_B until $\theta = 180^o$ where an approximate zero value is attained by the torques. This may be due to flow field separation, shedding of pair of vortices which the flow did not recover from before reattachment of the flow field to the blade's surface.

Further away from θ = 180°, with the flow fields almost reattached to the blade's surface, the T_{lift} rises until around θ = 225° signifying recovery from the effects of dynamic stall in the upwind section of the flow. Correspondingly, there is a low trough in the T_{drag} which cancelled out the impact of the T_{lift} increases, and due to the overpowering effects of the T_{drag}, a minimum T_B = -0.34Nm is attained at θ = 225°. Beyond θ = 225°, ripples are seen in the curves indicating a pitching-type motion due to the shedding of vortices by the blade after being stalled again in the downwind section of the rotation. With the combined effects of the blade interaction with its own shed vortices at the upwind section and the wake of the centre shaft, the pitching type motion continued until θ = 315° resulting in the dominance of drag. Due to the overpowering effects of drag, the blade T_B is seen in the negative region in most parts of the downwind section of the flow.

The torque curve of the blade at λ = 2.5 (Figure 3 (a)) is different from the torque curves at λ = 3 (Figure 4 (b)) not only in the obvious dissimilarities in the maximum and minimum values attained by the blade in both sections of the rotation but also in the frequency and size of the oscillation seen in the comparable curves. At the λ = 3 the blade attained a maximum T_{lift} = 1.18Nm at around θ = 65° before it stalled at θ = 80°, also with a loss of about 50% in the T_{lift}. Decreases are also seen in the T_{drag} and T_B between these azimuth positions. Beyond the stalled azimuth angle, due to flow field separation, vortices shed, and with the blade's trailing edge beginning to be more tangentially aligned into the wind stream with reductions in α as θ approaches 180°, the decreases in the T_{lift} continued while the T_{drag} increases. Again, due to the dominance of T_{drag}, at θ = 180°, -0.002Nm torque is attained by T_B and T_{drag} irrespective of the torque attained by the T_{lift}.

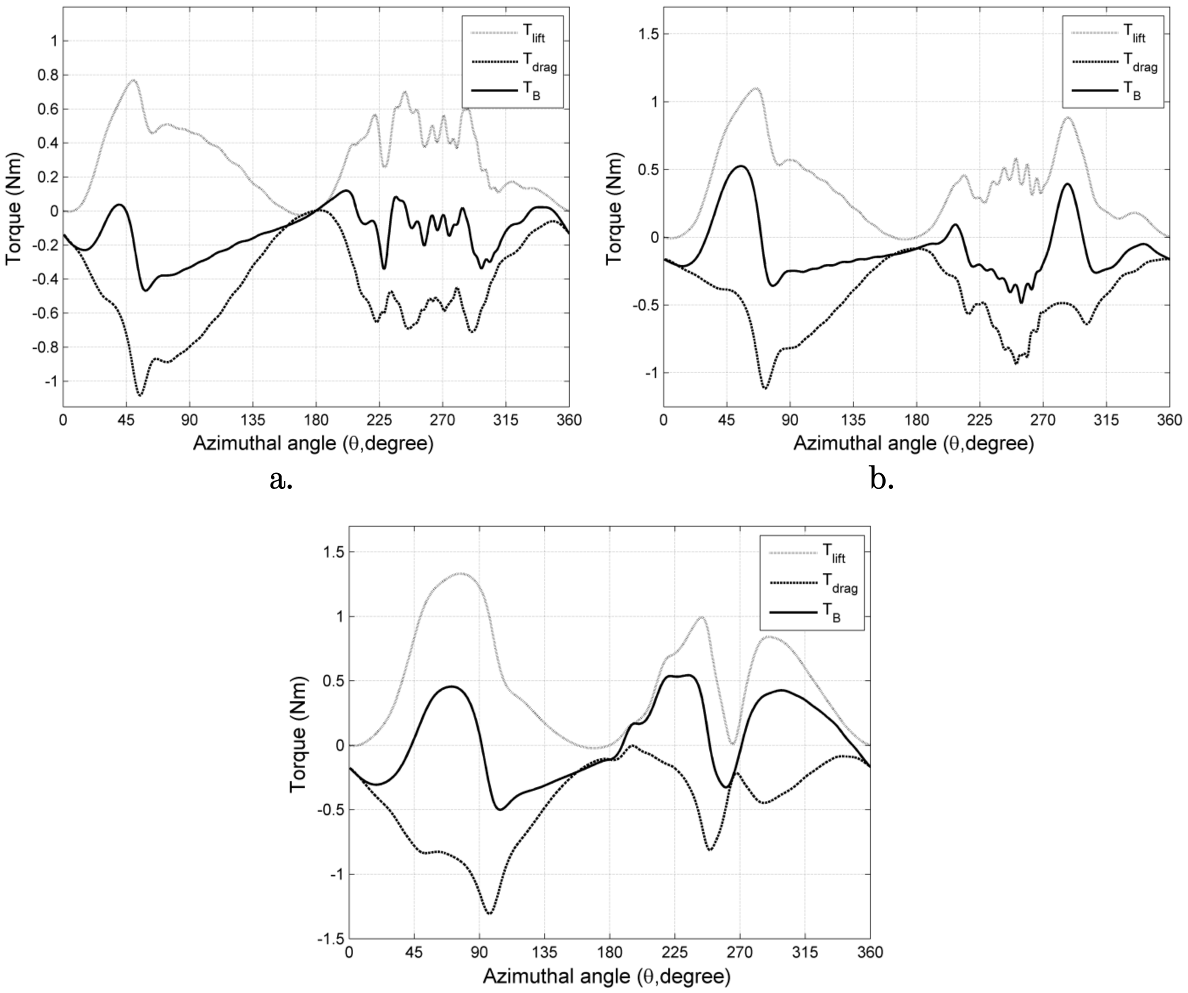

a.

b.

c.

Figure 6.4. Torques versus azimuthal angle for C = 0.03 at 6m/s, a) $\lambda = 2.5$, b) $\lambda = 3$, c) $\lambda = 4$.

At $\theta = 190^o$ and beyond (although the α is negative) the LE of the blade is inclined into the wind stream, and with the flow fields attached to the blade surface and increases in the relative velocity, T_{lift} and T_B increases, while T_{drag} drop to lower value is unable to cancel out the increases recorded by T_{lift} indicating the dominance of T_{lift} in this part of the rotation which stayed briefly until around $\theta = 220^o$ where the blade stalled again. Beyond this azimuth angle, the flow around the blade oscillates at higher frequency but with smaller amplitudes compared to $\lambda = 2.5$ in Figure 6.4 (a) which is due to the higher blade relative velocity and lower α that tend to induce less "periodic" shedding of vortices. While the T_{lift} oscillates within a median of 0.04Nm there is a reduction in the T_{drag} and T_B suggesting the dominance of drag until around $\theta =$

270^{o} where the blade is perpendicularly aligned to the wind stream and also, the flow is recovering from the effects of dynamic stall, interaction with upwind shed vortices and wake of the centre support.

Further away from $\theta = 270^{o}$, although the α is still negative (Figure 6.4 (a)), it begins to increase so the LE of the blade is more inclined towards the wind stream. Coupled with a reduction in the rate at which vortices are shed from the blade's surface and also increases in the relative velocity, the flow is seen to recover well from the pitching-type motion. The blade thereafter attained peak T_{lift} = 0.88Nm and T_{drag} = -0.49NM which result in a peak T_B = 0.39NM at $\theta = 290^{o}$ in the downwind section of the rotation. Beyond $\theta = 290^{o}$ the T_{lift} and T_B drop off rapidly until near zero torque is attained at $\theta = 360^{o}$. The performance of the VAWT at λ = 3 is much improved compared to that of λ = 2.5 due to the lower angle of attack and higher relative velocity at λ = 3 hence, the lesser effects of dynamic stall.

The λ = 4 case (Figure 6.4 (c)) is very different from the previous two cases (Figure 6.4 (a & b)) discussed earlier. The differences are not only the highest T_{lift} and lowest T_{drag} attained in the upwind section of the rotation, and the blade being stalled at a higher azimuth angle of $\theta = 110^{o}$. But also the peak region of the T_{lift} and T_B curves are wider, and the curves are smooth with no oscillations even at the regions ($\theta = 225 - 315^{o}$) where oscillation is very noticeable in the other two cases. These differences can be due to the low α in the upwind section of the rotation (Figure 6.4 (a)) and also the higher blade speed which is directly proportional to the relative velocity and Reynolds number. A lower α can limit the blade within or below the static stall angle hence delaying and suppressing the development of the vortex and the subsequent shedding of vortices. The observed wide T_{lift} peak region and delayed blade stalled until $\theta = 110^{o}$ suggests suppressed shedding of vortices with the attendant effects of the T_{lift} been sustained longer, so the flow recovered quickly from the effects of flow fields separation from the blade's surface and from the brief periods of vortices shedding.

With the best recovery from stall effects and the dominance of lift seen at this λ, a maximum T_{lift} = 0.99Nm and a higher T_{drag} = -0.60Nm is attained in the downwind section of the rotation resulting in a maximum T_B = 0.54Nm. The blade stalled again around θ = 260° and also interacts with the wake of the centre support shaft. It quickly recovered from the stall effects again, and with increased T_{drag}, the dominance of lift continued. Beyond θ = 300°, drop off is seen in the T_{lift} due to α approaching zero. Overall, the lift is more dominant than the drag at the λ = 4 and also of the three λ compared.

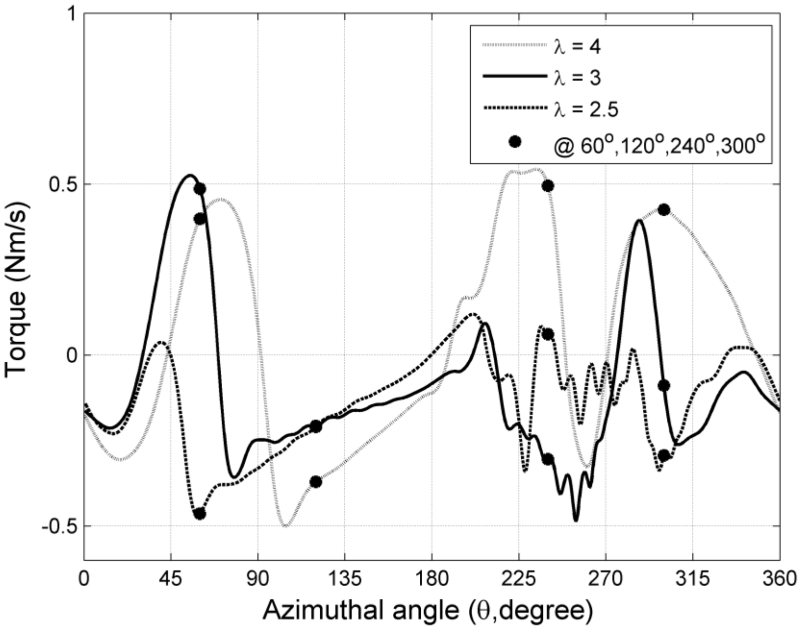

Figure 6.5. Compares torque versus azimuth angle for three λ at 6m/s, C = 0.03.

The T_B of the three λ is compared in Figure 6.5 to clearly ascertain how changes in λ can affect the forces and the aerodynamics of a VAWT. The markers on the curves are the selected azimuth positions at which the flow physics of the blades are also compared. In the upwind section of the rotation, the blade attained an average T_B = -0.198Nm at λ = 2.5, an average T_B = -0.074Nm at λ = 3 and an average T_B = -0.111Nm at λ = 4. It can be seen that despite the superior maximum T_{lift} = 1.33Nm attained at λ = 4 in the upwind section of the rotation (Figure 6.4(c)), its T_B average is lower than that of λ = 3 due to the low

T_{drag} recorded, and the performance at λ = 2.5 is lowest of the three λ due to the very low $T_{drag,}$ so the flow is drag driven at λ = 2.5 (Figure 6.4 (a)). This suggests that drag can impact on the overall performance of VAWTs since T_B is the sum of the T_{lift} and T_{drag}.

The flow fields (Figure 6.6) at the marked azimuth positions in Figure 6.5 can be seen to conform to the observed differences in the torque curves of the three λ indicating that, the noticeable differences in the torques have been influenced by how the blade interacts with the wind stream at the various λ. At $\theta = 60^o$, the blade is stalled at λ = 2.5 and the carry over effects of reduction in the T_{lift} and increase in T_{drag} caused the blade to attain a minimum T_B = -0.46Nm at λ = 2.5 in the upwind section of the rotation. The dynamic stall process has just commenced with the LEV being formed on the blade surface with a corresponding reduction in T_B at λ = 3, while the flow fields at λ = 4 is still attached to the blade's surface hence steady increase in T_B is sustained longer than at λ = 2.5 and λ = 3, until the dynamic stall process begins at this λ = 4.

At $\theta = 120^o$ the flow structures of the blade at λ = 2.5 and at λ = 3 show close similarities but the flow at λ = 4 is different although, the flow is seen separated from the blade surface at the three λ. The close similarities in the flow structures at λ = 2.5 and at λ = 3 is also obvious in Figure 6.5 where a T_B = -0.20Nm is attained at λ = 2.5 and at λ = 3. The main difference being the flow separation and vortex shedding from the blade's surface being more advanced at λ = 2.5. While at λ = 4, the blade has just passed its stalled azimuth angle at $\theta = 110^o$ hence, less shedding of vortices. Beyond $\theta = 120^o$ the flow around the blade begins to recover from the dynamic stall effects with corresponding increases of T_B at all the λ, but rapidly gaining most at λ = 2.5 at the start of the downwind section of the rotation due to the early start of and recovery from the dynamic stall process at this tip speed ratio. At $\theta = 240^o$, the blade attained a higher T_B = 0.0621Nm at λ = 2.5 than the lower T_B = -0.30Nm at λ = 3 and highest T_B = 0.49Nm at λ = 4. Beyond $\theta = 240^o$, the flow oscillates at λ = 2.5 with more visible amplitudes than at λ = 3, while there are no ripples at λ = 4 due to larger occurrence of stall at the lower λ.

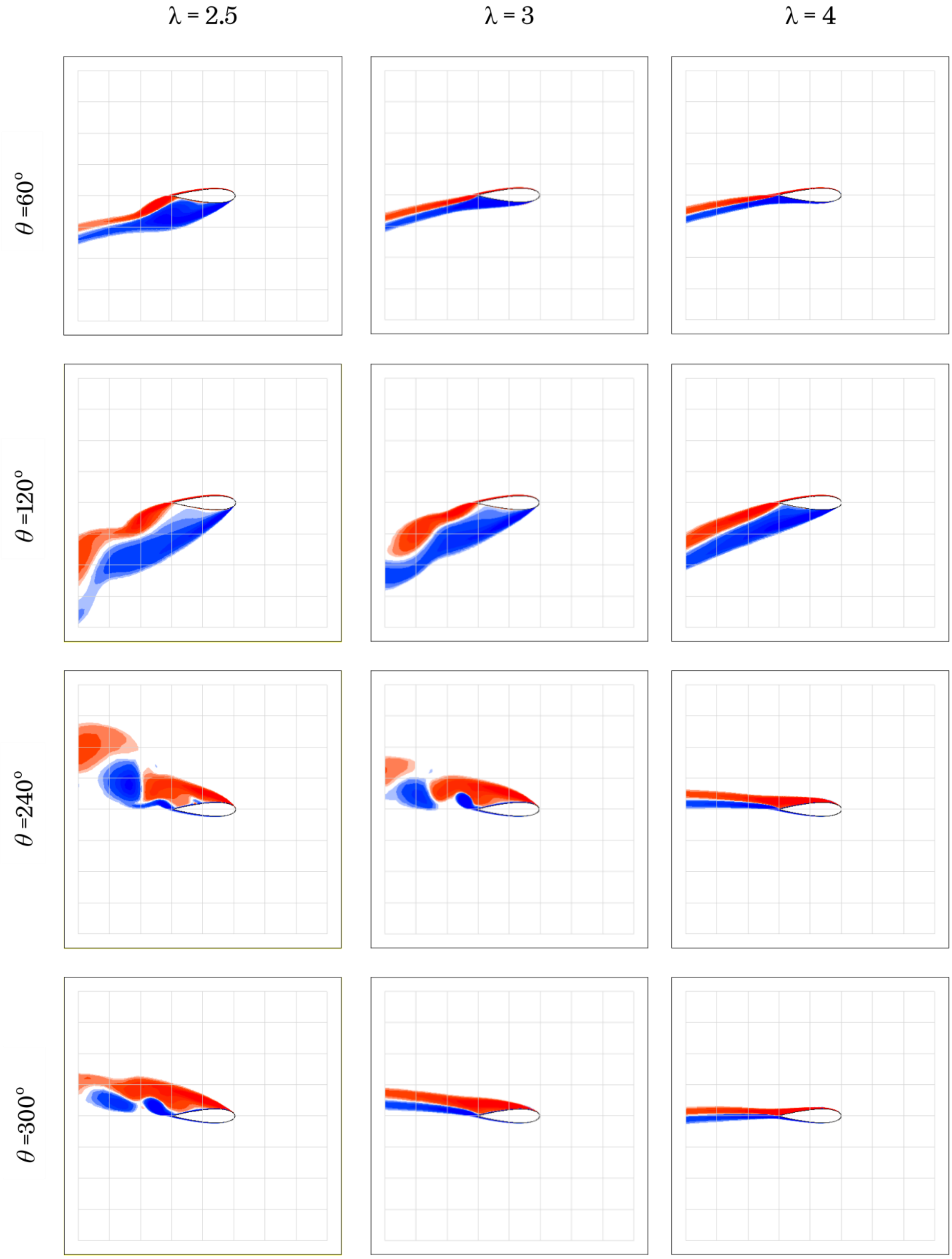

Figure 6.6. Compares CFD z-vorticity plots of three λ at 6m/s at four azimuth positions, C = 0.03m.

Again, these differences have been influenced by the flow physics at various λ of the blade in Figure 6.6. At λ = 2.5 and at λ = 3 the blade is engulfed in vigorous LEV and TEV shedding, while at λ = 4 the flow is attached to the blade's surface and since the dynamic stalling process was suppressed and delayed until θ = 110°, the dynamic stall process was very brief so the effects are minimal which can be advantageous in the quick recovery from the dynamic stall effects and also sustaining the gains. At θ = 300° there are distinct differences seen in the T_B at the three λ. At λ = 4 the blade attained a high T_B = 0.43Nm and a low T_B = -0.08Nm at λ = 3, while the lowest T_B = -0.293Nm is attained at λ = 2.5. The differences in the T_B at the three λ are influenced by the flow physics which is seen in the flow structures of the blades in the Figure 6.6. Flow separation from the blade surface and a pair of vortices are being shed at λ = 2.5 which can result in the reduction of lift while increasing drag, and the subsequent decrease in T_B which explains the low negative T_B attained by the blade at λ = 2.5. The onset of flow field reattachment to the blade surface and shedding of vortices are seen at λ = 3 so the reduction in T_B is due to the dynamic stall and also probable, due to the blade's LE inclination angle towards the wind stream. Despite the fully attached flow field to the blade's surface at λ = 4, the high T_B could not be sustained as a result of the angle of attack approaching zero.

The interaction of the blade with wind speed at the various λ resulted in the blade attaining an average T_B = -0.067Nm, T_B = -0.115Nm and T_B = 0.202Nm at λ = 2.5, λ = 3, and λ = 4 respectively in the downwind section of the rotation. The highest average T_B is attained at λ = 4 indicate high velocity induction so higher power was extracted due to the delayed stalled and quick recovery from dynamic stall effects, which, resulted in better overall average T_B = 0.045Nm hence, the low average torque attained in the upwind section is improved. The lowest average T_B in the downwind section at λ = 3 signify low velocity induction due to dynamic stall effects at the downwind section of the flow so the high average T_B attained at the upwind is undermined, hence a low overall T_B = -0.115Nm is attained. Whereas the flow at λ = 2.5 was drag dominated and the blade performed in the negative region in most parts of the rotation due to the greater occurrence of stall hence, lowest overall average T_B = -0.133Nm is attained.

6.5.2 Blade Chord = 0.03m (σ = 0.26) at 8m/s

The influence of λ on torque and flow physics of VAWT has been investigated at 6m/s in the previous section. To further the understanding of VAWT, this section seeks to examine the influence of λ on the torque and flow physics of the same VAWT but at a higher wind speed of 8m/s. In the preceding section, the direct dependence of T_B on the sum of T_{lift} and T_{drag} has been shown so emphasis will be focused on T_B at the various λ for the investigation in this section and in section 6.5.3 for brevity. So, Figures 6.7 and 6.10 are presented for comparison of trend with the other conditions.

The comparison of T_B at the three λ is presented in Figure 6.8. Unlike the C = 0.03m at 6m/s case, the T_B attained at all the λ for the C = 0.03m at 8m/s case is much improved and also in conformity with Figure 6.1, due to the differences in the wind speed, and consequently, the Reynolds numbers. The peak T_B attained by the blade at all λ and the corresponding angle is presented in Table 6.1, the differences are indicative of higher power extraction at λ = 4 and lower power extraction at λ = 3, and also early loss of lift at λ = 2.5, while lift is sustained longer at λ = 4 in the upwind section of the rotation. This is in conformity with the flow physics (Figure 6.9). At θ = 60°, the blade dynamic stall process had advanced beyond the formative stage at λ = 2.5 with a resultant drop in T_B until it stalled. The onset of stall is initiated at λ = 3 so the T_B is within its peak, while, the flow is still attached to the blade surface at λ = 4 hence, a steady increase in T_B is maintained until the peak is attained. Again, the flow structures of the blade at λ = 2.5 and at λ = 3 bear close similarities despite a large gap of T_B = 0.43Nm seen between the two λ, while the flow field at λ = 4 is very different at θ = 120°. The close similarities in the flow structures may be due to the pitching-type motion of the flow around the blade at the two λ which is indicative of the pattern of blade stalled and shedding of vortices. Obviously, distinct pairs of vortices with gap in between the preceding and the next pair of vortices can be seen at λ = 2.5 and at λ = 3 in Figure 6.9, with that at λ = 2.5 seem to be more advanced.

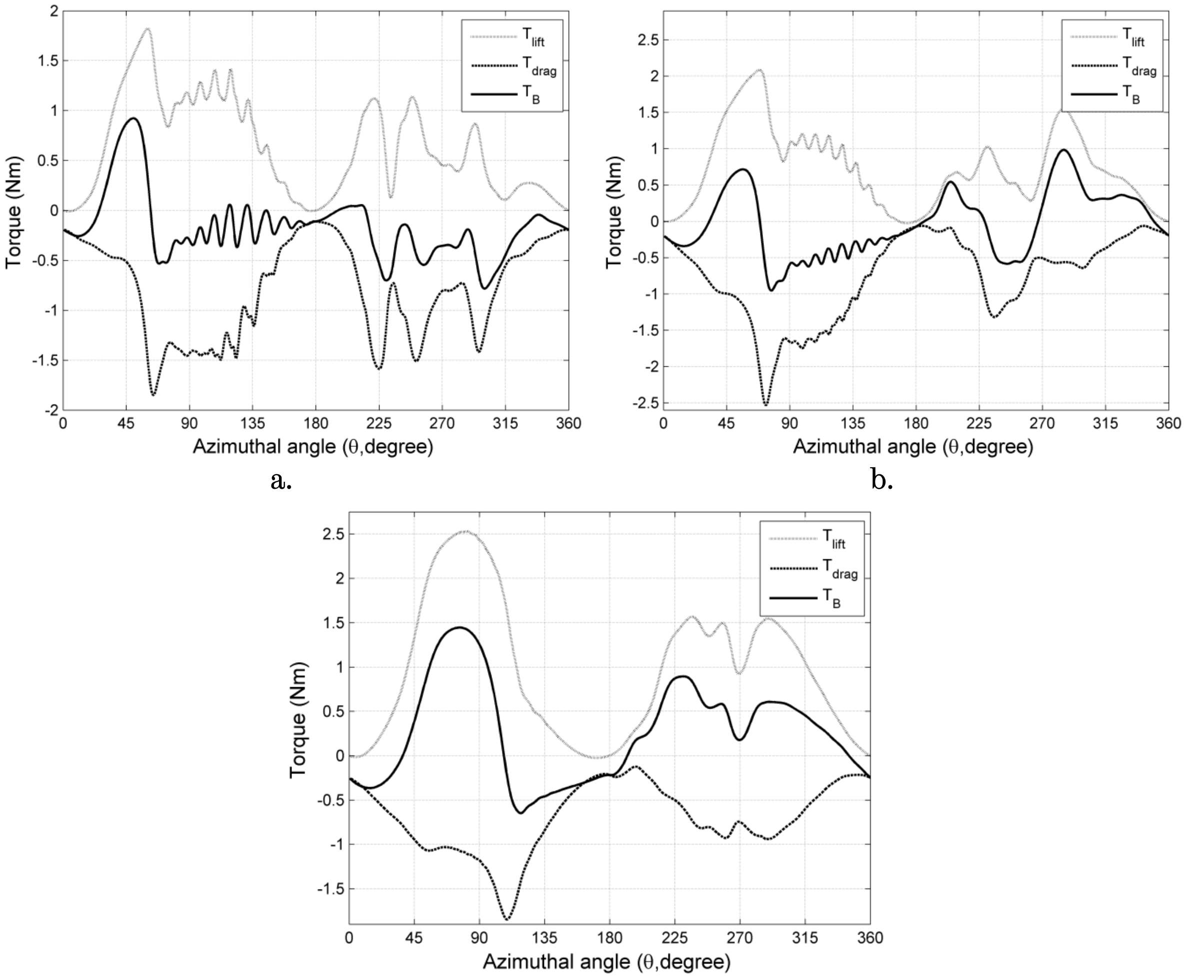

a. b.

Figure 6.7. Torque versus azimuth angle, C = 0.03m at 8m/s, a) λ = 2.5, b) λ = 3, c) λ = 4.

This pattern of vortex shedding can cause the very prevalent unsteadiness at the lower λ clearly seen as ripples on the curves at the two lower λ. While the blade is stalled at λ = 4, there are no ripples on the curve suggesting the delayed stalled can lead to less rigorous shedding of vortices. Based on the characteristic nature of the dynamic stall at the various λ, the blade attained an average T_B of – 0.04Nm, -0.22Nm, and 0.16Nm at λ = 2.5, 3 and 4 respectively in the upwind section of the rotation.

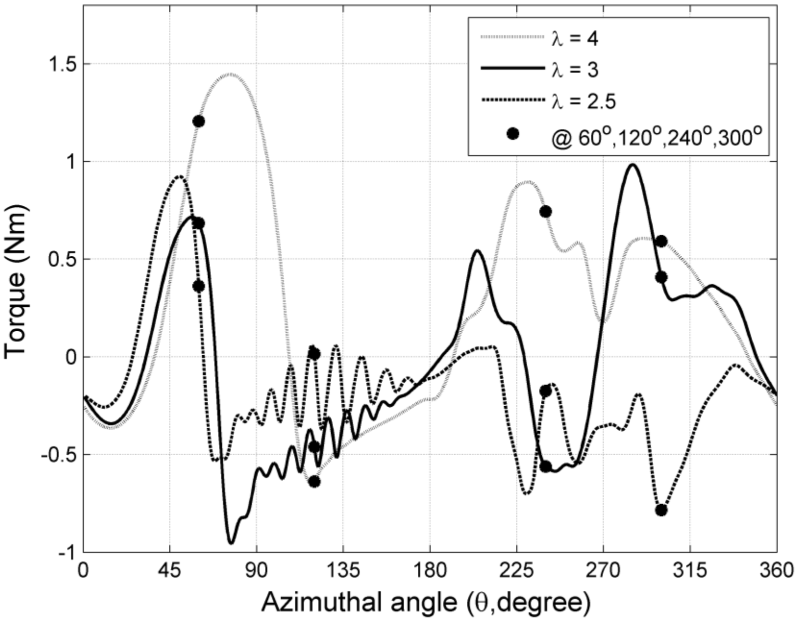

Figure 6.8. Compares torque versus azimuth angle, three λ at 8m/s, C = 0.03m.

λ	2.5	3	4
Peak T_B (Nm)	0.92	0.72	1.44
θ (degree)	50	56	77

Table 6.1. Peak torque of the λ, at 8m/s, C =0.03m.

At $\theta = 240^{\circ}$, the blade is engulfed in the shedding of distinct pairs of vortices at λ = 2.5. While only the vortex from the TE seem broken as vortices are shed by the blade at λ = 3, the flow fields though attached to the blade surface, an onset of dynamic stall can be seen on the initial formative stage at λ = 4 (Figure 6.9). Beyond this azimuth angle, ripples are seen on the λ = 2.5 curve (Figure 6.8) due to the greater occurrence of stall, the interaction of the blade with the vortices shed in the upwind section of the rotation and also with the wake of the central support shaft, hence, the fluid motion around the blade is very unsteady at this λ.

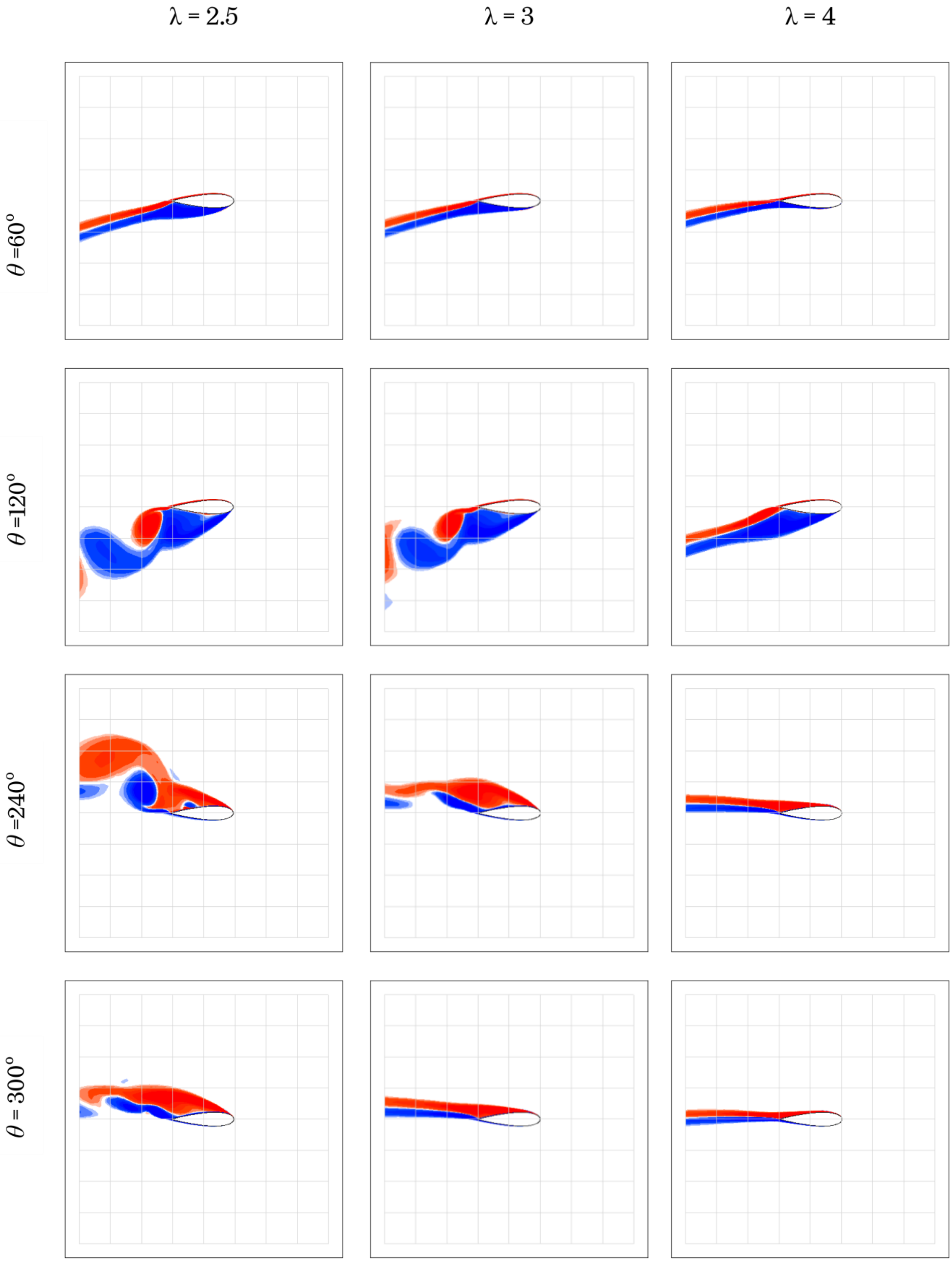

Figure 6.9. Compares CFD z-vorticity plots of three λ at 8m/s at four azimuth positions, C = 0.03m.

Despite the vortices being shed and, the interaction with vortices shed at the upwind and the wake of the central shaft at λ = 3, the flow recovered well from these effects and attained a maximum T_B = 0.98Nm at θ = 285^o suggesting higher power extraction in the downwind section of the flow. Whereas at λ = 4, a drop in T_B until it reached a T_B = 0.18Nm at θ = 270^o and poorer recovery is seen when compared to λ = 3.

At θ = 300^o, vortices are still being shed and with the combined effects of the blade interaction with the shed vortices in the upwind section and the wake of the central shaft, a minimum T_B = -0.77Nm is attained at λ = 2.5 in the downwind section. While the flow fields reattachment to the blade had advanced at λ = 3, the flow is attached to the blade surface at λ = 4 so a higher T_B is attained. Beyond this azimuth angle, reduction in T_B is seen at λ = 4 and at λ = 3 while, increase in T_B is seen at λ = 2.5 until a T_B = -0.19Nm is attained at all the λ at θ = 360^o. Judging from the nature of the flow associated with the blade at the various λ, an average T_B of -0.28Nm, 0.16Nm and 0.37Nm is attained at λ = 2.5, λ = 3 and λ = 4 respectively in downwind section of the rotation.

Overall, with an average T_B = 0.26Nm attained, the blade performed best at λ = 4 due to higher power extraction at both sections of the rotation and the low occurrence of dynamic stall at this λ. Poor performance is seen at λ = 3 with an average T_B = -0.03Nm when compared to the performance of the blade at λ = 4, due to the low velocity induction at the upwind section of the rotation so the better recovery from stall effects at the downwind section is undermined. Whereas the flow at λ = 2.5 was drag dominated and the blade performed in the negative region between θ = 78^o to θ = 360^o due to the greater occurrence of stall hence, lowest overall average T_B = -0.16Nm is attained. This explains the differences in the performance of the blade at the various λ at the 8m/s curve in Figure 6.1.

6.5.3 Blade Chord = 0.04m (σ = 0.34) at 6m/s

In the previous two sections, the influence of λ on torque and flow physics on the VAWT with C = 0.03m and σ = 0.26 blade has been examined at 6m/s and 8m/s. The blade performed better at the higher wind speed and so the high

Reynolds numbers at all the λ analysed based on the average torque attained. The revelations from the two cases of wind speeds analysed has been consistent in the dynamic stall process, velocity induction in relation to power extraction and available energy in the wind. However, altering the blade chord of a VAWT changes the Reynolds numbers and also the solidity, so, it is expedient to investigate the influence of λ on torque and flow physics on the C = 0.04m (σ = 0.34) VAWT. Therefore, similar investigation is conducted on the C = 0.04m blade at 6m/s in this section.

The T_B of the C = 0.04m blade at the three λ in Figure 6.11 is very different when compared to the previous two cases of C = 0.03m blade already analysed. The dissimilarity are not only in the maximum T_B attained but also on the azimuth angle the blade stalled and also the recovery from stall effects at corresponding λ. These observations are discussed in greater details in the succeeding sections where the performance of the two VAWTs is compared at different and the same Reynolds numbers.

At $\theta = 60^o$, the T_B is dropping off to lower values after attaining peak T_B = 0. 32Nm at λ = 2.5 due to the onset of stall (Figure 6.12). With the relatively attached flow to the surface of the blade, there is an increase in the T_B until the blade attained peak T_B of 0.99Nm and 0.76 Nm at λ = 3 and 4 respectively. At θ = 120°, the blade is engulfed in the shedding of periodic pairs of vortices at the two lower λ but with more advanced shedding at λ = 2.5 hence, the ripples seen in the curves. Whereas the onset of stall is just being initiated at λ = 4, again, suggesting delayed and suppressed stall. The differences in the flow structures in the upwind have impacted on the blade to attain average T_B of -0.21Nm, 0.06Nm and 0.07Nm at λ = 2.5, 3 and 4 respectively.

In the downwind section at θ = 240° a vortex pair is being shed at λ = 2.5 and the onset of the stall with the LEV separation bubble seen in the formative stage at λ = 3, so the blade dropped off to lower T_B beyond this point at both λ. Whereas, the flow is attached to the blade surface at λ = 4 hence the increase in $T_{B,}$ that probably have resulted from better recovery from stall effects in the upwind section of the rotation and higher power extraction from the wind streams at the downwind section of the flow.

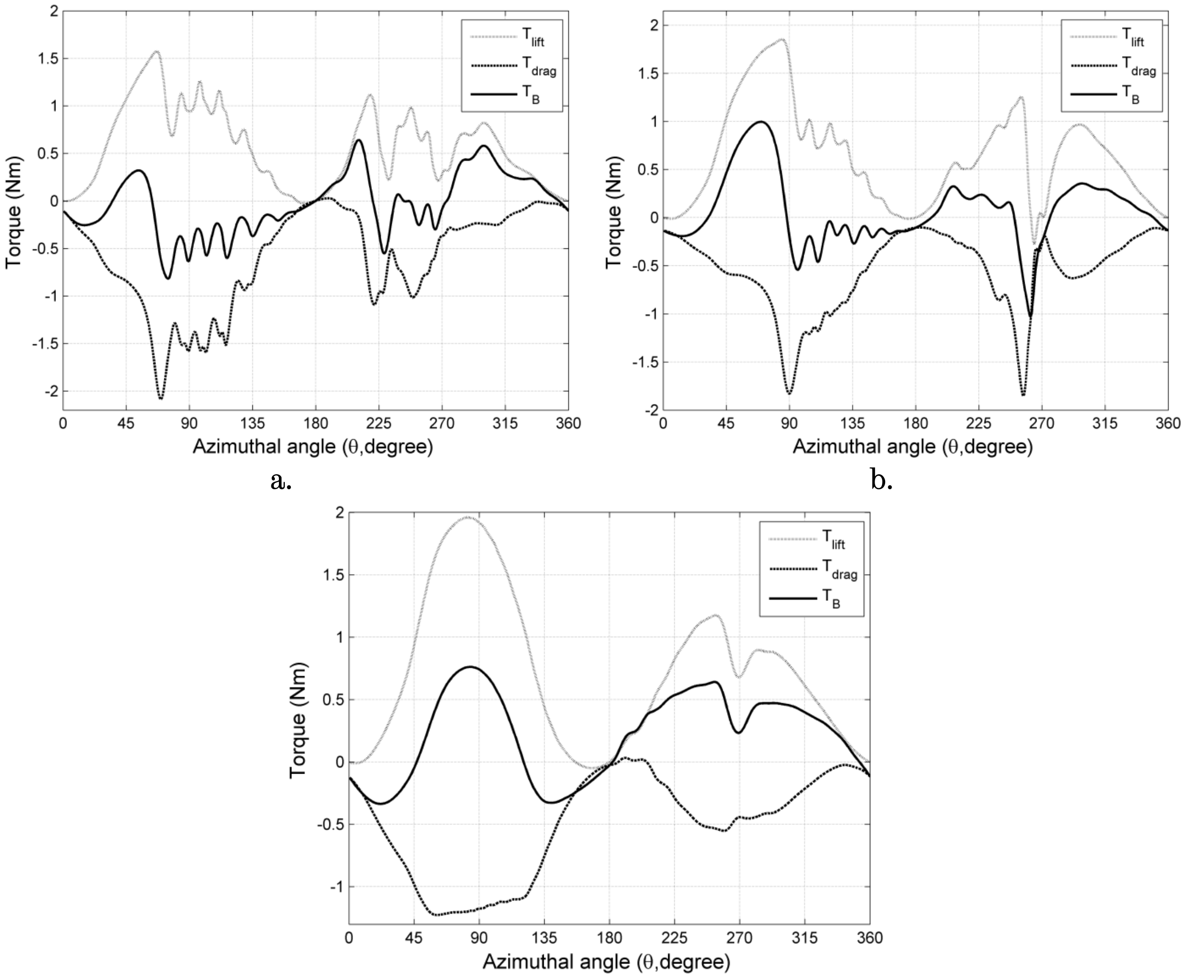

a. b.

c.

Figure 6.10. Torque versus azimuth angle, C = 0.04 at 6m/s, a) $\lambda = 2.5$, b) $\lambda = 3$, c) $\lambda = 4$.

The flow around the blade recovered poorly from the upwind stall effects at the $\lambda = 2.5$ and 3, and coupled with the blade stall, shedding of vortices, and the interaction with the upwind shed vortices and also the wake of the central shaft beyond $\theta = 240^{\circ}$, very poor performance is seen at the two lower λ and especially at $\lambda = 3$ where a minimum $T_B = -1.03$Nm is attained. Thereafter, the flow around the blade can be seen to struggle to improve on the poor performance at $\theta = 260^{\circ}$ at the two lower λ (Figure 6.11), and with higher available energy content in the wind stream for the $\lambda = 2.5$ in the downwind section, positive T_B is attained at all the λ with the highest at λ = 2.5. The positive T_B attained at $\theta = 300^o$ at all the λ have been influenced by the attached flow fields to the blade surface. (Figure 6.12). Beyond $\theta = 300^o$ azimuth angle, rapid reduction in the blade T_B is seen at all the λ until an approximate T_B = -0.12Nm is attained at $\theta = 360^o$. The flow physics has influenced the blade to attain an average T_B = 0.15Nm, 0.07Nm and 0.36Nm at λ = 2.5, 3 and 4 respectively.

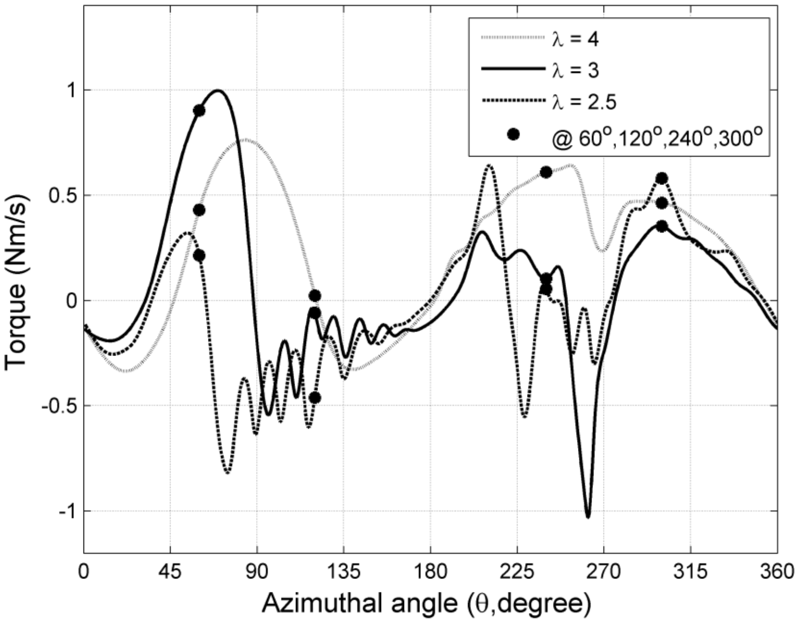

Figure 6.11. Compares torque versus azimuth angle for three λ at 6m/s, C = 0.04m.

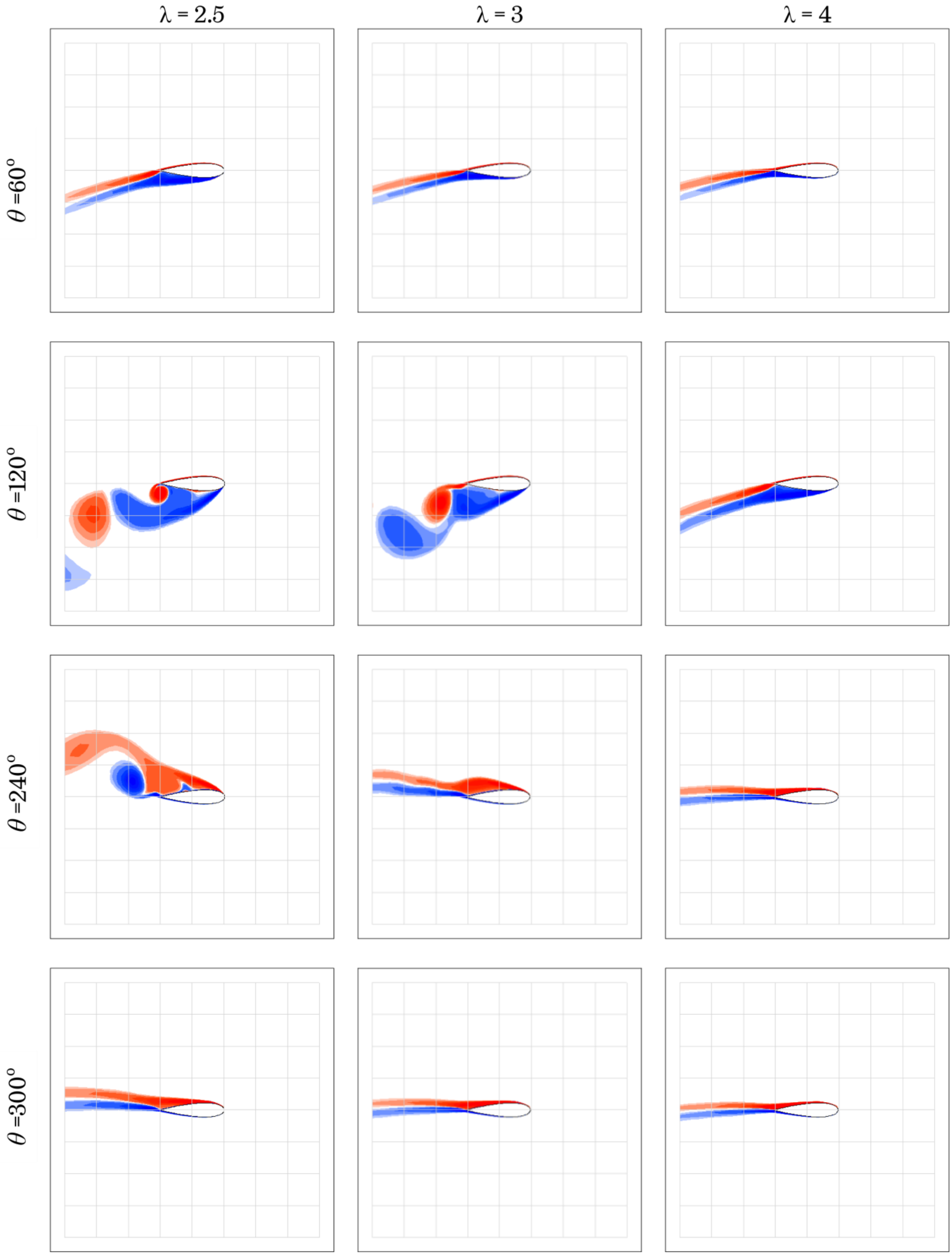

Figure 6.12. Compares CFD z-vorticity plots of three λ at 6m/s at four azimuth positions, C = 0.04m.

Overall, the blade performed best at λ = 4 again, with an average T_B = 0.21Nm attained, due to the lift dominated flow at both sections of the rotation. This is followed by the performance at λ = 3 with average T_B = 0.07Nm despite the very poor performance at $\theta = 265^o$, due to the higher power extracted in the upwind section of the rotation. Whereas the blade attained a very low average T_B = -0.03Nm at λ = 2.5 recording the worst performance due to the low power extracted at the upwind section of the rotation so the best recovery from stall effects in the downwind section of the rotation is undermined which explains the superior performance of the blade at the higher λ seen in the 6m/s curve in Figure 6.2.

6.6 Performance, Aerodynamics and Reynolds Numbers

The previous sections have shown how changes in λ can affect the flow features, the aerodynamics, and the forces of a VAWT. The understanding gained is being applied in the investigation into the influence of blade chord variation on the performance and aerodynamics of VAWT. This is achieved in two broad categories, namely:

- Performance and aerodynamics at different Reynolds numbers and
- Performance and aerodynamics at the same Reynolds numbers.

The investigation presented in the following sections which is aimed at furthering the understanding of the flow and performance associated with a VAWT, will also provide further revelations on how changes in blade chord can influence the performance of VAWT. This will also complement the findings from the experimental results presented and discussed earlier in chapter five.

6.6.1 Performance and Aerodynamics at Different Reynolds Number

The CP_{cfd} versus λ of the two configurations operating at 6m/s wind speed but different Reynolds numbers is shown in Figure 6.13. The differences in the performance between the two VAWT is very obvious in the low, medium and high λ, except at λ = 5.5 where both VAWTs attained the same CP_{cfd} = 0.165. A negative CP band is seen on the C = 0.04m (σ =0.34) curve between λ = 1.5 and λ = 2.65, while that of C = 0.03m (σ = 0.26) spanned from λ = 1.5 up to λ = 3.7. The C = 0.04m VAWT (σ = 0.26) attained a maximum CP_{cfd} = 3.34 at λ = 4.5 whereas the C = 0.03m VAWT reached a maximum CP_{cfd} = 0.221 at λ = 5.

The observed differences in the performance of the two VAWTs are explained by analysing and comparing their lift and drag coefficients, the blades torques and flow physics at the selected λ and also at the similar azimuth angles adopted in the previous section where the influence of the λ on the forces and flow physics were examined for consistency. The choice of the λ = 2.5 and λ = 4 corresponded to previous λ used in the chapter five for similar investigations based on experimental results and for brevity, λ = 3 is not analysed since the two λ can provide sufficient understanding and revelations from the problem.

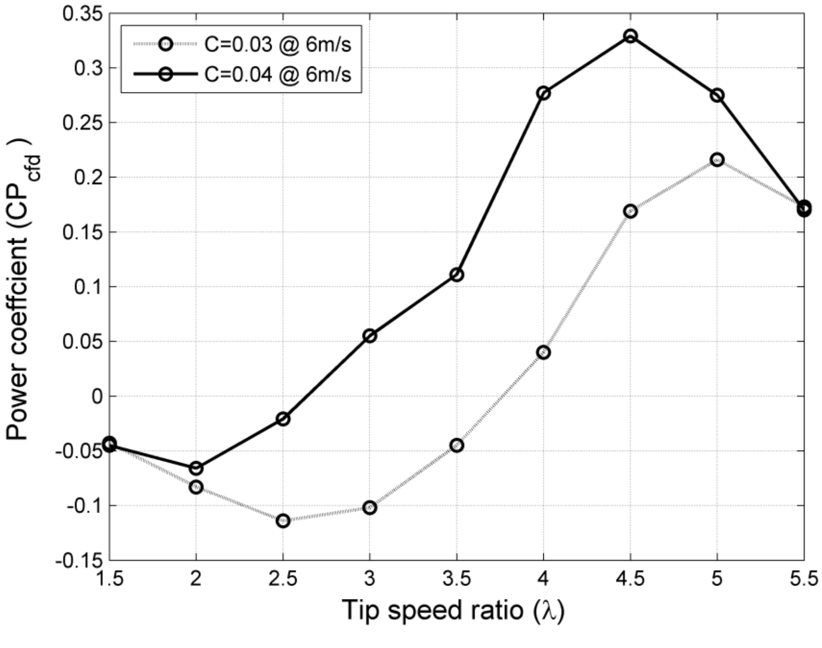

Figure 6.13. Compares power coefficient versus tip speed ratio for two blade chords at different Reynolds number (Table 5.3) .

6.6.1.1 Description of Performance, Force and Flow Fields at $\lambda = 2.5$

The CP_{cfd} of the two VAWT configurations can be seen in the negative performance region in Figure 6.13 with a difference of 300% in favour of the VAWT with the big blade chord. While the C = 0.4m VAWT with $\sigma = 0.34$ is increasing in performance further away from this λ, the C = 0.03m ($\sigma = 0.26$) VAWT is at its minimum and also gradually increasing in CP_{cfd} as it moves towards $\lambda = 3$ but still in the negative performance region. By the analysis and comparison of the non-dimensional lift and drag coefficients, the blades torques and flow physics of the two VAWTs blades at the similar azimuth angles used in the previous sections, the observed differences in the performance are explained at this λ.

Figure 6.14 presents a comparison of the lift and drag hysteresis and T_B curves for the two VAWT's blades at $\lambda = 2.5$. Non-zero negative values are seen for the C_L of the two blades at $\alpha = 0^o$ due to the dominance of drag torque at this position. The C = 0.03m rotor reached its maximum $C_L = 0.828$ around $\alpha = 13.2^o$ (Figure 6.14 (a)) caused by the onset of dynamic stall that stalled at $\alpha = 16.5^o$ with a corresponding decrease of $C_L = 0.44$ which is maintained until around $\alpha = 23.4^o$ ($\theta = 120^o$). These decreases are due to the shedding of vortices while it's C_D (Figure 14 (b)) increased from a low 0.26 to 0.32 and began to drop off before reaching $\alpha = 23.4^o$. The C = 0.04m rotor attained a maximum $C_L = 1.119$ at $\alpha = 17.4^o$ higher than that attained by C = 0.03m rotor, due to delayed stall, the C = 0.04m rotor eventually stalled at $\alpha = 19.6^o$ corresponding to around $\theta = 80^o$, thereafter the blade is engulfed in the vigorous shedding of vortices leading to the visible ripples seen on the curve between $\alpha = 19.6^o$ and 22.41^o. These ripples are also seen on the C_D and the T_B curves at the corresponding positions.

These observed differences in the upwind section of the rotation in Figure 6.14 (a and b) are also seen in the corresponding position in the T_B curves of the two VAWTs in Figure 6.14 (c). The C = 0.04m rotor attained a maximum T_B = 0.320Nm around $\theta = 50^o$ with an average T_B = - 0.21Nm while the C = 0.03m rotor attained a maximum T_B = 0.037Nm around $\theta = 40^o$ with an average T_B = - 0.20Nm in the upwind section. These differences in the torques attained by the rotors are due to the differences in the solidities and Reynolds numbers of the two rotors. At λ = 2.5, the C = 0.03m rotor with σ= 0.26 is operating at Re = 31,500 while that of the C = 0.4m rotor with σ = 0.34 is operating at Re = 42,000. At θ = 60° the C = 0.03m rotor is stalled while the C = 0.04m rotor dynamic stall process is still at the initial stage of formation (Figure 6.15) which explains the early drop in torque by the C = 0.03m blade at θ = 60°.

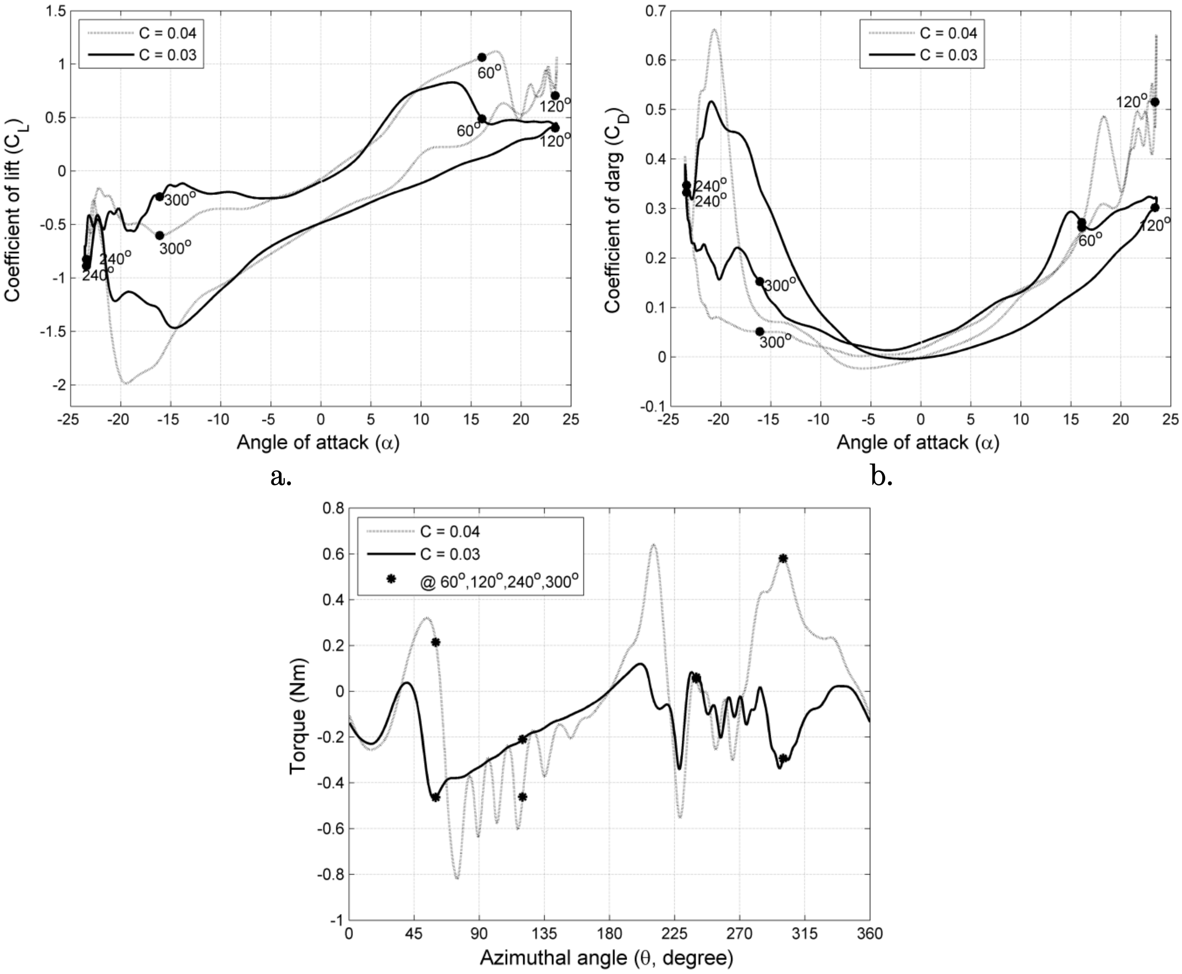

a. b.

c.

Figure 6.14. Compares VAWTs forces for two blades at $Re_{0.03m}$ = 31,500, $Re_{0.04m}$ = 42,500, λ = 2.5, a) coefficient of lift versus angle of attack, b) coefficient of drag versus angle of attack, c) torque versus azimuth angle.

Further away from θ = 60°, the C = 0.03m rotor begins to recover from the effects of blade stall, although it is shedding vortices with a smooth transition between pairs, as the T_B is seen to rise beyond $\theta = 180^{\circ}$. Whereas, the C = 0.04m blade is seen to drop off rapidly until it stalled at $\theta = 80^{\circ}$, and thereafter its flow begins to experience a pitching-type motion resulting from "phased" shedding of vortices that continued beyond $\theta = 120^{\circ}$ (Figures 6.15, 6.14 (a and b)) until around $\theta = 170^{\circ}$. Despite these ripples seen on the C = 0.04m blade, it still performed better slightly, than the C = 0.03m blade in the upwind section of the rotation due to the better extraction of power and also the delayed stalled.

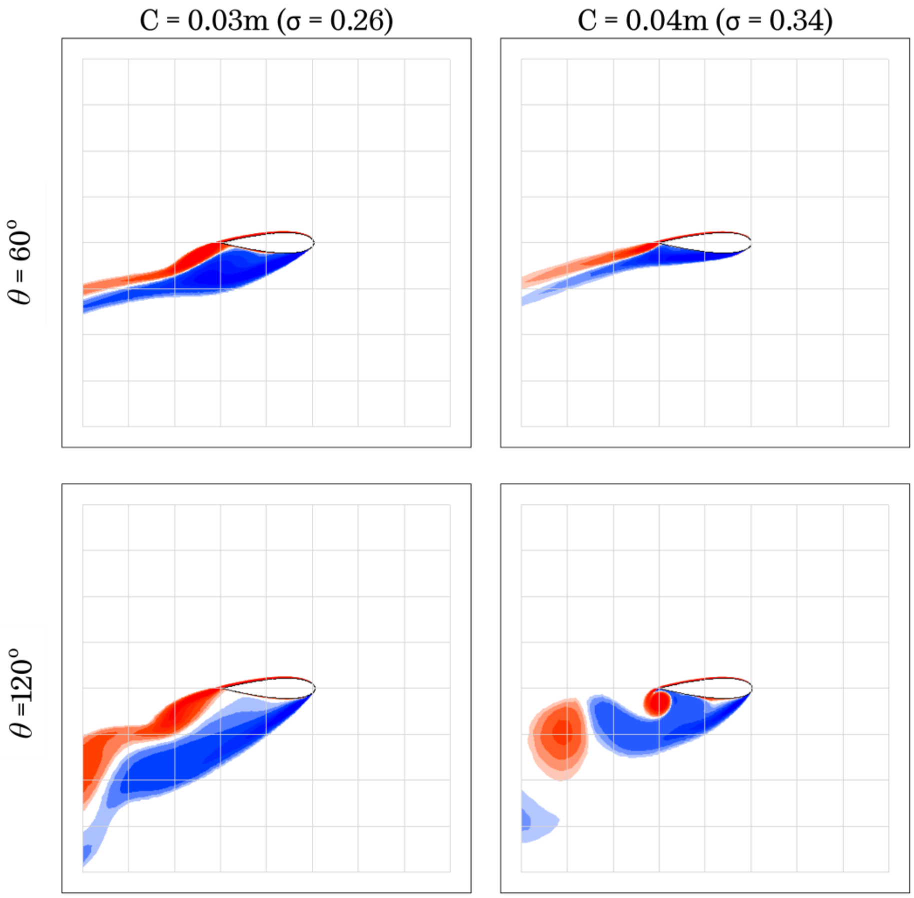

Figure 6.15. Compares z-vorticity plots of CFD simulations of two chords for two azimuth positions in the upwind section of the rotation at $Re_{0.03m} = 31{,}500$, $Re_{0.04m} = 42{,}500$, $\lambda = 2.5$.

In the downwind section of the rotation, a non- zero value of $C_L = -0.5$ is also attained by the two blades at $\alpha = 0^{\circ}$ (Figure 6.14 (a)), while the blades attained a zero value of C_D at the same $\alpha = 0^{\circ}$ (Figure 6.14 (b)) corresponding to $\theta = 180^{\circ}$. The blades also recorded $T_B = 0$Nm (Figure 6.14 (c)) at this azimuth angle which also confirmed the dominance of drag over the lift force due to the position of the blade relative to the wind streams in the flow cycle.

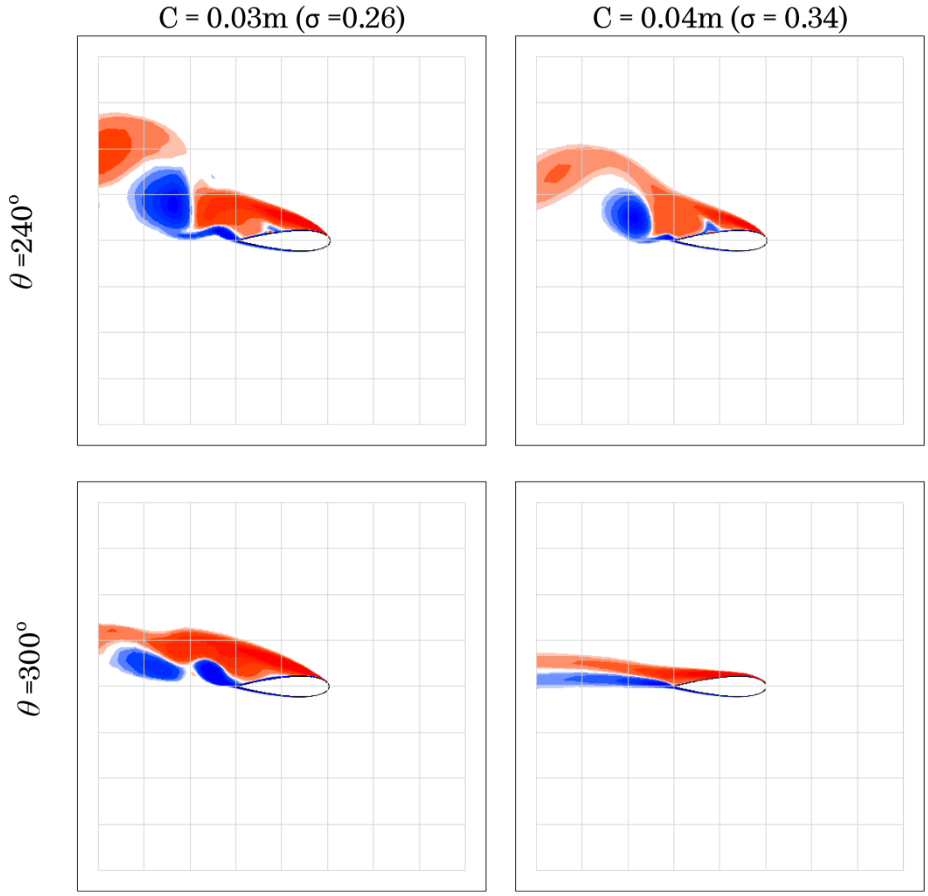

Figure 6.16. Compares z-vorticity plots of CFD simulations of two chords for two azimuth positions in the downwind section of the rotation at $Re_{0.03m}$ = 31,500, $Re_{0.04m}$ = 42,500, λ = 2.5.

At this azimuth angle of $\theta = 180^{\circ}$ the blade is horizontally aligned with the LE away but in the direction of the wind streams. Beyond this position, the C_L for both blades reduces rapidly with the C = 0.03m (σ = 0.26) rotor stalled earlier again at $\alpha = 15^{\circ}$ followed by the subsequent intermittent shedding of vortices at $\theta = 240^{\circ}$ (Figure 6.16) which also prolonged beyond $\theta = 240^{\circ}$ up to θ = 285. Due to the sequence of vortices shedding and the interaction of the σ = 0.26 rotor with upwind shed vortices and the wake of the support shaft, the flow of the C = 0.03m blade begins to pitch, causing hysteresis on the $C_{L,}$ and C_D curves and also ripples on the torque curve (Figure 6.14 (c)). Whereas the blade of the high solidity stalled later at α = -19.48°. Although, following the C = 0.04m (σ= 0.34) blade stalled was the shedding of vortices, the vortices were less sporadic, intermittent and brief hence good recovery from the effects of vortex shedding is seen on the curve at θ = 300° (Figure 6.14 (c)) where a maximum torque of 0.58Nm is attained.

The flow physics has influenced the observed differences in the performance of the two rotors due to the differences in solidity and Reynolds numbers between the VAWTs. At θ = 240° (Figure 6.16) the two blades are shedding pairs of vortices with the LEV bigger in both cases but the features of the pair of vortices shed by the C = 0.03m blade of the smaller solidity, σ = 0.26, is broken between pairs of shed vortices while that of C = 0.04m rotor of the bigger solidity, σ = 0.34, is continuous as there is no gap between pairs of previously shed and the next vortices to be shed.

This caused the flow around the C = 0.03m blades of the σ = 0.26 rotor experience a pitch-type motion that resulted in the ripples and hysteresis seen in the curves, while that of the C = 0.04m (σ = 0.34) rotor can be said to be due mainly to the interaction of the blade with the vortices previously shed at the upwind section of the rotation and also the wake of the centre shaft. At θ = 300° corresponding to α = -16^0, the gap that was previously seen between the shed pairs of vortices has disappeared from the LEV but still present in the TEV of the C = 0.03m blade. The presence of the gap in the TEV has minimal effects as the hysteresis and ripples are no longer visible on the curve signifying that the flow around the blade no longer experiences the pitch-type motion, while the reattachment of the flow field to the blade surface of C = 0.04m (σ = 0.34) rotor had advanced.

Overall, the C = 0.04m blade with σ = 0.34 performed better with an average torque of -0.033Nm against a lower average torque of -0.133Nm attained by the C = 0.03m (σ = 0.26) blade due to the higher solidity and also the higher Reynolds number resulting from the blade chord that influenced the flow physics. At the higher Reynolds numbers the dynamic stall process is delayed so lift is sustained longer than at a lower Reynolds number which directly determined the overall performance attained by a VAWT. As explained, these differences in the Reynolds numbers and solidities resulting from the blade chord caused better aerodynamic performance of the C = 0.04m VAWT over that of the C = 0.03m rotor.

6.6.1.2 Description of Performance, Force and Flow Fields at $\lambda = 4$

There is an obvious difference in the performance of the two VAWTs at $\lambda = 4$ as can be seen in Figure 6.13. While the C = 0.04m VAWT with $\sigma = 0.34$ is close to the λ at which the maximum CP_{cfd} is attained that of C = 0.03m rotor with $\sigma = 0.26$ is far behind within, approximately zero performance mark. This causes a CP_{cfd} difference of over 400% in favour of the C = 0.04m VAWT with the higher solidity. A comparison of the lift and drag hysteresis and torque curves for the two VAWT's blades at $\lambda = 4$ are presented in Figure 6.17. Again, as was observed earlier in Figure 6.14 (a), a non- zero negative values are seen for the C_L of the two blades at $\alpha = 0^o$ for the upwind travel which could also be attributed to the dominance of drag at this position. The C = 0.03m blade with the smaller solidity, $\sigma = 0.26$, reached its maximum $C_L = 0.880$ around $\alpha = 12.96^o$ (Figure 6.17 (a)) while the C = 0.04m rotor attained a maximum $C_L = 0.983$ at $\alpha = 13.80^o$. Although a delay in the dynamic stall process is observed for the two blades at this λ, the C = 0.03m ($\sigma = 0.26$) blade stalled earlier at $\alpha = 14.41^o$ with a corresponding decrease of $C_L = 0.351$ resulting from the flow separation from the blade surface while it's C_D (Figure 6.17 (b)) also decreased from a high $C_D = 0.186$ to a low $C_D = 0.036$ at $\alpha = 0^o$ corresponding to $\theta = 180^o$. Whereas the C = 0.04m ($\sigma = 0.34$) rotor stalled later at $\alpha = 12.9^o$ corresponding to $\theta = 130^o$ after having attained a maximum $C_L = 0.98$ at $\alpha = 13.8^o$ higher than that attained by C = 0.03m rotor, the higher C_L may be due to delayed stall resulting from the higher Reynolds number and higher solidity. At this λ, the C = 0.04m ($\sigma = 0.34$) operates at a $Re = 6.7 x10^{-4}$, while the C = 0.3m ($\sigma =0.26$) rotor sees $Re = 5 x10^{-4}$. As was observed for the C = 0.03m rotor, there are also corresponding decreases in the C_D which is contrary to the revelation in $\lambda = 2.5$. This obviously shows that the lift force is dominant over the drag force at this $\lambda = 4$.

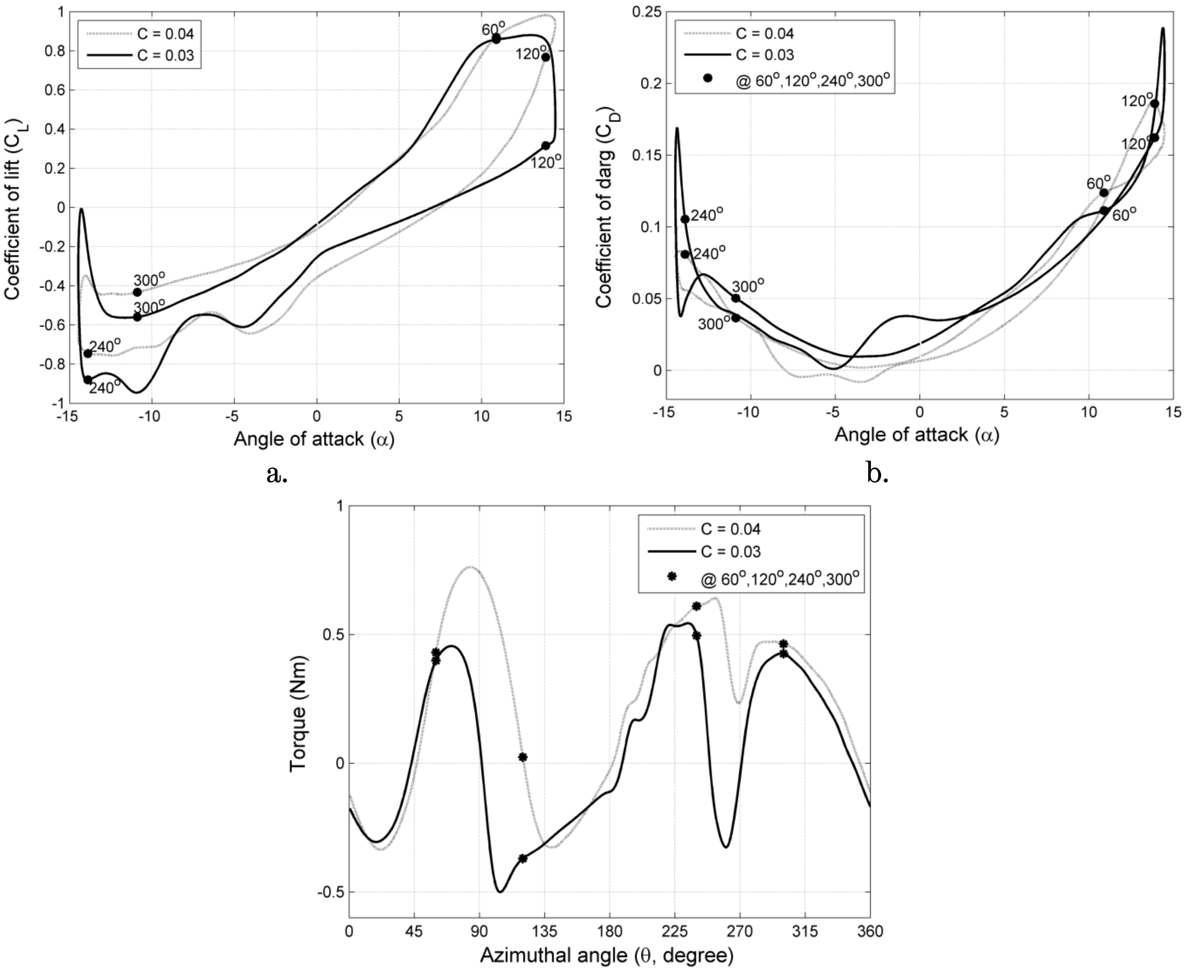

a. b.

c.

Figure 6.17. Compares VAWTs forces for two blades at $Re_{0.03m} = 50{,}400$, $Re_{0.04m} = 67{,}200$, $\lambda = 4$, a) coefficient of lift versus angle of attack, b) coefficient of drag versus angle of attack, c) torque versus azimuth angle.

The differences in the C_L and C_D curves of the two blades (Figure 6.17 (a and b)) can also be observed in the torque curves of the two blades in Figure 6.17 (c). The C = 0.04m rotor with $\sigma = 0.34$ attained a maximum blade torque of 0.762Nm around $\theta = 85^o$ close to $\alpha = 12.9^o$, with an average blade torque of 0.073Nm while the C = 0.03m blade with $\sigma = 0.26$ attained a maximum blade torque of 0.455Nm around $\theta = 70^o$ with an average of -0.111Nm in the upwind section. The flow fields being fully attached to the both blade surfaces at $\theta = 60^o$ (Figure 6.18), there are increases in the lift force, hence corresponding increases in blade torques are seen in (Figure 6.17 (c)).

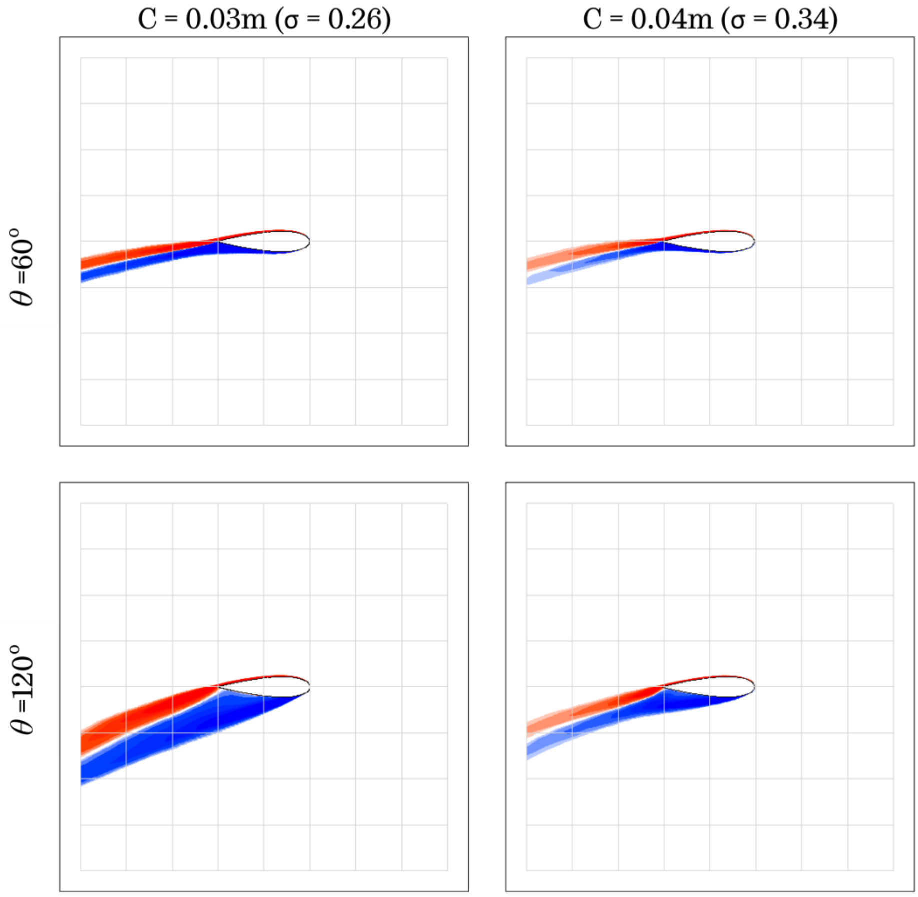

Figure 6.18. Compares z-vorticity plots of CFD simulations of two chords for two azimuth positions in the upwind section of the rotation at $Re_{0.03m}$ = 50,400, $Re_{0.04m}$ = 67,200,, λ = 4.

These increases in the blade torques for the two VAWTs blades is sustained beyond θ = 60° until the both blades attained their maximum torques signifying the onset of dynamic stall. As already mentioned, the C = 0.03m blade attained lower maximum torque compared to the C = 0.04m blade higher maximum torque that is attained later. Succeeding the maximum torque attainment, is the loss in torque with the loss of the C = 0.03m (σ = 0.26) blade seen to be more rapid and drop off to a lower trough where it stalled earlier than that of C = 0.04m (σ = 0.34). The dynamic stall process is also at different stages for both blades as C = 0.03m again is seen to be more advanced in Figure 6.18 at $\theta = 120^o$ ($\alpha = 13.89^o$), while the C =0.03m blade is shedding vortices after being stalled, the C = 0.04m blade has its LEV still in the formative stage of formation which stalled later on as the flow progress.

At $\theta = 180^o$ both blades are recovering from the stall effects with that of C = 0.04m blade better probably due to the bigger size of the blade chord and the higher Reynolds number causing more energy extraction than that of the smaller chord (figure 6.17(c)). Unlike was observed in the upwind section of the rotation at $\lambda = 2.5$, no ripples or hysteresis is seen in the curves especially in the C = 0.04m blade that the ripples were predominant. This is due to the differences in the dynamic stall pattern that is experienced by the blades with changes in the λ and Reynolds numbers.

The C = 0.03m blade attained a non- zero value of $C_L = -0.25$ and $C_D = 0.036$, while the C = 0.04m blade attained $C_L = - 0.36$ and $C_D = 0.007$at $\alpha = 0^o$ (Figure 6.17 (a & b)), corresponding to $\theta = 180^o$. Due to the higher C_D attained and the slow recovery from dynamic stall process, the C = 0.03m blade attained a blade torque of -0.111Nm (Figure 6.17 (c)), while the C = 0.04m blade attained 0Nm. This signifies that, at this azimuth position, the dominance of drag force over lift force is more for the $\sigma = 0.26$ rotor than that of the $\sigma = 0.34$ rotor.

Beyond $\theta = 180^o$, the torque for the two blades increases rapidly (Figure 6.17 (c)) until $\theta = 240^o$ corresponding to $\alpha = -13.89^o$ where C = 0.03m blade is seen to have started experiencing the onset of stall, while the torque for the C = 0.04m blade is increasing due to the flow field being still attached to the blade surface (Figure 6.19). With the C = 0.03m blade operating under stalled, beyond $\theta = 240^o$, it began to loss blade torque until it experienced a deep stall again at around $\theta = 260^o$ corresponding to $\alpha = -14.28^o$. Although the C = 0.04m blade stalled at the corresponding position, the drop in the blade torque is less and its flow recovery is also quicker when compared to that of C = 0.03m blade.

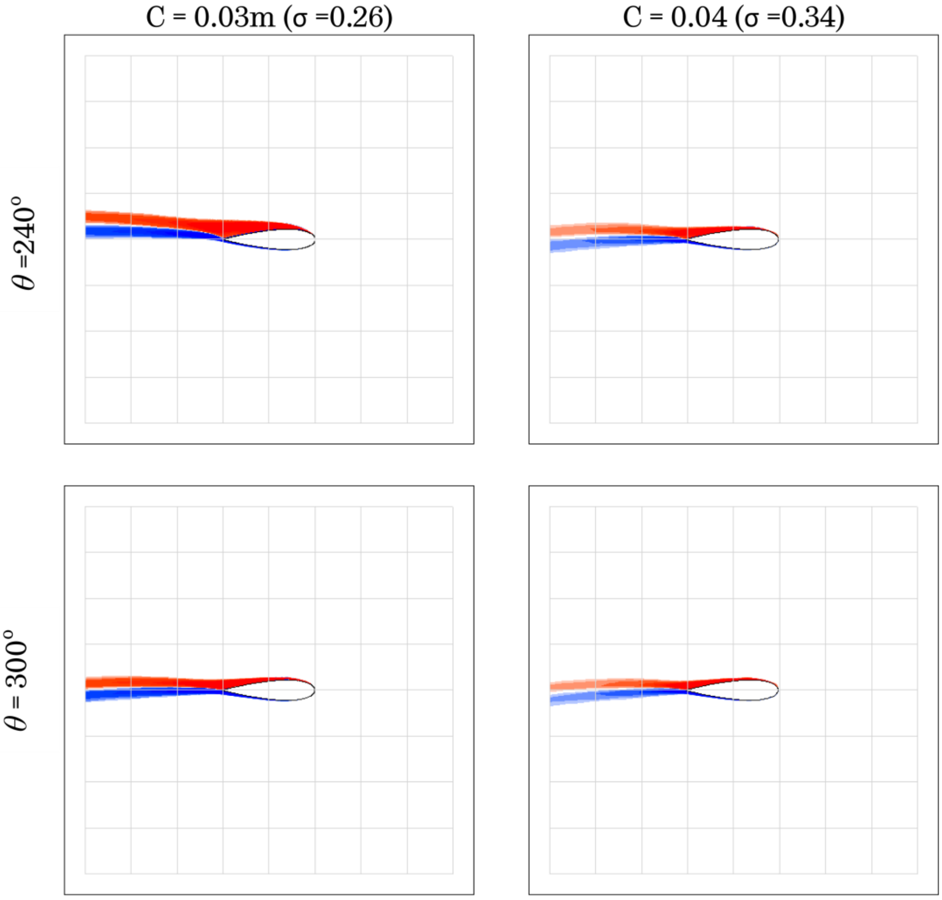

Figure 6.19. Compares z-vorticity plots of CFD simulations of two chords for two azimuth positions in the downwind section of the rotation at $Re_{0.03m} = 50{,}400$, $Re_{0.04m} = 67{,}200$, $\lambda = 4$.

At $\theta = 300^{o}$ the flow fields are attached to the surfaces of both blades (Figure 6.19), also the blade torque is seen to drop off rapidly as the blades moved away from $\theta = 300^{o}$ and attained negative torques at $\theta = 360^{o}$ despite the blades moving at the maximum relative velocities probably due to the near zero angle of attack of the blades in relation to the wind stream so drag force is dominant with zero or negative lift force.

Again the flow physics can be seen to have influenced the observed differences in the performance of the two VAWTs. At $\theta = 120^{o}$ (Figure 6.18) the C = 0.03m blade is shedding vortices having experienced deep stall earlier, while that of the C = 0.04m is just advancing towards blade stall, and at $\theta = 240^{o}$ the C = 0.03m blade is at the initial stage of the second dynamic stall process, while the C = 0.04m blade has its flow field attached to the blade surface. The attendant effects of early stall limited the lift force attained by the C = 0.03m blade which gave the C = 0.04m blade an advantage of attaining and sustaining higher torque than the C = 0.03m blade in virtually all the azimuth positions. The advantage gained from the delayed stalled by the C = 0.04m blade also results in the better blade torque average of 0.218Nm compared to a lower blade torque average of 0.045Nm attained by the C = 0.03m blade. The differences in the Reynolds number and solidity resulting from the blade chord have influenced the difference in the flow physics of the two blades, and as already explained, these differences in the Reynolds number and solidity have resulted in better aerodynamic performance of the C = 0.04m (σ =0.34) rotor over the C = 0.03m (σ = 0.26) rotor at this λ.

6.6.2 Performance and Aerodynamics at the Same Reynolds Number

The previous section has revealed why there can be differences in the performances of two VAWT configurations with different solidities and Reynolds numbers despite operating at the same wind speed as a result of the differences in their chord lengths. In this section the performance of the two VAWT configurations with different solidities is examined at the same Reynolds number to ascertain the similarities and differences in their performance. By operating the C = 0.03m (σ = 0.26) VAWT at 8m/s, while the C = 0.04 (σ = 0.34) rotor operates at 6m/s, both configurations operate at the same blade Reynolds number at the corresponding λ (Table 5.7).

The Figure 6.20 compares CP_{cfd} versus λ of the two rotors. The VAWT with C = 0.03m blade is operating at 8m/s wind speed, while that with C = 0.04m blade operates at 6m/s wind speed resulting in the Reynolds number of 42,000 at λ = 2.5 and 67,000 Reynolds number at λ = 4 for both rotors. Based on the VAWT configurations, the C = 0.03m rotor has a solidity of 0. 26 while the C = 0.04m VAWT has a solidity of 0.34. Obviously, the differences in the performance of the two VAWTs are very distinct in the low, medium and high λ. Although the two VAWTs show a negative CP band at the lower λ region, the negative band for the C = 0.03m VAWT is deeper and spanned from λ = 1.5 to λ = 3.2 while that of C = 0.04m VAWT is shallower and narrower. The VAWT with C = 0.03m blade attained its minimum CP_{cfd} = -0.09 at λ = 2.5 and a maximum CP_{cfd} = 3.24 at λ = 5 while that of C = 0.04 VAWTs attained its minimum CP_{cfd} = -0.07 at λ = 2 and a maximum CP_{cfd} = 3.34 at λ = 4.5. The peak power production region of the C = 0. 03m VAWT curve is wider and greatly slopped than that of C = 0.04m VAWT which is narrower and sharply slopped.

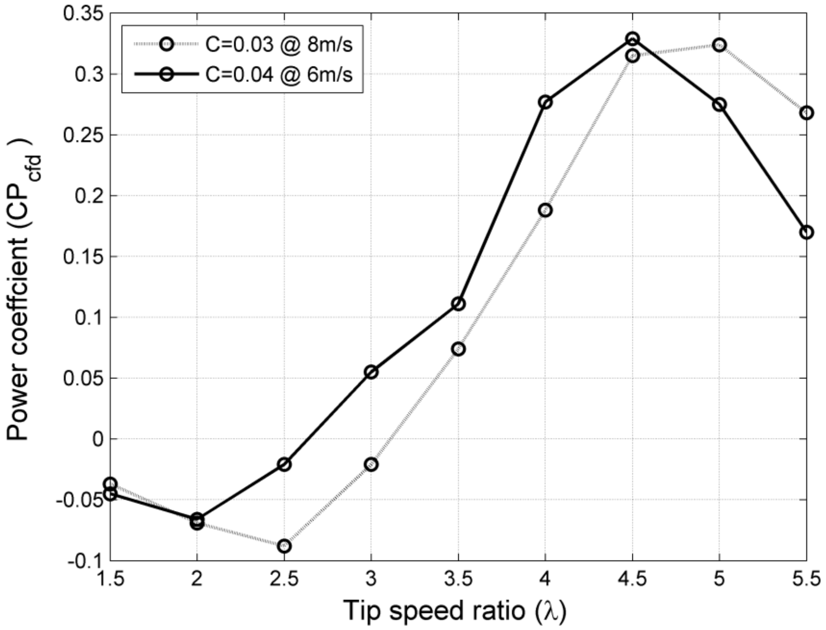

Figure 6.20. Compares power coefficient versus tip speed ratio for two blade chords at the same Reynolds numbers (Table 5.7).

6.6.2.1 Description of Performance, Force and Flow Fields at λ = 2.5

The CP_{cfd} of the two VAWT configurations at λ = 2.5 is in the negative performance region (Figure 6.20). It can be seen in Figure 6.20 that the power coefficient of the VAWT with the smaller blade chord is over 250% less than the VAWT with the big blade chord, and while the C = 0.03m VAWT is at its lowest CP_{cfd}, the C = 0.04m VAWT is rising towards the positive CP_{cfd} region.

Again, by analysing and comparing the lift and drag coefficients, the blades torques and flow physics of the two VAWT blades, the observed differences in the performance will be explained at this λ using the similar azimuth positions employed in the previous section.

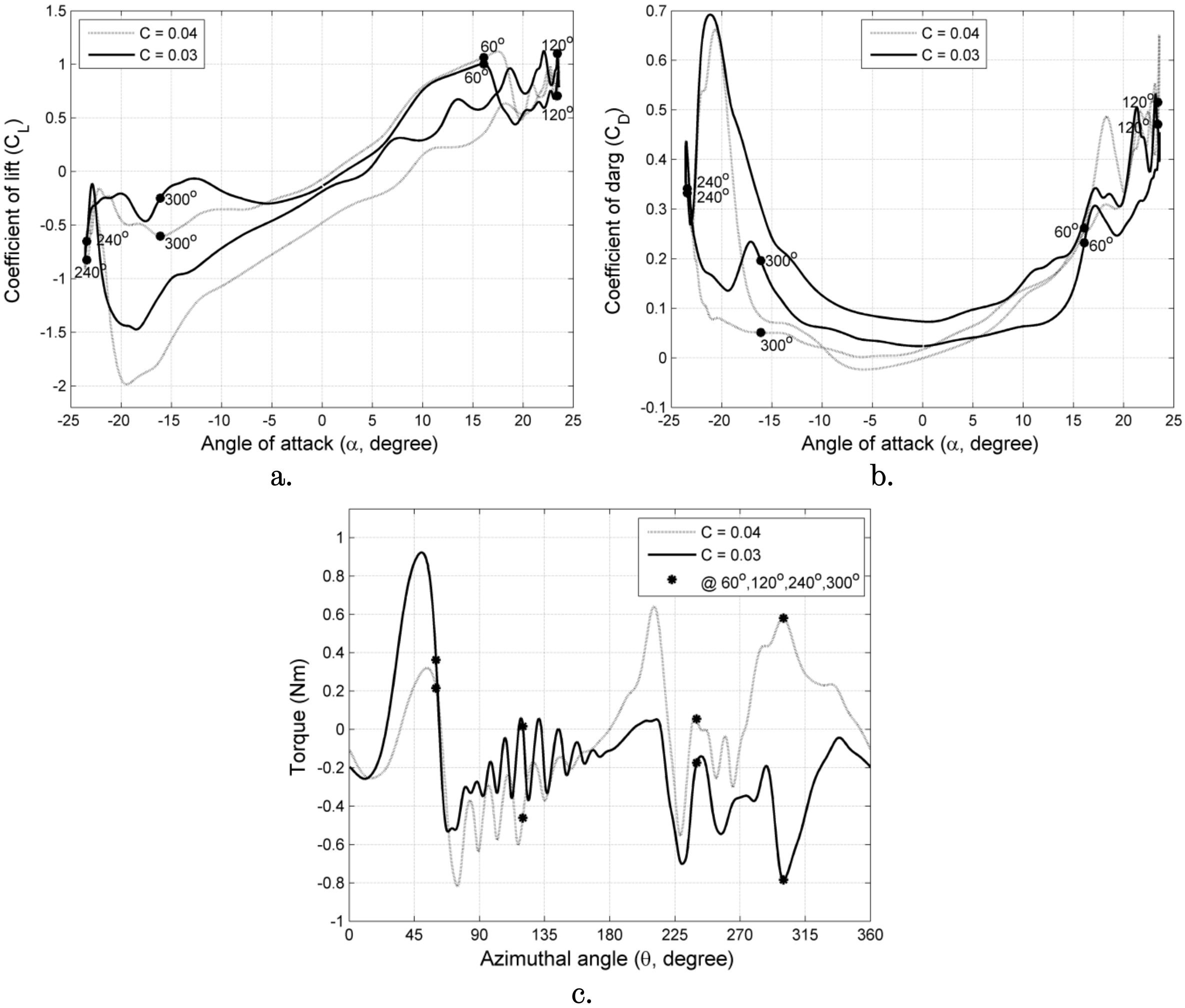

a.

b.

c.

Figure 6.21. Compares VAWTs forces for two blades at Re = 42,000, λ = 2.5, a) coefficient of lift versus angle of attack, b) coefficient of drag versus angle of attack, c) torque versus azimuth angle.

It can be observed from Figure 6.21 (c) that the upwind performance of C = 0.03m rotor is significantly better. It attained a blade torque (T_B) that is more than 200% higher than the T_B = 0.320Nm attained by C = 0.04m blade. The angle of attack of these points where the maximum T_B is attained is $\alpha = 13.7^o$ for C = 0.03m blade with a corresponding $C_L = 0.93$ and $C_D = 0.09$, and $\alpha = 14.6^o$ for C =

0.04m with a corresponding C_L= 1.01 and C_D = 0.20 (Figure 6.21 (a and b)) indicating drag dominated flow for the bigger blade (higher solidity) which explains the differences in the maximum T_B attained between $\theta = 0^o$ up to 90^o of the rotation. The onset of stall is already initiated at $\theta = 60^o$ on both blades but that of C = 0.03m is seen to be more advanced as the LEV is almost three quarter chord length (Figure 6.22) and eventually stalled earlier than the C = 0.04m blade. Although a drop in T_B is seen on both curves at the points where the blades stalled in the first dynamic stall cycle, the drop in T_B for the VAWT with C = 0.04m blade is more which further signify a drag dominated flow. As expected after the blade stalled, the two blades begin to shed vortices.

The hysteresis seen on the C_L and C_D curves, the ripples on the T_B curves are due to the pitching-type motion relative to the flow which the blades are subjected to as they shed vortices during the dynamic stall process. Due to the early start of the dynamic stall process on C = 0.03m blade, the pair of vortices shed are more advanced than the vortices shed by the C = 0.04m blade. At θ = 120^o corresponding to $\alpha = 23.41^o$, the pair of vortices shed are almost convected downstream with only a small part of the TEV seen and the supposed succeeding pair is fully developed to be shed by the C = 0.03m blade. Whereas for the C = 0.04m blade, the correspondingly shed pair of vortices is yet to be convected downstream, while the following pair to be shed is just midway in its formation. These distinct pairs of vortices shed by the blades actually caused the oscillating motion (pitching-type motion relative to the flow) experienced by the blades resulting in the ripples and hysteresis seen in the curves.

The dynamic stall patterns in the upwind section of the flow has influenced the C = 0.03m blade to attain a higher average T_B = -0.05Nm and a lower average T_B = -021Nm for the C = 0.04m blade. At $\theta = 180^o$, midway through the rotation, the flow around the C = 0.03m blade is unable to recover from the stall effects in the upwind section since it experienced higher velocity induction due to the higher power extracted. This resulted in lowering the available energy in the wind, hence, it attained a lower T_B = -0.11Nm. Whereas the C = 0.04m blade experienced lower velocity induction in the upwind section of the rotation, hence the lower power extracted, sees a higher wind velocity magnitude beyond θ = 170°, so its recovery from the stall effects is enhanced thereby attaining a higher T_B = 0.001Nm at θ = 180°. This point corresponds to a C_L = -0.48 and C_D = -0.001 for the C = 0.04m blade, and also to a lower C_L = -0.19 and higher C_D = 0.07 for the C = 0.03m blade which explains the better performance of the C = 0.04m blade over the C = 0.03m blade at this azimuth position.

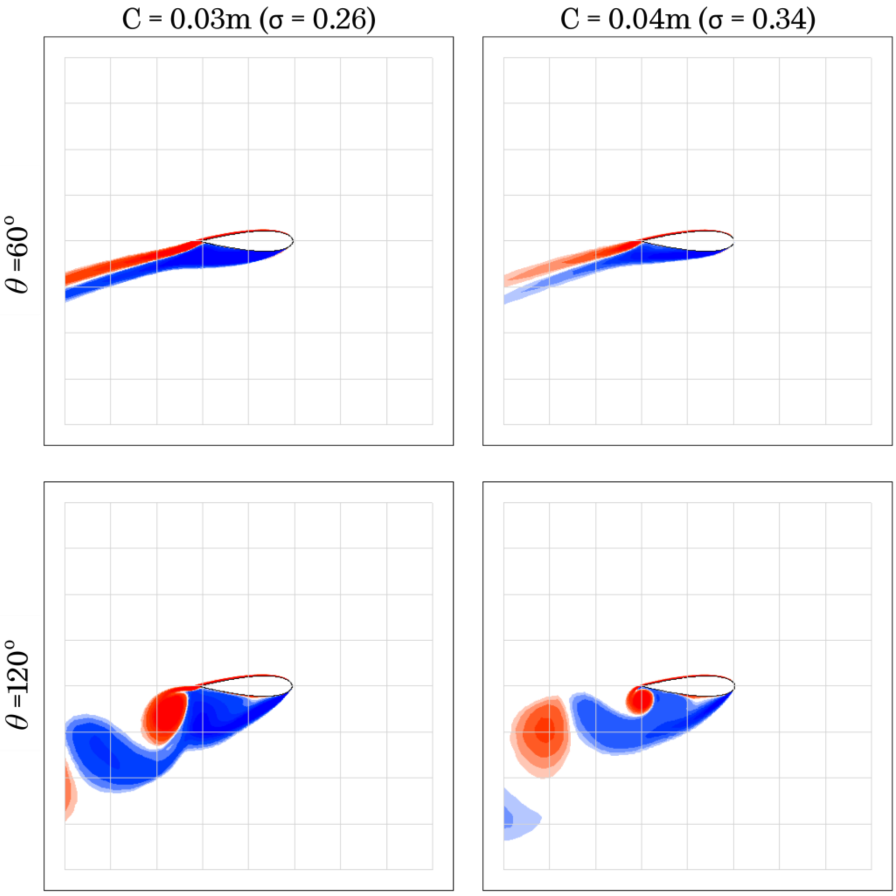

Figure 6.22. Compares z-vorticity plots of CFD simulations of two chords for two azimuth positions in the upwind section of the rotation at Re = 42,000, λ = 2.5.

The flow around the C = 0.04m blade having recovered quickly from the stalled effects in the upwind section, attained a maximum T_B = 0.64Nm around θ = 210° with corresponding C_L = -1.85 and C_D = 0.12 at α = -17.21°. At the same position, the C = 0.03m blade attained a lower T_B = 0.05Nm with corresponding lower C_L = -1.32 and higher C_D = 0.38. The comparable high drag and very low lift resulting from the low available energy content in the wind at the downstream section of flow causes poorer recovery of the C = 0.03m blade from the dynamic stall effects in the upwind section.

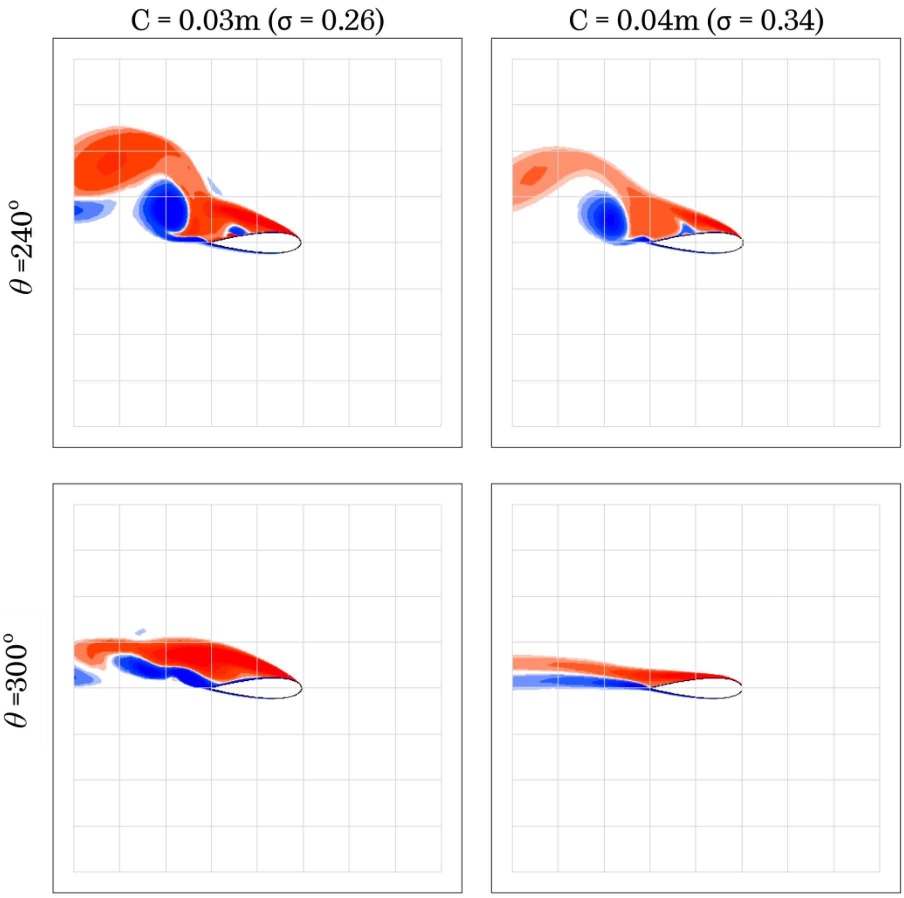

Figure 6.23. Compares z-vorticity plots of CFD simulations of two chords for two azimuth positions in the downwind section of the rotation at Re = 42,000, λ = 2.5.

Beyond this position the blades are stalled again. Unlike was observed in the upwind section of the rotation it is the C = 0.03m blade that experiences a deep stall at $\theta = 225^{\circ}$ in the downwind section of the rotation and attained a lower T_B = -0.70Nm, while the C = 0.04m blade stalled without delays at the same azimuth angle, attained a higher T_B = -0.55Nm. At $\theta = 240^{\circ}$ the two blades had begun to shed vortices with the C = 0.03m blade shedding larger vortices (Figure 6.23) due to the deep stall and thereafter both blades interacted with the wake of the centre support shaft and with the their own vortices shed in the upwind section resulting in the ripples seen on the curves in the downwind section of the rotation. At $\theta = 300^{\circ}$ the flow of the C = 0.04m blade had recovered again from the dynamic stall effects due to the higher available energy content in the wind and the higher solidity of the VAWT so the velocity induction is high resulting in higher power extraction, hence it attained a maximum T_B = 0.58Nm with a C_L = - 0.6 and a C_D = 0.05. Whereas that of C = 0.03m blade could not recover from the stall effects due to the lower energy content in the wind and the smaller chord resulting from an overpowering drag, so a minimum T_B = -0.79Nm is attained despite a higher C_L = -0.25.

The flow physics can be seen to have influenced the obvious dissimilarity in the performance of the blades at this azimuth angle, while the flow fields are almost attached to the C = 0.04m blade surface, the C = 0.03m blade is still shedding distinct pairs of vortices. The attendant follows-on flow effects associated with the C = 0.03m blade dynamic stall process confined it to operate within the negative region in most parts of the downwind section resulting in a lower overall average T_B = -0.16Nm, while the C = 0.04m blade attained an overall higher average T_B = -0.03Nm which explains the performance differences observed between the two rotors at λ = 2.5 in Figure 6.20.

6.6.2.2 Description of Performance, Force and Flow Fields at λ = 4

There is improved performance of the two VAWT configurations at this λ, the CP_{cfd} is attained in the positive region different from the poor and negative CP_{cfd} attained by the two VAWT rotors at λ = 2.5, and with the size of the VAWT configurations under investigation, a Re = 25000 difference in favour of λ = 4 can influence the gap in the performance seen between λ = 2.5 and λ = 4 for both VAWTs (Figure 6.20). So the observed large differences in performance between the two λ is due to higher power extraction resulting from the higher Re under which the VAWTs operated in, at λ = 4. Similar to the observations at the λ = 2. 5, the C = 0.04m VAWT's performance is better than that of the C = 0.03m but with about 37% increase in CP_{cfd}. For consistency, the observed difference in the performance is explained at this λ, by analysing and comparing the lift and drag coefficients, the torques and flow physics of the two VAWTs blades at the similar azimuth angle employed in the previous section.

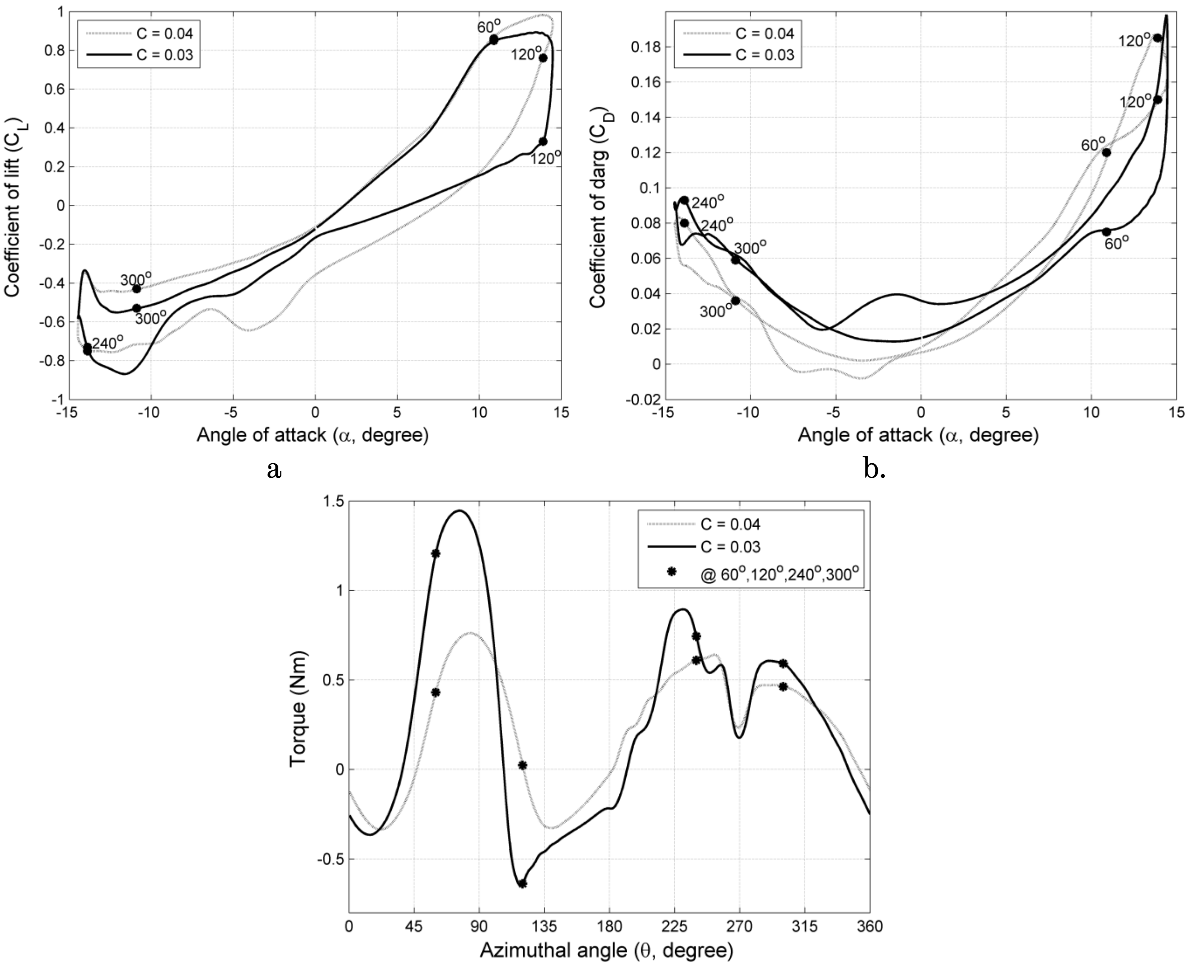

a

b.

c.

Figure 6.24. Compares VAWTs forces for two blades at Re = 67,000, λ = 4, a) coefficient of lift versus angle of attack, b) coefficient of drag versus angle of attack, c) torque versus azimuth angle.

Figure 6.24 presents a comparison of the C_L, C_D and T_B for the two VAWTs blades. Significant differences can be seen in the T_B curves at the upwind section of the rotation. The maximum T_B attained by C = 0.03m blade with corresponding C_L = 0.88 and C_D = 0.09 at α = 12.93 almost doubled the maximum T_B = 0.76Nm attained by the C = 0.04m with corresponding C_L = 0.97 and C_D = 0.14 at α = 13.62, despite the higher C_L attained by C = 0.04m blade. This is due to the flow associated with the C = 0.04m blade from $\theta = 0^o$ up to $\theta = 90^o$ hence the flow can be seen being dragged dominated while that of C = 0.03m blade is lift dominated.

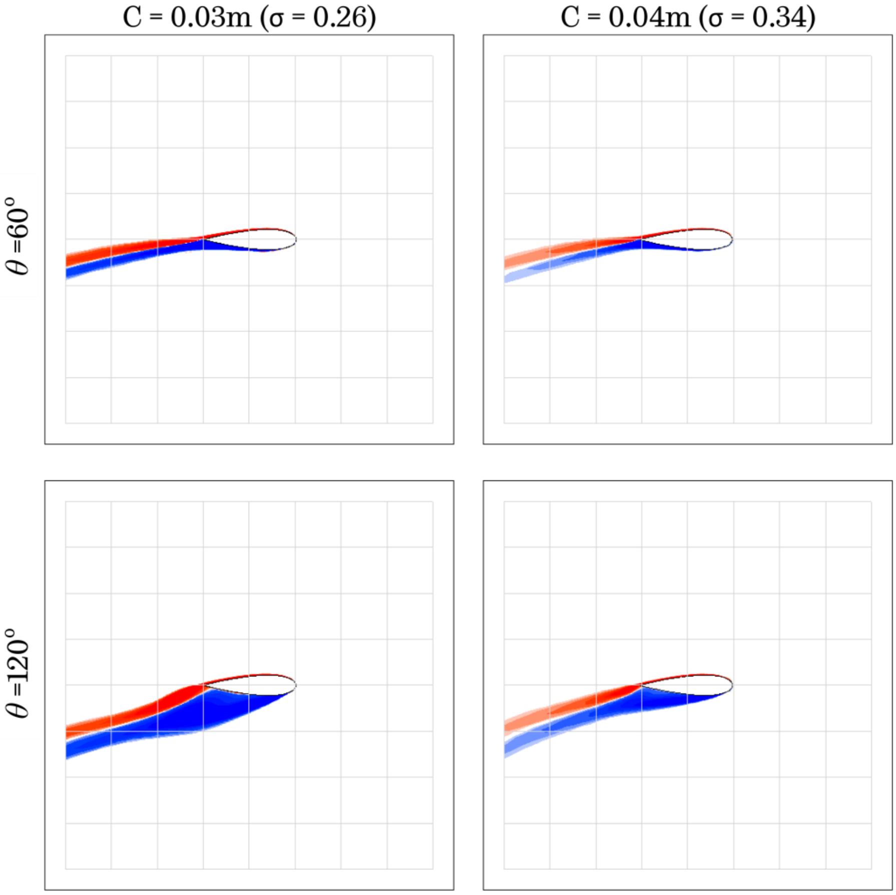

Figure 6.25. Compares z-vorticity plots of CFD simulations of two chords for two azimuth positions in the upwind section of the rotation at Re = 67,000, λ = 4.

Unlike the dynamic stall of λ = 2.5 at θ = 60°, the flow field is attached to the surfaces of the two blades (Figure 6.25) hence the higher T_B attained by both blades at this λ. Also stall is delayed for both blades and the C = 0.03m blade stalled earlier at θ = 120° reaching a lower minimum T_B = -0.65Nm with a corresponding C_L= 0.35 and C_D = 0.17 at α = 14.00° while the C= 0.04 blade stalled later at θ = 140°, causing a phase difference of about 20°, with a drop in T_B = -0.32Nm. This point corresponds to a lower C_L= 0.30 and C_D = 0.12 at α = 11.33°.

The flow of C = 0.03m blade is dominated by drag after being stalled at θ = 120° (Figure 6.25) hence, the poor and slow recovery of C = 0.03m blade from stall effects with a resultant T_B = -0.22Nm at θ = 180°. The dynamic stall of the C = 0.04m blade is still in its formative stage due to delayed stalled, and when it eventually stalled, the stall process was brief so the C = 0.04m blade is seen to recover quickly from the stall effects and attained a higher T_B = 0Nm at $\theta = 180^{\circ}$. Despite the slow and poorer recovery of C = 0.03m blade from stall effects, a higher average T_B = 0.27Nm is attained in the upwind section of the rotation when compared to the lower average T_B = 0.21Nm attained by the C = 0.04 blade. The higher average T_B is due to the lift dominated flow experienced by C = 0.03m blade in the first part of the upwind section of the rotation.

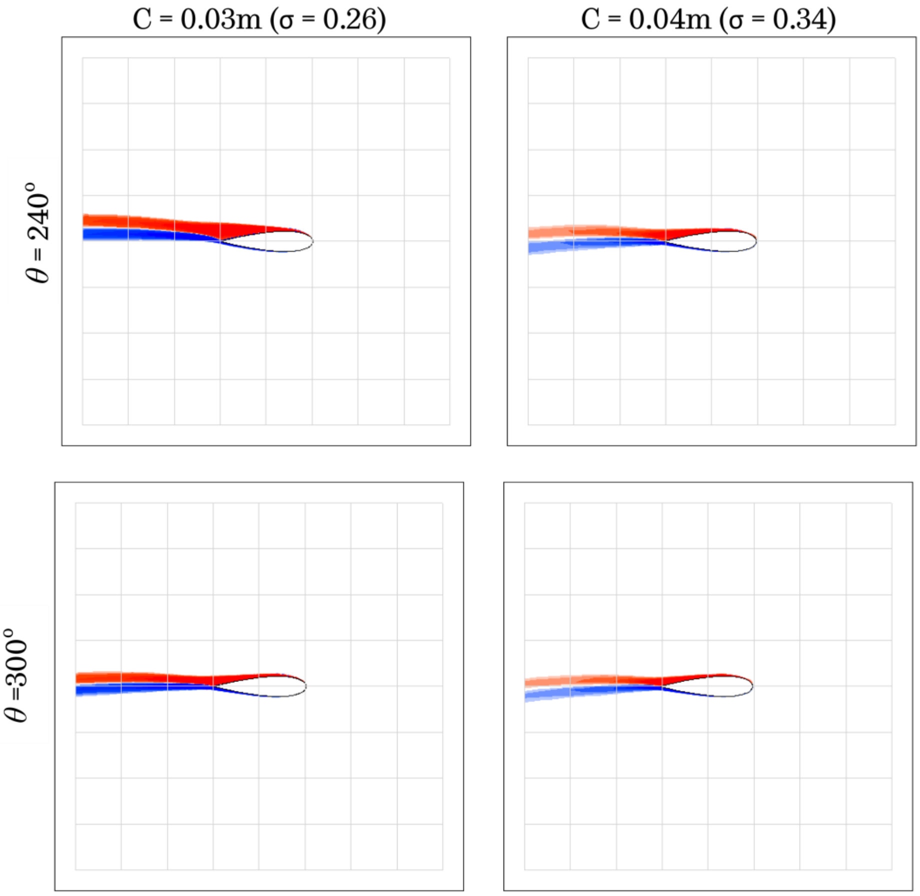

Figure 6.26. Compares z-vorticity plots of CFD simulations of two chords for two azimuth positions in the downwind section of the rotation at Re = 67,000, λ = 4.

The recovery from stall effects is sustained into the third quadrant of the cycle by the two blades but with the C = 0.04m blade still showing better recovery until around $\theta = 212^{\circ}$ where both blades attained T_B = 0.41Nm. This azimuth angle corresponds to $\alpha = -9.54^{\circ}$. Beyond this point the C = 0.03m blade rises rapidly above the C = 0.04m blade and thereafter attained a higher maximum T_B = 0.89Nm at θ = 230°, while the C = 0.04m blade attained a lower maximum T_B = 0.64Nm at θ = 253° in the downwind section of the rotation.

At θ = 240°, onset of stall is being initiated for the C = 0.03m blade (Figure 6.26) while the flow field of the C = 0.04m blade is fully attached to the blade surface. This explains the drop in T_B by the C = 0.03m blade while the C = 0.04m blade increased in T_B until it reached its maximum. The C = 0.03m blade advances in its dynamic stall beyond θ = 253° whereas the onset of stall is being initiated for the C = 0.04m blade, and at θ = 270° the blades drop in T_B with the C = 0.03m losing more. The drop in T_B by both blades at this azimuth angle is due to stalling and the interaction of the blades with the wake of the centre support shaft.

At θ = 300°, corresponding to α = 10.89, the blades had recovered quickly from the effects of the interaction with the wake of the centre support shaft and the dynamic stall, and with the C = 0.03m better recovered, it again attained a higher T_B = 0.59Nm while the C = 0.04m blade attained a lower T_B = 0.46Nm. Despite the attached flow fields to the blade surfaces (Figure 6.26), signifying the dominance of lift, the T_B for both blades rapidly drop off to lower negative values until the C = 0.03m blade attained lower T_B = -0.25Nm, while the C = 0.04m blade attained a higher T_B = -0.11Nm. The reduction observed in T_B of the blades beyond θ = 300° despite the attached flow fields to the blades' surface may be due to decreases in α as the blades move towards θ = 360°, and the LE of the blades is horizontally aligned into the wind stream at this α, insignificant lift is generated, resulting in overpowering of drag.

Overall, the C = 0.03m blade attained an average T_B = 0.26Nm while the C = 0.04m attained a lower average T_B = 0.21Nm, but with the C = 0.03m blade operating at 8m/s wind speed to match with the Re of the C = 0.04m blade operating at 6m/s, the available wind power of the C = 0.03m is higher hence the lower CP_{cfd} attained despite the better average T_B, which explains the superior performance of C = 0.04m ($\sigma = 0.34$) VAWT over the that of the C = 0.3m ($\sigma = 0.26$) VAWT at this λ.

6.7 Comparison of Results with Literature

The results from this investigation compared well with Edwards et al [51] numerical results on a similar scale conducted in 6.75m/s wind speed. The similarity is not only in the similar trend in the $CP_{cfd} - \lambda$ seen in the positive performance region but also the negative dead band is present in both studies. But for the different turbulence model deemed suitable for this investigation, the maximum CP was attained at $\lambda = 4.5$, higher than the $\lambda = 4$ at which the maximum CP is attained for the Edwards et al investigation, and correspondingly the minimum CP is also attained at different λ, but overall, the performance trend is similar despite the different turbulence models used in the two studies.

The forces, development of the flow field structures around the blade and the azimuth angle the blade stalled, are dependent on the λ at which the VAWT operates so at a low λ, large occurrence of dynamic stall and shedding of vortices are predominant. This is similar to the revelations of Fujisawa and Shibuya [44] experimental observation of dynamic stall on Darrius wind turbine blades. This also is in conformity with Iida et al [74] investigations in which the Large Eddy Simulation (LES) model was used to numerically simulate the unsteady flow and aerodynamic performance of VAWT. They observed large scale shedding of vortices at the lower λ, and small scale shedding of vortices and less effect of dynamic stall at the high λ.

The comparison of the $CP - \lambda$ of the two VAWT configurations at the same Reynolds number showed a shift of the λ at which the maximum CP was attained by the lower solidity VAWT to the right (a higher λ) and also a $CP - \lambda$ curve with a wider peak power region for the lower solidity VAWT. This is in conformity with the studies of Templin [20], Strickland [13], Mays and Holmes [24] and Consul et al [25]. Although these authors altered the number of blades to change the solidity of the VAWT configurations in their investigations, the influence of solidity has been observed to be similar in the CP – λ trend irrespective whether the number of blades, the blade chord or the scale that is altered, judging from the comparison of the results and especially when the effects of changes in the number of blades are insignificant on the VAWT Reynolds numbers. The results from this investigation are also in conformity with the blade profile and solidity investigation's findings by Eboibi et al [31] and that of the parametric studies of McIntosh [18] where VAWTs solidity was changed by altering the blade chord. A similar trend in the performance curves is seen in all these investigations; the maximum power coefficient is attained at the optimum solidity, the width of the performance curve increased with decrease in VAWT's solidity. The lower solidity performance curves are greatly slopped and flattened at the top while the high solidity performance curve are sharply slopped and pointed at the top. The observations from the torque comparison of the two VAWT blades at the same Reynolds number are also consistent with that of Consul et al [25] with ripples seen on the torque curve of the blade with the lower solidity at the low λ = 3 whereas no ripples are seen in the curves at higher λ with similar comparisons indicating occurrence of stall at the lower λ.

Changes in wind speed and blade chord resulted in changes in Reynolds numbers which has influenced the performance of the two VAWTs configurations in this investigation. With the performance observed to depend on the Reynolds number, the investigation can be adjudged to conform to the flow curvature investigations of Miglore [32] although the chord/radius ratio and scale of the VAWT studied differ in both investigations .

6.8 Summary

Computational Fluid Dynamics (Fluent 12.1) has been used to investigate two dimensional cross sections of two VAWT configurations of C = 0.03m with σ =

0.26 and 0.04m with $\sigma = 0.34$ VAWTs. The investigation has revealed the following:

- The results from the simulations of the two VAWTs at the three wind speeds are typical of the performance of wind turbines and due to the Reynolds numbers of the VAWTs under investigation the dead band is very visible in the lower λ region. While the dead band can hinder the self starting of VAWT, it increased in width and depth with decreased in either wind speed or blade chord so Reynolds number and solidity have significant impact on the aerodynamics and performance of a VAWT.
- The performance of the VAWTs increased with increasing the wind speed, blade chord, and Reynolds number, and within the range of λ tested, the bigger chord with the higher solidity attained higher peak CP at lower λ than the smaller chord at comparable wind speeds. So, the influence of Reynolds number and solidity of the VAWT is very evident in the performance of the two configurations.
- The angle of attack and the relative velocity has been shown to depend on the λ at which the VAWT operates. While the angle of attack increased with a decrease in λ at the upwind section of the rotation and increased with an increase in λ in the downwind section of the flow, the relative velocity is directly proportional to the λ at both sections of the cycle. The flow curvature and the forces of the blades are also influenced by the these two important parameters either positively or negatively in relation to the λ under investigation.
- The dependence of the VAWTs performance on λ has been shown as a fallout from the interaction of the VAWT blades with the wind speed at which the VAWT operates. The resulting average T_B attained by the blades of the two configurations at the various wind speeds are shown in Table 6.2. It can be seen that the poor performance of the VAWTs at the lower λ is consistent. At the lower λ, large scale divergent flow around the blade with the stalling and the sporadic

shedding of vortices is shown hence, the poor performances recorded while the opposite is seen at the higher λ so a better performance is attained.

C = 0.03m, σ = 0.26 at 8m/s			
	λ =2.5	λ = 3	λ = 4
Average T_B (Nm)	-0.16	-0.03	0.27
C = 0.03m, σ = 0.26 at 6m/s			
	λ =2.5	λ = 3	λ = 4
Average T_B (Nm)	-0.133	-0.03	0.04
C = 0.04m, σ = 0.34 at 6m/s			
	λ =2.5	λ = 3	λ = 4
Average T_B (Nm)	-0.03	0.07	0.22

Table 6.2. Average T_B attained by the rotor blades at various wind speeds

- The size of the structure of the shed vortices has been seen to be independent of the λ but depend on the azimuth angle at which the blade stalled while the subsequent shedding of vortices is dependent on the λ, Reynolds number and the solidity. At a lower λ, Reynolds number and smaller blade chord, stalling occur earlier at a lower azimuth angle with the resulting large scale shedding of vortices while at higher λ, Reynolds number and bigger blade chord there is delayed stall at a higher azimuth angle and less shedding of vortices.
- The flow physics has been shown to influence the performance of the two VAWT configurations when compared at the same λ. At different Reynolds number, the C = 0.03 blade attained an average T_B = -0.133 at λ = 2.5 and an average T_B = 0.04 at λ = 4 while the C = 0.04 blade attained an average T_B = - 0.03Nm at λ = 2.5 and an average T_B = 0.22Nm at λ = 4. Although both blades operated at the same wind speed and are subjected to stall, the C = 0.03m experienced earlier stall and shedding of vortices due to the smaller chord with a corresponding lower solidity and Reynolds number. This caused a poorer performance attained at the two λ tested, while the opposite is seen

for the $C = 0.04m$ blade because of the higher Reynolds number and also the higher solidity. The bigger blade also performed better when compared at the same Reynolds number, solely because of the higher solidity.

- The blade attained maximum lift at the onset of the stall and loss lift when stalled but begin to recover from stall effects when shedding vortices. Also, delayed stalled suppresses shedding of vortices which results in in increases and sustaining the lift in the positive performance region. The dynamic stall process is seen delayed with increases in Reynolds number and solidity.

Chapter 7

Conclusions and Recommendations

7.1 Conclusions

The blade chord influence on the aerodynamics and performance of vertical axis wind turbines has been investigated. The existing knowledge gaps relating to the blade chord influence on the aerodynamics and performance of VAWT in the published literature motivated this research. An additional VAWT configuration of different blade chord was manufactured based on the profiles of an existing VAWT of bigger blade chord for the appropriate comparisons and to achieving the aim of this study. Rigorous experimental tests were conducted on the two VAWT configurations for the determination of their power coefficients and also for the visualisation and measurements of the flow fields around a blade of each of the VAWTs. The spin down method was adopted for the measurement of the RPM and time aided the computation of the torque and the power coefficients were inferred. A thorough verification of settings was conducted before finally adopting a testing sequence, for the flow fields measurement using the PIV measurement techniques. These experiments were conducted in a wide range of wind speeds and also at various tip speed ratios. From the range of the wind speeds in which the VAWTs were tested, a reasonable map of a data set that includes performance and flow physics for the two configurations was acquired for the investigation.

The parametric studies were conducted to determine the selection of appropriate settings that led to the development of the two CFD models with the desired features. The developed CFD models are of the same scale with those used in the wind tunnel experimental measurements. The inclusion of the CFD investigation in this study was to complement the experimental investigation since all the required data for a thorough study could not be obtained through laboratory experiments only and also to further the understanding of VAWT while providing additional penetrating insights.

Following research tradition, the developed CFD models were validated by comparing results from the CFD simulations of the two models, with the authors experimentally acquired data of the wind tunnel models. Both the forces and the flow physics were compared. The rigorous validation campaign was initiated by turbulence modelling in which the list of available turbulence model, one equation fully turbulent S-A, two equations fully turbulent $\mathrm{k}-\varepsilon$ Realisable, $\mathrm{k}-\varepsilon$ RNG, Standard $\mathrm{k}-\omega$ and SST $\mathrm{k}-\omega$, was reduced to one turbulence model using a static aerofoil study. Thereafter the force validation followed by the by also including the Transitional SST model and then the final flow field validation. The Transitional SST model was considered the most appropriate and adopted for all he simulations presented in this study. The validation has also established the validity of the created CFD models since the degree of agreement between the authors experimental data and the results from the CFD model simulations was considered satisfactory based on literature.

With the validation campaigns satisfactorily concluded, detailed CFD tests were conducted at the same conditions in which the experimental data were acquired. The two CFD models were simulated at the desired three wind speeds in a wider range of tip speed ratios. The forces which include the drag, the lift and moments were monitored while running the simulations. A good map of a data set that includes the power coefficients, forces and flow physics was equally obtained from the CFD simulations that was used to complement those obtained from the experiments for further investigations. The following sections present the findings from this study which is broadly divided into revelation from experiments and revelation from CFD modelling.

7.1.1 Revelation from Experiments

The experimental investigations conducted in this study have revealed the following:

- The CP attained by a VAWT is dependent on the blade chord (solidity), wind speed and Reynolds numbers. The C = 0.03m (σ = 0.26) VAWT attained lower CP than the C = 0.04m (σ = 0.34) VAWT, both at the lowest and highest wind speeds the tests were conducted.
- At a smaller scale and tip speed ratios that extend to lower limits, two performance regions are attained by a VAWT; the negative performance region which prevents the VAWT from self starting and the positive performance region that also influence the design consideration of the VAWT. The width of the negative performance region increased with decrease in blade chord suggesting self starting of the VAWT of smaller chord is more difficult to attain than the VAWT with a bigger chord.
- In the positive performance region the VAWT of the bigger chord attained peak CP at a lower comparable tip speed ratio to that of the smaller chord in which peak CP is attained at a higher tip speed ratio.
- Deviation from the set wind speed resulting from solid blockage and power extraction from the wind speed was higher with the VAWT of the bigger blade chord and also at higher tip speed ratios indicating that higher extraction of power is mostly achieved at the optimum tip speed ratios than at the lower tip speed ratios.
- The four stages of the dynamic stall phenomenon; the onset of separation bubble, build up of the LEV, detachment of the LEV and build

up of the TEV, and detachment of the TEV and shedding of a pair of vortices are influenced by the blade chord, wind speeds and tip speed ratios.

- The start of the generation and shedding of vortices at a lower azimuth angle with predominantly higher occurrences of stall is earlier at lower tip speed ratios than at a higher tip speed ratio for the both VAWT configurations.
- The azimuth angle at which the generation and shedding of vortices begins is earlier at lower wind speeds and with the smaller blade chord.
- A comparison of the performance and flow fields of the two VAWT configurations at the same and different Reynolds numbers have been influenced by the solidity and the flow physics. A too early a start of the dynamic stall process has limited the VAWT to attaining lower performances while a late start of the dynamic stall process has caused the VAWT to attaining higher power coefficients at all the tip speed ratios, the comparisons were made. Also the higher solidity VAWT performed better than the lower solidity VAWT due to the influence of their blade chord in determining the Reynolds number the VAWT see.

7.1.2 Revelations from CFD Modelling

The computational fluid dynamics investigations conducted in this study have also revealed the following:

- The CFD modelling data of the two VAWT configurations at the desired three wind speeds have shown curves that are typical of the performance of wind turbines. The two performance regions revealed in the experimental investigation are also shown in the CFD CP-λ performance curves. The negative performance region (the dead band) is seen to increase in width and depth with decreased in either wind speed or blade chord.
- The performance of the VAWTs increased with increased in the wind speed and the blade chord for the cases studied, and within the range

of λ tested, the bigger chord attained higher peak CP at lower λ than the smaller chord at comparable wind speeds. The performance attained by the VAWTs are influenced by the solidity and the Reynolds numbers at which the VAWTs operates.

- The performance of the VAWT is dependent on the λ at which the VAWT operates. The λ also influence the angle of attack and the relative velocity. An increase in λ causes an increase in performance until peak performance is achieved and thereafter, the performance starts to drop off. Also increase in λ causes increase in the relative velocity at both the upwind and downwind sections of the rotation. Whereas an increase in λ causes decrease in the angle of attack at the upwind section and increase in angle of attack at the downwind section of the rotation. The combine effects of the relative velocity and the angle of attack influences the flow curvature of the blade at both sections of the rotation cycle.
- The structure of the shed vortices has been seen to be independent of the λ but the azimuth angle at which the blade stalled and the subsequent shedding of vortices is dependent on the λ, Reynolds number and the blade chord. At a lower λ, Reynolds number and smaller blade chord, stalling occur earlier at a lower azimuth angle with the resulting large scale shedding of vortices while at higher λ, Reynolds number and bigger blade chord there is delayed stall at a higher azimuth angle and less shedding of vortices.
- The flow physics has been shown to influence the performance of the two VAWT configurations when compared at the same λ. At different Reynolds numbers meaning the two configurations see the same wind speed, the C = 0.03m experienced an earlier blade stalled and shedding of vortices due to the nature of the smaller chord with a corresponding lower solidity and Reynolds number, hence the poorer performance attained at the two λ tested while a better performance is seen for the C = 0.04m blade because of the higher Reynolds numbers and also the higher solidity. The bigger blade also performed

better when compared at the same Reynolds number, solely because of the higher solidity.

- At the onset of stall, the blade attained maximum lift at and loses lift rapidly until the blade eventually stalled. But begin to recover from stall effects when shedding vortices. A delayed blade stalled causes the T_B curve to perform more in the positive region and also suppression of the stall process. The stall cycle is very brief when it eventually occurs. The delay in the occurrence of the dynamic stall process increases with increases in Reynolds numbers, tip speed ratios and blade chord.

7.2 Recommendations

A very important understanding about VAWT has been provided in this study. A combination of the power coefficient, forces and flow physics has been used to explain the performance of VAWT in greater details than what was obtained in the literature before this study was conducted. Although, the scale of the VAWTs used in this study are small when compared to the commercial VAWTs, the understanding gained and the applied methods in this study are adaptable in investigating lager scaled VAWT. The drawbacks of adapting the methods used in this study to larger scales is the cost of procuring a bigger test rig and the corresponding equipment, and construction of a bigger wind tunnel to fit the VAWT.

At comparable wind speeds and tip speed ratios, the performances attained by the two VAWT configurations; the power coefficients, forces and flow physics may not be attained by the commercial VAWTs operating in the fields due to variation and the unsteadiness of wind speed in the built environment, since the investigation presented in this study was conducted in a steady wind condition. However, the performance indices and understanding are the same. The following recommendations are made for future studies in VAWT:

- 3D CFD models and 3D PIV visualisation and measurement techniques, and also the extraction of forces from the PIV data should be implemented. This will enable a better comparison between the experimental data and numerical results which will eliminate the problems of infinite blade span and support arms which are always the reasons adduced for not achieving a complete match from validation of 2D CFD models against experimental results.
- The study has established the dependence of the VAWT performance on blade chord and since only two configurations were tested for brevity, it is recommended that more configurations that included a good range of $\sigma = 0.1$ to 1 inclusive be created and tested. Also, the results from the tests are used for detailed energy yield analysis to complement the force, power coefficient and flow physics investigations, to determine the best chord (solidity) or VAWT configuration that can guarantee the best performance under various wind fluctuations regimes.
- One of the constraints of conducting the experiments was the control of the wind tunnel fan to the desired RPM due to the distance of the fan control switch from the control desk. It is recommended, for future researches in the wind tunnel, that the fan be automated so a better and easier control over the fan can be achieved without moving between the desk and around the control switch to regulate the fan speed manually, and also for safety when the fan is required to be switched off immediately.

References

1. ’UK energy in brief” National Statistics Publication. URN 10D220. [accessed online 09/08/11], h.w.d.g.u.m.
2. Beri, H., Yao Y. (2011),"Effect of Camber Airfoil on Self-Starting of Vertical Axis Wind Turbines.” J. Environ. Sci. Technol. : 4, p 302 -312.
3. American Wind Energy Association, "Vertical axis wind turbine: the history of the DOE program" US Department of Energy, Sandia National Laboratories, American Wind Energy Association.
4. Dodd, H.H., Ashwill, T. D., Berg, D. E., Ralph, M. E., Stevenson, W. A., Veers, P. S., and Sandia National Laboratories.(1989), "Test Results and Status of the DOE/Sandia 34m Test Bed".The Canadian Wind Energy Association Conference.
5. Dodd, H.M. and Sandia National Laboratories. *Performance Predictions for an Intermediate-Sized VAWT Based on Performance of the 34m VAWT Test Bed.* in *The Ninth ASME WInd Energy Symposium.* 1990.
6. Berg, D.E., et al. *Aerodynamic Design and Initial Performance Measurements for the Sandia 34m Diameter Vertical Axis Wind Turbine.* in *The Ninth ASME Wind Energy Symposium.* 1990.
7. Mertens, S., Van Kuik, G., and Van Bussel, G., (2003), "Performance of an HDarrieus in the Skewed Flow on a Roof," Journal of Solar Energy Engineering, 125(4), pp. 433-440.
8. El-Samanuody, M., Ghorab, A. A. E., Youssef, Sh. Z. (2010), "Effects of some design parameters on the performance of a Giromill vertical axis wind turbine” Ain Shams Engineering Journal.,:1. p 85-95.
9. Jacobs, E.N. and A. Sherman, *Airfoil Section Characteristics as Affected by Variations of the Reynolds Number*, 1937.
10. Danao, L.A., Qin, N., Howell, R., (2012), "A numerical study of blade thickness and camber effects on vertical axis wind turbines". Proceedings of the Institution of Mechanical Engineers, Part A: Journal of Power and Energy; Pp 15.

11. Healy, J.V., *The Influence of Blade Thickness on the Output of Vertical Axis Wind Turbines.* Wind Engineering, 1978. **2**(1): p. 1-9.
12. Healy, J.V., *The Influence of Blade Camber on the Output of Vertical-Axis Wind Turbines.* Wind Engineering, 1978. **2**(3): p. 146-155.
13. Baker, J.R., (1983),"Features to Aid or Enable Self Starting of Fixed Pitch Low Solidity Vertical Axis Wind Turbines", Journal of Wind Engineering and Industrial Aerodynamics, 15 p.369-380.
14. Kirke, B.K., *Evaluation of Self-Starting Vertical Axis Wind Turbines for Stand-Alone Applications*, in *School of Engineering*1998, Griffith University.
15. Islam, M., D.S.K. Ting, and A. Fartaj, *Desirable Airfoil Features for Smaller Capacity Straight Bladed VAWT.* Wind Engineering, 2007. **31**(3): p. 165-196.
16. Islam, M., D.S.K. Ting, and A. Fartaj, *Aerodynamic Models for Darrieus-Type Straight-Bladed Vertical Axis Wind Turbines.* Renewable and Sustainable Energy Reviews 2008. **12**: p. 1087–1109.
17. Islam, M., et al., *Investigation on Low Reynolds Number Airfoils for Fixed-Pitch Straight-Bladed VAWT*, in *47th AIAA Aerospace Sciences Meeting*2009: Orlando, Florida.
18. McIntosh, S.C., *Wind Energy for the Built Environment*, in *Department of Engineering* 2009, Cambridge University: Cambridge. p. 164.
19. Sheldahl, R.E., P.C. Klimas, and L.V. Feltz, (1980) "Aerodynamic Performance of a 5m Diameter Darrieus Turbine with Extruded Aluminium NACA0015 Blades".
20. Templin, R.J., *Aerodynamic Performance Theory for the NRC Vertical-Axis Wind Turbine*, 1974, National Research Council of Canada: Ottawa, ON, Canada.
21. Glauert, H., *The Elements of Aerofoil and Airscrew Theory, 2nd Ed.*1948, Cambridge, UK: Cambridge University Press.
22. Strickland, J.H., *The Darrieus Turbine: A Performance Prediction Model Using Multiple Streamtubes*, 1975, Sandia National Laboratories: Albuquerque, New Mexico.

23. Wilson, R.E. and P. Lissaman, *Applied Aerodynamics of Wind Power Machines*, 1974, Oregon State University: Corvallis, OR, USA.
24. Mays, I. and B.A. Holmes, *Commercial development of the variable geomentry vertical axis windmill* International power generation, Surry, Uk, Sept, 1979.
25. Consul, C.A., et al., *Influence of Solidity on the Performance of a Cross-Flow Turbine* in *Proceedings of the 8th European Wave and Tidal Energy Conference.*2009: Uppsala, Sweden.
26. Blackwell, F.B., *Wind Tunnel Performance Data for the Darrieus Wind Turbine with NACA0012 Blades*, 1976.
27. Vassberg, J.C., A.K. Gopinath, and A. Jameson, *Revisiting the Vertical-Axis Wind-Turbine Design using Advanced Computational Fluid Dynamics*, in *43rd AIAA Aerospace Sciences Meeting and Exhibit - Meeting Papers*2005: Reno, Nevada, USA. p. 12783-12805.
28. Worstell, M.H., *Aerodynamic Performance of the 17-m-Diameter Darrieus Wind Turbine in the Three-Bladed Configuration: An Addendum. Technical Report No : SAND79-1753*, 1982.
29. Howell, R., et al., *Wind Tunnel and Numerical Study of a Small Vertical Axis Wind Turbine.* Renewable Energy, February 2010. **35**(2): p. 412-422.
30. Raciti Castelli, M., Betta, S.D., Benini, E., (2012), "Effect of Blade Number on a Straight-Bladed Vertical-axis Darreius Wind Turbine", World Academy of Science, Engineering and Technology; 61, Pp 305-311.
31. Eboibi, O., et al. *A Numerical Study of the Influence of Blade profile and Solidity on the Performance of Vertical Axis Wind Turbines.* in *51st AIAA Aerospace Sciences Meeting including the New Horizons Forum and Aerospace Exposition 07-10 January 2013, Grapevine (Dallas/Ft. Worth Region), Texas.* 2012.
32. Migliore, P., W. Wolfe, and J. Fanucci, *Flow Curvature Effects on Darrieus Turbine Blade Aerodynamics.* Journal of Energy, 1980. **4**(2): p. 49-55.

33. McIntosh, S.C. and H. Babinsky, *Aerodynamic Modelling of Swept Bladed Vertical Axis Wind Turbines*, in *47th AIAA Aerospace Sciences Meeting*2009: Orlando, Florida, USA.
34. Bertenyi, T., C. Wickins, and S.C. McIntosh. *"Enhanced Energy Capture through Gust-Tracking in the Urban Wind Environment,".* in *48th AIAA Aerospace Sciences Meeting Including the New Horizons Forum and Aerospace Exposition.* 2010. Orlando, Florida, USA.
35. Scheurich, F., T.M. Fletcher, and R.E. Brown. *2010, "The Influence of Blade Curvature and Helical Blade Twist on the Performance of a Vertical-Axis Wind Turbine,".* in *48th AIAA Aerospace Sciences Meeting Including the New Horizons Forum and Aerospace Exposition.* Orlando, Florida. USA.
36. Scheurich, F. and R.E. Brown, *2012, "Modelling the Aerodynamics of Vertical-Axis Wind Turbines in Unsteady Wind Conditions,.* Wind Energy,: p. pp. 17.
37. Ashwill, T.D., *Measured Data for the Sandia 34m Vertical Axis Wind Turbine*, 1992, Sandia National Laboratories: Albuquerque, New Mexico.
38. Shedahl, R.E., Klimas, P.C., Feltz L.V, 1980 "Aerodynamic performance of a 5-metre Diameter Darrieus Turbine with extruded NACA0015 Aluminiun Blade", Technical Report No: SAND80-0179
39. Edwards, J.M., (2012), "The Influence of Aerodynamic Stall on the Performance of VAWT Blades" Ph.D Thesis, Department of Mechanical Engineering, University of Sheffield, Sheffield.
40. Laitone E. V. (1997), Wind Tunnel Tests of Wings at Reynolds Numbers Below 70,000, Experiments in Fluids 23 p 405 - 409, Springer Verlage.
41. Kim, D., Chang, J., Chung, J., (2011), "Low-Reynolds-Number Effect on Aerodynamic Characteristics of a NACA0012 Airfoil", Journal of Aircraft, Vol. 48, 4, p.1212-1215.
42. McCroskey, W.J., McAlister, K. W.,Carr, L. W., and Pucci, S. L., (1982), An experimental study on dynamic stall on advanced airfoil sections. NASA TM-84245.

43. Carr, L.W., McAlister, K. W. and McCroskey, W. J., (1977) "Analysis of the development of dynamic stall based on oscillating airfoil measurements". NASA TN D-8382, and 1977.

44. Fujisawa, N., Shibuya, Satoshi, (2000), "Observations of dynamic stall on Darrieus wind turbine blades", Journal of Wind Engineering and Industrial Aerodynamics, 89 p.201-214.

45. Simão Ferreira, C.J., Bijl, H., van Bussel, G., and van Kuik, G., (2007), "Simulating Dynamic Stall in a 2D VAWT: Modeling strategy, verification and validation with Particle Image Velocimetry data". Journal of Physics: Conference Series, 2007. 75(1): p. 012023. , 2007.

46. Leishman, G., *Principles of Helicopter Dynamics*: Cambridge Aerospace Series.

47. Dabiri., J.O., (2011) "Potential Order-of-Magnitude Enhancement of Wind Farm Power Density Via Counter-Rotating Vertical-Axis Wind Turbine Arrays". Journal of Renewable and Sustainable Energy, 3(4).

48. Johnson S.F., "Proceeding of Vertical Axis Wind Turbine (VAWT) Design Technology Seminar for Industry", Sandia National Laboratry, Report No: SAND80-0984, USA.

49. Fielder, A., and Tullis, S., (2009), "Blade OUset and Pitch EUects on a High Solidity Vertical Axis Wind Turbine". Wind Engineering, 33 (3) : Pp 237–246.

50. Kiwata, T., Yamada, T., Kita, T., Takata, S.,Komatsu, N., and Kimura, S., (2010) "Performance of a Vertical Axis Wind Turbine with Variable-Pitch Straight Blades Utilizing a Linkage Mechanism", Journal of Enviroment and Engineering, Vol, 5 (1) Pp 213-225.

51. Bravo, R., Tullis, S., and Zaida, S., (2007) "Performance testing of a small scale Vertical Axix Wind Turbine" 21st Canadian Congress of Applied Mechanics, Toronto.

52. Li, Y., Tagawa, K., and Liu, W., (2010), "Performance Effects of Attachement on Blade on a Straight-Bladed Vertical axis Wind Turbine" Journal of Current Applied Physics, 10 Pp 335-338

53. Edwards, J.M., Danao, L. A., and Howell, R. J., 2012, "Novel Experimental Power Curve Determination and Computational Methods for the Performance Analysis of Vertical Axis Wind Turbines," Journal of Solar Energy Engineering, 134(3), pp. 11.
54. Danao, L.A., Edwards, J., Eboibi, O., Howell, R. J., (2013), "A Numerical Investigation into the Effects of Fluctuating Wind on the Performance of a Small Scale Vertical Axis Wind Turbine", Engineering letters, Vol, 21: 3 p 149-157. .
55. Danao, L.A., (2012), "The Influence of Unsteady Wind on the Performance and Aerodynamics of Vertical Axis Wind Turbines, Ph.D Thesis, Department of Mechanical Engineering, University of |Sheffield, Sheffield. , 2012.
56. Brochier, G., Fraunie P, Paraschivoiu, I., (1986), "Water Channel experiments of Dynamic Stall on Darrieus Wind Turbine Blades". AIAA Journal Propulsion September-October; 2 (5) Pp 445-459. .
57. Simão Ferreira, C.J., et al., *Visualization by PIV of Dynamic Stall on a Vertical Axis Wind Turbine.* Experiments in Fluids, 2009. **46**(1): p. 97-108.
58. Paraschivoiu, I., *Double-Multiple Streamtube Model for Darrieus Wind Turbines*, in *Second DOE/NASA wind turbines dynamics workshop NASA CP-2186*1981: Cleveland, Ohio, USA. p. 19-21.
59. Larsen, H.C., *Summary of a Vortex Theory for the Cyclogiro.*, in *Proceedings of the 2nd US National Conferences on Wind Engineering Research*1975: Colorado State University, Colorado, USA. p. V8-1-3.
60. Fanucci, J. and R. Walters. *Innovative wind machines: the theoretical performance of a vertical-axis wind turbine.* in *In: Proceedings of the vertical-axis wind turbine technology workshop.* 1976. Albuquerque, NM, USA.
61. Wilson, R.E., *Wind-turbine aerodynamics.* Journal of Wind Engineering and Industrial Aerodynamics, 1980. **5**(3–4): p. 357-372.
62. Holme, O. *A contribution to the aerodynamic theory of the vertical-axis wind turbine.* in *In: Proceedings of the International Symposium on Wind Energy Systems.* 1977. Cambridge, England.

63. Strickland, J.H., B.T. Webster, and T. Nguyen, *A Vortex Model of the Darrieus Turbine: An Analytical and Experimental Study.* Journal of Fluids Engineering, 1979. **101**(4): p. 500-505.
64. McIntosh, S.C., Babinsky, H., (2008), "UnsteadyPower Output of Vertical Axis Wind Turbines operating within a Fluctuating Free-stream", 46th AIAA Aerospace Siences Meeting and Exhibition, 7-10 January 2008, Reno, Nevada.
65. Beri, H., and Yao, Y., (2011), "Double Multiple Stream Tube Model and Numerical Analysis of Vertical Axis Wind Turbine". Energy and Power Engineering, 3 pp. 262-270.
66. Scheurich, F., Fletcher, T. M., and Brown, R. E., (2010), "Simulating the aerodynamic performance and wake dynamics of Vertical Axis Wind Turbine". Wind Energy, Pp
67. Mohamed, M.H., (2012), "Performance investigation of H-rotor Darrieus Turbine with new airfoil shapes". Energy; 47, Pp 522-530.
68. McLaren, K., S. Tullis, and S. Ziada, *Computational fluid dynamics simulation of the aerodynamics of a high solidity, small-scale vertical axis wind turbine.* Wind Energy, 2012. **15**(3): p. 349-361.
69. Amet, E., Maitre, T., Pellone, C., and Achard, J. L., (2009), "2D Numerical Simulations of Blade-Vortex Interaction in a Darrieus Turbine," Journal of Fluids Engineering, 131(11), pp. 111103-15.
70. Laneville, A., and Vittecoq, P., (1986), "Dynamic Stall: The Case of the Vertical Axis Wind Turbine," Journal of Solar Energy Engineering, 108(2), pp. 140- and 145.
71. Kok, J.C., (1999), "Resolving the Dependence on Free Values for K-w Turbulence model". National Aerospace Laboratory NLR, No, NLR-TP-99295.
72. Untaroiu, A., Wood, H. G., Allaire, P. E., and Ribando, R. J., (2011),"Investigation of Self-Starting Capability of Vertical Axis Wind Turbines Using a Computational Fluid Dynamics Approach," Journal of Solar Energy Engineering, 133(4), pp. 041010-8.

73. Hill, N., Dominy, R., Ingram, G., and Dominy, J., (2008), "Darrieus Turbines: The physics of Self- Starting". Proc. Inst. Mech. Eng., Part A, 223 pp. 21-29.

74. Iida, A., A. Mizuno, and K. Fukudome. *Numerical Simulation of Unsteady Flow and Aerodynamic Performance of Vertical Axis Wind Turbines with LES.* in *16th Australasian Fluid Mechanics Conference.* 2007. Gold Coast, Australia.

75. Raciti Castelli, M., A. Englaro, and E. Benini, *The Darrieus wind turbine: Proposal for a new performance prediction model based on CFD.* Energy, 2011. **36**(8): p. 4919-4934.

76. Raciti Castelli, M., Ardizzon, G., Battisti, L., Benini, E., and Pavesi, G., (2010), "Modelling Strategy and Numerical Validation for a Darrieus Vertical Axis Micro-Wind Turbine," ASME Conference Proceedings, 2010 (44441), pp. 409- 418.

77. Simão Ferreira, C.J., G.J.W. van Brussel, and G. van Kuik, *2D CFD Simulation of Dynamic Stall on a Vertical Axis Wind Turbine: Verification and Validation with PIV Measurements*, in *45th AIAA Aerospace Sciences Meeting and Exhibit*2007, AIAA: Reno, Nevada.

78. Lee, T. and P. Gerontakos, *Investigation of flow over an oscillating airfoil.* Journal of Fluid Mechanics, 2004. **512**: p. 313-341.

79. Danao, L.A., and Howell, R., (2012), "Effects on the Performance of Vertical Axis Wind Turbines with Unsteady Wind Inflow: A Numerical Study," 50th AIAA Aerospace Sciences Meeting including the New Horizons Forum and Aerospace Exposition, Nashville, Tennessee.

80. Baker, J., *Features to aid or enable self starting of fixed pitch low solidity vertical axis wind turbines.* Wind engineering and industrial aerodynamics, 1983. **15**: p. 369-380.

81. Al-Garni, A.M., 2007, "Low speed calibration of hot-wire anemometers". Flow Measurement and Instrumentation, 18 (2): p. 95-98.

82. Özahi, E., M.Ö. Çarpınlıoğlu, and M.Y. Gündoğdu, 2010, "Simple methods for low speed calibration of hot-wire anemometers". Flow Measurement and Instrumentation, 21 (2): p. 166-170.

83. Tutkun, M., et al.,2009, "In situ calibration of hot wire probes in turbulent flows". Experiments in Fluids. 46 (4): p. 617-629.

84. Lomars, C.G., 1986, "Fundamentals of Hotwire Anemometry" Cambridge: Cambridge University Press.

85. Singha, A.a.R.S., 2013, "In situ calibration of four-wire hot-wire probes for atmospheric measurement". Experimental Thermal and Fluid Science.44, p. 82-89.

86. Instruction Manual, "Model 9306A Six-Jet Atomizer." P/N 19300099, Revision B.

87. Lamb, H., (1994). Hydrodynamics, Cambridge University Press, 6th edition, p.599.

88. DanymicStudio v3.20 user 's guild.

89. Pierce, A.J., Lu, F.K, (2011). "New Seeding and Surface Treatment Methods for Particle Image Velocimetry", 49th AIAA Aerospace Sciences Meeting including the New Horizons Forum and Aerospace Exposition 4 - 7 January 2011, Orlando, Florida..

90. Simão Ferreira, C.J., et al., *PIV Visualization of Dynamic Stall VAWT and Blade Load Determination*, in *46th AIAA Aerospace Sciences Meeting and Exhibit*2008, AIAA: Reno, Nevada, USA.

91. Raffel, M., Willert, C., Wereley, S., and Kompenhams, J., (2007). "Particle Image Velocimetry: A Practical Guide". Springer, second edition edition.

92. Fujisawa, N., and Takeuchi, M., (1999), "Flow Visualisation and PIV Measurement of Flow Field Around a Darrieus Rotor in Dynamic Stall", Journal of Visualisation, Vol. 1,4 p.379-386.

93. Massey, B., (2006). "Mechanics of Fliuds", Taylor and Francis, London.

94. Ansys Inc. Fluent 12.1 Documentation.

95. ASME, "Standard for verification and validation in computational fluid dynamics and heat transfer", ASME V&V and A.S.o.M.E. 20-2009, New York, NY.

96. American Institute of Aeronautics and Astronautics, "Guide for Verification and Validation of Computational Fluid Dynamics Simulations", AIAA G-077-1998, Reston, VA.

97. Shedahl, R.E., and Klimas, P. C., (1981), "Aerodynamic Characteristics of Seven Symmetrical Airfoil Sections through 180-Degree Angle of Attack for Use in Aerodynamic Analysis of Vertical Axis Wind Turbines.," Technical Report No. SAND80-2114, Sandia National Laboratories, Albuquerque, New Mexico., ed.

98. Menter, F.R., 1993, "Zonal Two Equation k-ω Turbulence Models for Aerodynamic Flows", AIAA 31st Aerospace Sciences Meeting and Exhibition January 11-14, Reno, Nevada.

99. Danao, L.A., Edwards, J., Eboibi, O., Howell, R. J., "The Performance of a Vertical Axis Wind Turbine in Fluctuating Wind - A Numerical Study" Proceedings of the World Congress on Engineering 2013 Vol III,WCE 2013, July 3 - 5, 2013, London, U.K., ed.

100. Simão Ferreira, C.J., *The near wake of the VAWT - 2D and 3D views of the VAWT aerodynamics*, 2009.

101. Marini, M., A. Massardo, and A. Satta, *Performances of Vertical Axis Wind Turbines with Different Shapes.* Journal of Wind Engineering and Industrial Aerodynamics, 1992. **39**: p. 83-93.

Appendix

Experimental Error Analysis

The accuracy of measurements of physical quantities in the laboratory is error prone, so, there can be discrepancies of measured data. These discrepancies in measurements can be classified into two broad categories; precision and bias errors. The major source of the precision errors is error due to parallax which is also known as least count of the scale. This is often caused by the way the individual taking the measurements eye the scale. Precision errors can also result from the signal conversion of analog to digital and fluctuating test conditions, while the bias errors, also known as systematic errors, are mostly caused by a calibration error in measuring apparatus. Systematic errors usually can cause constant absolute error or a constant percentage error in all readings.

With the complexity of experimental measurements in this investigation, the errors in the acquired data are both precision and systematic. So the analysis presented is propagated from the measurements of the physical quantities to the final power coefficients. For brevity, the error analysis of the desired highest wind speed of 8m/s and at $\lambda = 4$ is presented, while noting that fluctuations in temperature and pressure can affect the free stream velocity during measurements. Error analysis of measurement of the wind speed variation that ranges between ± 0.05 is adopted since the standard error of the cascaded flow velocity measurement form pressure differential readings computed from the hot wire is within ±0.05m/s. The pressure differential was varied within ±0.01Pa, and the variation in flow velocity was calculated using Equation 3.3.

A.1 Wind Power Measurements

Table 1 presents the percentage error in the free stream wind speed and the wind power based on the variations of wind speed within ±0.05m/s. Percentage error of ±0.625% in wind velocity is computed which is propagated to 1.886%

and -1.863% in available wind power. The propagated errors in the wind power are in order, since wind power is related to the cube of wind velocity.

V_w (m/s)	ρ (Pa)	P_w (W)	% V_w error	% P_w error
8.00	1.225	131.712		
8.05 (+0.05)	1.225	134.197	0.625	1.886
7.95 (-0.05)	1.225	129.257	-0.625	- 1.863

Table 1. Errors in wind power relative to the errors in flow velocity measurements.

Wind velocity is an important parameter that actually determines the performance measurements of wind turbines. Errors arising from wind velocity measurement should be reduced to the minimum to achieve a reasonable level of measurement accuracy.

A.2 Blade Power Measurements

The variations in the wind velocity can also affect the RPM of the rotor. From the experimental data, the RPM of the wind speeds and the cascaded error estimate in the blade power are presented in Table 2. The small ±0. 05 error estimates in the flow speed can be seen to have caused ± 5.5 changes in the RPM. The effects in the RPM are equally seen in the total resistive torque measurements.

RPM	resT (Nm)	rotT(Nm)	T_B	P_B (W)	% P_B error
873	-0.2320	0.2922	0.5242	47.9268	
878.5 (+5.5)	-0.2334	0.2922	0.5256	48.7573	1.703
867.6 (-5.4)	-0.2309	0.2922	0.5231	47.5273	-0.8335

Table 2. Errors in blade power relative to the errors in RPM measurements.

The propagated effect is shown in the blade power, as the percentage error estimate of the P_B ranges from a low negative -0.8335% to a positive 1.703. These variations in the error estimates are in sync with the performance of the VAWT seen in Figure 5.15. At a higher RPM away from $\lambda = 4$, the increase in the error estimates will tend to reduce CP, which is a reflection of the reduced ratio of the blade power to the wind power in Table 3.

A.3 Cumulative Error in Power Coefficients

Table 3 is the propagated CP error estimates from the flow velocity through the wind power, and RPM to blade power. A maximum error estimates of approximately ±1% can be seen. Considering the size of the VAWTs used in this investigation the error estimates is reasonable. The major factors that tend to influence the error estimates of the CP, is the accuracy of the flow velocity measurements which is dependent on the precision and systematic errors.

P_w (W)	P_B (W)	CP	% CP error
131.712	47.9268	0.3638	
134.197 (+1.886%)	48.3552 (+1.703%)	0.3603	-0.962
129.257 (- 1.863%)	47.5273 (-0.8335%)	0.3676	1.044

Table 3. The errors in CP relative to P_B and P_W